



HAL
open science

Dirac equation approach to the spectroscopic properties of topological materials

Xin Lu

► **To cite this version:**

Xin Lu. Dirac equation approach to the spectroscopic properties of topological materials. Mesoscopic Systems and Quantum Hall Effect [cond-mat.mes-hall]. Université Paris-Saclay, 2021. English. NNT : 2021UPASP103 . tel-03466970

HAL Id: tel-03466970

<https://theses.hal.science/tel-03466970>

Submitted on 6 Dec 2021

HAL is a multi-disciplinary open access archive for the deposit and dissemination of scientific research documents, whether they are published or not. The documents may come from teaching and research institutions in France or abroad, or from public or private research centers.

L'archive ouverte pluridisciplinaire **HAL**, est destinée au dépôt et à la diffusion de documents scientifiques de niveau recherche, publiés ou non, émanant des établissements d'enseignement et de recherche français ou étrangers, des laboratoires publics ou privés.

Dirac equation approach to the
spectroscopic properties of
topological materials

*Propriétés spectroscopiques des matériaux
topologiques étudiées à l'aide de
l'équation de Dirac*

Thèse de doctorat de l'université Paris-Saclay

École doctorale n°564, Physique en Île-de-France (PIF)

Spécialité de doctorat : Physique

Unité de recherche : Université Paris-Saclay, CNRS, Laboratoire de Physique
des Solides, 91405, Orsay, France

Graduate School : Physique

Référent : Faculté des sciences d'Orsay

**Thèse présentée et soutenue à Paris-Saclay,
le 19/10/2021, par**

Xin LU

Composition du jury:

Pascal SIMON

Professeur, Université Paris-Saclay

Président

Dario BERCIoux

Maître de conférences (éq. HDR), DIPC Donostia-San Se-
bastián

Rapporteur & Examineur

Björn TRAUZETTEL

Professeur, University of Würzburg

Rapporteur & Examineur

Silke BIERMANN

Professeure, Ecole Polytechnique

Examinatrice

Milan ORLITA

Chargé de recherche, LNCMI Grenoble

Examineur

Direction de la thèse:

Mark-Oliver GOERBIG

Directeur de recherche, LPS Orsay

Directeur de thèse

Dirac equation approach to the spectroscopic properties of topological materials

by

Xin Lu

A document submitted in partial fulfillment of the requirements for the degree of

Doctor of Philosophy in Physics

at

UNIVERSITÉ PARIS-SACLAY

ACKNOWLEDGMENTS

Foremost, I would like to express my sincerest gratitude to my Ph.D. advisor, Dr. Mark-Oliver Goerbig, for his fatherly patience, enlightening guidance, and endless vitality. He taught me a lot of beautiful physics that I have dreamt of. He has shared with me his good research taste from which I will benefit from my career. All his insightful comments on my works have always been an invaluable source of inspiration to deepen my understanding. I also would like to thank Mark for his friendship, empathy, and great sense of humor. I will remember forever the comforting message that Mark sent to me during the first confinement in France. He is always prepared to listen to me and try to resolve my anxiety. Without Mark, I might have still finished my Ph.D. but I could never end it full of warm memories, happiness, and satisfaction.

My sincere thanks go to the rest of the jury of my thesis: Dr. Dario Bercioux and Pr. Björn Trauzettel as reporters, Pr. Silke Biermann, Dr. Milan Orlita, and Dr. Pascal Simon as examiners, for their acceptance to participate in the defense. Special thanks to Silke, who was my teacher of solid-state physics at Ecole Polytechnique and opened the door for me to the world of condensed matter theory, Milan, with whom I collaborate closely in the NbAs₂ project and who always has refreshing ideas, and Pascal, who taught me the basics of many-body physics and who continues to discuss with me in the lab. I would like to also thank my committee of thesis formed by Dr. Louis-Anne de Vaultier and Dr. Miguel Monteverde, who have given me many useful pieces of advice for my future career.

I thank all the collaborators I have worked with on various fascinating projects. In particular, I would like to thank Dr. Dibya Kanti Mukherjee for our brotherhood-like tight friendship and efforts on the project of Volkov-Pankratov plasmons, Jan Wyzula for all the informative exchanges on the NbAs₂ project, David Alspaugh who incited me to rephrase my work in a general mathematical context.

During my three years' stay in Laboratoire de Physique des Solides, I would like to thank all the permanents in the theory group, especially Dr. Frédéric Piechon, from whom I have learned a lot of physics, Pr. Marc Gabay, who is the mentor to initiate me in teaching, and Marie-France Mariotto for all her help in administration stuff.

Of course, I will not forget to thank all my young fellow lab-mates of which I cannot exhaust the list here. I am grateful to Dr. Pierre Bruneel, with whom I share the office as well as the knowledge in physics and who is the first listener of my complaints, Dr. Maxime Garnier for his French humor,

Ansgar Graf who was also my roommate during the workshop in Aussois, Dr. Jonathan Atteia with whom I discuss many papers on graphene, and Brendan Le Pennec who was my classmate during my master and told me recent progress on spin liquids.

Undoubtedly, I deeply thank all my relatives, especially my wife for her warm accompaniment through my thesis and comforting words of encouragement that offer me confidence and courage, and my parents and parents-in-law for their continuous support and care.

Finally, I would like to say something to encourage all other young physicists like me, who are trying to do a good thesis. Ph.D. is never easy. “Doing a Ph.D. is like having a baby”, said Mark, my Ph.D. advisor. One needs to give one’s motherly passion and patience to grow the baby, i.e., the thesis. One of my energy sources that I would like to share here was best said by the scientific giant, Paul Dirac, “Living is worthwhile if one can contribute in some small way to this endless chain of progress”. By the way, the time span of the thesis reminds me about Nezha the Third Lotus Prince, a protection deity in Chinese folk religion who was born after three years of pregnancy just like a thesis. I wish that my thesis could be Nezha in the sense that it could inspire other scientists and bring them courage and luck.

CONTENTS

1	INTRODUCTION	1
1.1	Dirac equation in a nutshell	3
1.2	High-energy physics in Dirac materials	6
1.2.1	Zoology of Dirac materials	7
1.2.2	Relativistic phenomena in graphene	10
1.3	Topology in materials	12
1.3.1	Topological band theory and Berry phase	14
1.3.2	Bulk-edge correspondence: emergence of gapless surface states	16
1.3.3	Topological heterojunction: Dirac equation approach	17
1.4	Outline of the thesis	20
2	SPECIAL RELATIVITY IN DIRAC MATERIALS	21
2.1	Special relativity in Graphene: crossed electric and magnetic fields	22
2.1.1	Unexpected massless Dirac equation in graphene	22
2.1.2	Refresher on special relativity	28
2.1.3	Landau levels in the presence of crossed electric and magnetic fields	29
2.2	Unitary and hyperbolic transformations	31
2.2.1	Unitary transformations: rotations	32
2.2.2	Hyperbolic transformations: Lorentz boost	33
2.2.3	Cheating sheet for unitary and hyperbolic transformations	35
2.2.4	Generalized unitary and hyperbolic transformations: recipe	37
2.3	Wavefunctions of Hamiltonian for graphene in crossed electric and magnetic fields	39
2.4	Landau levels of generic Dirac Hamiltonian	42
2.4.1	Three-dimensional Weyl semimetal: angle-dependent regime	44
2.4.2	Two-dimensional tilted gapped graphene: gap renormalization	45
2.4.3	Gapped dispersive nodal-line semimetal: gap closing	47
2.5	Renormalization effect in the language of condensed matter	48
2.5.1	Anisotropy of Fermi surface	48

Contents

2.5.2	Direct gap vs. indirect gap	52
2.6	Summary	54
3	THEORETICAL APPROACH TO SPECTROSCOPY	55
3.1	Quantum theory of optical properties	56
3.1.1	Electric dipole approximation	57
3.1.2	Linear response theory: Kubo formula	59
3.1.3	Magnetic Faraday and Kerr rotation: off-diagonal term	62
3.1.4	Landau quantization and selection rules	64
3.2	Magneto-optics of a gapped nodal-line semimetal	65
3.2.1	Optical conductivity in the absence of magnetic field	67
3.2.2	Selections rules in the presence of a magnetic field	68
3.3	Plasmon and electron energy loss spectroscopy	72
3.4	Summary	74
4	TOPOLOGICAL HETEROJUNCTION: EMERGENCE OF VOLKOV-PANKRATOV STATES	75
4.1	Topological heterojunction: theoretical models	76
4.1.1	Two-dimensional toy model	76
4.1.2	Three-dimensional topological insulator	77
4.1.3	Two-nodes Weyl semimetal	78
4.1.4	Linearization of the models	79
4.2	Origin of Volkov-Pankratov states	80
4.2.1	Smoothness as pseudo-magnetic field	81
4.2.2	Smoothness-induced confinement: Dirac quantum well	84
4.2.3	Coupling between two surfaces: double Dirac quantum well	88
4.2.4	Supersymmetry in Dirac equation	98
4.2.5	Leakage from bulk: lattice model	99
4.3	Summary	100
5	SPECTROSCOPIC PROPERTIES OF VOLKOV-PANKRATOV STATES	103
5.1	Optical conductivity: smoking gun for the existence of Volkov-Pankratov states	104
5.1.1	Two-dimensional toy model	106
5.1.2	Three-dimensional topological insulator	111
5.1.3	Bulk-surface transitions	118
5.1.4	Electric field perpendicular to the interface: relativistic renormalization	120
5.2	Faraday and Kerr rotation	121

5.3	Surface plasmons of Weyl semimetals	123
5.3.1	Hamiltonian, spectrum and wavefunctions	123
5.3.2	Non-interacting dynamical polarization and quasi-two-dimensional random phase approximation	126
5.3.3	Plasmon in the three-band model	127
5.4	Summary	133
6	CONCLUSIONS AND PERSPECTIVES	135
A	SHORT REVIEW ON SPECIAL RELATIVITY	139
A.1	Lorentz boost and four-vectors	139
A.2	Maxwell's equations are Lorentz invariant	141
B	SIMPLIFICATION OF THE GENERIC MODEL	143
B.1	Diagonalization of the symmetric velocity tensor	143
B.2	Rescaling of the wavevectors and the magnetic field	144
B.3	Direction of the tilting term	145
C	GAPPED NODAL LINE SEMIMETAL NIOBIUM DI-ARSENIDE	147
C.1	Crystal structure	147
C.2	Low Energy Model for two nodal lines	148
C.2.1	Position of the nodal lines	148
C.2.2	Low-energy Hamiltonian	148
C.3	Optical conductivity in the absence of a magnetic field	152
C.4	Fitting	152
C.5	Selection rules in the presence of a magnetic field	153
C.5.1	Landau levels	154
C.5.2	Velocity operators	155
D	CALCULATIONS FOR DOUBLE DIRAC QUANTUM WELL	157
D.1	Derive and solve the secular equation for double Dirac quantum well	157
D.2	Energy splitting for the topological state	159
E	MAGNETO-OPTICAL CONDUCTIVITY OF 2D TOPOLOGICAL HETEROJUNCTION	163
E.1	Wavefunctions of the 2D toy model	163
E.1.1	In the absence of a magnetic field	163
E.1.2	In the presence of a magnetic field	164

Contents

E.2	Derivation of the selection rules	165
E.2.1	In the absence of a magnetic field	165
E.2.2	In the presence of a magnetic field	166
E.3	Optical conductivity in the absence of a magnetic field	166
E.3.1	Polarization along the x -axis	166
E.3.2	Polarization along the y -axis	169
E.4	Optical conductivity in the presence of a magnetic field	170
E.4.1	Polarization along the x -axis	170
E.4.2	Polarization along the y -axis	172
SYNTHÈSE EN FRANÇAIS		175
ACRONYMS		181
LIST OF SYMBOLS		183
BIBLIOGRAPHY		185
CURRICULUM VITAE		205

1 INTRODUCTION

A great deal of my work is just playing with equations and seeing what they give.

Paul Dirac

The Dirac equation is a quantum mechanical wave equation originally proposed by Paul Dirac in 1928 [1, 2] to describe all spin-1/2 relativistic particles in high-energy physics moving at a speed v close to the speed of light c . It incorporates Einstein's theory of special relativity in the framework of quantum mechanics. The Dirac equation is thus a relativistic version of the Schrödinger equation that governs the motion of non-relativistic particles in quantum mechanics, or conversely, the Schrödinger equation is an approximate version of the Dirac equation when $v \ll c$.

In condensed matter physics, low-energy electrons moving at a speed $v/c \ll 1$ are soundly seen as non-relativistic particles. One might think that the Schrödinger equation would suffice to describe electrons in solids and the relativistic effects are a small correction term such as spin-orbit coupling (SOC) [3]. It seems that the ultra-relativistic, i.e., massless, Dirac equation (also known as the Weyl equation [4]) was thought to be only applicable for high-energy elementary particles. Surprisingly, by the interplay between the periodic crystal lattice potential and electrons, the massless Dirac equation emerges in the low-energy description of the electronic structure of solids, yet another manifestation of the idea "*More is different*" by Anderson [5]. This is one of the most spectacular recent findings in the realm of condensed matter physics. The relativistic massless Dirac equation or variations of it can actually describe the physics around the Fermi level of real materials such as graphene [6, 7], Dirac/Weyl semimetals [8, 9, 10], nodal-line semimetals [11], etc. These materials are named Dirac materials in which the mathematical treatment for the electrons is perfectly identical to that of relativistic high-energy elementary particles.

This discovery makes the high-energy physicists' dream come true that one can access relativistic systems in a table-top device in which one can simulate relativistic experiments. One requires much less experimental conditions than the usual ones in traditional high-energy physics. Therefore, high-energy physicists and field theorists now have a fascinating playground in these low-energy systems where their theory can be applied and verified.

1 Introduction

Reciprocally, the idea that relativistic physics is manifest in condensed matter is not uniquely rewarding for high-energy physicists. It is also enlightening for condensed matter physicists. Many unexpected observations in Dirac materials are thus attributable to the special relativity embedded in the Dirac equation. Described by the Dirac instead of Schrödinger equation, Dirac electrons must have peculiar transport and spectroscopic properties different from the usual Schrödinger ones. Especially, the arsenal of theoretical tools to study them are already well-established thanks to huge efforts made by high-energy physicists. Working in condensed matter theory, high-energy formalism refreshes the understanding of Dirac materials.

The discovery of Dirac materials accompanies also the development of the revolutionary concept of topology encrypted in wavefunctions. For long time since the proposal of Bloch's theorem [12], condensed-matter physicists have been interested mostly in the electronic band structure of solids and often forgotten information encoded in the wavefunctions apart from their symmetry properties which matter in optical transitions. The importance of wavefunctions is best illustrated by a brain-refreshing example that two Hamiltonians with exactly the same energy spectrum could have distinguishing electromagnetic responses as shown in the seminal paper of Haldane [13]! These two Hamiltonian are now classified as topologically different phases of matter by an index called *topological invariant*. The idea behind this is that the topology of a Hamiltonian describes how the energy bands are coupled to each other so that only responses involving interband process such as the Hall conductivity [14] can reveal the topological properties of matter. This is also the reason why people have overlooked the topological aspect of Hamiltonians for a long time while considering only one band alone, especially in semi-classical treatments [15]. Therefore, a matrix formulation of the Hamiltonian is necessary to study all the relevant bands together in order to capture the topological properties of solids. The scalar Schrödinger Hamiltonian should be thus replaced by the matrix Dirac Hamiltonian.¹ Hence, the Dirac equation and its variants are also suitable to describe the low-energy physics of topological materials (including Dirac materials), namely materials having intriguing properties due to the non-trivial topology of their Hamiltonian.

One of the tantalizing properties of topological materials is the bulk-edge correspondence which means that topologically protected conducting edge states exist when the bulk Hamiltonian is topologically non-trivial. These edge states are believed to enable the fabrication of more energy-efficient microelectronic components, better catalysts, improved thermoelectric converters, new magnetic storage media or even quantum computers [16]! The mechanism of emergence of the edge states of topological materials is the band inversion meaning that the order of valence and conduction bands in energy is inverted across the interface between materials and vacuum. To explicitly show the presence of the edge states, the Dirac equation, which now becomes spatially dependent, is the unavoidable theoret-

¹Especially, a linear conical band dispersion requires at least two bands where the use of the Pauli matrices are natural.

ical formalism. It is actually a unifying general approach to study all the surface states of topological systems related to band inversions.

In summary, the Dirac equation occupies an essential position in the recent progress of condensed matter physics. The reader will also find the Dirac equation throughout this thesis which is interested in the spectroscopic properties of topological materials using the Dirac equation. In the present introductory chapter, I would like to first recapitulate the history of the Dirac equation. Then, I will show some examples of Dirac materials of which the Hamiltonians are described by generalized versions of the Dirac equation. As a paradigm of Dirac materials, graphene is the best to illustrate the idea of “doing high-energy physics in low-energy systems” of which I will give three examples here. After that, I will briefly present topological band theory and topological materials using the model proposed by Haldane [13], also known as a quantum anomalous Hall insulator. Within this model, the bulk-edge correspondence manifests itself as a bulk insulating phase with topologically protected conducting channels at its edges. This will be explained by a general argument based on the topological band theory. Furthermore, I will derive the energy and the wavefunctions of these topological edge states with the help of the Dirac equation by which the band inversion mechanism is explicitly shown. The stability of the edge states is understood by the Jackiw-Rebbi argument [17] or by the Aharonov-Casher argument [18].

1.1 DIRAC EQUATION IN A NUTSHELL

** The historical aspect on the Dirac equation is entirely credited to Austin Kcon Cheng. I learned this fascinating history totally from his thesis [19] and rephrase it in this section.*

I cannot resist to sharing a historical perspective on the Dirac equation. In 1900, Max Planck postulated that electromagnetic energy could be emitted in quantized form, later known as photon, based on his experimental observation of black-body radiation. This observation is now seen as the ignition of the following explosion of knowledge on quantum mechanics. Twenty-six years later, to describe a particle as a wave in an explicit way, Erwin Schrödinger [20] came up with one of the most important equations in the Human history:

$$i\hbar \frac{\partial}{\partial t} \psi(\mathbf{r}, t) = \left[-\frac{\hbar^2}{2m} \nabla^2 + V(\mathbf{r}, t) \right] \psi(\mathbf{r}, t) \quad (1.1)$$

where $\hbar = h/2\pi$ is the reduced Planck constant, m is the mass of the particle of interest, $V(\mathbf{r}, t)$ is the energy potential which the particle experiences at a given position \mathbf{r} and time t and $\psi(\mathbf{r}, t)$ is the wavefunction that fully determines the particle’s movement in a probabilistic way. This equation is now given the name of *Schrödinger’s equation*. The right part in the square brackets can be seen as an

1 Introduction

operator known as the *Hamiltonian* acting on the wavefunction ψ . The eigenvalue of the Hamiltonian is the total energy of the particle including kinetic and potential energy. Solving the spectrum of a given particle is finding the eigenvalue of its corresponding Hamiltonian. By the principle of correspondence, one can write the Hamiltonian for Eq. (1.1)

$$\hat{H} = -\frac{\hbar^2}{2m}\nabla^2 + V(\mathbf{r}, t) = \frac{\hat{\mathbf{p}}^2}{2m} + V(\mathbf{r}, t) \quad (1.2)$$

where the momentum operator $\hat{\mathbf{p}}$ is introduced. In this form, it is clear that Schrödinger's equation is only valid for non-relativistic particles, e.g., electrons with moderate velocity compared to the speed of light, because the kinetic energy part is $p^2/2m$. Then, Eq. (1.1) becomes

$$i\hbar\frac{\partial}{\partial t}\psi(\mathbf{r}, t) = \hat{H}\psi(\mathbf{r}, t). \quad (1.3)$$

However, in Einstein's special relativity [21], the energy of a relativistic particle is

$$E^2 = p^2c^2 + m^2c^4 \quad (1.4)$$

where E is the energy of the particle, p is the momentum, m is the rest mass of the particle and c is the speed of light. It is the famous Einstein's energy-momentum relation. Furthermore, Einstein suggested in his special relativity theory that the time dimension should play the same role as the spatial dimensions. But, the Schrödinger equation isolates the time dimension as a special one. It has the second derivative in space but only the first derivative in time. To write a relativistic equation for quantum mechanics, it is tempting to replace E by $i\hbar\partial_t$ and \mathbf{p} by $-i\hbar\nabla$ in Eq. (1.4). By doing so, one has

$$-\hbar^2\frac{\partial^2}{\partial t^2}\psi(\mathbf{r}, t) = [-\hbar^2c^2\nabla^2 + m^2c^4]\psi(\mathbf{r}, t) \quad (1.5)$$

which is known as the Klein-Gordon equation [22, 23].² It treats indeed the dimension of time and space both with second derivative. However, this equation is more suitable to describe relativistic bosons of integer spin. The use of this equation for fermions such as electrons is rather limited.

When Paul Dirac was facing the Klein-Gordon and Schrödinger equations, his solution was to transform the spatial and time derivatives to first order. It turns out that the price to pay to make Eq. (1.5) a first-order equation is that the equation must be written in matrix form. Paul Dirac introduced a four-

²As an anecdote, the proposal of the Klein-Gordon equation was in fact before the Schrödinger equation.

component wavefunction and four-by-four matrices that would allow him to deal with the square root of the operators. The final form in the four-dimensional spacetime world was:

$$i\hbar \frac{\partial}{\partial t} \psi(\mathbf{r}, t) = [-i\hbar c \boldsymbol{\alpha} \cdot \boldsymbol{\nabla} + \beta m c^2] \psi(\mathbf{r}, t), \quad (1.6)$$

in terms of³

$$\beta = \begin{bmatrix} \sigma_0 & 0 \\ 0 & -\sigma_0 \end{bmatrix}, \quad \alpha_i = \begin{bmatrix} 0 & \sigma_i \\ \sigma_i & 0 \end{bmatrix}, \quad (1.7)$$

where σ_0 is the two-by-two identity matrix and σ_i ($i = 1, 2, 3$) are the Pauli matrices⁴

$$\sigma_1 = \begin{bmatrix} 0 & 1 \\ -1 & 0 \end{bmatrix}, \quad \sigma_2 = \begin{bmatrix} 0 & -i \\ i & 0 \end{bmatrix}, \quad \sigma_3 = \begin{bmatrix} 1 & 0 \\ 0 & -1 \end{bmatrix}. \quad (1.8)$$

As for the Schrödinger equation, one can define the associated Hamiltonian as

$$\hat{H} = -i\hbar c \boldsymbol{\alpha} \cdot \boldsymbol{\nabla} + \beta m c^2 = \hbar c \boldsymbol{\alpha} \cdot \hat{\mathbf{p}} + \beta m c^2, \quad (1.9)$$

which is also called the Dirac Hamiltonian, so that Eq. (1.6) can be also written as Eq. (1.3). It is sometimes useful to write the original Dirac equation in the covariant form

$$[i\hbar \gamma^\mu \partial_\mu - m c^2] \psi(\mathbf{r}, t) = 0. \quad (1.10)$$

which is invariant under Lorentz transformations. Here the notation implies summation over repeated indices μ (Einstein convention). The indices take the values 0, 1, 2, 3 and correspond to the t, x, y, z space-time dimensions, respectively, while ∂_μ is the covariant four-gradient and γ^μ are the four-by-four matrices obeying the Clifford algebra

$$\{\gamma^\mu, \gamma^\nu\} = 2\eta^{\mu\nu} I_4 \quad (1.11)$$

where $\eta^{\mu\nu} = \text{Diag}(1, -1, -1, -1)$ is the metric tensor and I_4 is the four-by-four identity matrix. This anti-commutation ensures the square root of the operators is possible.

Here, I do not specify an explicit set of matrices for γ^μ because there are different possibilities due to the Lorentz invariance of Eq. (1.10). One can thus choose a set of γ^μ matrices, i.e., a coordinate

³This is only one of many basis, called the *Dirac basis*, in which the matrices α_i and β are written. This will be further explained in terms of γ matrices in the following.

⁴Depending on the context, I will also denote the three Pauli matrices as σ_i with $i = x, y, z$.

1 Introduction

system for the space-time dimensions in the convenience of the problem of interest. For example, if the particle is massless, it is worthy to write the Dirac Hamiltonian (1.9) in the *Weyl basis* in which the γ^μ matrices are

$$\gamma^0 = \begin{bmatrix} 0 & I_2 \\ I_2 & 0 \end{bmatrix}, \quad \gamma^i = \begin{bmatrix} 0 & \sigma_i \\ -\sigma_i & 0 \end{bmatrix} \quad (1.12)$$

where $i = 1, 2, 3$ and I_2 is the two-by-two identity matrix. The Weyl basis has the advantage that the four-component spinor is divided into two decoupled two-component spinors with opposite handedness or chirality. The four-by-four Dirac Hamiltonian decomposes into two two-by-two Weyl Hamiltonians

$$\hat{H}_\lambda = \lambda \hbar c \boldsymbol{\sigma} \cdot \hat{\mathbf{p}} \quad (1.13)$$

where $\boldsymbol{\sigma} = (\sigma_1, \sigma_2, \sigma_3)$ and λ is the chirality of the particle [24]. The corresponding equation is called the Weyl equation [4].

1.2 HIGH-ENERGY PHYSICS IN DIRAC MATERIALS

Thanks to the periodicity and space group symmetry of some crystal lattices, the low-energy physics of electrons in solids can be sometimes modeled by the Dirac-type Hamiltonians. In hindsight, the hints for the previous fact are already given in Bloch's theorem which states that the energy spectrum of solids consists of several bands. In particular, if one considers excitations from valence to conduction bands, a matrix formulation is inevitable. It is thus not surprising that the analogy of the notion of particle and anti-particle [25] with that of electron and hole fascinated physicists in the great epoch of semiconductors in the 1960s [26]. While the massive Dirac Hamiltonian easily finds its application in condensed matter physics, it is unexpected that the massless Dirac Hamiltonian can also emerge in real materials. Although some theoretical predictions were already made in 1980s [27, 28], these studies did not attract much attentions until the synthesis of graphene in 2004 [6].

Then begins the gold rush for Dirac materials. People are searching in the periodic table all the candidates whose low-energy band structure can be modeled by the variations of the Dirac Hamiltonian.⁵ The advent of graphene also inspires field theorists to verify in materials their theories initially proposed for elementary particles in high-energy physics.

⁵Here, I call Dirac materials all the materials described by a Dirac-type Bloch Hamiltonian with only linear terms in momentum no matter whether they are gapped or gapless.

In this section, I will present several Dirac materials which I will investigate further in the following chapters. Some of them are widely surveyed and some of them have been realized only recently. Then, I will take graphene as an example to demonstrate three relativistic phenomena already seen in materials.⁶

1.2.1 ZOOLOGY OF DIRAC MATERIALS

The genesis of Dirac materials starts at the synthesis of graphene thanks to Geim and Novoselov, two Nobel prize laureates in physics of 2010. Graphene is a two-dimensional (2D) semimetal which possesses two inequivalent band touching points in the first Brillouin zone at the charge neutral point. In the vicinity of these band crossing points, the Hamiltonian to first order in momentum reads

$$H = \hbar v(\xi k_x \sigma_x + k_y \sigma_y), \quad (1.14)$$

where $\xi = \pm$ indicates two inequivalent valleys. The low-energy spectrum is known as the Dirac cones (see Fig. 1.1). A full derivation of this Hamiltonian from the tight-binding model is given in Chapter 2. Here, one retrieves the 2D massless Dirac Hamiltonian in which the two sublattices of graphene's honeycomb lattice play the role of the pseudo-spin. The energy degeneracy of the band touching points is simultaneously protected by the inversion and time-reversal symmetries. For example, graphene is easily gapped by introducing a staggered potential on two sublattices whose material realization is the hexagonal boron nitride h-BN with the Hamiltonian [27]

$$H = \hbar v(\xi k_x \sigma_x + k_y \sigma_y) + \Delta \sigma_z. \quad (1.15)$$

While the derivation of the original Dirac equation (1.6) or Hamiltonian (1.9) is based on Einstein's theory of special relativity which has to preserve the Lorentz symmetry, there is no such a constraint in the emergent Dirac Hamiltonian of Dirac materials. In particular, the velocity could be anisotropic for in the x, y -plane or the Dirac cones could be tilted such that the Hamiltonian becomes

$$H = \hbar w k_x + \hbar v(k_x \sigma_x + k_y \sigma_y) + \Delta \sigma_z \quad (1.16)$$

where the velocity w is the slope of tilt. See Fig. 1.1 for its energy spectrum. The massless version of the 2D tilted Dirac Hamiltonian can be realized in 8 - $Pm\bar{m}n$ borophene [30], quinoid-type graphene [31, 32], the organic conductor α - (BEDT TTF)₂I₃ [33]. Therefore, the physics in Dirac materials are even richer than the original Dirac Hamiltonian.

⁶There exist of course many other phenomena having a condensed matter representation, which are well-known in quantum field theory such as parity anomaly [27] and chiral anomaly [29].

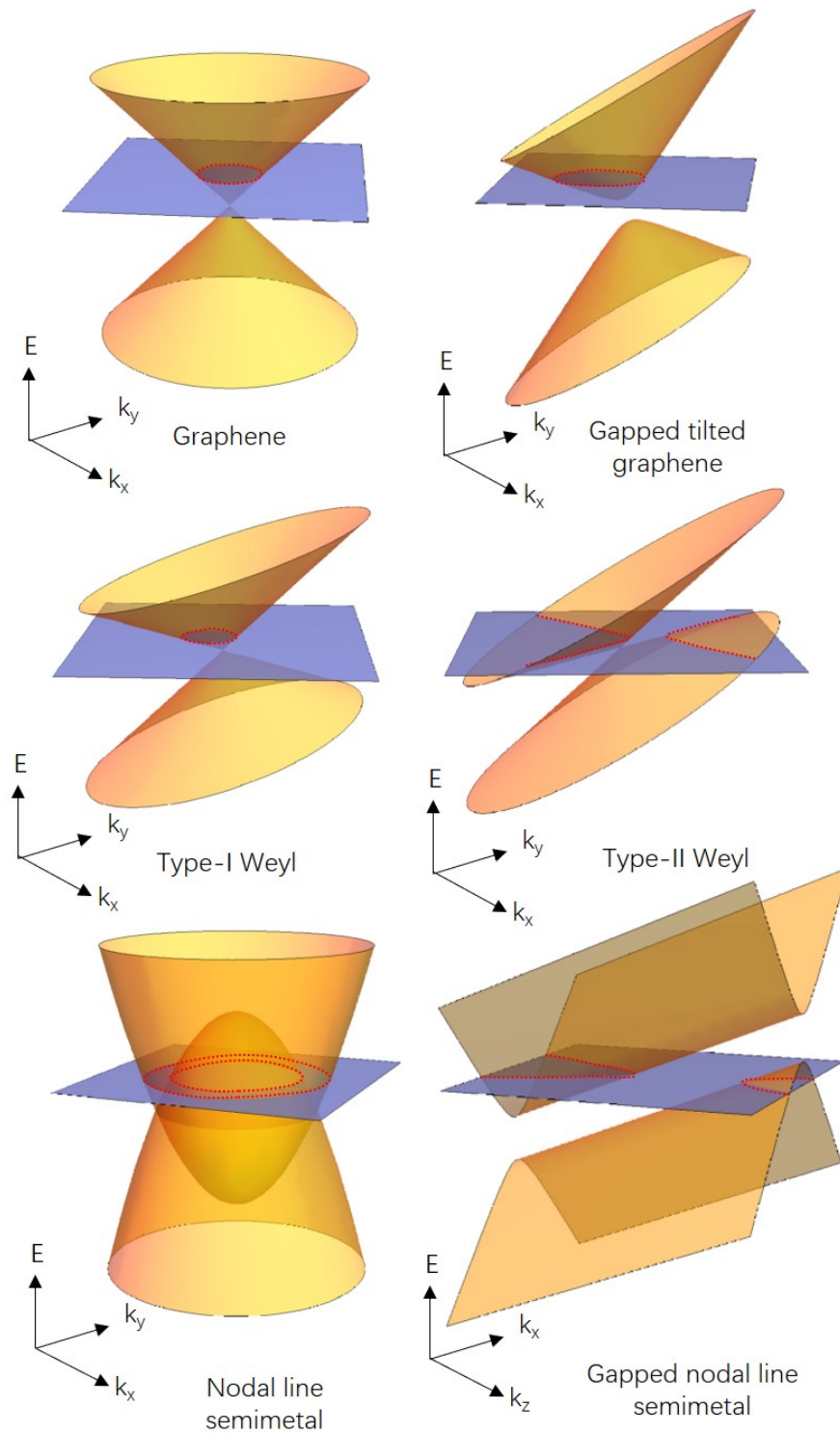


Figure 1.1: Energy spectra of several types of Dirac materials. For 3D materials, the third momentum is set to be zero. The blue plane represents the chemical potential which I choose to intersect with the conduction bands. The shape of the Fermi surface is depicted by the red dashed lines.

The three-dimensional (3D) Weyl Hamiltonian (1.13) can also emerge in materials known as Weyl semimetals (WSMs). The band touching points are called Weyl nodes. As shown by Nielsen and Ninomiya in [34], later known as *fermion doubling theorem* or *Nielsen-Ninomiya no-go theorem*, the number of the Weyl nodes of chirality $\lambda = +$ must be equal to that of chirality $\lambda = -$ in the lattice realization of the Weyl equation.⁷ Unlike in graphene, the band touching points of WSMs are generic and stable. This can be seen by considering the most general two-by-two Hamiltonian $H = f_0 + f_x\sigma_x + f_y\sigma_y + f_z\sigma_z$ whose spectrum is $E = f_0 + \pm\sqrt{f_x^2 + f_y^2 + f_z^2}$. The valence and conduction band touch if $f_x = f_y = f_z = 0$ simultaneously. In 3D space, each coefficient f_i depends on 3D momentum (k_x, k_y, k_z) so that three equations with three variables yields always solutions. Introducing a mass gap like $\Delta\sigma_z$ would not gap but only move the Weyl nodes in reciprocal space. However, the band touching in 2D requires symmetries or fine tuning. So, the term “generic touching point” means that while it is not guaranteed to find any such touching events in an arbitrary material, one should not be surprised to find them either. Nevertheless, inversion and time-reversal symmetries play important roles for WSMs. If the inversion symmetry is present and time-reversal symmetry is broken, the minimum model needs only two Weyl nodes. In contrast, if the inversion symmetry is broken and time-reversal symmetry is present, the minimum model needs at least four Weyl nodes. The reason is that one must verify the fermion doubling theorem while the time-reversal operation preserves the chirality of the Weyl nodes and the inversion switches it. If the Hamiltonian commutes with both inversion and time-reversal symmetries, then all bands are Kramers degenerate already and any additional touchings would generate points of fourfold degeneracy known as Dirac points. The associated material is called Dirac semimetal.

The first theoretical proposal of material realization of WSMs was given by Herring in 1937 [36]. More recently, the book by Volovik published in 2003 [37] has been influential in re-drawing the attention of theorists to the Weyl physics in materials. Similar to the 2D massless Dirac Hamiltonian, the anisotropy of velocity and the tilt are also allowed in the 3D Weyl Hamiltonian. For example, a tilted WSM’s Hamiltonian reads

$$H = \hbar w k_z + \hbar v(k_x\sigma_x + k_y\sigma_y + k_z\sigma_z). \quad (1.17)$$

Depending on the ratio $|w/v|$, WSMs are classified into two phases [38]: type-I WSMs if $|w/v| < 1$ and type-II WSMs if $|w/v| > 1$. The crucial difference between the two types of WSMs is that the Fermi surface is ellipsoid and closed for type-I but it is hyperbolic and opened for type-II (see Fig. 1.1). The two shapes of the Fermi surface induce distinguishable responses to magnetic field as I will show in Chapter 2.

⁷A more elementary proof is given in [35].

1 Introduction

Many materials are now theoretically and experimentally identified as instances of the Weyl Hamiltonian. For example, as a representative of the transition metal monopnictide, TaAs is a non-magnetic and non-centrosymmetric material and confirmed to be an inversion-broken WSM with twelve pairs of Weyl nodes (multiple of four) near the Fermi surface [39]. The examples of Dirac semimetals are Cd_3As_2 [40] and Na_3Bi [41]. In spite of the fact the time-reversal broken magnetic WSMs has the simplest theoretical modeling [42], the material realization has not been recognized yet. Possible candidates would be pyrochlore iridates [43].

In addition to Weyl and Dirac nodes, the band touching points can form a continuous line in reciprocal space in materials called nodal line semimetals [44] (see Fig. 1.1). They have been predicted and observed via the angle-resolved photoemission spectroscopy (ARPES), for example, in ZrSiS [45, 46]. However, the combination of inversion and time reversal alone cannot protect the nodal line from being gapped out if the SOC is included. The resulting phase of matter is thus called gapped nodal line semimetal. An example that I will explain thoroughly in Chapter 2 and 3 is the transition metal dipnictides NbAs_2 described by a low-energy Hamiltonian

$$H = \hbar v k_z + \hbar v (k_x \sigma_x + k_y \sigma_y) + \Delta \sigma_z. \quad (1.18)$$

Its energy profile is shown in Fig. 1.1.

As I have shown in this section, without the constraint of the Lorentz symmetry, a wide range of the variations of the Dirac Hamiltonian is unleashed in the context of condensed matter. The freedom of adding new terms in the Dirac Hamiltonian have blazoned the Dirac physics in materials. In Chapter 2, I will talk about the Landau quantization in most of Dirac materials mentioned above. In particular, the spectroscopic properties of the gapped nodal line semimetal NbAs_2 are discussed in detail in Chapter 3.

1.2.2 RELATIVISTIC PHENOMENA IN GRAPHENE

Nowadays, many relativistic phenomena have already been observed in Dirac materials via methods that are well-known in the condensed matter community. Since the Hamiltonian of graphene matches perfectly the original 2D massless Dirac Hamiltonian, it is the first material lab of high-energy experiments. One of such examples is the Klein tunneling paradox according to which relativistic massless electrons can tunnel through a potential step with perfect transmission. This particular phenomenon has been shown to be relevant in electron scattering in graphene. When electrons pass through an extremely narrow graphene bipolar junctions, the Klein tunneling manifests itself as the phase shift observed in the conductance fringes at low magnetic fields, a signature of the perfect transmission

of normally incident electrons [47, 48]. A theoretical pedagogical review on the Klein tunneling in graphene can be found in [49].

Another famous phenomenon in atomic physics to mention is termed “atomic collapse” [50, 51]: an atom with an atomic number beyond a critical value ($Z = 172$) cannot exist because of the leakage to the negative energy spectrum. To experimentally prove this theoretical prediction is extremely difficult. Looking at the periodic table, the highest atomic number that can be achieved by all the present high-energy techniques is only below 120, still long way to go. However, atomic collapse is shown to be able to be simulated in graphene with point charge impurities over it [52]. The experimental demonstration is the observation of a resonant peak in the density of states in the hole band of graphene by scanning tunneling microscope (STM) if atom collapse happens. These two examples already depict a promising prospect of doing high-energy physics in a piece of Dirac materials.

The relativistic renormalization, a famous consequence of the Lorentz transformation, is also predicted to be able to see in graphene in the presence of crossed electric magnetic field [53]. One does not need to contemplate the Galaxy using immense astronomical telescopes to see the relativistic renormalization of electromagnetic fields. As I will show in Chapter 2 and 3, a tiny piece of crystal will suffice. The manifestation of the relativistic renormalization in graphene is that the Landau level structure collapses into a continuum in the presence of a magnetic field and an intense electric field given by a high potential barrier induced on graphene sheet. An indirect experimental signature of the phenomenon is that the oscillations of conductance are found to abruptly disappear when the strength of the magnetic field is reduced below a certain critical value [54]. I will also elaborate the theory on the relativistic renormalization in Dirac materials in Chapter 2 and 3 where I will show a more direct and unambiguous experimental signature for it.

Although the projection of relativistic phenomena to Dirac materials is exciting, one must keep in mind that the pseudo-relativity in Dirac materials is purely formal and mathematical. It does not mean that the particles in our treatment are really relativistic. They are indeed in the non-relativistic regime. For example, electrons in graphene move with the Fermi velocity far below the speed of light ($v/c \approx 1/300$). For the same reason, the analogy with special relativity is not always guaranteed in Dirac materials. Additional terms, with no known relativistic counterpart, arise naturally in the Hamiltonian describing general Dirac materials as I have shown previously. Although many high-energy phenomena have their corresponding condensed matter representation, one should remember that they must be understood in the language of condensed matter, that is non-relativistic. I will unfold this point in Chapter 2.

1.3 TOPOLOGY IN MATERIALS

Topology is initially a mathematical term to describe the geometrical properties of manifolds which are robust to continuous deformations without any “violent event”. In algebraic topology, objects of different topology are classified by discrete and countable numbers known as topological invariant. A violent event is thus defined as a transformation on objects switching abruptly the topological invariant from one value to another. At the moment of the violent event, the topological invariant is not well-defined. For example, 3D objects can be classified by the number of holes, i.e., the genus, though themselves. The number of holes will not change if one just pinches the object without cutting it or pasting together its parts, namely without violent events.

Unlike the Gaussian curvature which is a local property of manifold, topological properties are global geometrical properties. Topology can be thus thought to be the integrated geometry of manifolds. This idea is best illustrated by the Möbius strip which is formed by cutting a trivial strip as a scotch tape, twisting one end by 180 degrees and then pasting the two ends together (see Fig. 1.2).⁸ Intuitively, the Möbius strip is topologically different object from the trivial strip for a Human surviving in 3D space. However, it is not evident for an ant living on the 2D strip which seems to only feel the local curvature of the strips.⁹ Nevertheless, an ant knowing topology can distinguish the two strips as illustrated in Fig. 1.2. It can mark its starting position and orientation in space before looping on the strip. When it arrives for the first time back to its initial position, it will know on which strip it has had this journey. If it finds itself on the same side of the strip as the starting point, namely the same orientation, it knows the strip is the trivial one. In contrast, if it finds on the opposite side of the strip, it must live on the Möbius strip. Another equivalent way to classify the two strips is to count the winding number (a topological invariant), namely the number of times that an ant loops on the strip to go back to its initial position on the same side of the strip as that of departure. The ant needs twice for the Möbius strip but only once for the trivial one.

The previous idea can be applied in physics as shown by Berry in 1984 [55]. Given a parameter-dependent Hamiltonian $H(\phi)$, its corresponding wavefunction $|\psi(\phi)\rangle$ depends thus also the parameter ϕ .¹⁰ When one changes adiabatically ϕ along a closed path and back to the initial value in the manifold for the parameter, the energy spectrum of the Hamiltonian $H(\phi)$ remains unchanged but the wavefunction $|\psi(\phi)\rangle$ accumulates a geometric phase $\exp(i\theta)$ depending on the topology of the

⁸Cutting and pasting are the two violent events that change the topology of the strip.

⁹Here, the ant is considered as a point moving on the two sides of the strip. Although the strips are 2D objects, the dimension of the width of the strip is irrelevant in the discussion so that the strip is effectively considered as a 1D object.

¹⁰Note that an eigenstate multiplied by a phase factor is still an eigenstate of the same energy. Choosing the phase as a function of ϕ is choosing a gauge for the eigenstates. The fact that all the observables should be independent of the choice of gauge is one of the fundamental principles of quantum mechanics. However, it does not mean that the gauge phase is not important as I will show in the following by the Aharonov-Bohm effect and all the topological effects.

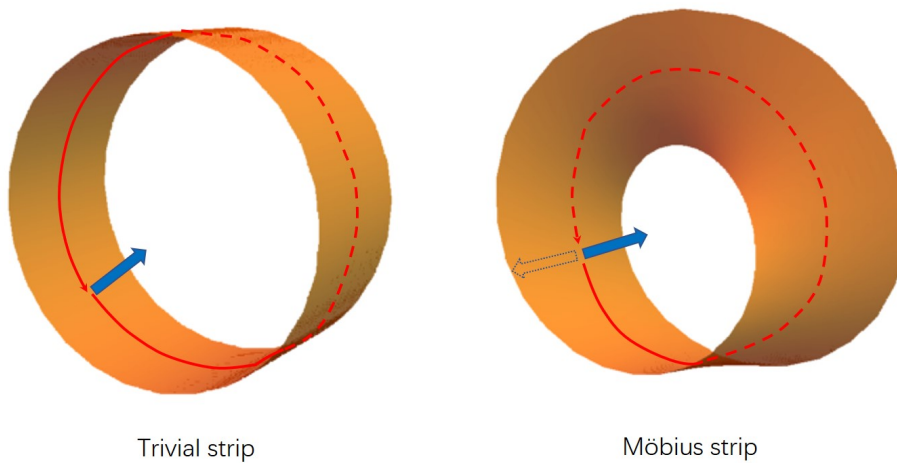


Figure 1.2: 3D illustration of the trivial and Möbius strip. The ant living on the strips is represented by the blue arrow. The trajectories by the ant are represented by the red lines: dashed lines if the trajectory is hidden behind the strip and solid lines if not. When the ant travels for one loop on the trivial strip, it coincides with itself. However, when it travels for one loop on the Möbius strip, it finds itself on the opposite side of the strip.

closed path. The phase θ is now known as the Berry phase. The revolutionary message from Berry in his seminal paper [55] is that the Berry phase θ is gauge-independent when the path tracked by the parameter ϕ in its manifold is closed. In other words, the phase ϕ is in principle a physical observable. The notion of the Berry phase may be more understandable if one compares it with the ant on the strip. In that case, the position of the ant on the strip plays the role of the parameter ϕ , the ant itself is regarded as the wavefunction and the strip is thus the manifold of the parameter-dependent Hamiltonian. Then, a closed path traveled by ϕ is equivalent to a loop by the ant. The Berry phase associated to the closed path is 0 if the ant goes back to the initial position with the same orientation; the Berry phase is π if the ant finds itself upside down after a loop on the strip. Therefore, the two different Hamiltonians associated to the trivial and Möbius strip are called topologically trivial and non-trivial Hamiltonian, respectively. Sometimes, the topologically non-trivial Hamiltonian is said to be twisted by the analogy with the Möbius strip.

The first proposal and observation of the Berry phase can be traced back to the paper published in 1959 and in 1960 [56, 57] on the Aharonov-Bohm effect.¹¹ In this case, the Berry phase is the phase accumulated by a charged particle in the vector potential along a closed loop so that it is proportional

¹¹As an anecdote, this result was too shocking to be accepted by the physicists of that time. There was even a paper with the title “Nonexistence of the Aharonov-Bohm effect” published in 1978 [58].

1 Introduction

to the magnetic flux. On the one hand, the Aharonov-Bohm effect demonstrates the wave nature of electrons by interference. On the other hand, it also reveals the importance of the gauge in modern theoretical physics and inspires the notion of the Berry phase.

In the Aharonov-Bohm effect, the parameter to change is the position in real space. One can thus transplant this idea in reciprocal space in which the crystal momentum \mathbf{k} is a natural choice of the parameter. In this section, I will show how Berry phase arises in electronic band theory of solids while studying Bloch Hamiltonians $H(\mathbf{k})$. Then, I will present one of the important consequences of the Berry phase effect, i.e., the bulk-edge correspondence. Besides general topological arguments, I will provide a treatment by the Dirac equation to explain the bulk-edge correspondence.

1.3.1 TOPOLOGICAL BAND THEORY AND BERRY PHASE

As shown by Bloch in 1929 [12], the energy of electrons in a periodic crystal lattice can be indexed by the crystal momentum \mathbf{k} , which yields electronic band structure.¹² Given the Hamiltonian H , the corresponding eigenstates $|\psi_n(\mathbf{k})\rangle$ of energy $E_n(\mathbf{k})$ can be written as

$$|\psi_n(\mathbf{k})\rangle = e^{i\mathbf{k}\cdot\mathbf{r}}|u_n(\mathbf{k})\rangle \quad (1.19)$$

where $|u_n(\mathbf{k})\rangle$ is the cell-periodic Bloch state. Via a unitary transformation, the Bloch Hamiltonian

$$H(\mathbf{k}) = e^{-i\mathbf{k}\cdot\mathbf{r}} H e^{i\mathbf{k}\cdot\mathbf{r}} \quad (1.20)$$

has the same spectrum $E_n(\mathbf{k})$ as H and the corresponding eigenstates $|u_n(\mathbf{k})\rangle$ verify

$$H(\mathbf{k})|u_n(\mathbf{k})\rangle = E_n(\mathbf{k})|u_n(\mathbf{k})\rangle. \quad (1.21)$$

The crystal momentum \mathbf{k} is thus the parameter to vary in the definition of Berry phase in topological band theory. The quantity to measure the variation of the phase accumulated by $|u_n(\mathbf{k})\rangle$ while varying \mathbf{k} is called Berry connection defined as

$$\mathcal{A}_n(\mathbf{k}) = i\langle u_n(\mathbf{k})|\nabla_{\mathbf{k}}u_n(\mathbf{k})\rangle \quad (1.22)$$

¹²A pedagogical introduction of Bloch's theorem can be found in [15, 59].

where n is the band index.¹³ By definition, the integration of Berry connection along a closed loop is equal to Berry phase. One can also define the associated Berry curvature as

$$\mathcal{B}_n(\mathbf{k}) = \nabla \times \mathcal{A}_n. \quad (1.23)$$

In the context of topological band theory, the closed path in reciprocal space often refers to paths going through the first Brillouin zone. Therefore, the corresponding Berry phase θ_n of a band n is given by

$$\theta_n = \int_{\partial BZ} d\mathbf{k} \cdot \mathcal{A}_n(\mathbf{k}) = \int_{BZ} d^2\mathbf{k} \cdot \mathcal{B}_n \quad \text{modulo } 2\pi. \quad (1.24)$$

As implied by the notation, the Berry connection and curvature are said to be the vector potential and magnetic field in reciprocal space, respectively.

The Berry phase is closely related to the topological invariant of materials whose definition depends on the dimensionality of the parameter space. For example, the topological invariant for a 2D band of index n is the first *Chern number* defined as

$$C_n = \frac{\theta_n}{2\pi} \in \mathbb{Z} \quad (1.25)$$

which must be an integer on lattice according to the Atiyah-Singer index theorem [34, 60, 61]. The topological properties of a given Hamiltonian are thus determined by the sum of the Chern numbers of all the filled bands. Note that the Chern number is only well-defined in a gapped system. In the case of degeneracies in multi-band systems, one can generalize the definition of Berry connection and phase to a tensor form

$$\mathcal{A}_{mn}(\mathbf{k}) = i \langle u_m(\mathbf{k}) | \nabla_{\mathbf{k}} u_n(\mathbf{k}) \rangle \quad (1.26)$$

as in the Yang-Mills gauge theory where the non-abelian Wilson loop in a matrix form is more suitable [24, 62]. In the following discussions, I suppose that all the bands are separated from each other and there exists a gap between the bands. The Chern number is indeed one of the topological invariants for 2D insulators [63]. If the Chern number is non-zero, the insulator is called *topological insulator* (TI) [64]; otherwise, the insulator is trivial in terms of Chern number. But, this does not mean that Hamiltonians with zero-Chern number are topologically trivial. The insulator of zero Chern number can be topological because it can be further classified by other topological invariants [63]. One can further classify them using other topological invariant, such as \mathbb{Z}_2 invariant for Kane-Mele spinful Hamiltonian and other time-reversal TI. Here, I stop the topological classification at Chern number.

¹³Here, I assume the band n is separated from all other bands.

1 Introduction

The reader may wonder that the above expressions [see for example (1.22)] give the impression that the topological properties encoded in the Berry curvature in the n th band only depends on a single band contrary to what I have said at the beginning of the present chapter. Actually, this is only a pseudo-paradox if one remembers that the first derivative of the vector field is orthogonal to itself, i.e., it can be written as a combination of vectors orthogonal to itself. To explicitly show that the Berry curvature is related to virtual transitions between bands (at fixed \mathbf{k}), one uses first-order perturbation theory for wavefunction so that the Berry curvature for a 2D band reads

$$\mathcal{B}_n(\mathbf{k}) = i \sum_{n' \neq n} \frac{\langle u_n | \partial_{k_x} H | u_{n'} \rangle \langle u_{n'} | \partial_{k_y} H | u_n \rangle}{(E_{n'} - E_n)^2} + c.c. \quad (1.27)$$

where the energies E_n are supposed to be non-degenerate. The reader should now be convinced that topological band theory is a band theory considering the coupling between bands via the virtual inter-band transitions.

1.3.2 BULK-EDGE CORRESPONDENCE: EMERGENCE OF GAPLESS SURFACE STATES

The consequence of virtual interband transitions was proposed by Karplus and Luttinger in 1954 [65, 66] well before the paper by Berry [55]. They noticed that the velocity in ferromagnets acquires an additional term later known as anomalous velocity, which is the origin of the anomalous Hall effect [67]. Nevertheless, a true understanding of the topology in band theory should wait until the discovery of the integer quantum Hall effect by von Klitzing et al. in 1980 [68] and its topological interpretation by Thouless et al. in 1982 [14]. The integer quantum Hall effect is also seen as the paradigm of the bulk-edge correspondence of topological phases.

The integer quantum Hall effect is that the Hall conductivity of a 2D electron gas in the presence of a magnetic field is quantized into integer times of the conductivity quantum e^2/h . As shown by Thouless et al. in [14], the integer quantum Hall effect is present when the chemical potential is between Landau levels so that the Hall conductivity can be written as

$$\sigma_{xy} = \frac{e^2}{h} \sum_n^{\text{filled bands}} C_n \quad (1.28)$$

where C_n is the Chern number for the band n . This formula yields a topological invariant known as T.K.N.N. invariant for 2D integer quantum Hall phases. As the manifestation of the bulk-edge correspondence, the number of the conducting edge channels are determined by the topology of the bulk system characterized by the topological invariant.

The emergence of conducting edge states in an insulating bulk phase does not require necessarily a magnetic field, as shown by Haldane in 1988 [13]. One only requires that the time-reversal symmetry is broken in an insulator known as quantum anomalous Hall insulator or Haldane insulator [69].¹⁴ The Hamiltonian of the Haldane insulator built from a honeycomb lattice reads

$$H = \hbar v(k_x \tau_z \sigma_x + k_y \sigma_y) + \Delta \tau_z \sigma_z \quad (1.29)$$

where the third Pauli matrix τ_z is the valley degrees of freedom. The time-reversal symmetry is broken by a valley-resolved mass and the total Chern number C of filled bands equals thus to 1 at the charge neutral point. Most saliently, C does not change unless the gap is closed. This reflects the fact that the topological properties are robust to continuous deformation without violent events, which are the gap closing events in this context. Since the vacuum can be seen as a trivial insulator with large gap, the associated Chern number is zero. Therefore, the gap must be closed at the interface between the Haldane insulator and vacuum because the Chern number has to change its value from one to zero while moving out of the Haldane insulator into the vacuum. Gapless conducting edge states emerge precisely at the position where the gap is closed. The Haldane insulator possesses one conducting channel at its edge ($C = 1$) and the Hall conductivity in the absence of a magnetic field is e^2/h , yet another example of the bulk-edge correspondence. As long as the gap of the Haldane insulator is not closed, the edge state is present. Here comes the notion of the protection by the gap.

Note that the above argument of the emergence of edge states is general and independent how to model the edge. “You cannot get rid of the surface state. You take a hammer, you hit the sample, and the surface state still remains.”¹⁵ The robustness of edge states is precisely the reason why topological materials attract so much attention recently.

1.3.3 TOPOLOGICAL HETEROJUNCTION: DIRAC EQUATION APPROACH

Although the general topological argument dictates already the presence of robust edge states at the surface of topological insulators, it gives no information how it looks like. As first proposed by Jackiw and Rebbi [17], one can use the Dirac equation with a spatially variant mass gap to explicitly show the presence of edge states. This approach was first used in the Su-Schrieffer-Heeger model for polyacetylene [71]. Here, I adapt this method to the Haldane insulator.

¹⁴“Anomalous” because it is a Hall effect in the absence of magnetic field.

¹⁵Quote from Bernevig, one of the founders [70] of topological band theory [16].

1 Introduction

For the reason of simplicity, I consider an interface between the Haldane insulator and a trivial one in 2D described by a Hamiltonian of similar structure called Semenoff insulator [27, 69]. The Hamiltonian for the latter reads

$$H = \hbar v(k_x \tau_z \sigma_x + k_y \sigma_y) + \Delta \sigma_z \quad (1.30)$$

where the mass gap remains the same value for two valleys. The spectrum of the Semenoff insulator is exactly the same as that of the Haldane one. The Chern number at the charge neutral point for (1.30) is zero meaning that the Semenoff insulator is topologically trivial and its Hall conductivity in the absence of a magnetic field is zero. This is precisely a concrete example of what I have said at the beginning of the chapter: two Hamiltonians of identical spectrum can have different response to electric field.

An interface between two topologically different phases is called *topological heterojunction* [72]. Suppose that the interface between the two insulators is formed around $x = 0$ in space. When $x \rightarrow -\infty$, one finds the Haldane insulator; when $x \rightarrow +\infty$, one finds the Semenoff insulator. To model the topological heterojunction connecting a Haldane and Semenoff insulator, one can replace the constant mass gap by a position-dependent one

$$\Delta(x) = \begin{cases} \Delta_0 \tau_z & \text{if } x \rightarrow -\infty \\ \Delta_0 & \text{if } x \rightarrow +\infty. \end{cases} \quad (1.31)$$

The order in energy of valence and conduction bands is inverted in the valley $\tau_z = -1$ (band inversion) since the gap change its sign. Note that the mass gap is inverted only for $\tau_z = -1$ so that one can focus on the valley $\tau_z = -1$. The resulting Hamiltonian reads

$$H = \hbar v(-k_x \sigma_x + k_y \sigma_y) + \Delta(x) \sigma_z \quad (1.32)$$

where

$$\Delta(x) = \begin{cases} -\Delta_0 & \text{if } x \rightarrow -\infty \\ \Delta_0 & \text{if } x \rightarrow +\infty \end{cases} \quad (1.33)$$

and k_x should be considered as the derivative $-i\partial_x$. The wavefunction of the eigenstate of the Hamiltonian can be written as

$$\psi = e^{ik_y y} \chi(x). \quad (1.34)$$

First, considering $k_y = 0$, one can show that $E = 0$ is also an eigenvalue of the Hamiltonian [69, 73] with the two possible wavefunctions

$$\chi_{\pm}(x) = \exp\left[\frac{\pm 1}{\hbar v} \int_{x_0}^x dx' \Delta(x')\right] \begin{pmatrix} 1 \\ \pm i \end{pmatrix} \quad (1.35)$$

which is also the eigenstate of the Hamiltonian (1.32) with energy $E = \mp \hbar v k_y$. However, only one of the two wavefunction is square-integrable depending on the sign of Δ_0 . Given $\Delta_0 > 0$, the only physically viable solution is

$$\chi_{-}(x) = \exp\left[-\frac{1}{\hbar v} \int_{x_0}^x dx' \Delta(x')\right] \begin{pmatrix} 1 \\ -i \end{pmatrix} \quad (1.36)$$

with the energy $E = +\hbar v k_y$. Therefore, only one edge mode is present at the surface of the Haldane insulator. Most saliently, it propagates only in the positive k_y -direction with a definite chirality given by the spinorial part of its wavefunction. So, it is also called chiral state. Since there is no counter-propagating partner nearby this edge mode, it is immune to the back-scattering.

The argument of the emergence of edge states using the Dirac equation is rather general. One only relies on the fact that the mass gap $\Delta(x)$ changes its sign across the topological heterojunction so that the bands are inverted. The only way to get rid of the edge state $E = \hbar v k_y$ is to invert the gap of one of the two bulk phases. Since this would cost large amount of energy, the edge state is stable and protected by the gap.

Additional surface states called *Volkov-Pankratov* states can arise when the interface is smooth enough as shown by Volkov and Pankratov in their work [74, 75]. Since the gap changes its sign across the topological heterojunction, one can generally linearize the gap function in the vicinity of the gap closing point, e.g., $x = 0$. The wavefunction of the chiral state becomes

$$\chi_{-} \sim \begin{cases} e^{-\frac{\Delta}{\hbar v \ell} x^2} & \text{for } |x| \ll \ell \\ e^{-\frac{\Delta}{\hbar v} |x|} & \text{for } |x| \gg \ell, \end{cases} \quad (1.37)$$

where ℓ is the length scale associated with the smoothness of the topological heterojunction. The smoothness of the surface can be interpreted as a pseudo-magnetic field [72] so that the stability of the chiral state is also understood by the argument given by Aharonov and Casher [18]. In their work, they showed an universal presence of zero mode for the 2D Dirac Hamiltonian in the presence of a magnetic field. More details on the smooth topological junction and additional surface states can be found in Chapter 4 and 5.

1.4 OUTLINE OF THE THESIS

The present thesis is thus organized as follows. In the first part (Chapter 2 and 3), I elaborate how the relativistic renormalization arises in the electrodynamics of Dirac materials. I also interpret the relativistic phenomena using the language of condensed matter at the end of Chapter 2. In particular, I show in Chapter 3 how to reveal the relativistic renormalization by magneto-optics in a gapped nodal line semimetal NbAs₂. In the second part of the thesis (Chapter 4 and 5), I discuss Volkov-Pankratov states in smooth topological heterojunctions. I give various explications on the origin of Volkov-Pankratov states in Chapter 4. In particular, I am interested in the spectroscopic properties of these states shown in Chapter 5, which offer a smoking gun for their identification by experiments. Throughout the thesis, the Dirac equation appears everywhere. It is THE equation of my PhD.

For those who are interested in topics mentioned in the present chapter, I suggest the following references on

- Berry phase [67, 73, 76],
- Quantum field theory for condensed matter [77]
- Quantum Hall effect [78, 79],
- Special relativity [80],
- Topological band theory [73, 76],
- Topological insulators and semimetals [8, 62, 64, 81]
- Topology in physics [61].

2 SPECIAL RELATIVITY IN DIRAC MATERIALS

The mathematical education of the young physicist [Albert Einstein] was not very solid, which I am in a good position to evaluate since he obtained it from me in Zurich some time ago.

Hermann Minkowski

The present chapter will show in detail how frame-dependent electrodynamics, known in Einstein's special relativity, can be also observed in Dirac materials. On the one hand, the reader will see the full derivation of how relativistic electrodynamics emerges in graphene and how to solve it using so-called hyperbolic transformations, a spinor representation of Lorentz boosts. On the other hand, I will show how to extend the use of hyperbolic transformation to a generic problem in the condensed-matter community: Landau quantization for Dirac Hamiltonians with tilting term.

I will start from the prototypical Dirac material, i.e., graphene, and discuss how an out-of-plane magnetic field and an in-plane electric field conspire to reconstruct the low-energy spectrum of graphene. I will solve the problem in two different ways: one is to map it to a problem in Einstein's special relativity and the other one is to solve it quantum mechanically using hyperbolic transformations. These two methods are physically equivalent. However, the latter provide a general approach to solve a larger set of problems: the energy spectrum of tilted Dirac materials in the presence of magnetic field. Besides, it also provides wavefunctions that will be crucial for the next chapter on the spectroscopic properties of Dirac materials. Apart from graphene, I will illustrate the application of hyperbolic transformations to the problem of Landau quantization with three other examples: tilted gapped graphene, tilted Weyl semimetal and a gapped nodal-line semimetal, NbAs₂. As for the latter material, I have studied the role of the tilt in magneto-optical spectroscopy within a collaboration with Milan Orlita's group at the Grenoble High-Field Lab (LNCMI). While previous studies focus on the gapless system like Dirac/Weyl semimetals [82, 83], I am mostly interested in systems with gap.

After this more abstract relativistic description of Dirac materials, I will bring the discussion to earth with my proper understanding by interpreting the pseudo-relativity in the language of condensed matter and clarifying their mechanisms. This less fancier way of looking at these system is, in my view, as important as the relativistic description. It emphasizes that the analogy with special relativity can

2 *Special relativity in Dirac materials*

be viewed in simple geometric terms. The two conceptually different perspectives are actually the two sides of the same coin.

2.1 SPECIAL RELATIVITY IN GRAPHENE: CROSSED ELECTRIC AND MAGNETIC FIELDS

Being the first experimental realization of Dirac materials, graphene is also the simplest one to study both experimentally and theoretically. In particular, if one wants to study the energy spectrum of Dirac materials in the presence of crossed electric and magnetic fields [53, 78], it is the best candidate to begin with. The system is two-dimensional so that only the out-of-plane components of the magnetic field is relevant to the spectrum. For the same reason, the electric field can be supposed to be applied in the plane of graphene because an out-of-plane electric field cannot induce any current but only dopes the system changing the chemical potential. Since its low-energy Hamiltonian is isotropic, the electric field is equivalently applied in each direction. All the traits justify selecting graphene as the starter of the banquet.

In this section, I will first show how the Dirac equation emerges in graphene after a short introduction to the Dirac equation in $2 + 1$ space-time. Before introducing the electric field, the energy spectrum with only a magnetic field will be shown to form a series of Landau levels indexed by an integer. Then, I will solve the spectrum when the electric field is also present by analogy to special relativity. To be self-contained, a short reminder of electrodynamics in special relativity will be given in advance.

2.1.1 UNEXPECTED MASSLESS DIRAC EQUATION IN GRAPHENE

Graphene is an atomically thin monolayer of carbon atoms. Electrons of graphene live in a two-dimensional space. To show the emergence of the Dirac equation in graphene, I will first derive the Dirac equation in the $2 + 1$ space-time dimensions. Then, I will compare it with the low-energy Hamiltonian of graphene derived from the tight-binding model. The reader will see soon that the low-energy Hamiltonian of graphene has exactly the same mathematical structure as the $2 + 1$ Dirac equation.

DIRAC EQUATION IN TWO DIMENSIONS

So far, the reader has encountered the Dirac equation in the form of Eq. (1.10) in the introduction for $3 + 1$ (three spatial and one temporal) dimensions. Now I derive its $2 + 1$ dimensional counterpart. The equation has the same form as Eq. (1.10) but now $\mu = 0, 1, 2 \Leftrightarrow t, x, y$. Furthermore, γ^μ only

2.1 Special relativity in Graphene: crossed electric and magnetic fields

need to be two-by-two matrices¹ to satisfy the respective anti-commutation relation by replacing I_4 by I_2 in Eq. (1.11) and $\eta^{\mu\nu} = \text{Diag}(1, -1, -1)$. A possible choice is to set

$$\gamma^0 = \sigma_3, \quad \gamma^1 = -i\sigma_2, \quad \gamma^2 = -i\sigma_1, \quad (2.1)$$

so that the 2 + 1 Dirac equation reads

$$i\hbar \frac{\partial}{\partial t} \psi(\mathbf{r}, t) = [-i\hbar c \boldsymbol{\sigma} \cdot \nabla + mc^2 \sigma_z] \psi(\mathbf{r}, t). \quad (2.2)$$

where I interchangeably use the notation σ_i with $i = x, y, z$ and 1, 2, 3 and $\boldsymbol{\sigma} = (\sigma_x, \sigma_y)$. Finally, the corresponding Dirac Hamiltonian is

$$\hat{H} = \hbar c \boldsymbol{\sigma} \cdot \hat{\mathbf{p}} + mc^2 \sigma_z. \quad (2.3)$$

This is the Dirac Hamiltonian for a massive fermion living in the 2 + 1 space-time dimensions.

LOW-ENERGY THEORY OF GRAPHENE: TIGHT-BINDING MODEL

The carbon atoms of graphene are arranged in a honeycomb-like two-dimensional lattice. Each unit-cell has two atoms which form two hexagonal Bravais lattice, i.e., sublattice A and B . In a given unit-cell, $A = (0, 0)$ and $B = (0, -d)$ [see Fig. 2.1(a)]. The Bravais lattice vectors are:

$$\mathbf{a}_1 = a(1, 0), \quad \mathbf{a}_2 = a \left(\frac{1}{2}, \frac{\sqrt{3}}{2} \right) \quad (2.4)$$

where a is the lattice constant and has a value of around 2.46 Å. Each carbon has three nearest neighbors. Given a carbon atom, its nearest neighbors are situated at the positions

$$\boldsymbol{\delta}_1 = d \left(\frac{\sqrt{3}}{2}, \frac{1}{2} \right), \quad \boldsymbol{\delta}_2 = d \left(-\frac{\sqrt{3}}{2}, \frac{1}{2} \right), \quad \boldsymbol{\delta}_3 = d(0, -1) \quad (2.5)$$

where $d = a/\sqrt{3}$ is the nearest neighbor distance.

Electron-electron interaction is omitted so that electrons are considered independently in the periodic background potential emanating from the carbon lattice. I am only interested in the low-energy physics of graphene which are governed by the valence electrons of p_z orbital of carbon atoms. Since the typical Fermi wavelength λ_F is much longer than the length of chemical bond between the nearest

¹The dimension of γ matrices must be an even number since they obey Clifford algebra. One can prove that the dimension should be $2^{\lfloor D/2 \rfloor}$ where $\lfloor D/2 \rfloor$ is the integer part of half of the space-time dimension [84].

2 Special relativity in Dirac materials

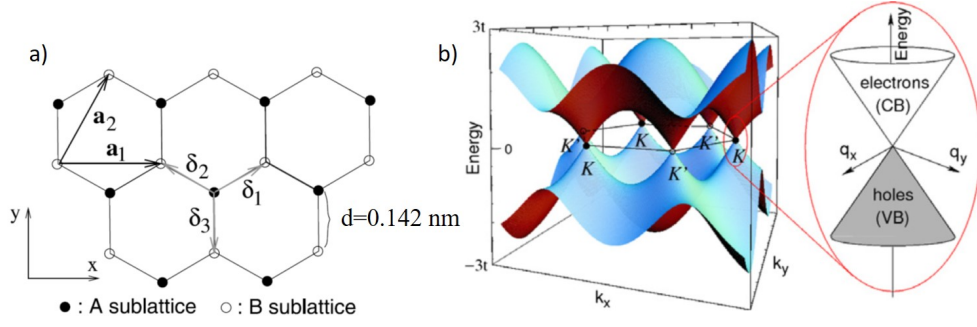


Figure 2.1: (a) Honeycomb lattice of graphene. (b) Spectrum of the tight-binding model (2.6) with a zoom-in at one of the K points to show the linear Dirac cone structure at low energy. Figures adapted from [85].

carbon atoms and the typical amplitude of lattice ripple, the electrons are supposed to be confined in two-dimensional space. It turns out that a tight-binding model considering only the nearest neighbor hopping is able to capture the low-energy physics of graphene [86]. In the second quantization, the tight-binding Hamiltonian is

$$H = -t \sum_{\mathbf{R}} \left[c_{\mathbf{R},A}^\dagger c_{\mathbf{R},B} + c_{\mathbf{R},A}^\dagger c_{\mathbf{R}-\mathbf{a}_1,B} + c_{\mathbf{R},A}^\dagger c_{\mathbf{R}+\mathbf{a}_2,B} + \text{H.c.} \right] \quad (2.6)$$

where $c_{\mathbf{R},\alpha}^{(\dagger)}$ is the annihilation (creation) operator of an electron in a p_z orbital situated in the unit-cell at a Bravais lattice point of \mathbf{R} , t is the hopping amplitude, and H.c. stands for the Hermitian conjugate taking into account the reversed hopping. By the lattice Fourier transformation, we can write the Hamiltonian in reciprocal space in the basis of $\{c_{\mathbf{k},A}, c_{\mathbf{k},B}\}$

$$H(\mathbf{k}) = -t \begin{bmatrix} 0 & \sum_{n=1}^3 e^{-i\mathbf{k}\cdot\delta_n} \\ \sum_{n=1}^3 e^{i\mathbf{k}\cdot\delta_n} & 0 \end{bmatrix} \quad (2.7)$$

with the spectrum of two bands

$$E^\pm(\mathbf{k}) = \pm t \left| \sum_{n=1}^3 e^{i\mathbf{k}\cdot\delta_n} \right| \quad (2.8)$$

As shown in Fig. 2.1(b), the two bands of $H(\mathbf{k})$ touch each other at two inequivalent points in the first Brillouin Zone dubbed \mathbf{K} and \mathbf{K}' points:

$$\mathbf{K} = \frac{4\pi}{\sqrt{3}a}(1, 0), \quad \mathbf{K}' = \frac{4\pi}{\sqrt{3}a}(-1, 0). \quad (2.9)$$

2.1 Special relativity in Graphene: crossed electric and magnetic fields

Since the p_z orbitals are occupied by only one electron, the resulting band structure is half-filled and the Fermi energy is situated at the band touching points. To describe the low-energy electronic dynamics, one can therefore expand the Hamiltonian (2.7) to linear order around \mathbf{K} and \mathbf{K}' points, with $\mathbf{q} = \mathbf{k} - \mathbf{K}(\prime)$. This yields the low energy Hamiltonian of graphene around \mathbf{K} and \mathbf{K}' valleys:

$$H_\xi(\mathbf{q}) = \hbar v_F (\xi q_x \sigma_x + q_y \sigma_y), \quad (2.10)$$

where $\xi = \pm 1$ stands for \mathbf{K} and \mathbf{K}' valley, respectively, and $v_F = 2ta/2\hbar \approx c/300$ is the Fermi velocity.² The spectrum of the Hamiltonian is linear:

$$E(\mathbf{q}) = \pm \hbar v_F |\mathbf{q}|, \quad (2.11)$$

which is isotropic around the Dirac point $\mathbf{q} = 0$ and also electron-hole symmetric.

Comparing (2.10) with the 2+1 Dirac Hamiltonian (2.3), the low-energy Hamiltonian of graphene coincides letter-by-letter with the 2 + 1 massless Dirac Hamiltonian simply after replacing the speed of light c by the Fermi velocity v_F . Hence, the low-energy electrons in graphene moving at the Fermi velocity obey mathematically the same laws of physics as the truly relativistic massless fermions moving at the speed of light. This emergent Lorentz symmetry at low energy is nowadays a paradigmatic example of emergence in condensed matter physics [5]. In particular, the Lorentz invariance, a symmetry property of Dirac equation, should manifest in graphene as shown in the following.

GRAPHENE IN THE PRESENCE OF A MAGNETIC FIELD: LANDAU LEVELS

Before tackling the problem about graphene in the presence of crossed electric and magnetic fields, I recall how to deal solely with the magnetic field [79]. In the following discussions, I do not consider the Zeeman effect and thus the spinless model (2.10) is applicable. With the help of the Peierls substitution [87], one can describe electrons of graphene in a magnetic field by replacing the momentum by its gauge-invariant form

$$\mathbf{p} \rightarrow \mathbf{\Pi} = \mathbf{p} + e\mathbf{A}(\mathbf{r}), \quad (2.12)$$

where e is the absolute value of elementary charge and $\mathbf{A}(\mathbf{r})$ is the vector potential that gives rise to the magnetic field $\mathbf{B} = \nabla \times \mathbf{A}(\mathbf{r})$. Consider the Hamiltonian for valley \mathbf{K} and the results for valley

²One should not confound here the speed of light c with the annihilation operator.

2 Special relativity in Dirac materials

\mathbf{K}' follow naturally once the problem for valley \mathbf{K} is solved. Henceforth, I set $\hbar = 1$ to simplify the calculations except when the restoration of \hbar is mentioned explicitly.³ Then, the Hamiltonian reads

$$H(\mathbf{q}) = v_F[\mathbf{q} + e\mathbf{A}(\mathbf{r})] \cdot \boldsymbol{\sigma} \quad (2.13)$$

where the momentum is equivalent to the wavevector. To explicitly do the calculations, I choose the following Landau gauge for the vector potential

$$\mathbf{A}(\mathbf{r}) = B(0, x, 0), \quad (2.14)$$

where $B > 0$. The corresponding magnetic field is thus $\mathbf{B} = B\mathbf{e}_z$. While q_y remains a good quantum number, q_x should be treated as a derivative operator with respect to x . Remarkably, the off-diagonal terms can be written in terms of ladder operators as for quantum harmonic oscillator. The two ladder operators are defined as

$$a = \frac{1}{\sqrt{2}} \left(q_x \ell_B - i \frac{x + q_y \ell_B^2}{\ell_B} \right), \quad (2.15)$$

$$a^\dagger = \frac{1}{\sqrt{2}} \left(q_x \ell_B + i \frac{x + q_y \ell_B^2}{\ell_B} \right), \quad (2.16)$$

$$\text{and} \quad 1 = [a, a^\dagger], \quad (2.17)$$

where the magnetic length $\ell_B = \sqrt{\hbar/eB}$ is introduced. Using the ladder operators, the Hamiltonian becomes

$$H = \frac{\sqrt{2}v_F}{\ell_B} \begin{bmatrix} 0 & a \\ a^\dagger & 0 \end{bmatrix} \quad (2.18)$$

so that its eigenvectors can be written as

$$|\psi_n\rangle = \begin{pmatrix} \sin \alpha_n |n-1\rangle \\ \cos \alpha_n |n\rangle \end{pmatrix} \quad \text{if } n \geq 1, \quad |\psi_n\rangle = \begin{pmatrix} 0 \\ |0\rangle \end{pmatrix} \quad \text{if } n = 0 \quad (2.19)$$

where $|n\rangle$ is the wavefunction of a one-dimensional quantum harmonic oscillator defined by the previous ladder operators, $a^\dagger a |n\rangle = n |n\rangle$. The center of $|n\rangle$ is linear in q_y

$$\langle x \rangle = -q_y \ell_B^2. \quad (2.20)$$

³For example, in numerical applications or experimentally relevant formula.

2.1 Special relativity in Graphene: crossed electric and magnetic fields

Applying the Hamiltonian to a given $|\psi_n\rangle$, the matrix to diagonalize becomes

$$H_n = \frac{\sqrt{2}v_F}{\ell_B} \begin{bmatrix} 0 & \sqrt{n} \\ \sqrt{n} & 0 \end{bmatrix} \quad (2.21)$$

and its spectrum is

$$E_n^\pm = \pm \hbar v_F \frac{\sqrt{2n}}{\ell_B} \quad (2.22)$$

where \hbar is restored (see Fig. 2.2).

If a staggered potential of type $\Delta\sigma_z$ is introduced in (2.10), the new Hamiltonian describes the low energy band structure of graphitic boron nitride hBN. Adopting the same notation as for graphene, the Hamiltonian of BN for the valley \mathbf{K} in the presence of magnetic field reads

$$H = \frac{\sqrt{2}v_F}{\ell_B} \begin{bmatrix} \Delta & a \\ a^\dagger & -\Delta \end{bmatrix} \quad (2.23)$$

with the Landau levels

$$\begin{aligned} E_n^\pm &= \pm \sqrt{\Delta^2 + \hbar^2 v_F^2 \frac{2n}{\ell_B^2}} && \text{if } n \geq 1, \\ E_0 &= -\Delta && \text{if } n = 0. \end{aligned} \quad (2.24)$$

Note that the spectrum is not particle-hole symmetric, i.e., a manifestation of the parity anomaly of the 2 + 1D Dirac equation [24, 27]. This pseudo-paradox is solved by considering together two valleys \mathbf{K} and \mathbf{K}' where $E_0 = \Delta$ for \mathbf{K}' Fig. 2.2.

Discrete Landau levels are formed when the magnetic field is perpendicular to the graphene sheet. If the magnetic field is not perpendicular but tilted with an angle θ to the plane of graphene, one only needs to consider the out-of-plane part $B \sin \theta$. The in-plane magnetic field which can be generated by an out-of-plane component of vector-potential does not couple to any in-plane momentum. Thus, it will not show up in a Hamiltonian of two-dimensional system. As a result, the Landau levels for an arbitrary magnetic field remain the same except that B is replaced by $B \sin \theta$ in the definition of the magnetic length.

2 Special relativity in Dirac materials

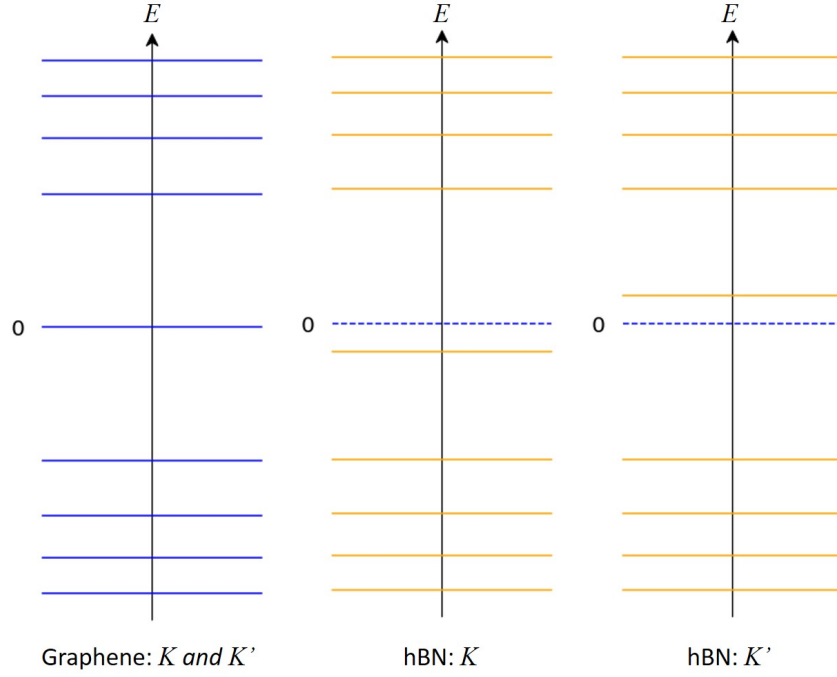


Figure 2.2: Schematics of Landau levels for graphene and hBN. The zero energy is marked by blue dashed lines in the plots for hBN. For illustration purpose only, I use a rather strong magnetic field so that the Landau level spacing is even larger than the band gap of hBN (~ 6 eV).

2.1.2 REFRESHER ON SPECIAL RELATIVITY

Before using the relativistic analogy to solve our problem, one needs the four-vector formalism used in Einstein's theory of special relativity. The reader can refer to App. A.1 and A.2 for a short summary of the formalism.

Here, I recall some useful results. If a frame \mathcal{R}' moves relative to the lab frame \mathcal{R} at velocity \mathbf{v} , then the electric and magnetic field in the two frames transform in the following manner:

$$\begin{aligned} \mathcal{E}'_{\parallel} &= \mathcal{E}_{\parallel}, & \mathcal{E}'_{\perp} &= \gamma(\mathcal{E}_{\perp} + \mathbf{v} \times \mathbf{B}), \\ \mathbf{B}'_{\parallel} &= \mathbf{B}_{\parallel}, & \mathbf{B}'_{\perp} &= \gamma\left(\mathbf{B}_{\perp} - \frac{1}{c^2}\mathbf{v} \times \mathcal{E}\right) \end{aligned} \quad (2.25)$$

where the longitudinal and transverse directions are defined with respect to \mathbf{v} and the Lorentz factor $\gamma = 1/\sqrt{1 - \beta^2}$ with $\beta = v/c$.

2.1 Special relativity in Graphene: crossed electric and magnetic fields

Using the electromagnetic field tensor, one can write two Lorentz invariants :

$$F_{\mu\nu}F^{\mu\nu} = 2\left(B^2 - \frac{\mathcal{E}^2}{c^2}\right) \quad (2.26)$$

$$\epsilon_{\mu\nu\rho\sigma}F^{\mu\nu}F^{\rho\sigma} = \frac{8}{c}\mathcal{E} \cdot \mathbf{B} \quad (2.27)$$

where $\mathcal{E}, B > 0$ is the magnitude of field. The value of the two invariants is universal for all the inertial frames. The first invariant says that if the magnitude of the magnetic field is larger or smaller than that of the electric field (in Gaussian units) in one frame, then the inequality holds in all other frames. One can thus distinguish two different regimes: the magnetic regime for $B > \mathcal{E}/c$ and the electric regime for $B < \mathcal{E}/c$ [80]. The second invariant has a profound topological consequence in quantum field theory [24, 77]. A non-vanishing value of $\mathcal{E} \cdot \mathbf{B}$ is responsible for axion electrodynamics which is theoretically shown to govern in topological materials [76, 88, 89]. Here, I am only interested in the case where $\mathcal{E} \cdot \mathbf{B} = 0$, i.e., the magnetic field is perpendicular to the electric field. Notably, depending on the sign of the first invariant, one can always find a frame where one of the two fields is absent. For example, if $B > \mathcal{E}/c$ ($B < \mathcal{E}/c$), there exists a frame in which $\mathcal{E} = 0$ ($B = 0$). At the critical value $B = \mathcal{E}/c$, there is no frame in which one of the two fields is zero while the other remains finite. This is coherent with the fact that light is Lorentz invariant and a transverse electromagnetic wave that requires both an electric and a magnetic component.

2.1.3 LANDAU LEVELS IN THE PRESENCE OF CROSSED ELECTRIC AND MAGNETIC FIELDS

Now I am ready to solve the spectrum of graphene in the presence of crossed electric and magnetic fields, with an in-plane electric and an out-of-plane magnetic field, along the lines initially proposed by Lukose et al. [53]. This configuration of electric and magnetic field is exactly the one that I have just discussed. To apply the previous results in Einstein's special relativity in graphene, I just replace the limiting speed, i.e., the speed of light c , by the Fermi velocity v_F .

Since the Hamiltonian (2.10) is isotropic, one can suppose without losing generality that the electric field is applied in the x -direction, $\mathcal{E} = \mathcal{E}e_x$ ($\mathcal{E} > 0$). The magnetic field \mathbf{B} is always in the z -direction, perpendicular to the graphene sheet. Using the Landau gauge $\mathbf{A}(\mathbf{r}) = B(0, x, 0)$, the Hamiltonian of graphene in the presence of crossed electric and magnetic fields is

$$H(\mathbf{q}) = e\mathcal{E}x + v_Fq_x\sigma_x + v_F(q_y + eBx)\sigma_y, \quad (2.28)$$

where the first term on the right is the potential energy of an electron exposed to an electric field \mathcal{E} . One might want to solve the spectrum by writing the Hamiltonian in terms of ladder operators as

2 Special relativity in Dirac materials

in the previous section. However, the first term would be proportional to $i(a - a^\dagger)$ such that the wavefunction expressed in Eq. (2.19) is no longer an eigenvector of the Hamiltonian. This problem cannot be avoided by any unitary transformation on the Hamiltonian since the new term is scalar. I will explain this fact in detail in the following section.

This problem may be solved elegantly by appealing to Lorentz invariance of the Dirac equation [53]. Here, I reformulate this method in a more elementary way that leads to the spectrum of the Hamiltonian without invoking explicitly the Dirac equation. Using the analogy with special relativity, one is able to find a moving frame other than the lab frame where the Hamiltonian is written so that the electric or the magnetic field is zero. In this moving frame, one can solve the problem that graphene is subjected only to an electric or magnetic field. Finally, one does an inverse Lorentz transformation to get the energy attached to the lab frame. Almost immediately from the result of the previous section, one knows without any calculations that there are two possible regimes: the electric regime where the electric field is stronger than the magnetic field ($B < \mathcal{E}/v_F$) and the magnetic regime for the opposite ($B > \mathcal{E}/v_F$). From now on, I am only interested in the the magnetic regime where the magnetic field is larger than a critical value set by the electric field, $B_c = \mathcal{E}/v_F$.⁴ There exists then a frame of reference where one has $\mathcal{E}'_{\parallel} = \mathcal{E}'_{\perp} = 0$ in Eq. (2.25). As a result, the frame of reference \mathcal{R}' in question moves in the y -direction with the speed $\mathbf{v} = -\mathcal{E}/B\mathbf{e}_y$ with respect to the lab frame. The Lorentz factor is defined as

$$\boldsymbol{\beta} = -\frac{\mathcal{E}}{v_F B}\mathbf{e}_y = -\frac{v_D}{v_F}\mathbf{e}_y, \quad \gamma = \frac{1}{\sqrt{1 - \beta^2}}, \quad (2.29)$$

where $\|\boldsymbol{\beta}\| < 1$ is the modulus of the drift velocity $v_D = \mathcal{E}/B$ divided by v_F . Then, the magnetic field in the moving frame is renormalized to $\mathbf{B}' = B/\gamma\mathbf{e}_z$. In the frame of reference \mathcal{R}' , electrons are thus subjected to an out-of-plane magnetic field of magnitude B/γ in the absence of electric field. The energy spectrum in \mathcal{R}' can then simply be read off from Eq. (2.22)

$$E'_n{}^{\pm} = \pm\hbar\frac{v_F}{\ell_B}\sqrt{\frac{2n}{\gamma}} \quad (2.30)$$

⁴The reason is that graphene is a (semi-)metal with no gap. An electric field should induce a current making the system in non-equilibrium whereas the Hamiltonian only makes sense at equilibrium. However, tunneling phenomena such as Klein tunneling are possible in the electric regime where the transmission coefficient and the conductance are renormalized by the magnetic field [90].

where the magnetic length is still defined by \mathbf{B} in the lab frame. To get the spectrum in the lab frame, it suffices to do an inverse Lorentz transformation on the four-momentum from p'^{μ} to p^{μ} defined by

$$\Lambda^{-1} = \begin{pmatrix} \gamma & 0 & \gamma\|\boldsymbol{\beta}\| \\ 0 & 1 & 0 \\ \gamma\|\boldsymbol{\beta}\| & 0 & \gamma \end{pmatrix} \quad (2.31)$$

so that $p^{\mu} = (\Lambda^{-1})^{\mu}_{\nu} p'^{\nu}$. Note that one has only $2 + 1$ dimensional space-time. Finally, the energy spectrum of graphene in the presence of crossed electric and magnetic fields in the magnetic regime is derived

$$E_n^{\pm} = \pm \hbar \frac{v_F}{\gamma \ell_B} \sqrt{\frac{2n}{\gamma}} - \hbar v_F \beta q_y, \quad (2.32)$$

where $\beta = v_D/v_F$. To be complete, one anticipates here that the underlying Lorentz transformation also transforms the Hamiltonian and the spinorial wavefunctions as shown later in this chapter. Nevertheless, the spectrum of graphene is obtained without making hands dirty by solving analytically the Hamiltonian (2.28).

RENORMALIZATION BY LORENTZ BOOST

As explicitly shown in Eq. (2.32), the spacing between Landau levels is renormalized down by a factor of $\gamma^{-3/2}$. In addition, the previous calculations show that the exponent of $-3/2$ is the sum of $-1/2$ and -1 stemming from the magnetic field and the four-momentum being renormalized when the frame is changed, respectively. Compared to the completely flat Landau levels in the absence of the electric field [see Eq. (2.22)], the spectrum acquires a dispersion in q_y with a velocity $-v_D e_y$. This is precisely the drift velocity⁵ of a classical electron⁶ due to the Lorentz force created by crossed electric and magnetic fields.

To conclude, a relativistic renormalization effect characterized by the Lorentz factor γ can indeed manifest in the energy spectrum of originally non-relativistic electrons!

2.2 UNITARY AND HYPERBOLIC TRANSFORMATIONS

In this section, I will show the techniques to solve analytically general Hamiltonians of the form (2.28) and obtain not only its spectrum but also its eigenstates. The latter will be necessary to discuss the spectroscopic properties of Dirac materials. It turns out that one can solve the problem elegantly thanks to

⁵This is also the reason why I call it drift velocity in the first place.

⁶The word classical is here the antonym of quantum mechanical.

2 Special relativity in Dirac materials

the symmetry properties of the Dirac equation (or the Dirac Hamiltonian). One does not have to resort to look into the differential equation but just two sets of transformations acting on the Hamiltonian. These two kinds of transformations, i.e., the unitary and hyperbolic transformations, will considerably simplify the calculations. The reason why these transformations work is that the Dirac equation is Lorentz invariant but the spinors transform under the two transformations when the frame of reference is changed. So, solving the problem by the unitary and hyperbolic transformations is totally equivalent to switching back and forth the frame of observation as in the previous section.

Here I adopt the attitude of “reinventing the wheel”, that is deriving the results well-known in group theory [91, 92] according to the need and trying not to invoking too much group theory. This is a practical approach: I need some tools to do the job so I try to rephrase it from zero.

2.2.1 UNITARY TRANSFORMATIONS: ROTATIONS

A Dirac Hamiltonian only contains Pauli matrices which can be written as

$$H(\mathbf{x}) = \mathbf{x} \cdot \boldsymbol{\sigma} = x_1\sigma_1 + x_2\sigma_2 + x_3\sigma_3 \quad (2.33)$$

where σ_i are the three Pauli matrices. Here, I want to find a unitary transformation U on $H(\mathbf{x})$ so that given a rotation R

$$UH(\mathbf{x})U^\dagger = H(R\mathbf{x}) \quad (2.34)$$

where $H(R\mathbf{x})$ reads

$$H(R\mathbf{x}) = (R\mathbf{x}) \cdot \boldsymbol{\sigma} = R_{ij}x_j\sigma_i = x_i(R^{-1})_{ij}\sigma_j \quad (2.35)$$

This result justifies why one can organize the Pauli matrices in the form of vector in the previous Hamiltonian: $\boldsymbol{\sigma}$ acts like a real vector under rotations.

Since the spectrum of $H(R\mathbf{x})$ and $H(\mathbf{x})$ are both $\pm\|\mathbf{x}\|$, valid matrices U belong to the group $U(2)$. So, I call transformations defined by U unitary transformations. One can even suppose matrices U is in the group $SU(2)$ since additional phase factor of a unitary matrix is canceled by applying both U and U^\dagger . Given $U \in SU(2)$, one can thus write

$$U = e^{i\frac{\theta}{2}\hat{\mathbf{n}} \cdot \boldsymbol{\sigma}} = \cos \frac{\theta}{2} I_2 + i \sin \frac{\theta}{2} \hat{\mathbf{n}} \cdot \boldsymbol{\sigma} \quad (2.36)$$

where $\hat{\mathbf{n}}$ is the normalized vector of the axis of rotation and θ is the angle of rotation.⁷ One can check this for a rotation of θ around the z -axis. The corresponding unitary transformation is defined as

$$U = e^{i\frac{\theta}{2}\sigma_3} = \begin{bmatrix} e^{i\frac{\theta}{2}} & 0 \\ 0 & e^{-i\frac{\theta}{2}} \end{bmatrix}. \quad (2.37)$$

This would give

$$\begin{aligned} (\sigma_1, \sigma_2, \sigma_3) &\rightarrow (\cos \theta \sigma_1 - \sin \theta \sigma_2, \sin \theta \sigma_1 + \cos \theta \sigma_2, \sigma_3) \\ H(x_1, x_2, x_3) &\rightarrow H(\cos \theta x_1 + \sin \theta x_2, -\sin \theta x_1 + \cos \theta x_2, x_3) \\ &\equiv H(x'_1, x'_2, x'_3). \end{aligned} \quad (2.38)$$

which precisely do the rotation on \mathbf{x} .

One may be curious why only half of the angle appears in the definition of U . The reason is encoded in the relation between the group $SU(2)$ and $SO(3)$. In group theory, $SU(2)$ doubly covers $SO(3)$, meaning that for each $R(\theta\hat{\mathbf{n}})$ one can find two different $SU(2)$ matrices doing the same transformation, namely $\pm U(\theta\hat{\mathbf{n}}/2)$. This is precisely the meaning of half angle that $\theta/2 \rightarrow (\theta + 2\pi)/2$ add a negative sign in front of U while $R(\theta) = R(\theta + 2\pi)$.

2.2.2 HYPERBOLIC TRANSFORMATIONS: LORENTZ BOOST

In some problems like Eq. (2.28), the Hermitian Hamiltonian matrix can always be written as

$$H(\underline{x}) = \eta_{\mu\nu} x^\mu \sigma^\nu = x^0 \sigma^0 - x^1 \sigma^1 - x^2 \sigma^2 - x^3 \sigma^3 \quad (2.39)$$

where the two-by-two identity $\sigma^0 = I_2$ is present compared to above. The position of indices has a meaning: contravariant if it shows as superscript and covariant if it shows as a lower index. So,

$$\{\sigma^0, \sigma^1, \sigma^2, \sigma^3\} \equiv \{I_2, -\sigma_x, -\sigma_y, -\sigma_z\} \quad (2.40)$$

$$\{\sigma_0, \sigma_1, \sigma_2, \sigma_3\} \equiv \{I_2, \sigma_x, \sigma_y, \sigma_z\}. \quad (2.41)$$

⁷The last equality can be verified by expanding the exponential in the series.

2 Special relativity in Dirac materials

In analogy with the above discussion, \underline{x} is considered as a four-vector in the sense that its components transform under the Λ matrices in the Lorentz group, i.e., $SO(3, 1)$. I want to find a transformation M on $H(\underline{x})$ so that given a Lorentz transformation Λ

$$MH(\underline{x})M^\dagger = H(\Lambda\underline{x}), \quad (2.42)$$

where $H(\Lambda\underline{x})$ reads

$$H(\Lambda\underline{x}) = (\Lambda\underline{x}) \cdot \underline{\sigma} = \eta_{\mu\nu} \Lambda^\mu{}_\rho x^\rho \sigma^\nu = \eta_{\mu\nu} x^\mu \Lambda^\nu{}_\rho \sigma^\rho = \underline{x} \cdot (\Lambda^{-1} \underline{\sigma}). \quad (2.43)$$

This result justifies why one can organize σ^μ in the form of four-vector in the previous Hamiltonian. Indeed, $\underline{\sigma}$ acts like a real four-vector under Lorentz transformations.

Concretely, Λ matrices are the matrices for Lorentz boosts and rotations. Since rotations have already been discussed, I focus on how to find a transformation M on σ_μ associated to a Lorentz boost on x^μ . Clearly, M cannot be a unitary matrix because a Lorentz boost alters x^0 in front of I_2 which is invariant under any unitary transformations. One has to look for candidates in a larger group namely $SL(2, \mathbb{C})$, i.e., the complex special linear group. This group is actually the optimal choice one can have. On the one hand, the Lorentz transformations preserves the Minkowski metric $x^\mu x_\mu$ which is also the determinant of the Hamiltonian matrix. A matrix M preserving the determinant of the Hamiltonian belongs to $SL(2, \mathbb{C}) \times U(1)$. On the other hand, as before, since both M and M^\dagger apply, one can only deal with M with unity determinant, that is precisely the $SL(2, \mathbb{C})$. Given $M \in SL(2, \mathbb{C})$, one can write

$$M(\phi \hat{\mathbf{n}}_\phi, \theta \hat{\mathbf{n}}_\theta) = e^{(-\frac{\phi}{2} \hat{\mathbf{n}}_\phi + i \frac{\theta}{2} \hat{\mathbf{n}}_\theta) \cdot \boldsymbol{\sigma}} \quad (2.44)$$

where $\hat{\mathbf{n}}_{\phi, \theta}$ are the normalized vector of the axis of boost and rotation and (ϕ, θ) are the rapidity of boost and angle of rotation, respectively. Here, $\boldsymbol{\sigma} = (\sigma_x, \sigma_y, \sigma_z)$. Focusing on Lorentz boosts, one sets $\theta = 0$ so that

$$M = e^{-\frac{\phi}{2} \hat{\mathbf{n}} \cdot \boldsymbol{\sigma}} = \cosh \frac{\phi}{2} I_2 - \sinh \frac{\phi}{2} \hat{\mathbf{n}} \cdot \boldsymbol{\sigma} \quad (2.45)$$

where hyperbolic functions appear, that is the reason why M is called hyperbolic transformation. The boost Λ determined by the hyperbolic transformation M shows how a four-vector \underline{x}' of the frame \mathcal{R}' , moving relative to \mathcal{R} with a speed $v/c = \tanh \phi e_z$, is written in terms of \underline{x} of \mathcal{R} .

One can check this for a Lorentz boost of rapidity ϕ along the z -axis. The corresponding matrix M is $\exp(-\phi\sigma_z/2)$. Applying MHM^\dagger would give

$$\begin{aligned}
 (I_2, \sigma_x, \sigma_y, \sigma_z) &\rightarrow (\cosh \phi I_2 - \sinh \phi \sigma_z, \sigma_x, \sigma_y \sinh \phi I_2 - \cosh \phi \sigma_z) \\
 (\sigma^0, \sigma^1, \sigma^2, \sigma^3) &\rightarrow (\cosh \phi \sigma^0 + \sinh \phi \sigma^3, \sigma^1, \sigma^2, \sinh \phi \sigma^0 + \cosh \phi \sigma^3) \\
 H(x^0, x^1, x^2, x^3) &\rightarrow H(\cosh \phi x^0 - \sinh \phi x^3, x^1, x^2, -\sinh \phi x^0 + \cosh \phi x^3) \\
 &\equiv H(x'^0, x'^1, x'^2, x'^3).
 \end{aligned} \tag{2.46}$$

This is exactly what does the given Lorentz boost to a four-vector \underline{x} .

Similar to unitary transformations, only half rapidity appears in the definition of M because the $SL(2, \mathbb{C})$ group double covers the Lorentz group $SO(3, 1)$ consisting of all the Lorentz transformation matrix Λ . The definition of M given here is called $(0, 1/2)$ projective representation, thus two-by-two matrices acting on spinors, of the $SO(3, 1)$ group. In fact, the two possible definitions of $M(\pm\phi\hat{n}_\phi, \theta\hat{n}_\theta)$ map a matrix in $SL(2, \mathbb{C})$ to a matrix in $SO(3, 1)$. Unlike the mapping from $SU(2)$ to $SO(3)$, the two spin-1/2 projective representations, $(0, 1/2)$ and $(1/2, 0)$, with opposite sign in front of ϕ in the definition of M are inequivalent. However, this fact is irrelevant for the practical usage in the following.

The reader should now understand the relation between unitary transformations and rotations and that between hyperbolic transformations and Lorentz boosts. Within each pair, the two different operations are the two different representations of the same physical transformation acting on their corresponding mathematical objects. Talking about the transformation of the frame of reference, the four-vector is transformed by the Lorentz boost Λ while the Hamiltonian and the spinorial wavefunctions are transformed by the hyperbolic transformation M . In the jargon of group theory, Hamiltonian, spinorial wavefunctions and four-vectors provide different representations of the same group $SO(3, 1)$.

2.2.3 CHEATING SHEET FOR UNITARY AND HYPERBOLIC TRANSFORMATIONS

To emphasize the difference between the unitary and hyperbolic transformations, I list the properties of both transformations in this part. This would also facilitate the calculations without always doing matrix product such as THT^\dagger .

2 Special relativity in Dirac materials

UNITARY TRANSFORMATIONS

Unitary transformations are two-dimensional representation of rotations. A matrix U of unitary transformations is defined as

$$U = e^{i\frac{\theta}{2}\hat{\mathbf{n}}\cdot\boldsymbol{\sigma}} = \cos\frac{\theta}{2}I_2 + i\sin\frac{\theta}{2}\hat{\mathbf{n}}\cdot\boldsymbol{\sigma} \quad (2.47)$$

with the following properties:

- When one applies a unitary transformation on a Hamiltonian H , it means: UHU^\dagger .
- U conserves the spectrum of Hamiltonian.
- U is in general non-hermitian. $U^{-1} = U^\dagger$ represents the inverse transformation.
- U forms a multiplicative group namely $SU(2)$ such that the product of two unitary transformations is also a unitary transformation.
- If $U = \exp(i\theta\sigma_i/2)$, then

$$U\sigma_jU^\dagger = \sigma_j \quad \text{if} \quad i = j \quad (2.48)$$

where $\sigma_{i,j}$ are the Pauli matrices.

- Sometimes it is useful to think of unitary transformation $U(\theta\hat{\mathbf{n}})$ as a rotation $R(\theta\hat{\mathbf{n}})$ on $\boldsymbol{\sigma}$ so that $\boldsymbol{\sigma}' = R\boldsymbol{\sigma}$. This is done by $U^\dagger\boldsymbol{\sigma}U$ (be careful to the order of matrices).

HYPERBOLIC TRANSFORMATIONS

Hyperbolic transformations are two-dimensional representation of Lorentz boosts. A matrix M of hyperbolic transformations is defined as

$$M = e^{-\frac{\phi}{2}\hat{\mathbf{n}}\cdot\boldsymbol{\sigma}} = \cosh\frac{\phi}{2}I_2 - \sinh\frac{\phi}{2}\hat{\mathbf{n}}\cdot\boldsymbol{\sigma} \quad (2.49)$$

with the following properties:

- When one applies a hyperbolic transformation on a Hamiltonian H , it means: MHM^\dagger .
- M modifies the spectrum of Hamiltonian as a Lorentz boost does to the component 0 of a four-momentum namely energy.
- M is hermitian so that one can write $MHM^\dagger = MHM$.
- $M^{-1} \neq M^\dagger$ represents the inverse transformation.
- The pure Lorentz boosts M do not form a multiplicative group so that the product of two hyperbolic transformations are in general not another hyperbolic transformation. This is in line

with the fact that the product of two non-collinear Lorentz boosts is the product of another Lorentz boost and a rotation called Thomas-Wigner rotation.⁸ Alternatively, if M is defined by Eq. (2.44), they form a multiplicative group named $SO(3, 1)$ including Lorentz boosts and rotations.

- If $M = \exp(-\phi\sigma_i/2)$, then

$$M\sigma_jM = \sigma_j \quad \text{if} \quad i \neq j \quad (2.51)$$

where σ s are the Pauli matrices.

- Sometimes it is useful to think of a hyperbolic transformation $M(\phi\hat{\mathbf{n}})$ as a Lorentz boost $\Lambda(\phi\hat{\mathbf{n}})$ on $\underline{\sigma} \equiv (I_2, \sigma_x, \sigma_y, \sigma_x)$ such that $\underline{\sigma}' = \Lambda\underline{\sigma}$. This is also done by $M\underline{\sigma}M$.

2.2.4 GENERALIZED UNITARY AND HYPERBOLIC TRANSFORMATIONS: RECIPE

In the previous section, I considered only Pauli matrices since the Hamiltonian of interest can always be decomposed into their linear combination. One might think that unitary and hyperbolic transformations are only useful for this form of Hamiltonians, but this is not the case. In this section, I will extend the use of unitary and hyperbolic transformations to all the Dirac Hamiltonians that can always be written as a linear combination of the tensor products of the Pauli matrices, in which the Lorentz invariance is generally absent. Rather than a generalization of Lorentz transformations to general Dirac Hamiltonians, it is more appropriate to think of Lorentz transformations as just one particular manifestation of hyperbolic transformation.

Nevertheless, the “generalization” allows us to solve all the Dirac $\mathbf{k} \cdot \mathbf{p}$ Hamiltonians in the presence of a crossed magnetic and electric fields and alike with only linear momentum such as

$$H = \sum_{i=1}^d t_i k_i + \sum_{i,j=1}^d v_{ij} k_i M_j \quad (2.52)$$

where M_i are tensor products of the Pauli matrices and the two-by-two identity matrix I_2 .⁹ In particular, I give a recipe to find the unitary and hyperbolic transformations according to need. The core of this

⁸This can be seen by the Baker–Campbell–Hausdorff formula:

$$e^A e^B = e^C \quad \text{with} \quad C = A + B + \frac{1}{2}[A, B] + \dots \quad (2.50)$$

If A, B are two different Pauli matrices so that the commutator of A and B is two times the complex i times the third Pauli matrix where a rotation emerges.

⁹One can even generalized further the Hamiltonian to allow the index j to have a different range than i . Nevertheless, the present Hamiltonian is sufficiently generalized for the discussions in the thesis.

2 Special relativity in Dirac materials

recipe is to reduce the number of matrices in the Hamiltonian of interest by unitary transformations and then solve the problem by a Lorentz boost defined by a hyperbolic transformation.

Before introducing any external field, one should render the $\mathbf{k} \cdot \mathbf{p}$ Hamiltonian as simple as possible. A practical criterion for simplicity is that every non-identity matrix is only accompanied by one component of the momentum. To do so, one factorizes the Hamiltonian by momentum k_i and then focuses on those components with two or more matrices associated, $v_{ij}M_j$. Recall that two matrices written in a tensor product of the Pauli matrices and I_2 either commute or anti-commute. To merge two matrices, say M_1 and M_2 , into a simple one by unitary transformation, they must anti-commute so that there exist a matrix R that M_1, M_2, R form a Lie algebra like the Pauli matrices. In particular, $M_1M_2 = iR$. So the desired unitary transformation is defined by $U = \exp(i\theta R/2)$ where θ is found by writing the coefficients of M_1 and M_2 in trigonometric functions. For example, given $H = v_x\sigma_x + v_y\sigma_y$ and thus $R = \sigma_z$, one can write

$$\begin{aligned} v_x\sigma_x + v_y\sigma_y &= v \cos \theta \sigma_x + v \sin \theta \sigma_y \\ \text{with } v &= \sqrt{v_x^2 + v_y^2} \\ \tan \theta &= \frac{v_x}{v_y}. \end{aligned}$$

The unitary transformation $U = \exp(i\theta\sigma_z/2)$ can thus simplify H to $UHU^\dagger = v\sigma_x$. One can repeat this step for all the pairs of matrices in factor that anti-commute until the Hamiltonian cannot be simplified further.

Once the Hamiltonian is simplified, one can introduce electric and magnetic field by the Peierls substitution choosing a Landau gauge so that only one spatial coordinate appears in the Hamiltonian which does not commute with one of the components of the momentum. Thus, the other components k_i remains good quantum numbers. When a real or an effective electric field is present, the spatial coordinate appears in front of two matrices, say N_1 and N_2 , that commute. To merge these two matrices, one has to use a hyperbolic transformation $T = \exp(-\phi N/2)$. The choice of matrix N depends on the coefficient in front of N_1 and N_2 . If the coefficient of N_1 is larger in absolute value, then $N = N_1$. Otherwise, $N = N_2$. Here, one also determines the regime of the Hamiltonian of interest, electric or magnetic regime. The rapidity ϕ is then found by writing the coefficients in hyperbolic functions. Once all the steps are done, the transformed Hamiltonian has only either magnetic or electric field and it is thus easy to solve. while this recipe might seem horribly abstract for the moment, I will repeatedly illustrate it in the following part of this chapter as well as in Chapter 3, 4 and 5.

2.3 WAVEFUNCTIONS OF HAMILTONIAN FOR GRAPHENE IN CROSSED ELECTRIC AND MAGNETIC FIELDS

Let me illustrate the recipe mentioned in the previous section with the example of graphene in crossed electric and magnetic fields. Using the hyperbolic transformations, one can now solve the Hamiltonian (2.28) in the magnetic regime which I recall here

$$H = e\mathcal{E}x + v_F q_x \sigma_x + v_F (q_y + eBx) \sigma_y = v_F Bx \left(\frac{v_D}{v_F} + \sigma_y \right) + v_F (q_x \sigma_x + q_y \sigma_y) \quad (2.53)$$

where $v_D = \mathcal{E}/B < v_F$ and the Landau gauge $A_y = Bx$ is used so that k_y is a good quantum number. Since one knows how to solve the case with only magnetic field, it is tempting to get rid of $e\mathcal{E}x$ (or equivalently v_D/v_F) using a hyperbolic transformation. Replacing v_D/v_F by $-\tanh \phi$, the Hamiltonian becomes

$$H = v_F Bx (-\tanh \phi \mathbb{I} + \sigma_y) + v_F (q_x \sigma_x + q_y \sigma_y) \quad (2.54)$$

$$= v_F \frac{B}{\cosh \phi} x (-\sinh \phi \mathbb{I} + \cosh \phi \sigma_y) + v_F (q_x \sigma_x + q_y \sigma_y) \quad (2.55)$$

where I emphasize the matrix structure by adding the general identity matrix \mathbb{I} which is two-by-two in the context. Here, one finds the structure mentioned in Sec. 2.2.4 with the two commuting matrices $N_1 = \mathbb{I}$ and $N_2 = \sigma_y$, since $\cosh \phi > \sinh \phi$, the required hyperbolic transformation is generated by σ_y ,

$$T = e^{\frac{\phi}{2} \sigma_y}. \quad (2.56)$$

The trick to find quickly this transformation is to note that σ_y is the Pauli matrix in the exponential because the hyperbolic transformation is effective only when the Pauli matrix in the exponential commutes with the one of interest. The rapidity ϕ is already given in the form above. Finally, one just needs to set the sign in front of ϕ to be the opposite of the relative sign between the two terms in study. After the hyperbolic transformation, we have

$$H_T = THT = v_F q_y \sinh \phi + v_F q_x \sigma_x + v_F \left(q_y \cosh \phi + e \frac{B}{\cosh \phi} x \right) \sigma_y. \quad (2.57)$$

2 Special relativity in Dirac materials

Since T does not conserve the spectrum of H , one needs the relation between the spectra of two Hamiltonians. Given $|\psi\rangle$ an eigenstate of H , we can write $THTT^{-1}|\psi\rangle = ET^2T^{-1}|\psi\rangle$. Thus, we can define $|\psi_T\rangle = \mathcal{N}T^{-1}|\psi\rangle$ with a normalization factor \mathcal{N} such that

$$H_T|\psi_T\rangle = ET^2|\psi_T\rangle = E(\cosh \phi + \sinh \phi \sigma_y)|\psi_T\rangle \quad (2.58)$$

from which one finds a Hamiltonian H_E of eigenstate $|\psi_T\rangle$, $H_E = (H_T - E \sinh \phi \sigma_y) / \cosh \phi$, having the same spectrum as the original Hamiltonian H

$$H_E = v_F q_y \tanh \phi + \frac{1}{\cosh \phi} \left[v_F q_x \sigma_x + v_F \left(q_y \cosh \phi + e \frac{B}{\cosh \phi} x - \frac{E \sinh \phi}{v_F} \right) \sigma_y \right]. \quad (2.59)$$

Even if the Hamiltonian H_E depends itself on the energy E , I will show that the energy-dependent term in H_E is irrelevant to the spectrum but encoded in the wavefunction $|\psi_T\rangle$. As only the magnetic field is present, the off-diagonal terms can be also written in terms of energy-dependent ladder operators. We define

$$a_E = \sqrt{\frac{\cosh \phi}{2}} \left(q_x \ell_B - i \frac{x + q_y \ell_B^2 \cosh^2 \phi - \frac{E}{v_F} \ell_B^2 \sinh \phi \cosh \phi}{\ell_B \cosh \phi} \right), \quad (2.60)$$

$$a_E^\dagger = \sqrt{\frac{\cosh \phi}{2}} \left(q_x \ell_B + i \frac{x + q_y \ell_B^2 \cosh^2 \phi - \frac{E}{v_F} \ell_B^2 \sinh \phi \cosh \phi}{\ell_B \cosh \phi} \right), \quad (2.61)$$

$$1 = [a_E, a_E^\dagger] \quad (2.62)$$

where $\ell_B = \sqrt{\hbar/eB}$. Using the ladder operators, H_E becomes

$$H_E = v_F q_y \tanh \phi + \frac{v_F}{\ell_B \cosh \phi} \sqrt{\frac{2}{\cosh \phi}} \begin{bmatrix} 0 & a_E \\ a_E^\dagger & 0 \end{bmatrix} \quad (2.63)$$

so that its eigenvectors can be written as

$$|\psi_n\rangle = \begin{pmatrix} \sin \alpha_n |n-1\rangle_E \\ \cos \alpha_n |n\rangle_E \end{pmatrix} \quad \text{if } n \geq 1, \quad |\psi_n\rangle = \begin{pmatrix} 0 \\ |0\rangle_E \end{pmatrix} \quad \text{if } n = 0 \quad (2.64)$$

2.3 Wavefunctions of Hamiltonian for graphene in crossed electric and magnetic fields

where $|n\rangle_E$ is the wavefunction of the one-dimensional quantum harmonic oscillator defined by the previous ladder operators, $a_E^\dagger a_E |n\rangle_E = n |n\rangle_E$. The lower index E indicates that the center of $|n\rangle_E$ is energy-dependent namely

$$\langle x \rangle_E = -q_y \ell_B^2 \cosh^2 \phi + \frac{E}{v_F} \ell_B^2 \sinh \phi \cosh \phi \quad (2.65)$$

where the energy-dependent term in H_E is absorbed in the definition of the ladder operator so that it is irrelevant to the spectrum. However, the center of the wavefunction depends on the energy. In particular, the eigenstates for the same momentum q_y for different Landau levels are not orthogonal to each other due to the mismatch of its energy-dependent guiding centers. This induces new selection rules in Landau level spectroscopy which I will present in Chapter 3.

Applying H_E on $|\psi_n\rangle$, the spectrum is found

$$E_n^\pm = \pm \hbar \frac{v_F}{\ell_B \cosh \phi} \sqrt{\frac{2n}{\cosh \phi}} + \hbar v_F q_y \tanh \phi \quad (2.66)$$

where \hbar is restored. The relation between hyperbolic transformations and Lorentz boosts is clear if one compares this method using hyperbolic transformations with the relativistic argument in the previous section of this chapter. Identifying $\cosh \phi = \gamma > 0$ and $\tanh \phi = \beta < 0$, the spectrum solved with the help of hyperbolic transformations is identical to (2.32). Furthermore, the hyperbolic transformation T can be seen as $\exp(-(-\phi)\sigma_y/2)$. The physical meaning of T is a Lorentz boost that allows to write a four-vector \underline{x}' of the moving frame in terms of \underline{x} of the lab frame. \underline{x} and \underline{x}' are two observations of the same physical quantity associated to the lab frame and the moving frame, respectively. Mathematically, it means that $\underline{x}' = \Lambda(-\phi)\underline{x}$. This interpretation is useful if one works always in the lab frame. However, if one wants to work in the moving frame, as I did in the previous section, one should interpret it as a Lorentz boost that changes the frame of reference from $\underline{\sigma} \equiv \{I_2, \sigma_x, \sigma_y, \sigma_z\}$ of the lab frame to $\underline{\sigma}'$ of the moving frame. This means that

$$\underline{\sigma}' = \Lambda(\phi)\underline{\sigma}. \quad (2.67)$$

After this transformation, one works in the moving frame. The speed of the moving frame relative to the lab frame is $v_F \tanh \phi \mathbf{e}_y$ namely $-v_D \mathbf{e}_y$. This is precisely the moving frame found in the previous section to cancel the electric field. Hence, the hyperbolic transformation is the mathematical formalism to incorporate the effect of a Lorentz boost on the Dirac Hamiltonian and its eigenstates.¹⁰

¹⁰One can derive hyperbolic transformation from calculating how Lorentz boost changes the eigenstates to keep Dirac equation Lorentz invariant [91].

2 Special relativity in Dirac materials

Another way to see this is to compare (2.59) with (2.28):

$$q_y \rightarrow q_y \cosh \phi - \frac{E \sinh \phi}{v_F} = \gamma q_y - \gamma \beta \frac{E}{v_F}. \quad (2.68)$$

This is exactly how q_y momentum transforms under a Lorentz boost of rapidity ϕ in the y -direction, namely relativistic Doppler effect [80]. Hence, the two methods presented in this chapter to solve the problem are physically equivalent.

Besides offering the wavefunction, the advantage of hyperbolic transformation is not limited to a specific problem such as the one treated in this section. For example, the Lorentz invariance of the Dirac equation describing graphene is not necessary for the usage of hyperbolic transformations. In other words, the problem to solve for Dirac materials is not limited to those having a high-energy cousin as graphene having neutrino. As a mathematical tool, hyperbolic transformation can be extended to solve a larger set of problems that I will show immediately.

2.4 LANDAU LEVELS OF GENERIC DIRAC HAMILTONIAN

Dirac Hamiltonians appear generically in the low-energy theory of Dirac materials such as Dirac and Weyl semimetals. Unlike graphene or relativistic particles in high-energy physics, most low-energy Hamiltonians of Dirac materials are anisotropic, meaning that the Fermi velocity depends on crystal axis. Some acquire also a mass term. The following generic Hamiltonian can cover all the Dirac materials I treated during my Ph.D. studies:

$$H(\mathbf{q}) = \mathbf{w} \cdot \mathbf{q} + \sum_{i,j=1}^3 v_{ij} q_i \sigma_j + \Delta \sigma_3 \quad (2.69)$$

where $\hbar = 1$, the velocity \mathbf{w} is the tilted velocity, $\Delta \sigma_3$ is the Dirac mass term, and v_{ij} is a symmetric velocity tensor. An immediate example of this model is graphene where $w = \Delta = 0$ and v_{ij} is proportional to the Kronecker symbol δ_{ij} . I would like to emphasize that the generic model serves only as a unified mathematical framework. In principle, it does not have a physical meaning until I bestow one upon it in a particular material.

In this section, I discuss the spectrum of the Hamiltonian (2.69) in the presence of a magnetic field. By rescaling the Fermi velocity and also the applied magnetic field, one can always equivalently treat a simpler isotropic model,

$$H(\mathbf{q}) = wq_z + v\mathbf{q} \cdot \boldsymbol{\sigma} + \Delta(\sin \theta \sigma_x + \cos \theta \sigma_z) \quad (2.70)$$

$$\text{or} \quad H(\mathbf{q}) = w_z q_z + w_x q_x + v\mathbf{q} \cdot \boldsymbol{\sigma} + \Delta \sigma_z \quad (2.71)$$

where two forms are exchangeable by a unitary transformation after redefining the axes (see in App. B). Three models that will be discussed in this section are:

- Three-dimensional type-I and type-II Weyl semimetals (WSM):

$$H(\mathbf{q}) = wq_z + v\mathbf{q} \cdot \boldsymbol{\sigma} \quad (2.72)$$

where the energy is $E^\pm = wq_z \pm v|\mathbf{q}|$. Remember that for type-I WSMs, one has $|w| < |v|$, while $|w| > |v|$ for type-II WSMs.

- Two-dimensional tilted gapped graphene:

$$H(\mathbf{q}) = wq_x + vq_x \sigma_x + vq_y \sigma_y + \Delta \sigma_z \quad (2.73)$$

where the energy is $E^\pm = wq_x \pm \sqrt{v^2 q_x^2 + v^2 q_y^2 + \Delta^2}$.

- Gapped dispersive nodal-line semimetals in 3D:

$$H(\mathbf{q}) = wq_z + vq_x \sigma_x + vq_y \sigma_y + \Delta \sigma_z, \quad (2.74)$$

where the energy is $E^\pm = wq_z \pm \sqrt{v^2 q_x^2 + v^2 q_y^2 + \Delta^2}$.

In these models, I suppose for simplicity w, v, Δ are strictly positive. In the presence of a magnetic field, an electric-field-like term appears in the Hamiltonian due to the tilting term, i.e, the one proportional to the two-by-two identity. For example, by Peierls substitution,

$$wq_x \rightarrow w(q_x - eBy) = wq_x + e\mathcal{E}_{\text{eff}}y$$

where the effective electric field $\mathcal{E}_{\text{eff}} = -Bw$ is in the y -direction. If one adopts this point of view, the Hamiltonian to solve is an analogue one to that of graphene in crossed electric and magnetic fields. Although the tilting term $\mathbf{w} \cdot \mathbf{q}$ excluding the effective electric field term cannot be incorporated into a Lorentz invariant Dirac equation, the mathematical treatment makes no difference because it is di-

2 Special relativity in Dirac materials

agonalized with respect to the matrix structure and also diagonal in \mathbf{q} upon the appropriate choice of the Landau gauge.

One can even push the discussion to include also a real electric field perpendicular to the applied magnetic field. As a matter of text length, I will not include any real electric field in this discussion because the Hamiltonian to solve has exactly the same mathematical structure after well-chosen unitary transformations. Combined with unitary transformations, hyperbolic transformations serve to solve the generic problem of the Landau levels in the presence of crossed electric and magnetic fields of a generic Dirac Hamiltonians.

2.4.1 THREE-DIMENSIONAL WEYL SEMIMETAL: ANGLE-DEPENDENT REGIME

The Landau quantization for tilted WSM was solved by Tchoumakov et. al. in 2016 [83]. Since a WSM is a three-dimensional version of graphene, a magnetic field can in principle point in any direction of the three-dimensional space. Thanks to the Hamiltonian (2.72) being isotropic in the x, y -plane, one can suppose without losing generality that $\mathbf{B} = B(\cos \theta \mathbf{e}_z + \sin \theta \mathbf{e}_x) = B\mathbf{e}'_z$ for $0 < \theta < \pi/2$. Here, a new basis is defined

$$\{\mathbf{e}'_x, \mathbf{e}'_y, \mathbf{e}'_z\} = \{\cos \theta \mathbf{e}_x - \sin \theta \mathbf{e}_z, \mathbf{e}_y, \cos \theta \mathbf{e}_z + \sin \theta \mathbf{e}_x\}. \quad (2.75)$$

If one writes the Hamiltonian in this new basis followed by a unitary transformation $U = \exp(i\theta\sigma_y/2)$, it becomes

$$H(\mathbf{q}) = w \cos \theta q_z - w \sin \theta q_x + \mathbf{q} \cdot \boldsymbol{\sigma}. \quad (2.76)$$

Choosing the Landau gauge $\mathbf{A} = -By\mathbf{e}'_x$, the final Hamiltonian to solve is

$$\begin{aligned} H &= -w \sin \theta (q_x - eBy) + v(q_x - eBy)\sigma_x + w \cos \theta q_z + v(q_y\sigma_y + q_z\sigma_z) \\ &= e\mathcal{E}y + v(q_x - eBy)\sigma_x - w \sin \theta q_x + w \cos \theta q_z + v(q_y\sigma_y + q_z\sigma_z) \end{aligned} \quad (2.77)$$

where I remove the prime for \mathbf{q} . One identifies an effective electric field $\mathcal{E} = Bw \sin \theta$ applied in the y -direction. Compared to (2.28), one manages to map this new problem to a problem that one knows how to solve by hyperbolic transformations. Depending on the drift velocity of the problem $v_D = w \sin \theta$, the system is in the electric regime with a continuum spectrum if $v_D > v$, or in the magnetic regime described by Landau levels if $v_D < v$. Thus, there are two control parameters to distinguish the regimes. If the WSM is of type-I ($w < v$), it is in the magnetic regime regardless the

orientation of the magnetic field. However, if the WSM is of type-II ($w > v$), there exists a critical angle

$$\sin \theta_c = \frac{v}{w} \quad (2.78)$$

beyond which the Landau levels collapse into a continuum. Experimentally, one can thus tweak the system continuously from one regime to another by varying the angle θ if $w > v$.

In the magnetic regime, the Landau levels are

$$\begin{aligned} E_n^\pm &= w \cos \theta q_z \pm \frac{v}{\gamma} \sqrt{q_z^2 + \frac{2n}{\gamma \ell_B^2}} && \text{for } n > 0 \\ E_0 &= w \cos \theta q_z - \frac{v q_z}{\gamma} && \text{for } n = 0 \end{aligned} \quad (2.79)$$

where $\gamma = 1/\sqrt{1 - \beta^2}$ and $\beta = w \sin \theta/v$. The results are obtained with the help of a hyperbolic transformation $M = \exp(\phi \sigma_x/2)$ where $\tanh \phi = \beta$. As in graphene, the spacing between the Landau levels is renormalized by a factor of $\gamma^{-3/2}$. Since one considers only one Weyl node, the Landau levels are not symmetric with respect to zero energy due to the parity anomaly.

2.4.2 TWO-DIMENSIONAL TILTED GAPPED GRAPHENE: GAP RENORMALIZATION

Apart from the tilting, one also adds a gap to graphene's two-dimensional Hamiltonian. This model describes the low energy bands of an organic compound $\alpha - (\text{BEDT-TTF})_2\text{I}_3$. The Landau quantization in this material has been discussed by Sári et al. [82]. As in graphene, the only relevant direction for magnetic field is perpendicular to the 2D plane namely in the z -direction. The resulting Hamiltonian is thus

$$H(\mathbf{q}) = w(q_x - eBy) + v(q_x - eBy)\sigma_x + vq_y\sigma_y + \Delta\sigma_z \quad (2.80)$$

where one identifies an effective electric field $\mathcal{E} = -Bw$ applied in the y -direction and thus the drift velocity $\mathbf{v}_D = -w\mathbf{e}_x$. The Hamiltonian is in the magnetic regime only if $w < v$ because the magnetic field is fixed to be out-of-plane unlike in three-dimensional Weyl semimetals. Using the hyperbolic

2 Special relativity in Dirac materials

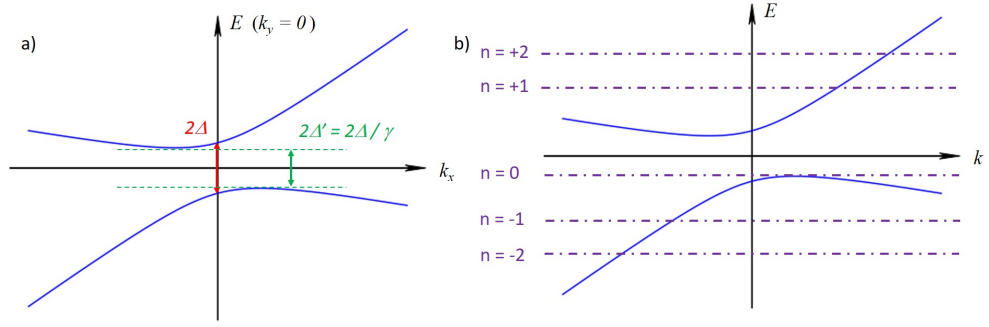


Figure 2.3: (a) Schematic of the spectrum for 2D tilted gapped graphene at $k_y = 0$ in the absence of magnetic field. The direct band gap marked by red is 2Δ while the indirect band gap by green is $2\Delta' = 2\Delta/\gamma$. (b) Landau levels of 2D tilted gapped graphene where I generalize the definition of n to include the sign of energy.

transformation $M = \exp(\phi\sigma_x/2)$ where $\tanh \phi = -w/v$, the spectrum of the Hamiltonian in the magnetic regime is

$$\begin{aligned}
 E_n^\pm &= \pm \frac{1}{\gamma} \sqrt{\Delta^2 + \frac{2nv^2}{\gamma\ell_B^2}} && \text{for } n > 0 \\
 E_0 &= -\frac{\Delta}{\gamma} && \text{for } n = 0
 \end{aligned} \tag{2.81}$$

where $\gamma = 1/\sqrt{1 - \beta^2}$ and $\beta = -w/v$ [see Fig. 2.3(b)].

Only one valley in the gapped graphene is considered. Therefore, the spectrum is not particle-hole symmetric due to the parity anomaly. The spacing between the Landau levels are also renormalized by the same factor of $\gamma^{-3/2}$. Most saliently, the Dirac mass is renormalized by a factor of γ^{-1} and so does the gap measured by extrapolating the Landau levels to the zero field limit, $2\Delta' = 2\Delta/\gamma$. This is analogue to the definition of relativistic mass in special relativity. However, as it is well-known in solid state physics, one would measure 2Δ for the direct band gap of (2.73) by spectroscopy. It sounds strange that the magnetic field modifies the optical gap of the tilted Dirac Hamiltonian. If it was true, one should have questioned the general method of gap measurements in Landau level spectroscopy. As will be explained at the end of this chapter, $2\Delta/\gamma$ is actually the indirect gap of the band structure [see Fig. 2.3(a)].

2.4.3 GAPPED DISPERSIVE NODAL-LINE SEMIMETAL: GAP CLOSING

Now I consider the gapped nodal-line semimetal NbAs₂, the low-energy Hamiltonian of which is described by Eq. (2.74).¹¹ Since Eq. (2.74) describes a system that is isotropic in the x, y -plane, one sets with no loss of generality that $\mathbf{B} = B(\cos \theta \mathbf{e}_z + \sin \theta \mathbf{e}_x) = B\mathbf{e}'_z$ for $0 < \theta < \pi/2$. Here, a new basis is defined

$$\{\mathbf{e}'_x, \mathbf{e}'_y, \mathbf{e}'_z\} = \{\cos \theta \mathbf{e}_x - \sin \theta \mathbf{e}_z, \mathbf{e}_y, \cos \theta \mathbf{e}_z + \sin \theta \mathbf{e}_x\}. \quad (2.82)$$

Writing the Hamiltonian in this new basis and choosing the Landau gauge $\mathbf{A} = -By\mathbf{e}_x$, the Hamiltonian becomes

$$H = w[\cos \theta q_z - \sin \theta (q_x - eBy)] + v[\cos \theta (q_x - eBy) + \sin \theta q_z] \sigma_x + vq_y \sigma_y + \Delta \sigma_z \quad (2.83)$$

where I also remove the prime. One can define the effective electric field $\mathcal{E} = Bw \sin \theta$ applied in the y -direction and the drift velocity $\mathbf{v}_D = w \sin \theta \mathbf{e}_x$. Since the limiting speed is $v \cos \theta$ instead of v , one needs to compare $w \sin \theta$ with $v \cos \theta$ to determine whether the system is in the magnetic or electric regime. Compared to Weyl semimetals, the angle θ plays a more decisive role in the the gapped nodal-line semimetal since the value of $\tan \theta$ can take any real number. Although the material-related parameter w/v cannot be varied experimentally, one can always find a critical angle θ_c below which the Hamiltonian is in the magnetic regime. Conversely, the Landau levels can be continuously tuned to extinction by increasing θ to θ_c . The critical angle called the angle of extinction is defined as

$$\tan \theta_c = \frac{v}{w}. \quad (2.84)$$

Using the hyperbolic transformations $M = \exp(\phi \sigma_x / 2)$ with $\tanh \phi = w \tan \theta / v$, the spectrum in the magnetic regime reads

$$\begin{aligned} E_n^\pm &= \frac{wq_z}{\cos \theta} \pm \frac{1}{\gamma} \sqrt{\Delta^2 + \frac{2nv^2 \cos \theta}{\gamma \ell_B^2}} && \text{for } n > 0 \\ E_0 &= \frac{wq_z}{\cos \theta} - \frac{\Delta}{\gamma} && \text{for } n = 0 \end{aligned} \quad (2.85)$$

where $\gamma(\theta) = 1/\sqrt{1 - \beta^2}$ and $\beta(\theta) = w \tan \theta / v$. For the same reason as previously shown, the Landau levels are not particle-hole symmetric and the spacing between them is renormalized by $\gamma^{-3/2}$.

¹¹More details on NbAs₂ in Chapter 3 and App. C where I discuss also the magneto-optics of this gapped nodal-line semimetal.

2 *Special relativity in Dirac materials*

Moreover, the Dirac mass is renormalized by a factor of γ^{-1} . The main difference is that γ now can be tweaked by the angle θ . Therefore, the extrapolated gap depends on the orientation of the magnetic field. Most saliently, the gap is closed when $\theta = \theta_c$. The gap closing is an unambiguous signature to demonstrate special relativistic renormalization in a material like NbAs₂. It is especially easy to experimentally show since the orientation of the magnetic field is freely configurable. Concerning the solid-state mechanism of this gap closing, I invite the readers to go to the next section.

In summary, hyperbolic transformations allow one to solve completely the problem of Landau quantization for tilted Dirac Hamiltonians by giving the energy spectrum and wavefunctions. By the Peierls substitution in the Landau gauge, an effective electric field is generated due to the presence of tilting term. One can still make an analogy with special relativity as I did for graphene. However, this analogy is only partially valid because the tilting term includes momentum (see, for example, 2D tilted gapped graphene), which breaks the Lorentz invariance of Dirac equation. In other words, one cannot write a Dirac equation associated with the generalized linear Hamiltonian in a Lorentz invariant form. Another thing to pay attention to is that one might think the tilting speed w and the Fermi velocity v as the drift velocity and the speed of light c , respectively. This is explicitly proved to be wrong in the calculations for tilted Weyl semimetal where the definition of speed is angle-dependent. Hence, the analogy with special relativity is only physically valid after the Peierls substitution and the identification of an effective electric field. All these caveats make hyperbolic transformation even more tempting for its multiple interpretations of calculations and elegance of simplicity.

2.5 RENORMALIZATION EFFECT IN THE LANGUAGE OF CONDENSED MATTER

In this section, I will elucidate the solid-state mechanism of the fancy relativistic renormalization in Dirac materials, so far not yet discussed in the community. I will retrieve the energy spectrum of the previous models by the semi-classical method. One can interpret the relativistic renormalization effect as an anisotropy of the Fermi surface introduced by the tilting. The criterion for electric and magnetic regime is whether the cross section of the Fermi surface perpendicular to the magnetic field is compact, i.e., finite and closed. Furthermore, I will explain the microscopic mechanism that leads to the renormalization of the optical gap: the energy dispersion is flattened by Landau quantization.

2.5.1 ANISOTROPY OF FERMI SURFACE

Quantum oscillations are the phenomena related to response functions, for example magneto-resistance and magnetic susceptibility, that oscillate as a function of magnetic field. They offer information on

the Fermi surface of a given material by looking at the oscillation pattern since response functions are related to the density of states at the Fermi level.¹² The interpretation of quantum oscillations relies on the formation of Landau levels. Semi-classically, the Onsager relation [94] or equivalently the Roth-Gao-Niu relation [95, 96] provide a quantization condition to derive Landau levels from the geometry of the Fermi surface:

$$S(E_F) = 2\pi eB[n + \gamma(E_F, B)], \quad (2.86)$$

where $S(E_F)$ is the reciprocal-space area of a closed cyclotron orbit at the Fermi level and $\gamma(E_F, B)$ is a phase shift whose Taylor series in B is given by [97]

$$\gamma(E_F, B) = \frac{1}{2} - M'_0(E_F) - \frac{B}{2}\chi'_0(E_F) - \sum_{p \geq 3} \frac{B^{p-1}}{p!} R'_p(E_F), \quad (2.87)$$

where the first term is the Maslov index, the second term is the sum of Berry curvature and the derivative of orbital magnetization, the third term is the derivative of magnetic susceptibility and the last term is derivatives of other higher order response functions. In the following, I take $\gamma(E_F, B) \approx 0$ since I am interested in Dirac Hamiltonians for which $M'_0(E_F) = 1/2$. I also neglect further higher order terms of B . Here, it will be shown that the relation Eq. (2.86) can accurately give Landau levels in tilted Dirac Hamiltonians and thus furnishing a complementary understanding of the relativistic renormalization in Dirac materials, namely the induced anisotropy of Fermi surface.

TWO-DIMENSIONAL TILTED GAPPED GRAPHENE

Suppose the Fermi level is above the gap such that

$$E_F = wq_x + \sqrt{\Delta^2 + v^2q_x^2 + v^2q_y^2}. \quad (2.88)$$

This equation defines the trajectory of a cyclotron motion in the reciprocal space. Given that $\beta = w/v$ and $\gamma = 1/\sqrt{1 - \beta^2}$, I transform this equation into a more explicit form

$$1 = \frac{v^2 \left(q_x + \frac{E_F}{v} \beta \gamma^2 \right)^2}{\gamma^4 \left(E_F^2 - \frac{\Delta^2}{\gamma^2} \right)} + \frac{v^2 q_y^2}{\gamma^2 \left(E_F^2 - \frac{\Delta^2}{\gamma^2} \right)} \quad (2.89)$$

¹²This statement is actually true for the Shubnikov-de Haas oscillations of conductivity but not true for the de Haas-van Alphen oscillations of magnetization [93].

2 Special relativity in Dirac materials

which has the shape of the defining equation of an ellipse. Several conditions need to be fulfilled if this equation actually describes an ellipse:

$$|\beta| < 1 \quad \text{and} \quad E_F > \frac{\Delta}{\gamma}, \quad (2.90)$$

where the first condition is precisely that for the magnetic regime, and the second condition says the smallest gap of the system is $2\Delta/\gamma$. Note that the center of the ellipse is not at $\mathbf{q} = 0$ but shifted in the q_x -direction such that $2\Delta/\gamma$ denotes the indirect gap (see Fig. 2.3). With the area of the ellipse

$$S = \pi\gamma^3 \frac{E_F^2 - \frac{\Delta^2}{\gamma^2}}{v^2} = \pi\gamma \frac{\gamma^2 E_F^2 - \Delta^2}{v^2}, \quad (2.91)$$

the Onsager relation gives

$$E_F = \frac{1}{\gamma} \sqrt{\Delta^2 + \frac{2nv^2}{\gamma\ell_B^2}}, \quad (2.92)$$

in agreement with the above result (2.81) for Landau levels.

If $w = 0$, the Hamiltonian describes an isotropic gapped graphene. The equation of ellipse becomes

$$1 = \frac{v^2 q_x^2}{E_F^2 - \Delta^2} + \frac{v^2 q_y^2}{E_F^2 - \Delta^2}, \quad (2.93)$$

which actually depicts a circle centered at $\mathbf{q} = 0$. Therefore, the tilting term wq_x squeezes the circular Fermi surface (contour) to an elliptic one along the x -direction by a factor of γ . This induces an anisotropy of Fermi surface. Furthermore, the tilting term also modifies the density of states so that the Fermi energy is renormalized by another factor of γ for a fixed number of electron. These two effects give together the factor of γ^3 in the equation above.

THREE-DIMENSIONAL TILTED WEYL SEMIMETAL

To proceed the calculations for Weyl semimetal, one simply has to replace Δ by vq_z in the previous calculations,¹³ The trajectory of cyclotron is now the contour of a cross section of the ellipsoid Fermi surface of Weyl semimetal. The ellipsoid Fermi surface is described by

$$1 = \frac{v^2 \left(q_x + \frac{E_F}{v} \beta \gamma^2 \right)^2}{\gamma^4 E_F^2} + \frac{v^2 q_y^2}{\gamma^2 E_F^2} + \frac{v^2 q_z^2}{\gamma^2 E_F^2} \quad (2.94)$$

¹³Here, I replace wq_z by wq_x in (2.72) which is another valid simple model to describe Weyl semimetals.

where $\beta = w/v$ and $\gamma = 1/\sqrt{1 - \beta^2}$. Condition of an ellipsoid Fermi surface is $|\beta| < 1$. But this is not necessary to find a closed orbit for cyclotron because the orientation of magnetic field matters. Depending the orientation of the magnetic field, one has to rewrite the previous equation to an elliptic equation. Here, I show only two particular orientations: the magnetic field is in the z - or the x -direction. The general geometric calculation can be found in the literature [98].

For a magnetic field in the z -direction, one just needs to replace Δ by vq_z in the results for two-dimensional tilted gapped graphene

$$E_F = \frac{1}{\gamma} \sqrt{v^2 q_z^2 + \frac{2nv^2}{\gamma \ell_B^2}}. \quad (2.95)$$

The condition for a closed orbit is $|\beta| < 1$.

For a magnetic field in the x -direction parallel to the tilting term wq_x , q_x remains a good quantum number and thus wq_x can be treated as an additive constant to the energy. The resulting spectrum is given by Landau levels in a non-tilted WSM adding wq_x . The calculations using the Onsager relations are more involved since one need rewrite the ellipsoid equation considering q_x as constant. This leads to

$$1 = \frac{v^2 q_y^2}{\gamma^2 E_F^2 \left(1 - \frac{v^2 \left(q_x + \frac{E_F}{v} \beta \gamma^2\right)^2}{\gamma^4 E_F^2}\right)} + \frac{v^2 q_z^2}{\gamma^2 E_F^2 \left(1 - \frac{v^2 \left(q_x + \frac{E_F}{v} \beta \gamma^2\right)^2}{\gamma^4 E_F^2}\right)} \quad (2.96)$$

with no conditions on w/v . The area enclosed by a cyclotron orbit in reciprocal space is

$$S = \pi \gamma^2 \frac{E_F^2}{v^2} \left(1 - \frac{v^2 \left(q_x + \frac{E_F}{v} \beta \gamma^2\right)^2}{\gamma^4 E_F^2}\right). \quad (2.97)$$

Finally, the Onsager relation gives the correct Landau levels

$$E_F = wq_x + \sqrt{v^2 q_x^2 + \frac{2nv^2}{\ell_B^2}}. \quad (2.98)$$

GAPPED NODAL-LINE SEMIMETAL

Starting from the Hamiltonian discussed previously

$$H = w(\cos \theta_{q_z} - \sin \theta_{q_x}) + v(\cos \theta_{q_x} + \sin \theta_{q_z})\sigma_x + vq_y\sigma_y + \Delta\sigma_z, \quad (2.99)$$

2 Special relativity in Dirac materials

I choose the magnetic field to be oriented in the z -direction. The cyclotron trajectory is described by

$$1 = \frac{v^2 \tilde{q}_x^2 \cos^2 \theta}{\gamma^4 \left(E_F - \frac{v\beta q_z}{\sin \theta} \right)^2 - \gamma^2 \Delta^2} + \frac{v^2 q_y^2}{\gamma^2 \left(E_F - \frac{v\beta q_z}{\sin \theta} \right)^2 - \Delta^2} \quad (2.100)$$

where

$$\beta(\theta) = \frac{w}{v} \tan \theta \quad \gamma(\theta) = \frac{1}{\sqrt{1 - \beta(\theta)^2}} \quad (2.101)$$

$$\tilde{q}_x = q_x + \frac{(v^2 + w^2) q_z \sin \theta \cos \theta - w E_F \sin \theta}{v^2 \cos^2 \theta - w^2 \sin^2 \theta}. \quad (2.102)$$

This equation describes an ellipse when $|\beta(\theta)| < 1$ and $E_F > \Delta/\gamma + wq_z/\cos \theta$. The first condition gives rise to the critical angle beyond which Landau levels collapse. The second condition states that the Fermi energy should be above the renormalized gap at a given momentum q_z so that the carrier density is non-zero. Invoking the Onsager relation, one gets the spectrum

$$E_F = \frac{w}{\cos \theta} q_z + \frac{1}{\gamma} \sqrt{\Delta^2 + \frac{2nv^2 \cos \theta}{\gamma \ell_B^2}} \quad (2.103)$$

which is perfectly in line with the results obtained quantum mechanically.

To conclude, the renormalization effect in tilted Dirac materials in the presence of a magnetic field is a relativistic interpretation of the consequence of an anisotropic Fermi surface. The Lorentz factor γ actually quantifies the degree of anisotropy of Fermi surface induced by the tilting term. To some extent, the relativistic renormalization should be measurable in quantum oscillations experiments which would probe a squeezed Fermi surface due to the tilting term. The Lorentz factor γ would emerge as a multiplicative factor on the periodicity of quantum oscillations. However, in the language shared by experimentalists, it is more understandable to talk about the anisotropy of Fermi surface rather than the relativistic renormalization.

2.5.2 DIRECT GAP VS. INDIRECT GAP

Anisotropic Fermi surfaces are ubiquitous in materials. However, when referring to anisotropy, different velocities or effective masses along the crystalline axis are considered. In parabolic bands, the tilting has no effect on the shape of Fermi surface because it is absorbed in the quadratic term by redefining the origin of momentum \mathbf{q} . However, this is impossible in linear bands describing the low-energy physics of Dirac materials. Most saliently, unlike the anisotropy in the Fermi velocity, the tilting term does not

only make the longitudinal and transverse directions inequivalent but can also modify the gap of the system. To see this, one takes the tilted gapped graphene as a starting example [99].

In the absence of magnetic field, one can easily calculate the energy spectrum of (2.73)

$$E^\pm = wq_x \pm \sqrt{v^2q_x^2 + v^2q_y^2 + \Delta} \quad (2.104)$$

where the direct gap 2Δ is formed at $\mathbf{q} = 0$. However, the smallest energy difference between valence and conduction band is not the direct gap but the indirect gap. Direct calculation of the extrema of the two bands shows the band edges of the valence and conduction band is at momenta $vq_x = \pm\gamma\beta\Delta$ and $vq_y = 0$ where $\beta = w/v$ and $\gamma = 1/\sqrt{1-\beta^2}$. The energy difference between these two band edges, i.e., the indirect gap, reads $2\Delta/\gamma$. Without appealing to relativity one notices that the indirect gap equals the direct gap renormalized by the Lorentz factor γ defined in the language of special relativity. The relativistic gap renormalization is just a smaller indirect gap induced by the tilting term! The optical gap measured in the absence of magnetic field is to find the smallest energy difference between valence and conduction band conserving the same momentum \mathbf{q} . However, in the presence of magnetic field in the z -direction, q_x and q_y are no longer good quantum numbers so that it makes no sense to define a direct gap preserving the momentum q_x and q_y . In other words, the role of magnetic field is to flatten the energy dispersion in the transverse direction q_x and q_y . Since the optical gap measured in the presence of magnetic field is obtained by extrapolating the Landau levels to zero, the measured gap is now an *indirect* gap.

Generalizing the argument from two to three dimensions, the gap measured by extrapolating the Landau levels to zero field limit is the lowest energy difference between the two bands when varying the two momenta perpendicular to the direction of the magnetic field. The longitudinal momentum along the magnetic field is untouched by the Peierls substitution and the two transverse momenta are no longer good quantum numbers. Therefore, the transverse dispersion is flattened by the magnetic field and turns into Landau levels while the longitudinal dispersion is intact. For example, in the gapped nodal-line semi-metal, the spectrum in the absence of magnetic field reads

$$E^\pm = w(\cos\theta q_z - \sin\theta q_x) \pm \sqrt{v^2q_y^2 + \Delta^2 + v^2(\cos\theta q_x + \sin\theta q_z)^2} \quad (2.105)$$

$$= w\frac{q_z}{\cos\theta} - w\sin\theta\tilde{q}_x \pm \sqrt{v^2q_y^2 + \Delta^2 + v^2\cos^2\theta\tilde{q}_x^2} \quad (2.106)$$

where q_z is the longitudinal momentum, (q_x, q_y) are transverse ones and $\tilde{q}_x = q_x + q_z \tan\theta$ is the recentered q_x . While minimizing the energy difference between E^+ and E^- , q_z is irrelevant and q_y must be zero. Since I want to find the smallest gap no matter whether it is direct or indirect, one can separately maximize E^- and minimize E^+ . Taking derivative of E^\pm , the condition of zero derivative

2 *Special relativity in Dirac materials*

gives precisely the condition of the magnetic regime, i.e. $|\beta| < 1$. Most prominently, the minimal gap is again found to be $2\Delta/\gamma$, in line with the previous quantum mechanical calculations. In this example, one realizes once more that the renormalized gap is merely the minimal gap of the energy dispersion transverse to the magnetic field. This is the one probed by Landau level spectroscopy. Nevertheless, it is still surprising that one can tune the indirect gap of a material by the orientation of magnetic field in this particular model.

2.6 SUMMARY

In this chapter, I have shown by several examples that the renormalization effect of relativistic electrodynamics can manifest itself in Dirac materials. Using unitary and hyperbolic transformations inspired by the analogy to the special relativity, the Landau quantization in tilted Dirac materials is completely solved. Traditional experimental techniques in condensed matter can thus demonstrate the relativistic renormalization. For example, the gap renormalization is measurable by magneto-optics as I will show in detail in the next chapter.

In the absence of magnetic field, only direct optical transitions are possible since the photon momentum is negligible. As shown in the next chapter, where I will discuss Landau level spectroscopy, the magnetic field induces mismatch between wavefunctions of different energy so that dipole transitions from one Landau level to another do not respect the usual selection rules. In other words, photons probe the indirect gap.

3 THEORETICAL APPROACH TO SPECTROSCOPY

A theoretical physicist can spend his entire lifetime missing the intellectual challenge of experimental work, experiencing none of the thrills and dangers — the overhead crane with its ten-ton load, the flashing skull and crossbones and danger, radioactivity signs. A theorist's only real hazard is stabbing himself with a pencil while attacking a bug that crawls out of his calculations.

Leon M. Lederman

Optical properties of solids are tangible in daily life. For example, the color of materials is a manifestation of all the complex interactions between light and matter. In electromagnetism, light is considered as an electromagnetic wave described by the Maxwell's equations. As it is well-known from the basic electrodynamics classes, the wide-ranging optical properties observed in materials are encoded in the constitutive equations

$$\mathbf{D} = \epsilon_0 \epsilon_r \mathbf{E}$$

$$\mathbf{B} = \mu_0 \mu_r \mathbf{H}$$

$$\mathbf{j} = \sigma \mathbf{E}$$

where the fields \mathbf{D} , \mathbf{E} , \mathbf{B} , \mathbf{H} are displacement, electric, magnetic and magnetizing field, respectively; \mathbf{j} is charge current density; the coefficients ϵ_0 , ϵ_r , μ_0 , μ_r , σ are vacuum electric permittivity, relative electric permittivity, vacuum magnetic permeability, relative magnetic permeability, conductivity, respectively. These equations are valid when an incident light is not so intense that the response of material to an incident electromagnetic wave is linear. However, these optical coefficients are not measured directly by spectroscopy but can be derived from other measurable optical constants such as refractive index, extinction coefficient, transmission and reflectivity.

The frequency-dependent complex dielectric function $\epsilon(\omega)$ or the complex conductivity $\sigma(\omega)$ are directly related to the electronic energy band structure of solids. Therefore, light is an excellent probe to resolve the band structure of materials. In fact, one can also use electrons in the spectroscopy encoded also in the complex dielectric function. However, the momentum of electron is no longer negligible with respect to the size of Brillouin zone, the dielectric function must be momentum-dependent, i.e., $\epsilon(\mathbf{q}, \omega)$.

In this chapter, I present succinctly the theoretician's way to study the spectroscopic properties of materials, namely how to calculate dielectric function and conductivity knowing the Hamiltonian. Especially, I elaborate some known results in magneto-optics, which will be useful in Chapter 5. As an illustration, I will apply the theoretical formalism in a real material that I have been recently working on with experimentalists at LNCMI (Grenoble). Then, I will talk about the physics of plasmon and how to measure it by spectroscopy.

3.1 QUANTUM THEORY OF OPTICAL PROPERTIES

In this section, I introduce the tool that theoreticians would use to study the optical properties of materials, namely the optical conductivity $\sigma(\omega)$. The goal is not to develop the full construction of the theory¹ but to emphasize on key ingredients of the theory and mention the approximations used in the theory.

In a complete quantum mechanical treatment, light is quantized in bosonic fields known as photons. The light-matter interaction is then described by a vector potential $\mathbf{A}(\mathbf{r}, t)$ including the bosonic ladder operators for the photons. This treatment is necessary when the number of photons is very small such as in a single-photon source used in quantum optics [103, 104, 105]. In most cases in condensed matter physics, one uses classical light sources so that light can be treated as an electromagnetic wave because light is used as a probe of the electronic properties of materials rather than the object of a physical study itself. When the light source is not an intense laser, the light-matter interaction is modeled as a small perturbation to the matter by the electromagnetic field. This approach is semi-classical in the sense that light is modeled by an electromagnetic wave and matter is described by a fully quantum mechanical Hamiltonian.

Generally, a crystal coupled to an electromagnetic field is described by the following Hamiltonian

$$H = \frac{(\mathbf{p} + e\mathbf{A})^2}{2m_0} + V(\mathbf{r}) \quad (3.1)$$

¹For the construction of theory from zero, I suggest the following references [100, 101, 102] from which I am inspired to formulate this section.

where $V(\mathbf{r})$ is a periodic lattice potential, $e > 0$ is the elementary charge and m_0 is the rest mass of the electron. The above Hamiltonian can be written as a sum of the Hamiltonian in the absence of \mathbf{A} denoted H_0 , and a perturbation term H' . To first order in \mathbf{A} , H' reads

$$H' = \frac{e}{m_0} \mathbf{p} \cdot \mathbf{A} \quad (3.2)$$

where the Coulomb gauge $\nabla \cdot \mathbf{A} = 0$ is used so that $\mathbf{p} = -i\hbar\nabla$ and \mathbf{A} commute. As an electromagnetic wave, \mathbf{A} is written in the following form

$$\mathbf{A}(\mathbf{r}, t) = \mathbf{A}_0 \exp(i\mathbf{k} \cdot \mathbf{r} - i\omega t) \quad (3.3)$$

where \mathbf{A}_0 is in the direction of electric field indicating the polarization of light. In time-dependent perturbation theory, Fermi's golden rule tells that the transition rate from the state 1 to the state 2 is

$$W_{1 \rightarrow 2} = \frac{2\pi}{\hbar} |M_{12}|^2 g(\hbar\omega) \quad (3.4)$$

where $g(\hbar\omega)$ is the density of states (DOS)² and M_{12} is the matrix element

$$M_{12} = \langle 2 | H' | 1 \rangle = \int d^3\mathbf{r} \psi_2^*(\mathbf{r}) H'(\mathbf{r}) \psi_1(\mathbf{r}). \quad (3.5)$$

Note that the time-dependence in $\exp(-i\omega t)$ is already taken into account in Fermi's golden rule.

3.1.1 ELECTRIC DIPOLE APPROXIMATION

Since the frequency domain that I am interested in is the visible-infrared regime where the wavelength of light is much larger than the periodicity of lattice potential, one can legitimately omit the spatial dependence in \mathbf{A} , namely $\exp(i\mathbf{k} \cdot \mathbf{r}) \sim 1$. In other words, the momentum of photon is negligible in front of the lattice momentum of electron. In this approximation, the matrix element reads

$$M_{12} = \frac{e}{m_0} \langle 2 | \mathbf{p} \cdot \mathbf{A}_0 | 1 \rangle. \quad (3.6)$$

²When the two involved states are two discrete levels, $g(\hbar\omega)$ represents the DOS of photon. If one considers the transition between \mathbf{k} -dependent bands of solids, one should use the joint density of states summing over \mathbf{k} .

3 Theoretical approach to spectroscopy

This is called *electric dipole approximation*. The name for this approximation is justified by writing the equation of motion of the position operator \mathbf{r} . Note that $\mathbf{p} = m_0 d\mathbf{r}/dt$, the equation of motion reads

$$\mathbf{p} = m_0 \frac{d\mathbf{r}}{dt} = m_0 \frac{i}{\hbar} [H_0, \mathbf{r}] \quad (3.7)$$

so that

$$M_{12} = ie \frac{E_2 - E_1}{\hbar} \langle 2 | \mathbf{r} \cdot \mathbf{A}_0 | 1 \rangle \quad (3.8)$$

where $E_{1,2}$ are the energy of two states. Since $\mathcal{E}_0 = i\omega \mathbf{A}_0$ and, if $\hbar\omega = E_2 - E_1$, the matrix element becomes

$$M_{12} = \langle 2 | e\mathbf{r} \cdot \mathcal{E}_0 | 1 \rangle \quad (3.9)$$

where the perturbation term H' becomes the energy of an electric dipole in an electric field \mathcal{E}_0 . The corresponding transition is called electric dipole transition.

If one pushes the Taylor expansion of $\exp(i\mathbf{k} \cdot \mathbf{r})$ to higher orders, other types of transition are possible. For example, $i\mathbf{k} \cdot \mathbf{r}$ yields magnetic dipole transition and $(\mathbf{k} \cdot \mathbf{r})^2$ yields electric quadrupole transition. These higher order corrections are 10^{-3} weaker than electric dipole transition in most cases thanks to large wavelength of light. However, they are essential to explain the optical activity,³ when the time-reversal symmetry is not broken, and the circular dichroism⁴ of chiral materials, which possesses neither an inversion center nor a mirror plane [106, 107]. This can be understood by looking the first order correction to the electric dipole approximation in Fermi's golden rule

$$\langle 2 | e\mathbf{r} \cdot \mathcal{E}_0 | 1 \rangle \langle 1 | (e\mathbf{r} \times \frac{\mathbf{p}}{m_0}) \cdot \mathbf{B}_0 | 2 \rangle \quad (3.10)$$

in which the second term is the magnetic dipole transition. If the system possesses an inversion center, the eigenstates are either even or odd under inversion operation. Since the electric dipole is odd under inversion, a non-zero electric dipole matrix element has to involve two states of different parity. However, this would kill the magnetic dipole matrix element due to the angular momentum $\mathbf{r} \times \mathbf{p}$ being invariant under inversion. If the system possesses a mirror plane, the eigenstates are either even or odd under reflection with respect to the mirror plane. Similarly, a polar vector as electric dipole and an axial

³Optical activity is the capability of a material to rotate the linear polarization of transmitted light.

⁴Circular dichroism is the property of materials whose absorption spectrum is different for left and right handed circularly polarized light.

vector as magnetic dipole imposes incompatible symmetry constrictions on the eigenstates involved in the transitions so that the first order correction to the electric dipole approximation is forbidden.

In organic chemistry, the optical activity is due to the chiral molecules. However, the optical activity of crystalline quartz arises from the crystal structure. The unit cell of quartz belongs to the trigonal crystal class labeled 32, which has no mirror symmetry, and is therefore chiral [101].

Nevertheless, the higher order corrections to electric dipole approximation is beyond the scope of the thesis. In all the following discussions, I consider only electric dipole transitions in optical properties.

3.1.2 LINEAR RESPONSE THEORY: KUBO FORMULA

Light-matter interaction is considered as a perturbation to the system. If the electric field of light is not too strong, which is the case I consider here, then the conductivity is independent of the electric field. It only depends on the material properties in the absence of electric field (at equilibrium). This type of response is called the linear response.

Linear response theory is developed through the Kubo formula [108]. It gives the expression of the retarded correlation function (conductivity σ) that relates the perturbation Hamiltonian H' to the observable of interest (current density \mathbf{j}).⁵ I am interested in the conductivity at finite frequencies, the Fourier transform of which is also called optical or dynamical conductivity. The full derivation of the Kubo formula for σ can be found in [108]. In general, one should consider the momentum dependence in the conductivity $\sigma(\mathbf{q}, \omega)$. In the electric dipole approximation, the momentum of photon is omitted so that the optical conductivity becomes local ($\mathbf{q} = 0$) and depends only on ω .⁶ All information on the optical properties of solids is encoded in the optical conductivity.⁷ Most saliently, the optical conductivity can be easily retrieved from the transmission coefficient and/or reflectivity that are directly measurable by experiments.⁸

⁵Here, the formulation of the perturbation is different from that in the time-dependent perturbation theory. In real space

$$H' = - \int d^3r \mathbf{j}(\mathbf{r}) \cdot \mathbf{A}(\mathbf{r}, t).$$

The current density has two parts, paramagnetic and diamagnetic. The latter plays an important role in superconductors but not in the present discussions. Nevertheless, this formulation is physically equivalent to the previous one.

⁶Equivalent to the electric dipole approximation, this is justified by the fact that the speed of light is typically several orders of magnitude larger than the electrons' velocity in materials.

⁷The transition rate given by Fermi's golden rule is of course related to the optical conductivity. See details in [100].

⁸While the absorption method is viable for 2D thin films, the reflectivity method is more suitable for 3D bulk materials.

3 Theoretical approach to spectroscopy

The Kubo formula of the optical conductivity reads

$$\sigma_{ij}(\omega) = \frac{i\hbar e^2}{V} \sum_{n,n',\mathbf{k}} \frac{f_D(E_n(\mathbf{k})) - f_D(E_{n'}(\mathbf{k}))}{E_{n'}(\mathbf{k}) - E_n(\mathbf{k})} \times \frac{\langle n'|\hat{v}_i|n\rangle\langle n|\hat{v}_j|n'\rangle}{E_{n'}(\mathbf{k}) - E_n(\mathbf{k}) - \hbar\omega + i0^+} \quad (3.11)$$

where V is the volume of system for normalization; n, n' are the band index; i, j represent the direction of polarization; \hat{v}_i is the velocity operator; $f_D(E)$ is the Fermi-Dirac distribution, and 0^+ ensures the causality of the response in the clean limit. In general, one can replace 0^+ by \hbar/τ with a phenomenological relaxation time τ to encounter the peak broadening due to disorders. Note that this expression includes both intra- and inter-band processes. When $n = n'$, the numerator and denominator of the first fraction on the right hand side has a finite limit. One would obtain the same results in the classical Drude's theory for metals [101].

In the following, I focus on the interband transition in solids caused by an incident light of energy $\hbar\omega$. The absorption process is related to the real part of the optical conductivity thinking of the dissipative Joule's effect. In the clean limit,⁹ the real part of the diagonal elements of the optical conductivity for $\omega \neq 0$ reads

$$\Re[\sigma_{ii}(\omega \neq 0)] = \frac{\pi e^2}{\omega} \sum_{n \neq n'} \int \frac{d^d k}{(2\pi)^d} (f_D(E_n) - f_D(E_{n'})) |\langle n'|\hat{v}_i|n\rangle|^2 \delta[\hbar\omega - (E_{n'} - E_n)] \quad (3.12)$$

where the dependence on \mathbf{k} is not explicitly shown, and the subscript d is the dimension of the system of study.

The formula (3.12) consists of three key ingredients of optical transitions:

1. The term $f_D(E_n) - f_D(E_{n'})$ is the mathematical formulation of Pauli blocking: only the transitions from an occupied to an empty state are possible. Thus, optical transitions are sensitive to the position of the chemical potential.
2. The term $\langle n'|\hat{v}_i|n\rangle$ is the same matrix element as in Fermi's golden rule remarking that $\hat{v} = \mathbf{p}/m_0$. It encodes the symmetry properties of the wavefunction and thus it stipulates the con-

⁹Here, I use the relation:

$$\frac{1}{x + i0^+} = P.V.\left(\frac{1}{x}\right) - i\pi\delta(x)$$

where $P.V.$ is the Cauchy principle value and δ is the Dirac distribution.

restrictions on the optical transitions dictated by group theory. Exactly like in atomic physics, these constrictions are called *selection rules*. By definition, the velocity operator is given by

$$\hat{v} = \frac{i}{\hbar}[\mathbf{r}, H] \quad (3.13)$$

where \mathbf{r} is the position operator. In practice, it is easier to work in the basis of the cell-periodic part of Bloch wavefunction to evaluate the matrix element. A crystal Hamiltonian

$$H = \frac{\mathbf{p}^2}{2m_0} + V(\mathbf{r}) \quad (3.14)$$

with a periodic lattice potential $V(\mathbf{r})$ and the energy is $E_n(\mathbf{k})$ for the Bloch wavefunction $|\psi_{n,\mathbf{k}}\rangle$, the \mathbf{k} -dependent effective Hamiltonian, i.e., the Bloch Hamiltonian, reads

$$H_{\mathbf{k}} = e^{-i\mathbf{k}\cdot\mathbf{r}} H e^{i\mathbf{k}\cdot\mathbf{r}} = \frac{(\mathbf{p} + \hbar\mathbf{k})^2}{2m_0} + V(\mathbf{r}) \quad (3.15)$$

with the same energy $E_n(\mathbf{k})$ for the eigenstate $|u_{n,\mathbf{k}}\rangle$. The velocity operator in this basis reads

$$\hat{v}_{\mathbf{k}} = e^{-i\mathbf{k}\cdot\mathbf{r}} \hat{v} e^{i\mathbf{k}\cdot\mathbf{r}} = \frac{1}{\hbar} \nabla_{\mathbf{k}} H_{\mathbf{k}}. \quad (3.16)$$

When working on $\mathbf{k} \cdot \mathbf{p}$ Hamiltonians [26], this is the most suitable way to calculate the matrix elements.

3. The term $\sum_{\mathbf{k}} \delta[\hbar\omega - (E_{n'} - E_n)]$ is called the *joint density of states* (JDOS) which is actually the DOS of the difference between the two bands n and n' . The JDOS counts the number of states available for an optical transition induced by an incident photon of energy $\hbar\omega$. Like the DOS, the JDOS is extremely sensitive to the dimension and the band dispersion. It determines the functional form of the optical conductivity as a function of ω . A simple thumb rule

$$\Re[\sigma(\omega)] \sim \frac{\text{JDOS}}{\omega} \times \text{Selection rules} \quad (3.17)$$

can track the functional behavior of the optical conductivity. This is further corroborated by Fig. 3.1 in which the optical conductivities for different dispersion and dimensions are shown. Note that the optical conductivity for parabolic bands in 2D and 3D is not divergent in the vicinity of $\hbar\omega = E_g$ thanks to the regular functional form of the DOS in 2D and 3D for parabolic bands.

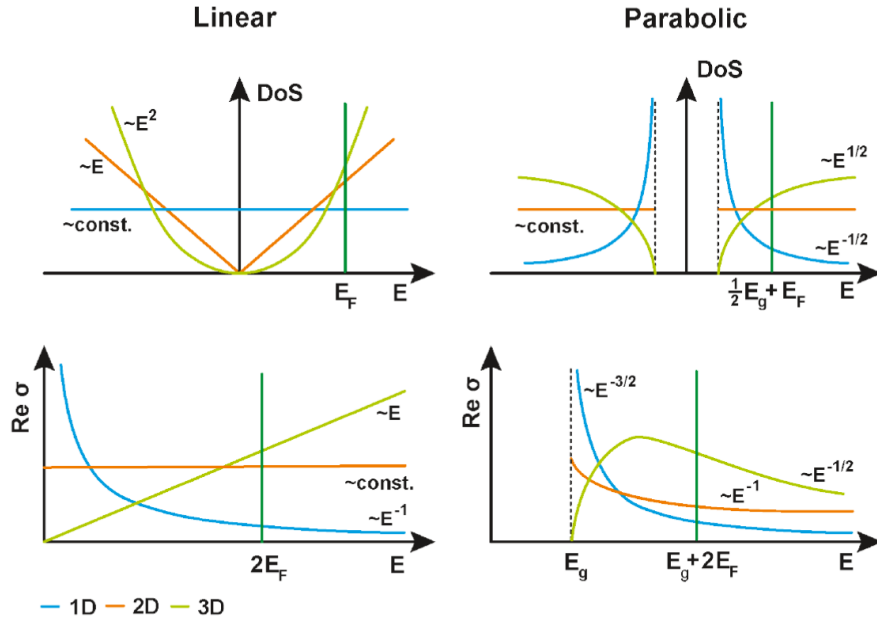


Figure 3.1: Illustration on how the dimension of bands affects the optical conductivity for linear and parabolic bands. Figure reprinted from [109].

The Kubo formula (3.12) of the diagonal part of the optical conductivity allows one to understand many optical properties of solids. One of the most spectacular examples is the optical conductivity of graphene which has a 2D linear dispersion at low energy. Since the JDOS scales as ω , the corresponding optical conductivity is a constant! This yields a constant transmission coefficient of a monolayer graphene written only in terms of the fine-structure constant [110, 111, 112].

3.1.3 MAGNETIC FARADAY AND KERR ROTATION: OFF-DIAGONAL TERM

Optical activity can be induced in non-chiral materials by applying a magnetic field that yields magneto-optical phenomena. When a linearly polarized photon propagates through a material slab in the z -direction of the magnetic field (see Fig. 3.2), the polarization of the transmitted light is rotated with respect to the incident light. Depending on whether the rotation of the polarization is observed in transmission or reflection, these phenomena are called the magnetic Faraday rotation or the magneto-optical Kerr rotation, respectively. If the medium is absorbing, the field can induce magnetic circular dichroism, namely the polarization of the transmitted light is no longer linear but elliptic (see Fig. 3.2). This is called Faraday ellipticity.

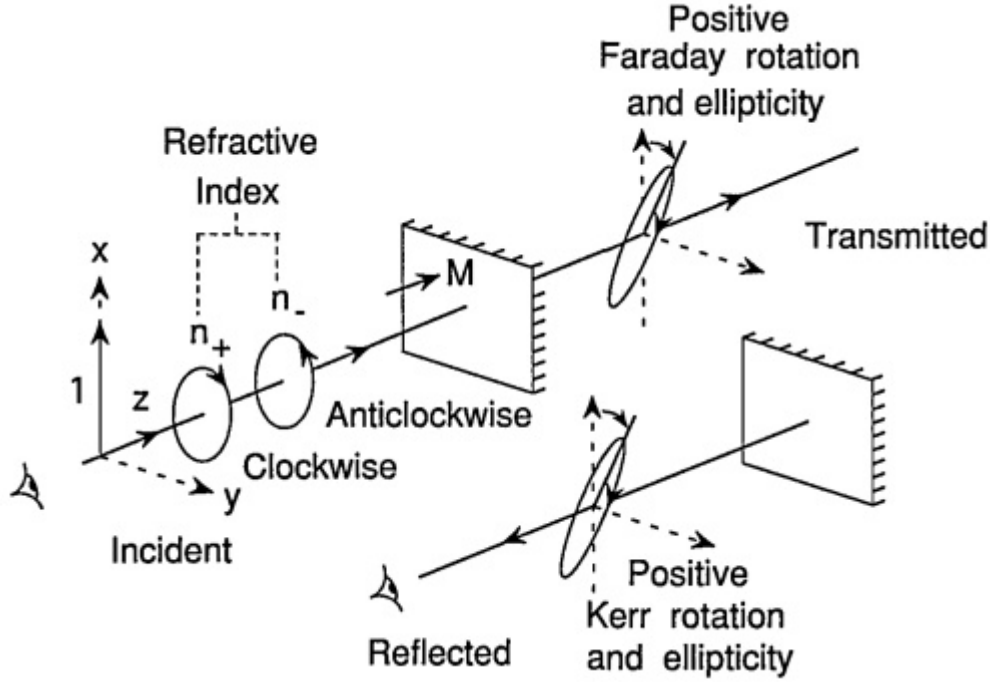


Figure 3.2: Schematic to illustrate the magnetic Faraday rotation and ellipticity, magnetic Kerr rotation and ellipticity. Magnetic field or magnetization of materials is in the z -direction. Figure reprinted from [113].

These magneto-optical phenomena are encrypted in the off-diagonal part of the optical conductivity tensor. Linear polarization is the equal weight sum of the left and right handed circular polarization.¹⁰ Reasoning in the circular polarization instead of linear one is equivalently doing a basis transformation $\exp(i\pi\sigma_y/2)$ ¹¹ on the optical conductivity 2D matrix where I suppose the light propagates in the z -direction. In the circular polarization basis, the diagonal part is not equal if $\sigma_{xy} \neq \sigma_{yx}$, which is the cause of the magneto-optical phenomena.

By Onsager's reciprocal relation [114], the conductivity tensor should be symmetric when time-reversal symmetry (TRS) is verified. However, TRS is broken by the magnetic field yielding non-zero opposite Hall conductivities $\sigma_{xy} = -\sigma_{yx}$. In other words, Faraday rotations are possible if TRS is broken.

However, the inverse statement is not true because the optical activity is also present in chiral materials in the absence of magnetic field. A key difference between the optical activity in the presence and in the absence of magnetic field is whether the TRS is broken. For example, preserving the TRS, the optical activity manifests itself only in the transmitted light but not in the reflected light, namely

¹⁰The convention of handedness is defined from the point of view of the source.

¹¹One should not confound the Pauli matrix σ_y with the conductivity tensor σ_{ij}

no Kerr effect is observed. When the direction of propagation is reversed, the rotation angle of linear polarization does not invert its sign in the absence of TRS. But it does so in the presence of a magnetic field, namely the TRS is broken. Therefore, only the optical activity induced by TRS-breaking is called Faraday effect. One does not have to invoke the magnetic dipole moment to explain the optical activity in the presence of a magnetic field, which is already present in the electric dipole approximation.

3.1.4 LANDAU QUANTIZATION AND SELECTION RULES

Intense magnetic fields induce Landau quantization of the electronic bands in 2D, i.e., quantization into separated levels indexed by n as elaborately shown in Chapter 2 for graphene.¹² With a fixed magnetic field, the optical conductivity has the shape of a series of peaks and each peak corresponds to one possible transition between two Landau levels. The plot of the evolution of these peaks in the optical conductivity upon variation of the photon energy and the magnetic field is called Landau fan diagram. An example for graphene is shown in [115]. The trajectory of peaks depicts the energy of Landau levels as a function of Landau level index and the magnetic field.

Suppose the magnetic field is applied in the z -direction, the selection rules between Landau levels are [101, 116]:

Polarization	Selection rules
circular: clockwise propagating in the z -direction	$n \rightarrow n + 1$
circular: anti-clockwise propagating in the z -direction	$n \rightarrow n - 1$
linear: in the x, y -directions	$n \rightarrow n \pm 1$
linear: in the z -direction	$n \rightarrow n$

Somewhat surprisingly,¹³ the selection rules are the same for parabolic and linear bands. This is because the selection rules inherently originate from the symmetry of the Landau level wavefunctions. In other words, it is a consequence of the conservation of angular momentum. The latter point of view can be elaborated by incorporating the magnetic field through the vector potential in the symmetric gauge. Besides the index n which indicates Landau levels of different energy, another quantum number m emerges and counts the angular momentum L_z of the eigenstates if the rotation symmetry is present. However, n and m are not decoupled. In a vertical transition, $\Delta m = \Delta n$. So, a circular polarized photon carrying an angular momentum $+\hbar$ (clockwise) can only excite an electron from an initial state of angular momentum m to a final state of angular momentum $m + 1$ by the conservation of angular momentum. The same reasoning is applied for an anticlockwise circularly polarized photon

¹²Bands are quantized in Landau bands in 3D.

¹³If one uses the ordering rule of Landau levels, the obtained selection rules are different. In certain literature [117], people name the zeroth Landau level in my convention $n = 1$.

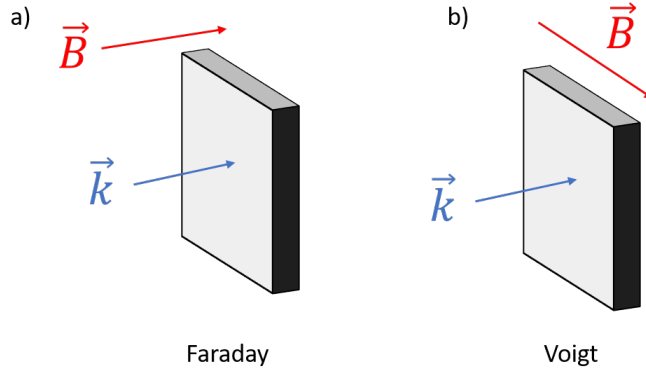


Figure 3.3: Schematic of Faraday and Voigt geometry for a transverse electromagnetic wave propagating in the z -direction.

carrying an angular momentum $-\hbar$. This yields the selection rules $n \rightarrow n \pm 1$ for the two circular polarizations, respectively. Since the linear polarization is the composition of two circular polarizations, the rules $n \rightarrow n \pm 1$ are both present.

Note that the selection rule for a photon polarized in the z -direction is distinct from other cases. This is because the photon polarized in the direction of the magnetic field does not carry any angular momentum in the z -direction¹⁴ so that the rule is $m \rightarrow m$ and thus $n \rightarrow n$. There are thus two different geometries in the optical experiments: Faraday and Voigt geometry. The magnetic field is parallel to the direction of light propagation in the Faraday geometry and perpendicular to the direction of light propagation in the Voigt geometry (see Fig. 3.3). As shown by the selection rules, Voigt geometry involves both the rules $n \rightarrow n \pm 1$ and $n \rightarrow n$. In contrast, Faraday geometry involves only the rule $n \rightarrow n \pm 1$ or even one of two possibilities if the circularly polarized light is used. This fact favors the use of Faraday geometry in the investigation of the magneto-optical properties of unknown materials.

To illustrate the power of Kubo formula, I show in the next section an example of theoretical magneto-optical study on a gapped nodal-line semimetal. The readers will see how the knowledge from Chapter 2 and 3 allows one to understand recent extraordinary and non-trivial magneto-optical experiments.

3.2 MAGNETO-OPTICS OF A GAPPED NODAL-LINE SEMIMETAL

NbAs₂ is a nodal-line semimetal which is gapped by the spin-orbit coupling (SOC). A pair of two mirror-symmetric nodal lines extends across the whole Brillouin zone. As shown in Fig. 3.4, each nodal-line has two optically relevant parts at infrared frequencies: a flat part and a dispersive part. The latter is modeled by the Hamiltonian (2.74) and the former by the same type of Hamiltonian with a

¹⁴ $L_z = xp_y - yp_x$.

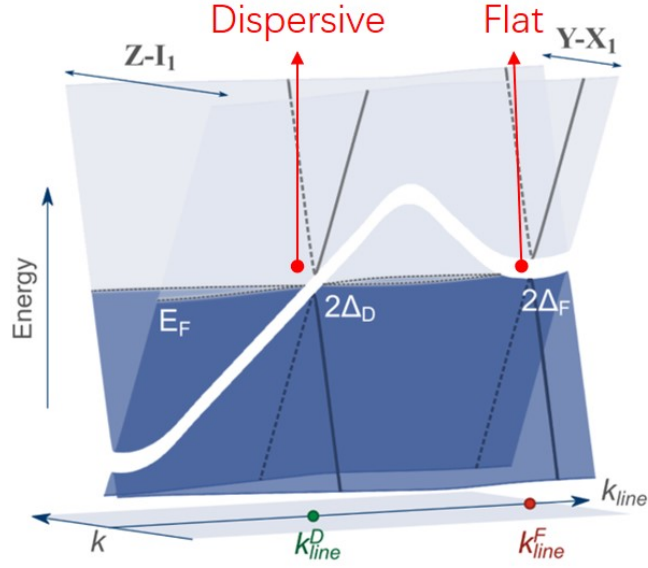


Figure 3.4: Energy profile of NbAs₂ tracing one of the two nodal lines. For incident photons of energy around 100 meV, only two parts are optically relevant as indicated in the figure. Figure credited to my collaborator, Jan Wyzula, of the LNCMI in Grenoble.

different value of gap and without the k_z -dependent term. The details on NbAs₂ and the construction of its low-energy Hamiltonian are given in App. C. In particular, one finds the relationship between the crystal axes and the axes used in the Hamiltonian (2.74).

Recently, Shao et al. [118] have conducted a magneto-optical study on NbAs₂. They have fitted the experimental data with the optical conductivity derived from a low-energy Dirac Hamiltonian. The results are satisfying for the data in the absence of a magnetic field. However, the magneto-optical results have not been properly explained in their work. This is the motivation that encourages my collaborators and me to study the magneto-optics of NbAs₂.

Two observations are elusive in the magneto-optical reflectivity data of NbAs₂ when a magnetic field is applied in the (001)-direction to the sample. First, the gap of the dispersive part measured from the Landau fan diagram is smaller than that derived from the zero field data. But, the gap of the flat part derived from the Landau fan diagram remains the same as that from zero field data (see Fig. 3.5). Second, the dispersive part yields a blurred Landau fan diagram and the flat part yields a clear-cut one. Most saliently, while Landau fan structure of the dispersive part is still visible if the incident photon is polarized along the b -axis of the crystal, it is almost washed out if the polarization of photon is along the a -axis, perpendicular to the b -axis (see Fig. 5 in [118]). The anisotropy in the Fermi velocity ($v_a/v_b \sim$

3.2 Magneto-optics of a gapped nodal-line semimetal

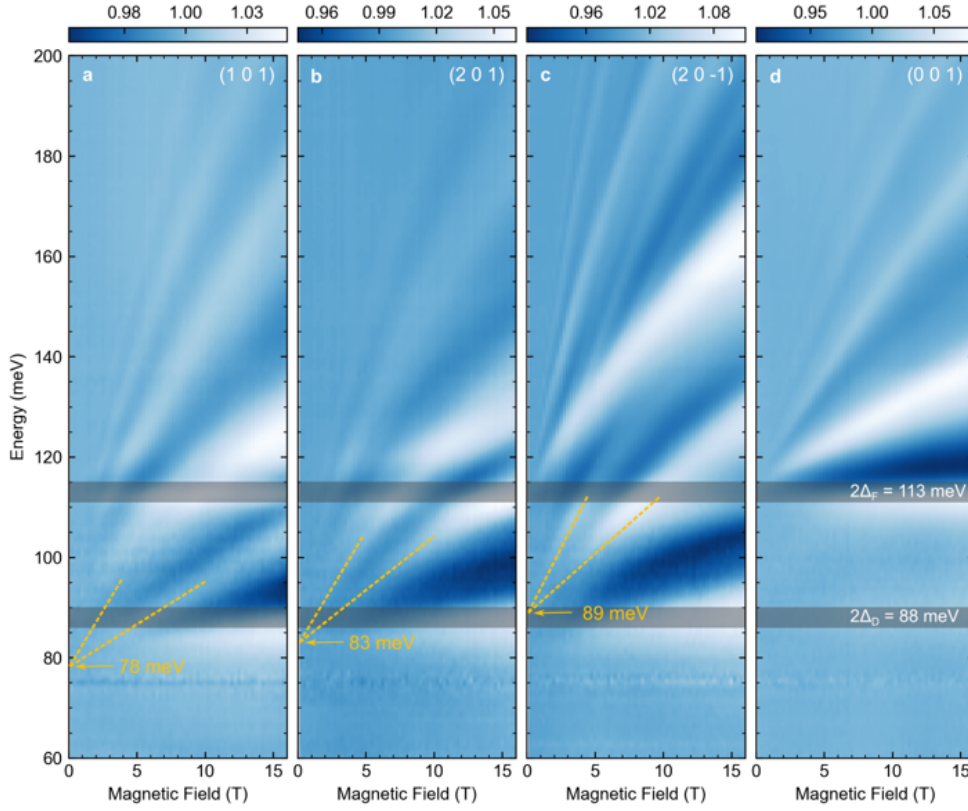


Figure 3.5: Measurement of the reflectivity of NbAs₂ for different facets $(m\ 0\ n)$, as a function of magnetic field and photon energy. One notices the evolution of the optical gap while varying the orientation of the magnetic field with respect to the nodal line. Figure credited to my collaborator of the LNCMI in Grenoble.

0.5 [118]) is unlikely to explain this effect since it would still yield the same order of magnitude of optical response ($\sigma_{aa}/\sigma_{bb} \sim 0.25$ [118]).

Compared to the flat part, it is clear that the magneto-optical response from the dispersive part of the nodal line is inherently different due to the tilting term. The first and probably most striking observation is the experimental configuration of the relativistic gap renormalization shown in Fig. 3.6(b), $2\Delta \rightarrow 2\Delta/\gamma$ [see Eq. (2.85)], as a function of the facet used in the reflectivity data. Here, I will spend more time on explaining the second observation.

3.2.1 OPTICAL CONDUCTIVITY IN THE ABSENCE OF MAGNETIC FIELD

Before explaining the magneto-optical observations, I want to show how well the conductivity calculated by Kubo formula can fit with that derived from the zero field data. One models the low-energy

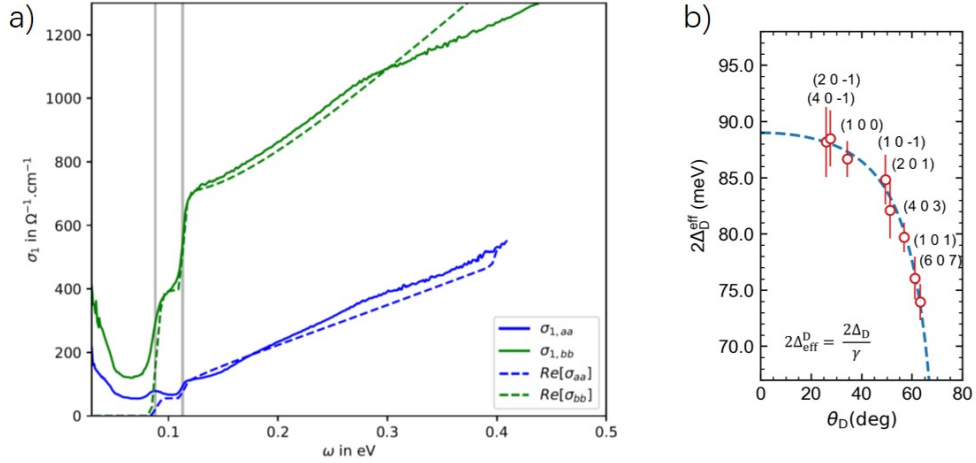


Figure 3.6: (a) Optical conductivities of a sample of NbAs₂ measured by my collaborators (solid lines) and those obtained using Kubo formula (3.12) for the low-energy model given in App. C (dashed lines). The fit is satisfying for energy below 0.3 eV. (b) Comparison between the experimentally measured gap by our collaborators of the LNCMI in Grenoble (points with error bar) and the one predicted by my theoretical calculations. The accuracy of the theory is highly satisfying. Figure honored to Jan Wyzula of the LNCMI.

physics of NbAs₂ by pasting together several Dirac Hamiltonian describing respectively different segments of the nodal line (see in App. C). The greatest advantage of the model is that the optical conductivity can be calculated analytically.

As shown in Fig. 3.6, the fit is mostly satisfying when the energy of photon is below 0.3 eV above which the interband transitions are possible between bands other than gapped nodal-line [118]. The Kubo formula manages to recover the two steps in the optical conductivity. Furthermore, one can identify the cause of the two-step feature, namely the onsets of the dispersive and the flat part of the nodal line with different gap, respectively.¹⁵ The ratio between the optical conductivities for two polarizations is also accurately retrieved. This allows one to evaluate the anisotropy of Fermi velocity. Here, I only consider the interband transitions so the Drude peak below 0.1 eV is not captured in Fig. 3.6(a). Nevertheless, one should be convinced by the predictive power of the Kubo formula (3.12) used in these rather simple low-energy models.

3.2.2 SELECTIONS RULES IN THE PRESENCE OF A MAGNETIC FIELD

To understand the obscure magneto-optical observations for the dispersive part of the nodal line, one must go back to the Hamiltonian (2.74) where I omit the anisotropy of the Fermi velocity. Since the Landau fan structure is still present, the system is in the magnetic regime (see Chapter 2). The angle

¹⁵More details are shown in App. C.

θ defined in (2.82) is thus smaller than the critical angle θ_c defined by (2.84). In the presence of a magnetic field in the z -direction, the Hamiltonian reads

$$H = w(\cos \theta q_z - \sin \theta (q_x - eBy)) + v(\cos \theta (q_x - eBy) + \sin \theta q_z) \sigma_x + vq_y \sigma_y + \Delta \sigma_z \quad (3.18)$$

where $\hbar = 1$ (also in the following discussions) and the Landau gauge $\mathbf{A} = (0, -eBy, 0)$ is used. The Hamiltonian H can be solved using the hyperbolic transformation $M = \exp(\phi \sigma_x / 2)$ with $\tanh \phi = w \tan \theta / v$ following the same procedure in Chapter 2 for graphene in a crossed electric and magnetic field. The transformed Hamiltonian reads:

$$\begin{aligned} H_T &= M H M \\ &= \frac{wv}{v^*} q_z + \frac{w^2 + v^2}{v^*} q_z \sin \theta \cos \theta \sigma_x + v^* (q_x - eBy) \sigma_x + vq_y \sigma_y + \Delta \sigma_z \end{aligned} \quad (3.19)$$

where a new velocity v^* is defined as

$$v^{*2} = v^2 \cos^2 \theta - w^2 \sin^2 \theta \quad \text{with} \quad \gamma = \cosh \phi = \frac{v \cos \theta}{v^*} \quad (3.20)$$

where $\gamma > 1$ is the relativistic Lorentz factor. Note that H_T does not have the same spectrum as H . In the basis of $|\psi_T\rangle = \gamma^{-1/2} M^{-1} |\psi\rangle$ given the eigenstate $|\psi\rangle$ of H , one can construct from H_T another Hamiltonian $H_E = (H_T - E \sinh \phi \sigma_x) / \cosh \phi$ with the same spectrum as H

$$H_E = \frac{wq_z}{\cos \theta} + \frac{1}{\gamma} \begin{bmatrix} \Delta & \frac{\sqrt{2vv^*}}{\ell_B} a_E \\ \frac{\sqrt{2vv^*}}{\ell_B} a_E^\dagger & -\Delta \end{bmatrix} \quad (3.21)$$

where a pair of energy-dependent ladder operators is defined

$$a_E = -\frac{\ell_B}{\sqrt{2vv^*}} \left(\frac{v^*}{\ell_B} (y - \langle y \rangle_E) + ivq_y \right) \quad (3.22)$$

$$a_E^\dagger = -\frac{\ell_B}{\sqrt{2vv^*}} \left(\frac{v^*}{\ell_B} (y - \langle y \rangle_E) - ivq_y \right) \quad (3.23)$$

$$\langle y \rangle_E = \frac{\ell_B^2}{v^*} \left(v^* q_x + q_z (w^2 + v^2) \sin \theta \cos \theta - E \frac{w \sin \theta}{v^*} \right) \quad (3.24)$$

with $[a_E, a_E^\dagger] = 1$. The subscript E indicates the dependence on energy E . In particular, the center of cyclotron $\langle y \rangle_E$ shifts with energy.

3 Theoretical approach to spectroscopy

Since the energy-dependent term in H_E is absorbed in the definition of the ladder operator, the energy spectrum is self-consistently found in the eigenstates of energy E_n^λ [see (2.85)] in the form

$$|\psi_{T,n,\lambda}\rangle = \begin{pmatrix} \sin \alpha_{n,\lambda} |n-1, E_n^\lambda\rangle \\ \cos \alpha_{n,\lambda} |n, E_n^\lambda\rangle \end{pmatrix} \quad (3.25)$$

where $\alpha_{n,\lambda}$ is an angle depending on n and the sign of energy $\lambda = \pm$; $|n', E_n^\lambda\rangle$ is the wavefunction of one-dimensional quantum harmonic oscillator defined by the previous ladder operators. Given the Landau level index $n, n' = n$ or $n-1$. As shown in Fig. 3.6(b), the gap measured by magneto-optics is indeed renormalized by γ , which depends on the orientation of the magnetic field.

To study the magneto-optical properties of NbAs₂, one evaluates the matrix element $\langle \psi_n | \hat{v}_{\mathbf{k}} | \psi_m \rangle$. Indeed, it is more practical with the basis $|\psi_{T,n}\rangle$ already at hands by remarking that

$$\langle \psi_n | \nabla_{\mathbf{k}} H | \psi_{n'} \rangle = \gamma \langle \psi_{T,n} | \nabla_{\mathbf{k}} H_T | \psi_{T,n'} \rangle \quad (3.26)$$

thanks to the fact that M is k -independent. So, in the basis $|\psi_T\rangle$, the velocity operators for H_T are

$$\hat{v}_{T,x} = v^* \sigma_x \quad (3.27)$$

$$\hat{v}_{T,y} = v \sigma_y \quad (3.28)$$

$$\hat{v}_{T,z} = \frac{wv}{v^*} + \frac{w^2 + v^2}{v^*} \sin \theta \cos \theta \quad (3.29)$$

where one notice an emergent anisotropy of Fermi velocity induced by the magnetic field. For the dispersive part in NbAs₂, the x, y -directions in the model (2.74) correspond to the a, b crystalline directions (see in App. C). The anisotropy of Fermi velocity yields a significant discrepancy in the optical conductivity¹⁶

$$\frac{\sigma_{aa}}{\sigma_{bb}} = \frac{\sin^2 \theta \sigma_{xx}}{\sigma_{yy}} \propto \frac{v^{*2} \sin^2 \theta}{v^2} = \frac{\sin^2 \theta \cos^2 \theta}{\gamma^2}. \quad (3.30)$$

Using the parameters in [118], the angle θ is $\sim \pi/3$ and thus $\gamma = 1.17$. Taking into account the inherent Fermi velocity $v_a/v_b \sim 0.5$, the optical conductivity for photon polarized along the a -axis is more than 20 times smaller than that of a polarization along b -axis! Using the same scale of plots, the Landau fan is thus apparent for σ_{bb} but difficult to see for σ_{aa} .

¹⁶If one follows the same calculations on the flat part, one would find the ratio between the conductivities is $\cos^2 \theta$. The relativistic renormalization is again demonstrated by the additional Lorentz factor γ .

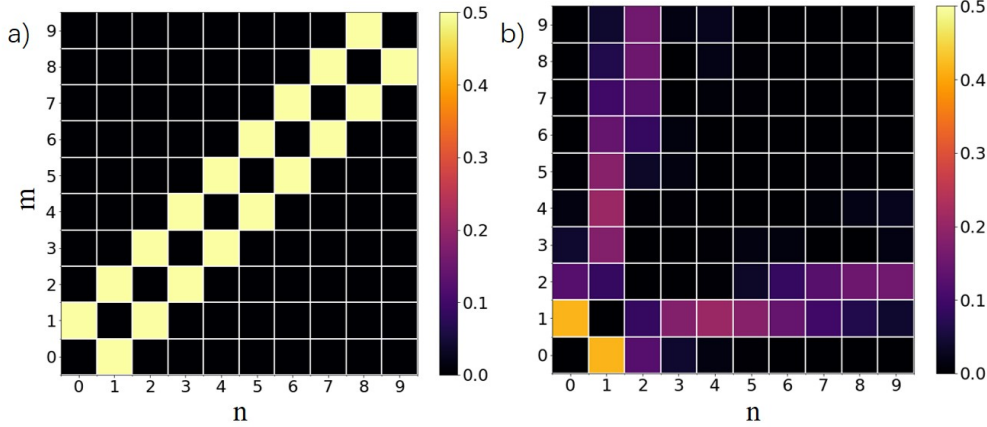


Figure 3.7: Coupling strength between the eigenstates $|\psi_{T,n,\lambda}\rangle$ and $|\psi_{T,m,\lambda'}\rangle$ where I consider only transitions from valence ($\lambda = -1$) to conduction bands ($\lambda = +1$). (a) When $\theta = 0$, the usual selection rules $n \rightarrow n \pm 1$ are given. (b) When $\theta = \pi/3$, many other transitions are also allowed.

With the velocity operators, one can a priori derive the selection rules. However, one encounters another difficulty here. When one calculates the matrix elements such as $\langle \psi_{T,n} | \hat{v}_{T,x} | \psi_{T,m} \rangle$, one has to deal with terms like $\langle n', E_n | m', E_m \rangle$ which is not 0 or 1 anymore because of the mismatch between their energy dependent orbital centers of the two states [see (3.24)]. In other words, one does not have the usual dipolar selection rules anymore. Instead, all of the direct transitions are in principle possible if Pauli's principle is satisfied. Peaks stemming from the selection rule other than $n \rightarrow n \pm 1$ ¹⁷ proliferate in the optical conductivity similarly to what has been predicted in 2D organics and 3D Weyl semimetals [82, 83]. By the sum rule, this would dilute the prominent Landau fan which reflects the $n \rightarrow n \pm 1$ rule. Therefore, the usual clear-cut Landau fan is blurred.

The different dipolar transitions differ a lot in amplitude from each other. As shown in Fig. 3.7, this can be seen by plotting the coupling strength, i.e., the square of the normalized matrix element like $|\langle \psi_{T,n} | \hat{v}_{T,x} / v^* | \psi_{T,m} \rangle|^2$ [82].¹⁸ In Fig. 3.7(a) where $\theta = 0$, only the selection rules $n \rightarrow n \pm 1$ are allowed. This is because the energy-dependence in the cyclotron center is canceled by $\sin \theta$ [see in (3.24)]. When the angle is non-zero, for example, $\theta = \pi/3$, some loose selection rules emerge such as $n \rightarrow 10n$ and $n \rightarrow n/10$ as shown in Fig. 3.7(b). For example, the transitions $0 \leftrightarrow 2$ are now allowed. Yet, the transition $0 \rightarrow 1$ is always well defined.

In this section, I have illustrated the usage of the Kubo formula in a frontier research problem on the magneto-optics of Dirac materials NbAs₂. Analyzing the matrix element, the fact that NbAs₂

¹⁷Here, Faraday geometry is implied.

¹⁸The technical trick to analytically evaluate the matrix element is given in the supplementary information of [83] and also in App. C

exhibits polarization-selective optical response is explained by the energy-dependent cyclotron center induced by the hyperbolic transformation. Combined with the gap renormalization, NbAs₂ is thus an excellent candidate to experimentally show the relativistic renormalization effect in the condensed matter systems.

3.3 PLASMON AND ELECTRON ENERGY LOSS SPECTROSCOPY

Metals consists of electrons at dynamic equilibrium, which move constantly creating local charge fluctuations. Therefore, some small regions have an excess of charges. The charges in those regions would be repelled away by the surrounding charges and acquire a velocity to overshoot their original position. Then, they would be pushed back in the opposite direction by a restoring force. This process can lead to oscillatory motion called plasma oscillations. Like any other oscillation, the plasma oscillations can be quantized into quasi-particles called plasmon.

Plasmons can be measured by *electron energy loss spectroscopy* (EELS), in which the incident electron scatters with the electrons in metals and thus loses a quantum amount of energy $\hbar\omega_p$, energy of the plasmon. Details of technique can be found in [119, 120]. Recently, even the momentum dispersion of plasmon energy has been resolved [121], which further boosts the study of plasmons in solids.

The physics of plasmons is encrypted in the polarization function $\chi(\mathbf{q}, \omega)$, i.e., the charge-charge correlation function in linear response theory, which is related to the dielectric function $\epsilon(\mathbf{q}, \omega)$. The theoretical way to study plasmon is then to calculate $\chi(\mathbf{q}, \omega)$ or $\epsilon(\mathbf{q}, \omega)$. However, this is difficult to do because the origin of plasmon is due to the Coulomb interaction between electrons, which is notoriously intractable. Some approximations must be used.

The simplest approximation to demonstrate the existence of plasmons is the random phase approximation (RPA) [122] applied on the dielectric function ϵ . It is exact if the electronic density is high. The main idea behind the RPA is to suppose that the local charge fluctuation is induced as a response of non-interacting electrons to a local potential, which is self-consistently determined by the sum of the external and induced potential (see Fig. 3.8). This yields the following equations

$$\phi_{\text{ind}} = V_C \chi \phi_{\text{ext}} \quad (3.31)$$

$$\phi_{\text{ind}} = V_C \chi^{(0)} \phi_{\text{loc}} \quad (3.32)$$

$$\phi_{\text{loc}} = \phi_{\text{ext}} + \phi_{\text{ind}} \quad (3.33)$$

where ϕ represent electric potentials, $\chi^{(0)}$ is the (non-)interacting charge susceptibility and V_C is the Coulomb potential. One thus finds the RPA charge susceptibility

$$\chi^{\text{RPA}} = \frac{\chi^{(0)}}{1 - V_C \chi^{(0)}} \quad (3.34)$$

By definition,¹⁹

$$\phi_{\text{ext}} = \epsilon^{\text{RPA}} \phi_{\text{loc}} \quad (3.35)$$

from which one retrieves the RPA dielectric function

$$\epsilon^{\text{RPA}} = 1 - V_C \chi^{(0)}. \quad (3.36)$$

The zero of ϵ^{RPA} is thus the plasmon mode, namely a long-lived charge oscillation (and thus a persistent oscillation in ϕ_{loc}) induced by a vanishingly small external potential [see (3.35)]. In Chapter 5, I will use the RPA to study surface plasmons arising from Volkov-Pankratov states as well as their spectroscopic signatures.

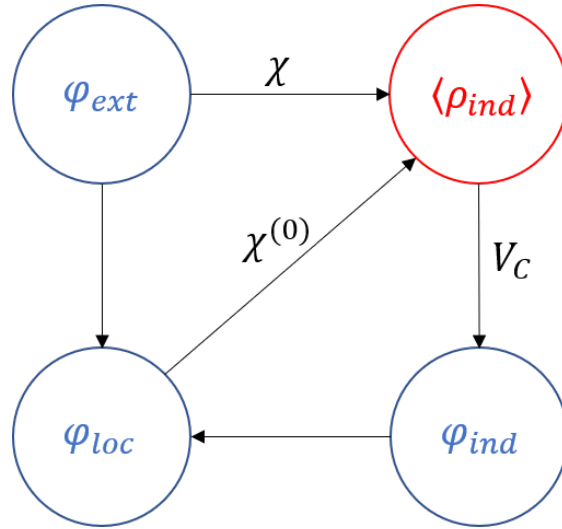


Figure 3.8: Illustration of the self-consistent approximations behind the RPA. $\langle \rho_{\text{ind}} \rangle$ is the average value of induced charge density. Since all other quantum fluctuations are neglected by taking the mean value, the RPA is indeed a mean-field theory.

¹⁹Similarly, in electrodynamics,

$$\mathbf{D} = \epsilon \mathbf{E} = \epsilon_0 \mathbf{E}_{\text{ext}}$$

where I distinguish Maxwell field and the external field. \mathbf{E}_{ext} plays the role of \mathbf{D} .

3.4 SUMMARY

In this chapter, I have introduced the arsenal of theoreticians to study the spectroscopic properties of solids, including both magneto-optical visible-infrared spectroscopy and EELS. I have illustrated the usage of theoretical formalism to rationalize the unraveled phenomena observed in a gapped nodal-line semimetal NbAs₂. My theoretical modeling of this material has been used namely in the identification of a relativistic renormalization of the magneto-optical gap, within a collaboration with the magneto-optics group led by Milan Orlita at LNCMI in Grenoble. Our results are at present written up for publication.

As shown in Chapter 5, the powerful theoretical tools also helps one to unequivocally identify the nature of states and guides the search of new optical and plasmonic applications.

4 TOPOLOGICAL HETEROJUNCTION: EMERGENCE OF VOLKOV-PANKRATOV STATES

Every theoretical physicist who is any good knows six or seven different theoretical representations for exactly the same physics. He knows that they are all equivalent, and that nobody is ever going to be able to decide which one is right at that level, but he keeps them in his head, hoping that they will give him different ideas for guessing.

Richard P. Feynman

In the introduction, the reader has seen that topologically protected edge states emerge at the surface of topological materials by means of gap closing. The wavefunction of topological edge states can be explicitly shown within the Dirac equation including a spatially dependent mass gap, for example $\Delta(x)$. Functional analysis indicates that the existence of an exponentially localized topological edge states only requires an inverted gap across the interface. This is in line with general arguments in topological band theory that do not rely on a particular form of $\Delta(x)$. Therefore, most studies on topological edge states are justified for using a sharp step-like $\Delta(x)$ for simplicity. However, the surface of real materials is never perfectly cleaved so that the mass gap $\Delta(x)$ has to be a smooth function rather than Heaviside function. For example, the surface of prototypical two-dimensional topological insulator (TI), HgTe/(Hg,Cd)Te quantum well, is notoriously difficult to handle [123, 124]. This solicits a study on the effect of smoothness on the surface of topological materials, which is another work in my thesis.

As I will show in this chapter, the study of smooth surfaces and interfaces is particularly rich. In addition to the topologically protected chiral states, massive surface states called *Volkov-Pankratov* (VP) states [72, 74, 75] emerge at the surface of topological materials when the surface is smooth enough. Indeed, they have been shown to arise not only in TIs [72, 124, 125, 126], but also in surfaces of Weyl semimetals (WSMs) [127, 128], topological graphene nanoribbons [129] and topological superconduc-

tors [130]. Here, I only call the massive surface states other than the topological ones the VP states to underline the particularities of the massive states.¹ The experimental realization of a topological heterojunction could be done by smoothly varying the chemical composition of material in space. For example, one can tune a 3DTI Bi_2Se_3 to a trivial one In_2Se_3 by continuously substituting Bi by In [131].

In this chapter, I will first present the three theoretical models I will constantly use in this chapter and the next one: a 2D toy model, a model for a realistic 3DTI and a model for a two-node WSM. The smoothness of the surface (or interface) is incorporated in Dirac Hamiltonian by a gap parameter that varies over a certain width ℓ across the interface. I will show that the exact functional form of $\Delta(x)$ is unimportant and can be linearized if one is interested in localized states in the vicinity of surface. Then, based on my work during my Ph. D., I will show by explicit calculations the emergence of VP states and topological states from different perspectives adopting certain well-chosen functional forms of the gap parameter to facilitate the calculations. Each perspective gives a conceptually different understanding on the origin of VP states. Furthermore, these perspectives shed light on the properties of VP states.

4.1 TOPOLOGICAL HETEROJUNCTION: THEORETICAL MODELS

Since the smooth (inter)surface of a topological material acquires a finite size, it may be more appropriate to call it a smooth junction connecting topological material and vacuum, which can be seen as a trivial insulator with large band gap. The two phases being topologically different, such junction is called a *topological heterojunction* [72]. More generally, a topological heterojunction is a smooth interface between two materials characterized by different values of a topological invariant. In this section, I present three models of topological heterojunctions.

4.1.1 TWO-DIMENSIONAL TOY MODEL

One of the simplest models of topological heterojunctions that one can propose consists of an interface between a trivial Semenoff [27] and a topological Haldane insulator [13], both stemming from the low-energy spinless model of graphene. They display both a band structure with two massive Dirac points, in other words two valleys. Suppose the half-space $x < 0$ is filled by a Semenoff insulator and the other half-space $x > 0$ by a Haldane insulator. The gap changes only its sign in one of the two valleys when passing across the topological heterojunction [69]. Say, the sign change occurs at the K point. The Dirac-type Hamiltonian for the valley K reads

$$H^{\xi=+1} = \Delta(x)\sigma_z + \hbar v(k_x\sigma_x + k_y\sigma_y) \quad (4.1)$$

¹In some literature [125], the topological surface state are sometimes called the topological/massless VP state.

where σ_α ($\alpha = x, y, z$) are Pauli matrices that represent the sublattice (A and B), $\xi = +1$ denotes the K valley [see Eq. (2.10)]. The interface is described by a position-dependent gap $\Delta(x)$, with $\Delta < 0$ for $x < 0$ and $\Delta > 0$ for $x > 0$. In the other valley K' , the Hamiltonian is similar to that in the K valley,

$$H^{\xi=-1} = \tilde{\Delta}(x)\sigma_z + \hbar v(-k_x\sigma_x + k_y\sigma_y) \quad (4.2)$$

where $\tilde{\Delta}(x)$ remains positive for both sides of the interface, even if its value may vary across the interface, and $\xi = -1$ denotes the K' valley. So, I will only consider the Hamiltonian for K valley in the following calculations.

The interface Hamiltonian has to match the bulk Hamiltonian when one is situated at a place far away from the position where the gap is closed. In this example, the Hamiltonian becomes the bulk Hamiltonian of Semenoff insulator in the limit $x \rightarrow -\infty$ and that of Haldane insulator when $x \rightarrow +\infty$. Concretely, $\Delta(x)$ verifies

$$\Delta(x) = \begin{cases} -\Delta_0 & \text{if } x \rightarrow -\infty \\ \Delta_0 & \text{if } x \rightarrow +\infty \end{cases} \quad (4.3)$$

where $\Delta_0 > 0$. To emphasize the fact that two topologically different phases at $x \rightarrow -\infty$ and $x \rightarrow +\infty$ cannot be distinguished from their spectrum, I have assumed additionally the gap of the two insulating phases to be the same. I will also make the same assumption in the following models. For interested readers, the case for different gap is discussed in the references [72, 132]. In the vicinity of $x \sim 0$ where the gap varies, k_x is no longer a good quantum number so that $[x, k_x] = i$. One already anticipates the quantization of the 2D bands into 1D bands.

Though this 2D toy model is simplistic, the present picture can however be generalized to the Bernevig-Hughes-Zhang model of 2D time-reversal-symmetric TI [70] with spin degree of freedom, $s_z = \pm$. One just replaces the valley index by s_z and considers the model near the Γ point retaining only linear terms.

4.1.2 THREE-DIMENSIONAL TOPOLOGICAL INSULATOR

A 3D TI can be described within several different Hamiltonians. For example, Bi_2Se_3 [133], known as a prototype material of 3D \mathbb{Z}_2 TIs, can be described by a low-energy model thanks to Zhang et al. [134]. Inspired by this model, one can construct a Hamiltonian to describe a 3D topological heterojunction

$$H_0 = \Delta(z)\tau_z + \hbar vk_z\tau_y + \hbar v\tau_x(k_y\sigma_x - k_x\sigma_y) \quad (4.4)$$

4 Topological heterojunction: emergence of Volkov-Pankratov states

where the Pauli matrices τ and σ represent orbital and spin degrees of freedom, respectively. As in the 2D model, one forms a 3D topological heterojunction by replacing the constant bulk gap by a spatially varying one which changes its sign across the interface along the z -axis.

For a 3D TI in \mathbb{Z}_2 classification as Bi_2Se_3 , the sign of Δ is also the topological invariant: topological if the gap is negative and trivial if positive [134]. Suppose the half-space $z < 0$ is filled by topological phase and the other half-space $z > 0$ filled by trivial phase. As before, I assume a symmetric topological heterojunction such that

$$\Delta(z) = \begin{cases} -\Delta_0 & \text{if } z \rightarrow -\infty \\ \Delta_0 & \text{if } z \rightarrow +\infty \end{cases} \quad (4.5)$$

where $\Delta_0 > 0$.

4.1.3 TWO-NODES WEYL SEMIMETAL

The way to construct a Hamiltonian describing the smooth interface between a WSM and a trivial insulator is slightly different from that for TIs. One starts by the simplest Hamiltonian of a time-reversal-broken two-node WSM [42]

$$H = \hbar v(k_x \sigma_x + k_y \sigma_y) + \left(\frac{k_z^2}{2m} - \Delta_0 \right) \sigma_z \quad (4.6)$$

where $\Delta_0, m > 0$ and two Weyl nodes are placed at $\mathbf{k} = (0, 0, \pm\sqrt{2m\Delta_0})$ between which the gap is inverted in reciprocal space. A topological transition occurs when two Weyl nodes of opposite chirality are annihilated by merging them together [8]. A trivial insulator is thus formed beyond the merge of two nodes by tuning the gap to zero and then to negative values. The desired Hamiltonian is modeled as

$$H = \hbar v(k_x \sigma_x + k_y \sigma_y) + \left(\frac{k_z^2}{2m} - \Delta_0 + \Delta(x) \right) \sigma_z \quad (4.7)$$

where $\Delta_0 > 0$ and

$$\Delta(x) = \begin{cases} 0 & \text{if } x \rightarrow -\infty \\ 2\Delta_0 & \text{if } x \rightarrow +\infty. \end{cases} \quad (4.8)$$

The bulk Hamiltonian of the trivial insulating phase interfacing with WSM is then

$$H = \hbar v(k_x \sigma_x + k_y \sigma_y) + \left(\frac{k_z^2}{2m} + \Delta_0 \right) \sigma_z \quad (4.9)$$

4.1.4 LINEARIZATION OF THE MODELS

Until now, the only artificial hypothesis for the gap parameter is that the two sides of a topological heterojunction have the same band gap. The condition on the gap parameter given above is to make the interface Hamiltonian match correctly the bulk Hamiltonian of two phases at $x \rightarrow \pm\infty$. None of the models imposes any explicit form for the position-dependent gap parameters. Yet, the above condition implicitly requires a valid function of a gap parameter describing a topological heterojunction, for example $\Delta(x)$ in the 2D toy model, to have the property that $\Delta(x)$ is vanishing somewhere at finite x only an odd number of times. Otherwise, the neighboring gap closing points can be annihilated pairwise by continuous transformation (see green dots in Fig. 4.1). The gap can reopens consuming a finite amount of energy, that is not topologically protected. Therefore, from the topological point of view, one is allowed to suppose without losing generality that the gap is closed only once at, for example, $x = 0$. A plausible choice for the gap parameter could be $\Delta(x) = \Delta_0 \tanh(x/\ell)$ where a length scale for smoothness ℓ describing the size of the interface is introduced (see blue line in Fig. 4.1).

Since the gap changes its sign only once at $x = 0$, one can always do a Taylor expansion of $\Delta(x)$ in the vicinity of the gap closing point where $\Delta(x)$ can be fairly supposed to be analytical at $x = 0$. This amounts to write $\Delta(x) = \Delta_0 x/\ell + O((x/\ell)^2)$ where the typical size of the interface ℓ serves as a cut-off. Therefore, one can always use a linearized gap parameter at the gap closing point whenever one focuses on the surface states localized in a topological heterojunction. In other words, the linearization of model is universally possible in any topological heterojunction. Every valid functional form of gap parameters is permitted to do such a linear expansion. For example, $\tanh(x/\ell)$ is linearized to x/ℓ as expected.

Introducing a length scale ℓ characterizing the smoothness of topological heterojunction, the linearized version of the three models are

- 2D toy model:

$$H = \Delta_0 \frac{x}{\ell} \sigma_z + \hbar v_F (k_x \sigma_x + k_y \sigma_y) \quad (4.10)$$

where the gap is closed at $x = 0$ and only one valley is considered.

- 3DTI:

$$H = \Delta_0 \frac{z}{\ell} \tau_z + \hbar v_F k_z \tau_y + \hbar v_F \tau_x (k_y \sigma_x - k_x \sigma_y) \quad (4.11)$$

where the gap is closed at $z = 0$.

4 Topological heterojunction: emergence of Volkov-Pankratov states

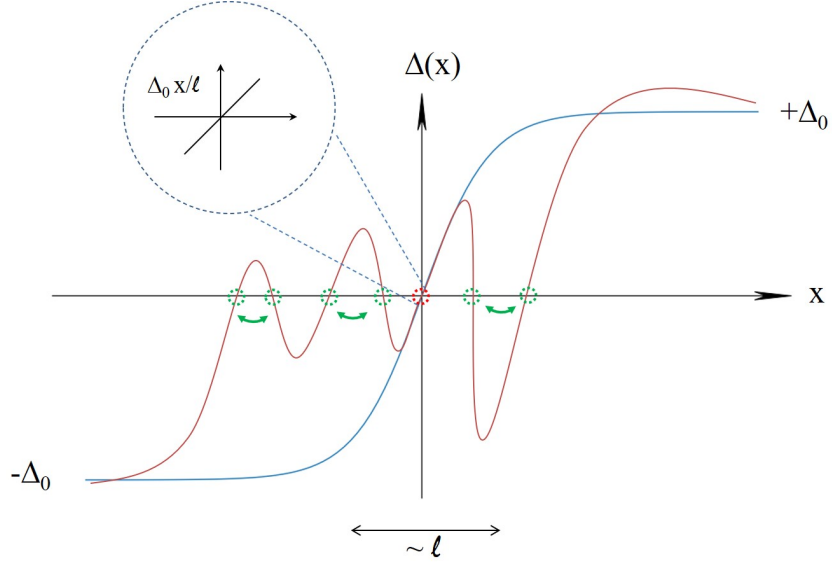


Figure 4.1: Schematics of two gap functions $\Delta(x)$: one is described by a tangent hyperbolic function (blue line) and another vanishes seven times across the interface (red line). Nevertheless, the neighboring gap closing points (green dots) can be continuously merged together for annihilation so that only one is left (red dot). If one focus on the physics of the interface, one can zoom in in the vicinity of the (last) gap closing point and suppose a linear $\Delta(x)$ by introducing the size of interface ℓ .

- Two-node WSM:

$$H = \hbar v(k_x \sigma_x + k_y \sigma_y) + \left(\frac{k_z^2}{2m} - \Delta_0 + 2\Delta_0 \frac{x}{\ell} \right) \sigma_z \quad (4.12)$$

where the inverted gap of WSM is closed at $x = \ell$.

In all the models above, I consider that two topologically different phases are semi-infinite so that only one interface is considered. This is valid when the typical size of two materials L is much larger than the size of the interface ℓ . The finite-size effect will be discussed in the following sections of the chapter.

4.2 ORIGIN OF VOLKOV-PANKRATOV STATES

Besides massless topological states, massive surface states also emerge in topological heterojunction thanks to a smooth interface. These states are called *Volkov-Pankratov* (VP) states, being first theoretically predicted by Volkov and Pankratov in 1980s [74, 75]. The VP states have been rediscovered recently by our group and collaborators [72, 124] with the advent of topological material.

In this section, the Hamiltonians of topological heterojunctions consisting of TIs are solved both analytically and numerically. Various methods are used and each of them reflects a conceptually different perspective on the origin of VP states. I will discuss the energy spectrum of topological heterojunctions made by TIs. The analysis for the surface states of WSM are postponed to the next chapter.

4.2.1 SMOOTHNESS AS PSEUDO-MAGNETIC FIELD

I start with the simplest model, i.e., the 2D toy model, which bears all relevant phenomena that are all present in the more complete models. Linearization of the gap parameter permits to solve analytically the Hamiltonian with the help of unitary transformations presented in Chapter 2. After the unitary transformation $T = \exp(-i\pi\sigma_x/4)$, the linearized Hamiltonian of the 2D toy model (4.10) reads:

$$H_T = THT^\dagger = \hbar v \begin{bmatrix} k_y & k_x + i\frac{x}{\ell\xi} \\ k_x - i\frac{x}{\ell\xi} & -k_y \end{bmatrix} \quad (4.13)$$

where a characteristic length $\xi = \hbar v/\Delta_0$ is defined. This length scale is intrinsic because its value depends only on the Fermi velocity v and the gap parameter Δ_0 given by the bulk material. The effect of the unitary transformation is to interchange σ_z and σ_y Pauli matrices so that the x -dependence of the linearized gap function is now placed in the off-diagonal elements with k_x . The Hamiltonian written in the new basis is reminiscent of the Hamiltonian of gapped graphene in the presence of magnetic field where the gap is replaced by $\hbar v k_y$ which is a good quantum number. However, the linear term due to the spatially varying gap parameter along with k_x quantizes the motion in the x -direction in the same way as a magnetic field does by the Peierls substitution. Hence, the smoothness of topological heterojunction can be seen as a pseudo-magnetic field. As a real magnetic field yields Landau quantization, the pseudo-magnetic field should also induce energy levels indexed by an integer n .

To explicitly show this surprising analogy, one can define a pair of ladder operators

$$\hat{a}^\dagger = \frac{\ell_S}{\sqrt{2}} \left(k_x + i\frac{x}{\ell_S^2} \right) \quad (4.14a)$$

$$\hat{a} = \frac{\ell_S}{\sqrt{2}} \left(k_x - i\frac{x}{\ell_S^2} \right) \quad (4.14b)$$

4 Topological heterojunction: emergence of Volkov-Pankratov states

that satisfy $[\hat{a}, \hat{a}^\dagger] = 1$ and $\ell_S = \sqrt{\ell\xi}$ which plays the role of a pseudo-magnetic length associated with the pseudo-magnetic field, i.e., the smoothness. This is mostly evocative by comparing the Hamiltonian

$$H_T = \frac{\sqrt{2}\hbar v}{\ell_S} \begin{bmatrix} \frac{k_y \ell_S}{\sqrt{2}} & \hat{a}^\dagger \\ \hat{a} & -\frac{k_y \ell_S}{\sqrt{2}} \end{bmatrix} \quad (4.15)$$

with (2.18). To solve this Hamiltonian, one thus proceeds in the same way as for graphene in a magnetic field using harmonic oscillator basis defined by the ladder operators (see Chapter 2). The center of harmonic oscillators $\langle x \rangle$ is precisely at the gap closing point $x = 0$. This is actually an artifact of using an odd function of $\Delta(x)$. Nevertheless, the wavefunction should be localized at $x = 0$. Unlike usual Landau level wavefunction, $\langle x \rangle$ is independent of k_y making the resulting energy levels non-degenerate.

The spectrum of H_T reads

$$\begin{aligned} E_n^\pm &= \pm \hbar v \sqrt{k_y^2 + \frac{2n}{\ell_S^2}} && \text{if } n \geq 1 \\ E_0 &= \hbar v k_y && \text{if } n = 0 \end{aligned} \quad (4.16)$$

where n is a positive integer. As shown in the left panel of Fig. 4.2, instead of discrete Landau levels that one would find for a gapped graphene in the presence of a magnetic field, the spectrum of the 2D topological heterojunction in the presence of a pseudo-magnetic field created by the interface smoothness consists of dispersing Landau bands indexed by an integer n . I will explain in detail in the next part that the analogy of smoothness with magnetic field is partial and formal. They are actually fundamentally different quantizing field. This difference is encoded in the definition of the ladder operators. The dispersion in k_y is an appreciable characteristic of VP states which distinguishes them from other disorder-induced surface states. This is the reason why spectroscopy could be a good tool to unambiguously reveal VP states as shown in the next chapter.

Nevertheless, the analogy of smoothness with magnetic field is both convincing and inspiring. On the one hand, the massless topological state, which emerges as the $n = 0$ Landau band, is soundly included in the model describing a smooth junction. Most saliently, the massless state with $E_0 = \hbar v k_y$ does not depend on any details of the interface, in particular the smoothness ℓ , as it should do by general topological argument. The massless state is chiral because it propagates only in the positive y -direction. This is due to the fact that one considers only one side of a topological Haldane insulator. The chiral state with opposite dispersion can be found if one takes into account the other side of a finite size TI. On the other hand, the emergence of massive VP states are explicitly shown by the states

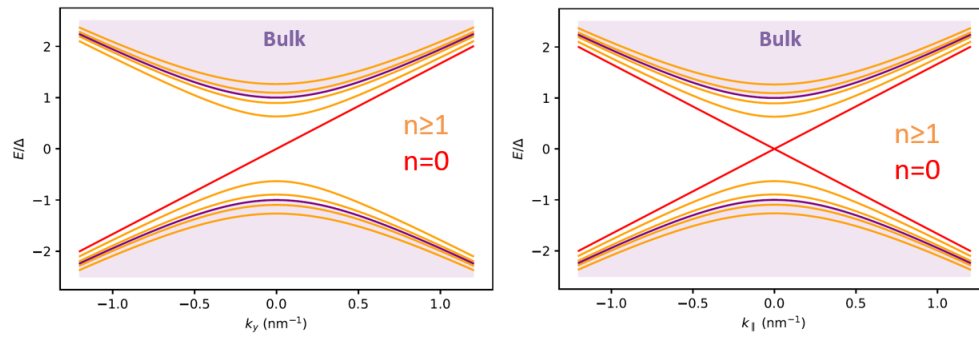


Figure 4.2: Spectrum for the 2D (left) and 3D (right) model including the chiral mode (red) the modes $n = 1 \dots 4$ (orange). The energy is measured in units of Δ_0 , i.e. half of the bulk gap. The modes $n = 3$ and $n = 4$ are immersed in the purple area which represents the bulk spectrum. So, they cannot give visible signal in experiments.

$n \geq 1$ with n being any large value. At first sight, it might seem that there is no bound for n . It might be tempting to think that the existence of the VP states would be universal on the surface of every topological materials because the surface smoothness is at least limited from below by the atomic length scale. This is however not the case and simply an artifact of the linearized model in which only surface states are considered. The presence of the bulk system prohibits the existence of the VP states on any surface of real samples above a certain value of n (see the left panel of Fig. 4.2). Here, the spectrum of the bulk system is $\pm \sqrt{\hbar^2 v^2 (k_x^2 + k_y^2) + \Delta_0^2}$. If the VP states with large n are immersed in the bulk continuum, they will not be localized on the surface due to the coupling with the bulk. Alternatively, only the VP states present in the gap is physically allowed and experimentally observable. Following this logic, one can define a critical length for smoothness only beyond which the interface is said to be smooth and the $n = 1$ VP state emerges in the gap. This critical length is precisely the intrinsic length scale ξ . The condition of the emergence of VP states in a topological heterojunction is thus $\ell \gg \xi$. This condition is fulfilled when the surface is very smooth (large ℓ) or the bulk gap is large enough (small ξ). For some large gap 3DTI, the intrinsic length scale is about 1 nm while the quintuple layer is also around 1 nm [135, 136]. The realization of a smooth topological heterojunction is promising. The above argument that the VP states of energy should be smaller than the bulk gap, $\sqrt{2n}\hbar v/\ell_S < \Delta_0$, yields an estimate of the maximum number n_{\max} of VP states that a given topological heterojunction can display,

$$n_{\max} \approx \frac{\ell}{\xi}. \quad (4.17)$$

Another mathematical understanding of the limit on n is to solve the model with $\Delta(x)$ for a full profile of space in which both the surface and bulk are considered [72]. Small value of ℓ admits only a

finite number of localized solutions to the differential equation. In comparison, one would prefer the analysis using linearized models since the argument is universally applicable and the physical picture is more intuitive.

It has been shown that the energy levels indexed by an integer n resemble Landau levels with dispersion justifying the similarity between smoothness and magnetic field. It is thus natural to ask how this pseudo-magnetic field and a real magnetic field interplay on the surface of topological materials. I invite the readers to go to the next chapter for this topic.

4.2.2 SMOOTHNESS-INDUCED CONFINEMENT: DIRAC QUANTUM WELL

In this part, I will elaborate a point of view on the origin of VP states that is conceptually different from the analogy with magnetic field. I have already mentioned several attributes of VP states distinct from Landau levels induced by a real magnetic field. The discrepancy is encoded in the definition of the ladder operators, which are independent of k_y . The VP states are thus non-degenerate, $(d - 1)$ -dimensional bands, indexed by n , if one considers a d -dimensional bulk system. For the same reason, the energy spectrum is a function of k_y but independent of k_x . The most prominent distinction is thus the dimensionality of the energy spectrum. Only one direction is quantized due to the position-dependent gap parameter. The dimension of system is thus reduced from d to $d - 1$, as one would expect for the relation between surface and bulk. However, a real magnetic field quantizes the motion in the plane perpendicular to itself so that the dimension is reduced from d to $d - 2$. In this sense, the smoothness affects the spectrum in a similar way as a quantum confining effect in the direction along which the gap varies.

Quantum confinement needs a potential quantum well which is not explicitly present in the model of the topological heterojunction. However, the Dirac Hamiltonian written in matrices can be decoded into a pair of conventional Schrödinger equations in a confining potential that arises from the (linearly) varying gap parameter for the components of the spinors. I will illustrate this point by a topological heterojunction formed by 3DTI (4.4). Working in the so-called Weyl basis $T = \exp(i\pi\tau_y/4)$, the Hilbert space can be decomposed into an orthogonal direct sum of two subspaces with opposite chiralities. The eigenstates $|\psi\rangle$ are four-component spinors,

$$|\psi\rangle = \begin{pmatrix} \chi_+(z) \\ \chi_-(z) \end{pmatrix}, \quad (4.18)$$

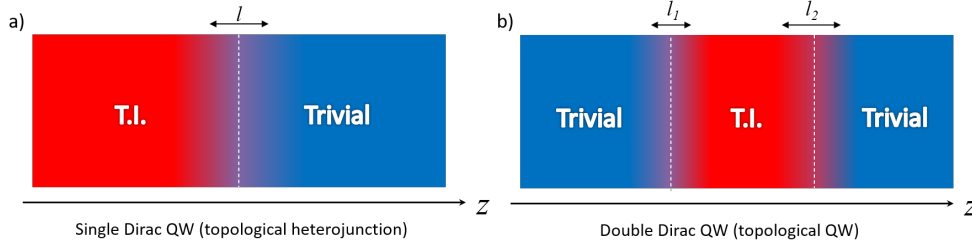


Figure 4.3: (a) Illustration of a single Dirac QW. (b) Illustration of a double Dirac QW. The spatially varying gap $\Delta(z)$ changes from positive sign to negative when one goes from the blue area (trivial phase) to the red area (topological phase) and the gap is closed somewhere in between. l , l_1 and l_2 characterize the smoothness of domain wall between phases. Figures adapted from the reference [137].

where χ_{\pm} are themselves two-component spinors of chirality \pm . One obtains thus a set of two decoupled differential equations:

$$\left(E^2 - \hbar^2 v^2 k_{\parallel}^2\right) \chi_{\lambda} = [\Delta(z) + \lambda \hbar v \partial_z][\Delta(z) - \lambda \hbar v \partial_z] \chi_{\lambda}, \quad (4.19)$$

where $k_{\parallel}^2 = k_x^2 + k_y^2$ and $\lambda = \pm$ represents the chirality. Most saliently, the equations can be rewritten as

$$\left(E^2 - \hbar^2 v^2 k_{\parallel}^2\right) \chi_{\lambda} = \tilde{E}_{\lambda}^2 \chi_{\lambda} = [-\hbar^2 v^2 \partial_z^2 + U_{\lambda}(z)] \chi_{\lambda}, \quad (4.20)$$

the right hand side of which shows now a second-order derivative in z , as it is the case for a 1D Schrödinger equation with a confining potential

$$U_{\lambda}(z) = \Delta(z)^2 + \lambda \hbar v \partial_z \Delta(z), \quad (4.21)$$

which itself depends on the chirality λ . One therefore has to deal effectively with the conventional quantum mechanical problem of a particle in a 1D quantum well, which I call henceforth *Dirac quantum well* (QW) [137]. A topological heterojunction is equivalent to two decoupled single Dirac QWs with opposite chirality λ [see Fig. 4.3 (a)].

In this treatment, solving E for the Dirac Hamiltonian (4.4) is equivalent to solving

$$\tilde{E}_{\lambda}^2 \equiv E^2 - \hbar^2 v^2 k_{\parallel}^2 \quad (4.22)$$

for this Schrödinger equation whose spectrum \tilde{E}_{λ}^2 must be non-negative. Be careful about the fact that the spectrum and the potential in the Schrödinger-type equation (4.20) have the physical dimension of a squared energy. To emphasize that I am working with such auxiliary quantities that do not have the dimension of energy (but its square), I invent the term *virtual energies* in the context of the Schrödinger

equation (4.20) to refer to the quantity \tilde{E}_λ^2 . The conversion relation from a virtual energy to a physical energy reads

$$E_\lambda^\pm(k_\parallel) = \pm \sqrt{\tilde{E}_\lambda^2 + \hbar^2 v^2 k_\parallel^2}. \quad (4.23)$$

With the help of the conversion relation, one can thus get the spectrum of the original Dirac Hamiltonian after solving the virtual energy of the corresponding the system of two Schrödinger equations. A given value of virtual energy corresponds to two opposite physical energies making the spectrum particle-hole symmetric. This is a distinguishable characteristic of VP states from other surface states. Though the particle-hole symmetry is an artifact of the Hamiltonian containing only linear terms in k , it still applies for the low-energy spectrum especially for $k_\parallel = 0$.

To illustrate a single Dirac QW, it is instructive to study the linearized form of the gap parameter

$$\Delta(z) = \begin{cases} -\Delta_0 & \text{if } z < -\ell \\ \Delta_0 \frac{z}{\ell} & \text{if } z \in [-\ell, \ell] \\ \Delta_0 & \text{if } z > \ell, \end{cases} \quad (4.24)$$

where the bulk is also included [see Fig. 4.4(a)]. Within this choice of gap parameter, one considers integrally a topological heterojunction consisting two semi-infinite bulk phases and their smooth interface. This choice of $\Delta(z)$ is by no means the best to describe the real experiments. But, it is the one that allows a simple analytical solution of the problem of a single Dirac QW. It is also the building block of the model for double Dirac QW. Most importantly, the functional behavior for all the parameters is independent of the choice of a $\Delta(z)$ verifying general features discussed above. The spectrum is thus quantitatively relevant (at least in the order of magnitude) compared to real situation in experiments.

A particularly interesting character of this choice could be that the gap parameter coincides with the linearized model (4.11) for $z \in [-\ell, \ell]$ where the gap is closed and the range of interface is defined. In this region, the Schrödinger Hamiltonian has the form of the Hamiltonian for a 1D quantum harmonic oscillator. This can be seen by formally substituting $\Delta_0/v^2 \rightarrow 2m$ and $v/l \rightarrow \omega_c/2$ (or equivalently $\Delta_0/l^2 \rightarrow m\omega_c^2/2$) in (4.20), such that the effective Schrödinger Hamiltonian reads

$$\frac{\tilde{E}_\lambda^2}{\Delta_0} \chi_\lambda = \left(-\frac{\hbar^2}{2m} \partial_z^2 + \frac{1}{2} m \omega_c^2 z^2 + \lambda \frac{\hbar \omega_c}{2} \right) \chi_\lambda \quad (4.25)$$

where an energy shift depending on the chirality due to a vertical shift between U_- and U_+ is determined by the interface width ℓ . Recall that the wavefunction of Landau levels in the Landau gauge is a 1D quantum harmonic oscillator as it is for the VP states. So, the form (4.25) suggests an alternative

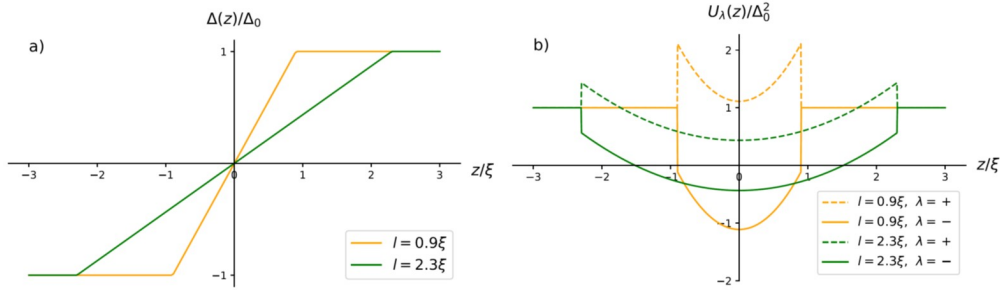


Figure 4.4: (a) Interface profiles described by a spatially varying gap $\Delta(z)$ for two values of characteristic interface width $\ell/\xi = 0.9, 2.3$. (b) Profiles of Dirac QWs for its corresponding $\Delta(z)$ and chirality $\lambda = \pm$. U_- is represented by solid lines and U_+ by dashed lines. Figures adapted from the reference [137].

way to understand the analogy of smoothness with magnetic field. The spectrum of this Hamiltonian of the linearized model is given by

$$\frac{\tilde{E}_\lambda^2}{\Delta_0} = \hbar\omega_c \left(n + \frac{1 + \lambda}{2} \right) \quad (4.26)$$

$$\text{or } \tilde{E}_\lambda = \sqrt{2\frac{\xi}{l} \left(n + \frac{1 + \lambda}{2} \right)} \Delta_0 \quad (4.27)$$

where $n \geq 0$ is an integer and $\lambda = \pm$. Only one zero mode exists with a definite chirality $\lambda = -$ while all other levels possess two chiralities. Using the conversion relation (4.23), the zero mode corresponds to the famed topologically protected single Dirac cone on the surface of 3DTI. The other Dirac cone is presented on the other side of 3DTI which is not considered in this single boundary model so that only one zero of one chirality is found here. The massive VP states manifest themselves as the non-zero energy levels of a 1D harmonic oscillator. They are thus not protected by topology from back-scattering [126].

The above solution is only correct if $\Delta(z) = \Delta_0 z/\ell$ for all over the space along the z -direction. Nevertheless, the reader already sees how a spatially variant gap parameter in Dirac Hamiltonian becomes a confining potential in the transformed Schrödinger Hamiltonian for the components of spinor. One can thus easily complete the full profile of the confining potential induced by the gap parameter (4.24). This is shown by Fig. 4.4 for two different values of the smoothness parameter ℓ/ξ .

Remember that I consider an odd function $\Delta(z)$, and $\Delta(z)^2$ and $\partial_z \Delta(z)$ are consequently even functions so that $U_\lambda(z)$ is a symmetric QW potential [see Fig. 4.4 (b)]. When the interface is abrupt ($\ell/\xi \ll 1$), only the 1D QW for the fermions with $\lambda = -$ is really confining [see the solid orange line in Fig. 4.4(b)]. In contrast, fermions with chirality $\lambda = +$ cannot be confined in the region

4 Topological heterojunction: emergence of Volkov-Pankratov states

$z \in [-\ell, \ell]$ because they can tunnel out of $z \in [-\ell, \ell]$ where the potential is no longer confining [see the dashed orange lines in Fig. 4.4 (b)]. An undergraduate level physics course [138] on 1D quantum mechanics tells one that there must be a bound state for $\lambda = -$, but not necessarily for $\lambda = +$. The virtual energy of bound states should be smaller than Δ_0^2 . Using (4.26), one estimates the number of bound state in the gap that a topological heterojunction can host, which is exactly the thumb rule (4.17).

Since the virtual energy potential U_λ is parabolic inside $z \in [-\ell, \ell]$ and constant outside, the wavefunction χ_λ for $n = 0$ behaves as a Gaussian within the interface and decays exponentially in the bulk. The standard deviation of the Gaussian part is thus described by a length scale $\ell_S = \sqrt{\ell\xi}$ which depends on the well width and the bulk gap, the same I have shown in the previous part. The width and depth of Dirac QW are both determined by the smoothness of the surface, which is encoded in $\Delta(z)^2$ and $\partial_z \Delta(z)$ [see the orange and green lines in Fig. 4.4]. This is essentially different from the conventional (square) QW of which one can independently engineer its depth and width. Most saliently, a smoother interface gives rise to a wider but shallower Dirac QW which can nevertheless host more bound states. This can be understood in terms of supersymmetric quantum mechanics as will be shown in the next part.

It is satisfying to find the same results on the bound states using a full profile $\Delta(z)$ as that on the localized states in the linearized model. Using $\Delta(z) = \Delta_0 \tanh(z/l)$ will of course provide the same conclusions [72, 74, 75]. This puts in evidence the argument that the band inversion mechanism allows one to linearize the spatially varying gap at the interface. Indeed, the validity of the linearized model to discuss the localized states is confirmed in the framework of Dirac QW as well as the statement that massive VP states can in principle emerge in any topological heterojunction when the interface is sufficiently smooth. In the language of quantum well physics, the Dirac QW can host more bound states if it is sufficiently wide.

4.2.3 COUPLING BETWEEN TWO SURFACES: DOUBLE DIRAC QUANTUM WELL

Knowing the spectrum of a single Dirac QW, it is appealing to study the coupling between two Dirac QWs. The configuration of two adjacent Dirac QWs arises naturally when a 3DTI is sandwiched between two trivial insulators, as depicted in Fig. 4.3(b). A confusion of jargon could be that the sandwich heterostructure is conventionally said to be a topological QW but with two interfaces so that it hosts two Dirac QWs. The thin film is thought to be a promising way to get rid of the metallic bulk states in TIs, which are undesirable for applications that rely on conduction from only the surface states [139]. In this part, I will show how the coupling strength between the states localized at different sides of a topological material depends on the thickness of the sample and also the smoothness of sur-

face. As shown below in a concrete example, the double Dirac QW is intrinsically asymmetric reflecting the topological protection of the topological surface state which is little affected by the presence of an adjacent Dirac QW. In contrast, the (virtual) energy of massive VP states are considerably shifted.

One chooses the following $\Delta(z)$ in the Hamiltonians (4.4) to model the above heterostructure:

$$\Delta(z) = \begin{cases} \Delta_0 & \text{if } z < -\frac{L}{2} - \ell \\ -\frac{\Delta_0}{\ell}(z + \frac{L}{2}) & \text{if } z \in [-\frac{L}{2} - \ell, -\frac{L}{2} + \ell] \\ -\Delta_0 & \text{if } z \in [-\frac{L}{2} + \ell, \frac{L}{2} - \ell] \\ \frac{\Delta_0}{\ell}(z - \frac{L}{2}) & \text{if } z \in [\frac{L}{2} - \ell, \frac{L}{2} + \ell] \\ \Delta_0 & \text{if } z > \frac{L}{2} + \ell \end{cases} \quad (4.28)$$

where L is the thickness of the 3DTI as indicated in Fig. 4.3(b). For a well-defined finite size sample, one should impose $2\ell < L$. The gap parameter $\Delta(z)$ and its corresponding Schrödinger potential $U_\lambda(z)$ are given in Fig. 4.5. Since the Schrödinger potential is invariant under simultaneous inversion of the chirality and spatial coordinate z , i.e., $U_\lambda(z) = U_{-\lambda}(-z)$, U_+ hosts a zero mode of chirality $\lambda = +$ only at the right QW and U_- hosts that of chirality $\lambda = -$ only at the left QW. However, since the gap parameter has the same sign at infinity, the Jackiw-Rebbi argument given in Chapter 1 is no longer valid. One can thus already anticipate that the zero mode is not protected anymore and acquires a non-zero energy. In terms of Dirac QW, it is understood as the possible tunneling between two adjacent Dirac QWs separated by a finite virtual energy potential barrier of height Δ_0^2 . For each U_λ , the Schrödinger Hamiltonian can be solved analytically by the usual method used in wave mechanics. Just like the problem of particle in a box, it suffices to transform the eigenvalue problem in an energy-dependent differential equation whose general solutions are analytically known. The boundary conditions then give rise to a secular equation that determines the spectrum. Here, I am only interested in localized states and the details of calculations can be found in App. D.

Since the presence of the second Dirac QW can be seen as a perturbation term to a single Dirac QW, especially for $L \gg \ell$, the energy spectrum of double Dirac QW will not deviate too much from that of single Dirac QW. Therefore, only the energy shift due to the double QW configuration is worth a careful analysis which I present here. Denote the deviation of the energy at k_\parallel for each index n as $\pm\Delta E_n$. Indeed, this deviation can be calculated with the help of the virtual energies \tilde{E}^2 ,

$$\Delta E_n = ||\tilde{E}| - |E_n^0(k_\parallel = 0)|| \quad (4.29)$$

where the energies at $k_\parallel = 0$ of a single Dirac QW are represented henceforth by the superscript 0, $E_n^0(k_\parallel = 0)$.

4 Topological heterojunction: emergence of Volkov-Pankratov states

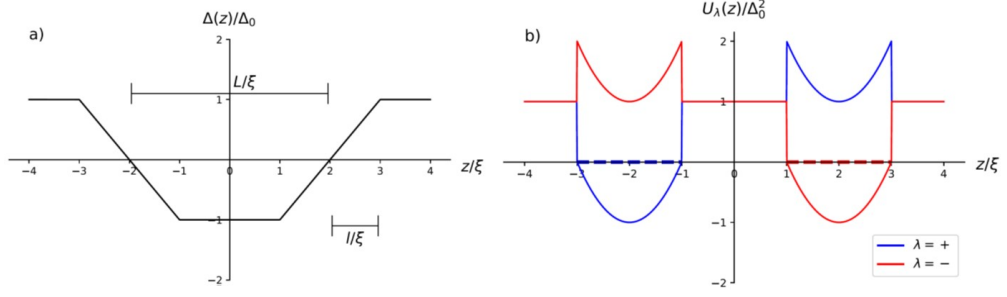


Figure 4.5: (a) Profile of the spatially varying gap $\Delta(z)$ for a 3DTI sandwiched between two trivial insulators with $\ell/\xi = 1$ and $L/\xi = 4$. (b) Profiles of two adjacent Dirac QWs for two chiralities. The two dashed lines, blue and red, indicate the energy level (close to zero) of the $n = 0$ states of $\lambda = \pm$, respectively. Figures adapted from the reference [137].

For the zero mode $n = 0$ which is no longer topologically protected, surface Dirac cones acquire a mass gap such that

$$E_{n=0}^\pm(k_\parallel) = \pm \sqrt{\Delta E_0^2 + \hbar^2 v^2 k_\parallel^2}. \quad (4.30)$$

In contrast to the $n = 0$ states, the massive VP states are “split” in energy by $\pm \Delta E_n$ with

$$E_n^\pm(k_\parallel) = \pm \sqrt{(E_n^0(k_\parallel = 0) \pm \Delta E_n)^2 + \hbar^2 v^2 k_\parallel^2}, \quad (4.31)$$

as a consequence of quantum tunneling between the two Dirac QWs and the resulting hybridization of the QW states.

Two possible regimes are discussed separately.

SHARP INTERFACE

When $\ell \ll \xi$, only the $n = 0$ modes exist at two sides of 3DTI and the presence of the other respective side yields a small mass gap. They live in two decoupled potential U_λ so that they cannot hybridize directly by quantum tunneling since their respective spinorial wavefunctions are orthogonal (see Fig. 4.5). One can only imagine an indirect tunneling with the help of the plane-wave bulk states that open a gap. However, this is not the dominant mechanism that opens the mass gap. As shown in the smooth surface regime where tunneling is even enhanced in the presence of VP states, it is more suitable to understand it in perturbation theory due to the exponential tail of the wavefunction probing an

adjacent Dirac QW nearby. In the sharp interface limit, one obtains by Taylor expansions of the secular equation the mass gap for the $n = 0$ modes²

$$\Delta E_0 = \Delta_0 e^{-\frac{L}{\xi}} \sqrt{1 + \frac{4l^2}{3\xi^2}}, \quad (4.32)$$

where the ratio L/ξ in the exponential illustrates the idea of topological protection by gap. Besides the exponential decay with increasing thickness which benchmarks the result with those in literature [140, 141, 142, 143], a correction arising from the smoothness of the surface is added. This formula gives a good estimation in order of magnitude for, for example, a thin film of Bi₂Se₃. For Bi₂Se₃, taking ξ as 1.5 nm [135, 136], one find a mass gap $2\Delta E_0 = 0.03$ eV close to the experimentally measured gap 0.05 eV [139]. In addition, this formula allows a quick estimation of the smoothness of the surface of topological material from the measured mass gap.

SMOOTH SURFACE

When $\ell > \xi$, massive VP states are also present in the region of confining potential wells. The calculations show that the energy splitting ΔE_n depends non-trivially on ℓ/ξ , L/ξ and the VP state index n fixing other material-related parameter such as v and Δ_0 . I define a reduced energy ω_r with dimension of unity used in the following plots

$$\omega_r = \sqrt{\frac{E^2 - \hbar^2 v^2 k_{\parallel}^2}{\Delta_0^2}} \in [0, 1]. \quad (4.33)$$

For $n = 0$, $\omega_r = \Delta E_0/\Delta_0$ [see Eq. (4.30)]. For $n \geq 1$, $\omega_r = |\Delta E_n^0(k_{\parallel} = 0) \pm \Delta E_n|/\Delta_0$ [see Eq. (4.31)]. I define also

$$\Delta\omega_r = \frac{\Delta E_n}{\Delta_0}. \quad (4.34)$$

With $\ell = 6\xi$ fixed, the energy splitting of the topological state and the VP states depends on the thickness of 3DTI L is shown in Fig. 4.6 [see solid lines in (a) and blue line in (b)]. The mass gap of the $n = 0$ state decays exponentially with L as for sharp surfaces. The splitting of the VP states also is exponentially small with increasing L/ξ showing no particular non-intuitive behavior. Also, the energy splitting of the $n = 0$ state is 10^2 times weaker than that of the massive VP states with given parameters.

²See in App. D.2

4 Topological heterojunction: emergence of Volkov-Pankratov states

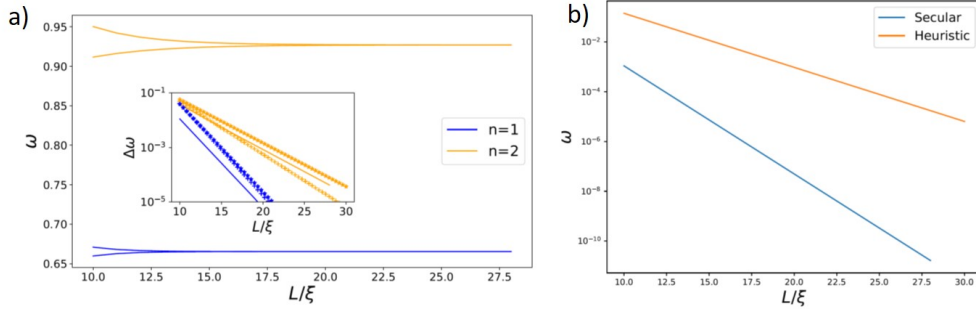


Figure 4.6: $\ell = 6\xi$ is fixed. (a) Reduced energy ω_r as a function of the distance between two Dirac QWs, L , for the massive VP states $n = 1$ and 2. The results are obtained by solving the secular equation given in App. D.1. Inset in (a): the reduced energy splitting $\Delta\omega_r$ decays exponentially with increasing L , only shown for the massive VP states $n = 1$ and 2. The solid lines indicate the splitting from the secular equation, while the crosses represent the results based on Eq. (4.36). The dotted lines show results based on the same formula, where one has used the exact energies for the VP states of a single Dirac QW instead of the approximate ones given in Eq. (4.26). (b) $\log_{10} \omega_r$ as a function of L/ξ for the $n = 0$ topological state. The numerical results from the secular equation are represented by blue line, that using Eq. (4.37) by orange line. Figures adapted from the reference [137].

Fixing $L/\xi = 20$, the evolution of the energy splitting of the VP states as function of ℓ/ξ is shown in Fig. 4.7. The spectrum of massive VP states follows as predicted to a small relative error the behavior $\omega_r = \sqrt{2n\xi/\ell}$ derived Eq. (4.26). Increasing the smoothness of the surface permits VP states with large n to emerge in the gap, or equivalently, be localized in the confining potential. The larger the index n is, the more prominent is the energy splitting.

The ℓ/ξ -dependence of the energy splitting of the VP states and the topological state is given in Fig. 4.8. In the range of ℓ/ξ with $L = 20\xi$ fixed, the splitting of the topological state is 10^4 times smaller than that of the VP states. The mass gap of the topological state is increasingly enhanced by the smoothness of the surface. The increase is likely to be exponential [see blue line in Fig. 4.8 (b)]. This observation is consistent with the intuition that the effective separation of two Dirac QWs is $L - 2\ell$ therefore giving an exponential behavior in ℓ/ξ . However, this argument cannot explain the non-trivial behavior of the energy splitting of the VP states [see solid lines in Fig. 4.8 (a)]. For the $n = 1, 2$ and 3, the energy splitting is not a monotonically increasing function of ℓ/ξ . Most saliently, it admits a minimum at different ℓ/ξ for each n . Larger values of n yield larger ℓ/ξ as the position of minimal splitting. When $n = 4$, the dependence on ℓ/ξ of the energy splitting becomes again monotonic.

One can explain the observations in the framework of the asymmetric double QW for a given chirality as shown in Fig. 4.9 by a thought experiment. Consider initially a thick sample of 3DTI so that the localized states in two complementary QWs feel little each other. Remember that all the energies in terms of Dirac QW has the dimension of the square of a physical energy and thus are called *virtual*

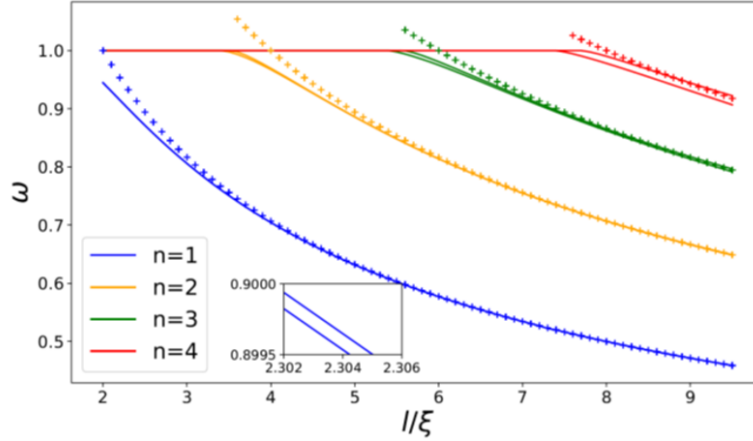


Figure 4.7: Reduced energy ω_r as a function of smoothness ℓ for the massive VP states $n = 1$ to 4 by solving the secular equation (solid lines). The ℓ -dependence of ω_r is well described by Eq. (4.26) (crosses). Inset: zoom-in to show the splitting for the VP state $n = 1$. Figures adapted from the reference [137].

energy [see Eq. (4.23)]. The virtual energy of the VP states are degenerate and the topological state remains at zero virtual energy. Imagine now that two Dirac QWs are brought together gradually by shrinking the thickness of the sample. Consequently, the tunneling becomes stronger and stronger and delocalizes the states which have been confined in their corresponding Dirac QW at the beginning of the thought experiment. States localized in two adjacent Dirac QWs hybridize to form new states and thus the energy degeneracy is lifted. Since the hybridization is strongest when they have the same energy, i.e., resonant hybridization, the massive VP states can hybridize strongly because their degenerate counterpart with the same energy living in the same U_λ is present in the adjacent Dirac QW. In contrast to VP states, the zero mode of a given chirality in one Dirac QW is little affected because the adjacent Dirac QW does not host a zero mode. This explains the huge difference in the order of magnitude of the energy splitting between the VP states and the topological states.

Pursuing the idea of tunneling, one can in principle estimate the energy splitting in order of magnitude using a heuristic formula. This formula is the result of a pedestrian exercise of undergraduate level that the energy splitting due to the tunneling between adjacent finite symmetric square QWs reads [138]

$$2\Delta E = \frac{\hbar^2 \pi^2}{4m\ell^2} \frac{4e^{-K(L-2\ell)}}{2K\ell}, \quad (4.35)$$

where 2ℓ is the width of a square QW, L the separation between the centers of the two square QWs and $K = \sqrt{2mV_0}/\hbar$ with the effective depth of the square QW, V_0 . The heuristic formula for double Dirac QW is thus derived after replacing $2m$ by $1/v^2$ and V_0 by $(1 - \omega_r^2)\Delta_0^2$ for the effective potential depth for a surface state of reduced energy ω_r . Since the energy splitting is that of the virtual energies

4 Topological heterojunction: emergence of Volkov-Pankratov states

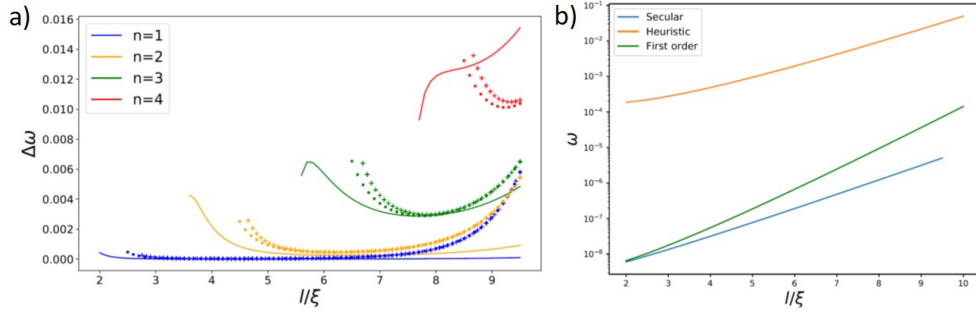


Figure 4.8: $L = 20\xi$ is fixed. (a) Reduced energy splitting $\Delta\omega_r$ as a function of smoothness ℓ for the massive VP states $n = 1$ to 4. The solid lines show the splitting numerically obtained from the secular equation and the crosses indicate the values obtained from the heuristic formula (4.36). The dotted lines show results based on the same formula, where one has used the exact energies for the VP states of a single Dirac QW instead of the approximate ones given in Eq. (4.26) (b) $\log_{10} \omega_r$ vs. ℓ for the $n = 0$ state and $L/\xi = 20$. The results from the secular equation are represented by blue line, that using Eq. (4.37) by orange lines and that using the first-order perturbation theory by green line. Figures adapted from the reference [137].

in the Dirac QW approach, one obtains actually a formula for $\Delta(E_n^2)$ instead of ΔE_n . One has to do an expansion of the virtual energies to linear order around the VP energies by writing $\Delta(E_n^2) \approx 2E_n\Delta E_n$ to translate the splitting of virtual energy into that of physical energy. The wavevector that describes the exponential suppression of the hybridization is given by $K = \sqrt{1 - \omega_r^2}/\xi$. Since the linearized version for the energy of the VP states matches the correct one to great accuracy, one can use it for ω_r so that the final formula reads

$$\Delta E_n = \frac{\pi^2}{4} \frac{\Delta_0}{\sqrt{2n}} \left(\frac{\xi}{\ell}\right)^{5/2} \frac{e^{-\sqrt{1 - \frac{2n\xi}{\ell}}(L-2\ell)/\xi}}{\sqrt{1 - \frac{2n\xi}{\ell}}} \quad (4.36)$$

for the VP states. As shown by dots and crosses in Figs. 4.6 (a) and 4.8 (a), the heuristic formula gives a good approximation on the order of magnitude of energy splitting, especially for $n = 1$ and 2. Most saliently, the non-trivial dependence on ℓ/ξ is captured by the formula (4.36). The non-monotonic behavior of energy splitting as a function of ℓ/ξ can be thus understood in terms of the antagonistic interplay between the effective separation of two Dirac QWs $L - 2\ell$ and the single QW energy dependence on ℓ . A smooth interface, i.e. large ℓ stabilizes the massive VP states so that the tunneling process should get through a higher potential barrier which prohibits the hybridization. However, it also reduces the effective distance between the two adjacent Dirac QWs so that the tunneling becomes more probable. The competition between the two effects manifests itself as the existence of a minimal value of the energy splitting while varying ℓ . Since the formula (4.35) itself is only valid for the states of small

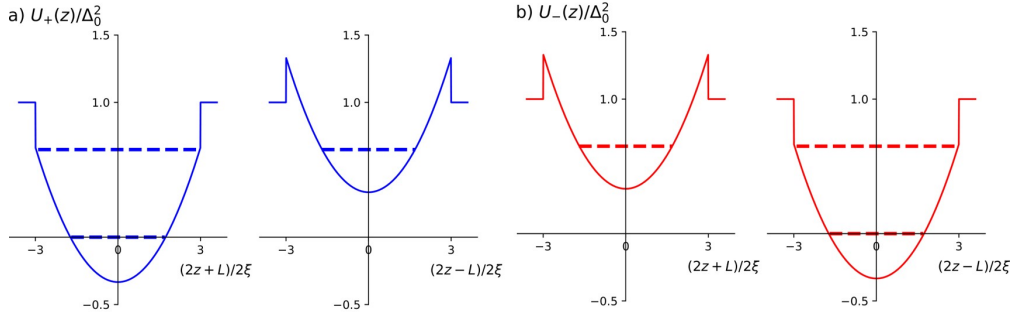


Figure 4.9: Profiles of two infinitely separated Dirac QWs for two chiralities with $\ell/\xi = 3$: (a) for $\lambda = +$ and (b) for $\lambda = -$. The dashed lines, blue and red, indicate the energy level of chiral states and $n = 1$ VP states for $\lambda = \pm$, respectively. Figures adapted from the reference [137].

n , the heuristic formula does not give a good approximation for the states of large n (here $n = 4$). These states have a virtual energy close to the virtual energy edge of Dirac QW. In other words, these VP states just emerge from the bulk continuum. In this case, the energy splitting of higher VP states increases with ℓ . The tunneling between two adjacent Dirac QWs is thus the reason to lift the degeneracy of the VP states. The formalism of Dirac QWs explicitly put in evidence the intuition on the mechanism of energy splitting and captures the essence of physics.

One might want to follow the same argument to derive a heuristic formula for the state $n = 0$. However, as I show in this paragraph, this approach yields an erroneous scaling of the energy splitting. Since the unperturbed $n = 0$ state has zero virtual energy, one must push to the second order in ΔE_0 unlike the $n > 0$ states, i.e., $\Delta(E_0^2) = (\Delta E_0)^2$. This would give a heuristic estimation

$$\Delta E_0 = \frac{\pi}{2} \Delta_0 \left(\frac{\xi}{\ell} \right)^{3/2} e^{-(L-2\ell)/2\xi} \quad (4.37)$$

which would describe the dependence of the mass gap for the topological state both on the smoothness ℓ/ξ and the thickness L/ξ . As shown in Figs. 4.6 (b) and 4.8 (b), the mass gap scales approximately as $\exp(-(L - \ell)/\xi)$ instead of $\exp(-(L - 2\ell)/2\xi)$ predicted by the heuristic formula. Actually, the tunneling on which the heuristic formula is based is not the predominant factor that opens a mass gap for the topological state. The $n = 0$ state has no partner in the adjacent Dirac QW with the same chirality so that tunneling is repressed. One has to find another mechanism than the resonant hybridization to account for the splitting for the $n = 0$ state. Indeed, a treatment in perturbation

4 Topological heterojunction: emergence of Volkov-Pankratov states

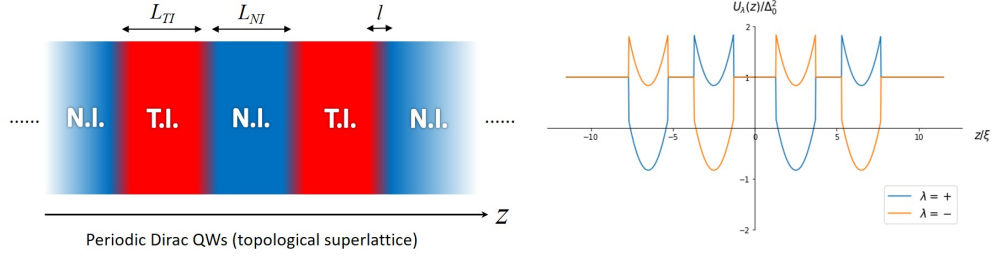


Figure 4.10: Illustration of a topological superlattice and its corresponding a series of periodic Dirac QWs. The parameters for the plot of U_λ are: $L_{\text{NI}}/\xi = 5$, $L_{\text{TI}}/\xi = 4$ and $\ell/\xi = 1.5$.

theory yields a better agreement in order of magnitude [see green line in 4.8 (b)]. The mass gap in this first-order perturbation approach reads

$$\Delta E_0 = \frac{\Delta_0}{2\pi^{1/4}} \left(\frac{\xi}{\ell}\right)^{5/4} e^{-\frac{L-1.5\ell}{\xi}}. \quad (4.38)$$

where the effective separation is $L - 1.5\ell$. The calculations are reported in App. D.2. To the leading order, the energy of the $n = 0$ state is affected by the deviation in $U_\lambda(z)$ induced by the second adjacent Dirac QW in the exponential tail of the wavefunction.

The absence of the resonant hybridization of wavefunctions explains why the the splitting for $n = 0$ states is by several orders of magnitude smaller than that for the $n > 0$ states. This is because a double Dirac QW is inherently asymmetry in contrast to the symmetric double square QW. The asymmetry in the double Dirac QW can be thus seen as another interpretation of topological protection.

SUPERLATTICE OF DIRAC QUANTUM WELL

As for thin film of topological material, there are both experimental [144, 145, 146, 147] and theoretical [148] efforts on topological superlattices which consists in alternating layers of topological and normal insulators. Forming a superlattice from topological materials is a strategy to enhance the surface response with respect to the bulk response in magneto-optics [146, 147]. In the framework of Dirac QW, the modeling of topological superlattice, which is just a periodic series of QWs as shown in Fig. 4.10, is conceptually intuitive and natural. One can use the knowledge of double Dirac QW to estimate the spectrum of topological superlattice. If a topological superlattice is periodic and composed of many layers, Bloch's theorem is applied and the spectrum acquires also a dispersion in the z -direction. The problem is thus converted to a 1D tight-binding model formed by Dirac QWs.

Suppose the layer thickness of TI is L_{TI} and that of normal insulator (NI) is L_{NI} . Two topologically different bulk phases are assumed to have the same bulk gap. The smoothness of interface is set to be

$\ell \gg \xi$ with $2\ell \ll L_{\text{TI}}, L_{\text{NI}}$. When $L_{\text{TI}} = L_{\text{NI}}$, the periodicity of the superlattice is $L = L_{\text{TI}} = L_{\text{NI}}$. The coupling between VP states at two surfaces of a NI is thus the same as that between VP states at two surfaces of a TI. Given n , one thus realizes a 1D chain in which each interface represents a site and the hopping amplitude is $t_n = \Delta E_n(L)$ where $\Delta E_n(L)$ is the expression (4.36). So, the splitting for VP states can be estimated

$$\Delta E_n = 2t_n \cos(k_z L). \quad (4.39)$$

If $L_{\text{TI}} \neq L_{\text{NI}}$, the periodicity of the superlattice is $L = L_{\text{TI}} + L_{\text{NI}}$ so that each unit-cell contains two interfaces TI/NI. The coupling between VP states at two surfaces of a NI is different from that between VP states at two surfaces of a TI. Given n , the hopping amplitude between two surfaces of a TI is $t_n = \Delta E_n(L_{\text{TI}})$ and that between two surfaces of a NI is $t'_n = \Delta E_n(L_{\text{NI}})$. One thus realizes a 1D chain which can be described by the SSH model! Most saliently, the ratio between the hopping terms t_n and t'_n are experimentally tunable simply by changing the thickness of TI and NI layer. Consequently, the splitting for VP states reads

$$\Delta E_n = \pm \sqrt{t_n^2 + t_n'^2 + 2t_n t_n' \cos(k_z L)}. \quad (4.40)$$

The estimation for the $n = 0$ state is more subtle. On the one hand, the $n = 0$ state has no partner at the nearest neighbor Dirac QW but at the second nearest neighbor Dirac QW. The expression (4.37) is thus valid by replacing L by $L_{\text{TI}} + L_{\text{NI}}$. On the other hand, the dominant mechanism to open a mass gap is still described by the first-order perturbation theory, i.e., Eq. (4.38). Consequently, the oscillating part due to the tunneling process is negligible compared to the term given by the first-order perturbation theory. Thus, the mass gap of the $n = 0$ state should be still almost dispersionless.

In summary, the idea shown by the Dirac QW is as follows. The emergence of VP states is a hidden quantum confinement effect which is explicitly revealed by the Dirac QW. Squaring the Dirac Hamiltonian yields two decoupled Schrödinger equations for an effective quantum well given by the chirality-dependent potential $U_\lambda(z)$. The motion parallel to the surface remains plane-wave-like by translation symmetry so that the problem to solve becomes a textbook 1D Schrödinger problem in wave mechanics. Once one has solved the secular equation derived from imposing boundary conditions on the wavefunction, one can retrieve the spectrum of the original Dirac Hamiltonian using (4.23). A single interface in the form of a topological heterojunction is physically equivalent to a single Dirac QW. Most saliently, the framework of Dirac QW is practical to treat the tunneling effect between two complementary sides of a finite-size topological material and of topological superlattice. The topological protection is encoded in the inherently asymmetric double Dirac QW.

4.2.4 SUPERSYMMETRY IN DIRAC EQUATION

One might be astonished by the fact there exists always a localized solution at zero energy in Eq. (4.19). In the linearized model, i.e, a 1D quantum harmonic oscillator, the zero mode is magically stipulated by a chirality-dependent shift in the confining potential so that the energy of the zero-point movement is compensated. As first remarked by Volkov and Pankratov et al. in their papers [74, 75, 117], the reason is given in terms of supersymmetric quantum mechanics. In Eq. (4.19), the confining potential is a linear combination of $\Delta(z)^2$ and $\partial_z \Delta(z)$ is called the *Witten equation* [149] in the literature for supersymmetric quantum mechanics.

To briefly illustrate the idea of supersymmetry, I consider only the band extrema where $k_{\parallel} = 0$ in Eq. (4.20). The Hamiltonian in the Weyl basis becomes:

$$H_s = -\Delta(z)\tau_x + \hbar v k_z \tau_y. \quad (4.41)$$

In the context of supersymmetric quantum mechanics [61], H_s plays role of the supercharge operator which connects linearly the subspaces of fermions and bosons (here two subspaces of chirality), and $\tilde{H} = H_s^2$ is thus the supersymmetric Hamiltonian. Containing only off-diagonal Pauli matrices, H_s maps χ_+ to χ_- and vice versa when it acts on χ_- . A functional analysis stipulates that only χ_{λ} gets a zero-energy mode with a definite chirality λ while $\chi_{-\lambda}$ does not whenever $\Delta(z)$ has opposite sign at $z = \pm\infty$. The massive VP states are thus the excited states in the boson-fermion correspondence. More mathematically, they are all the other solutions of the differential equation Eq. (4.20) that verifies the boundary condition of being vanishing at the infinity.

There is also a quasi-topological invariant called *Witten index* [149]:

$$I_W := \dim \ker H_s|_{V_-} - \dim \ker H_s|_{V_+} \quad (4.42)$$

where $\dim \ker H|_V$ is the dimension of the kernel of a linear operator H acting on a subspace V and V_{λ} are the two Hilbert subspaces of opposite chirality. Thus, I_W must be an integer and invariant under continuous changes of $\Delta(z)$. It dictates also the number of zero mode, zero or one, at the interface. The reader has just seen another beautiful example how a high-energy formalism, i.e., supersymmetry, emerges naturally in a condensed matter system such as topological materials.

Supersymmetric quantum mechanics is not only a beautiful mathematical formalism but also helps to understand something practical in Dirac QW formulation of the VP states. Recall that a smoother interface induces a wider but shallower Dirac QW which can nevertheless host more bound states. This can be understood in the language of supersymmetric quantum mechanics. If a non-zero mode $\chi_{n,-}$ exists in V_- , one can find a non-zero mode of same energy in V_+ by $\chi_{n-1,+} = H_s \chi_{n,-}$ because H_s

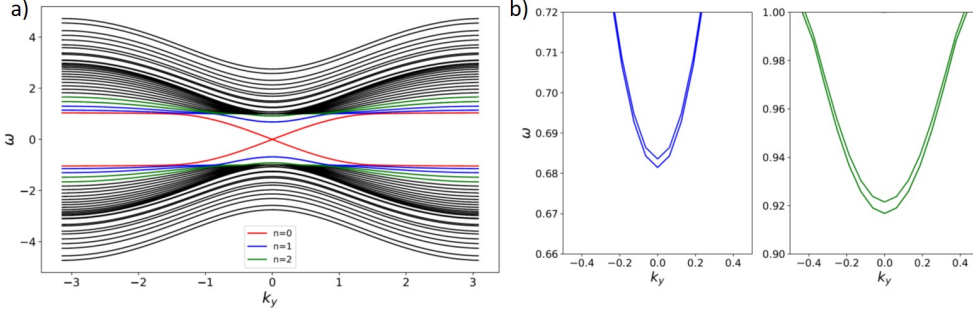


Figure 4.11: (a) Spectrum of the tight-binding model of a Chern insulator on a square lattice with $\ell/\xi = 4$ and $L/\xi = 20$. (b) Zoomed-in spectrum for the massive VP states $n = 1$ (left) and $n = 2$ (right).

commutes with \tilde{H} . Alternatively, if the potential U_- can host a bound state $n = 1$, the potential U_+ must host a bound state $n = 0$ of same energy [see for example (4.26)]. Due to the tunneling effect, a bound state in the potential U_+ must have a virtual energy below Δ_0^2 . A smoother interface with larger value of ℓ reduces exactly the vertical shift between the potentials U_λ and thus make the minimum of the potential U_+ sink below Δ_0^2 [see Fig. 4.4 (b)] so that a localized solution becomes viable. However, this is a necessary but not sufficient condition for the existence of bound states because the zero-point energy is finite. Yet, a smoother interface can host more bound states.

4.2.5 LEAKAGE FROM BULK: LATTICE MODEL

Until now, all the discussions are restricted to low-energy continuum models. Especially, the role played by the bulk system in a topological heterojunction is illusive. In this part, I will show how the VP states emerge in a lattice model.

Here, a Chern insulator on a square lattice [150] is modeled within the tight-binding approach. Since the low-energy surface physics are governed by the same chirality-dependent Schrödinger equation as Eq. (4.20), the discussions in this model can be extended to general consideration of topological heterojunction. The 2D system is cut along the y -direction so that k_y remains a good quantum number. Two edges are set to have the same smoothness $\ell/\xi = 4$ and the thickness of the system is $L/\xi = 20$.

The spectrum is shown in Fig. 4.11 (a). Two topological states from different edges cross at zero energy. Besides the topological states, only two massive VP states appear in the bulk gap. Their energy is consistent with the results shown in Fig. 4.7. The continuum model is thus validated by the lattice model. Especially, it shows that the specific form of $\Delta(z)$ is not important as long as one can linearize it at the band inversion point.

In Fig. 4.11 (b), the splitting of the massive VP states $n = 1$ and $n = 2$ is evaluated. The numerical simulations shows a splitting of $0.001\Delta_0$ for $n = 1$ and $0.004\Delta_0$ for $n = 2$. Compared to Fig. 4.8 (a),

the splitting of the massive VP states is underestimated in the continuum model. A likely explanation for the discrepancy could be due to the higher order terms in k in the lattice model which are not taken into account in the continuum model. Actually, the non-linear terms in k affects the value of the mass gap of the topological states due to finite-size effects [137, 140, 141, 142]. Since the energy splitting of the topological state is too weak to be captured in the numerical precision limited by a lattice cut-off, the mass gap for $n = 0$ is not visible in the spectrum of the lattice model.

Nevertheless, the lattice model not only confirms many conclusions from the continuum model but also clarifies how VP states descend from the bulk. As shown in Fig. 4.11 (a), the $n = 1, 2$ VP states in the gap connect adiabatically to bulk states by varying k_y . They are actually the consequence of the bulk states pervading to the surface. They are localized when the surface acquires a finite-size. One can continuously push the VP states into the bulk continuum by varying ℓ/ξ . This is essentially different from the topological states that the previous action is impossible. Since the VP states are the leakage of the bulk states to the surface, they are bulk states in nature so that the bulk-edge correspondence does not apply for them. This is also the reason why they are not topologically protected. But, this does not mean that they are not topological in a general sense. Their topological properties are embedded in, for example, the π Berry phase given by its massive Dirac fermion's spectrum and wavefunction leading to a quantized surface Hall conductivity [67].

4.3 SUMMARY

In this chapter, I have shown several different perspectives on the origin of the VP states that arise in smooth topological heterojunctions. Each perspective reveals an aspect on the nature of the VP states. First, smoothness can be seen as a source of a pseudo-magnetic field that gives rise to bands indexed by n similar to Landau levels in a real magnetic field. This encourages a study of magneto-optics on the VP states as I will shown in the next chapter. In the formulation of the topological heterojunction in terms of the Dirac QW that stems from squaring the original Dirac Hamiltonian, one interprets the topological protection of the topological zero modes in two parallel interfaces as the absence of a resonant hybridization due to the inherently asymmetric double Dirac QW. Meanwhile, the VP states are shown to be not topological. The fact that the two components of opposite chiralities are simultaneously non-zero enables the resonant hybridization. An estimation of the energy splitting is derived using the analogy to the tunneling problem for a symmetric square double QW. Furthermore, the Dirac equation encoded in the VP states is the one studied in supersymmetric quantum mechanics so that the VP states can be understood as excited states in the boson-fermion supersymmetric space. Finally, I corroborate the existence of the VP states by a lattice model from which the VP states descends from the bulk spectrum as a leakage of spectral flow from bulk to surface. Since this spectral flow can be

continuously deformed into the bulk continuum, the VP states are not topological as already shown in the other continuum approaches. My results on the double Dirac QW have been published in Physical Review B [137].

5 SPECTROSCOPIC PROPERTIES OF VOLKOV-PANKRATOV STATES

A scientist can be productive in various ways. One is having the ability to plan and carry out experiments, but the other is having the ability to formulate new ideas, which can be about what experiments can be carried out . . . by making [the] proper calculations. Individual scientists who are successful in their work are successful for different reasons.

Linus Pauling

In this chapter, I will present my studies on the spectroscopic properties of Volkov-Pankratov (VP) states. Two reasons pushed me to conduct my research in this direction. On the one hand, the spectroscopic properties are fundamentally appealing, because they allow one to understand the nature of VP states by comparing directly with those of the topological surface states. On the other hand, the calculated physical quantities related to spectroscopic properties are experimentally relevant. Every result of theoretical calculations has in principle its corresponding experiment to observe it. Sometimes, the spectroscopic study opens a route to new potential applications in optics and plasmonics.

Three theoretical tools are used in this chapter to study the spectroscopic properties of VP states. One is to calculate the optical conductivity of the VP states of topological heterojunctions in 2D and 3D. Then, I give a succinct description on the Faraday and Kerr rotation through a thin film of 3D topological insulator (TI) in the presence of VP states. Furthermore, I discuss surface plasmon modes in Weyl semimetals (WSMs) stemming from VP states that are measurable by electron energy loss spectroscopy (EELS). This is done by calculating the dielectric function in the random phase approximations (RPA).

This chapter is thus organized as follows. First, I will show the optical conductivity of a single topological heterojunction modeled by the Hamiltonians (4.10) and (4.11) for 2D and 3D, respectively, both in the absence and presence of a real magnetic field.¹ Most saliently, the specific features in the optical response from VP states provide a smoking gun for their identification. Then, I will briefly

¹Similar calculations have also been performed for WSMs within our group [151].

mention possible Faraday and Kerr effects for a thin film of 3DTI subject to an out-of-plane magnetic field. Finally, I will show how previously unknown plasmon modes arise on the surface of WSMs. The particular band structure of VP states in WSMs yields additional plasmon modes other than the one from the Fermi-arc (FA) states.

5.1 OPTICAL CONDUCTIVITY: SMOKING GUN FOR THE EXISTENCE OF VOLKOV-PANKRATOV STATES

Previous theoretical predictions of the universal presence of VP states on the smooth surface of topological material motivates an experimental hunting for these states. In the high mobility strained heterostructure HgTe/CdHgTe (3DTI), our collaborators at LPENS (Paris) [124] observed additional conductivity peaks and compressibility bumps in the bulk gap besides the ones attributed to the topological massless states [see Fig. 5.1(a)]. However, the results from transport measurement are only a partial proof for the existence of VP states. Strictly speaking, it only proves the existence of surface states other than the topological one. Surface states can generally arise at the interface of semiconductor heterostructures [152, 153]. Due to the mismatch of the valence and conduction bands between two semiconductors, the bulk states of the one with smaller gap induce surface states in the gap of the other semiconductor with larger gap. Another possible related mechanism is due to surface charges induced by the formation of defects on the surface [154]. Surface charges bend the bulk bands resulting in a confining potential at the surface and thus surface subbands. This effect was observed already in Si [155]. These could lead to false-alarms for the identification of VP states since the in-gap subbands also has a dispersion in the direction perpendicular to the surface so that not every spectroscopic method, for example, angle-resolved photoemission spectroscopy (ARPES) cannot provide an unambiguous proof [136, 156, 157] [see Fig. 5.1(b)].

Therefore, one must focus on unique features embedded in the wavefunction of VP states. An immediate proposal would be the particle-hole symmetry dictated by the duality between Dirac and Schrödinger equation, i.e., the supersymmetry. This is not the case for the surface states induced by the previous mechanisms. If the non-linear terms in k are considered, the particle-hole symmetry has a generalized version that VP states always emerge in pairs with opposite effective mass out of the bulk valence and conduction bands. The observation of this feature requires a very smooth surface or a large bulk gap so that none of the two VP states in pair is immersed in the bulk spectrum.²

The symmetry of the wavefunction of VP states provides an even stronger way to identify VP states. The matrix element in the definition of optical conductivity encodes precisely the symmetry of wave-

²However, the simultaneous appearance of conduction and valence subbands is still possible by surface band bending mechanism when the bulk bandwidth is small [158].

5.1 Optical conductivity: smoking gun for the existence of Volkov-Pankratov states

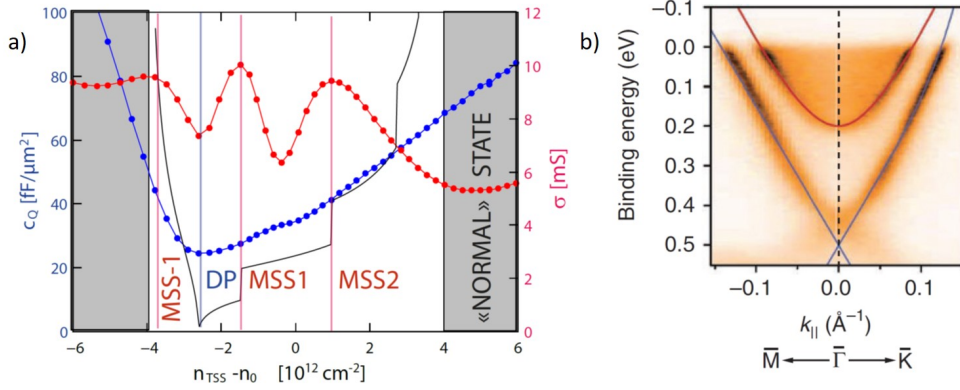


Figure 5.1: (a) Quantum capacitance and conductance data (blue-red data points in the heterostructure HgTe/CdHgTe) as a function of the surface electronic density. The latter is varied with the help of a backgate. VP states manifest as additional signals that cannot be attributed to the topological massless states. (b) ARPES data on the surface of Bi₂Se₃ several hours after cleavage reveal a 2D massive electron gas in addition to the topological 2D Dirac cone. Reminiscent of VP states formed due to a smoothing of the surface during the aging process, the data is also well fitted by the surface states induced by surface charges. Two figures adapted from the references [124, 136], respectively.

function. Since the smoothness is interpreted as a pseudo-magnetic field, some optical selection rules similar to those for the Landau levels in a real magnetic field should exist for the VP states. Furthermore, the interplay between smoothness and real magnetic field gives more defining features in the magneto-optical response of VP states that can further substantiate their presence. Therefore, the magneto-optical spectroscopy is believed to offer a clear-cut signature of VP states. This is indeed my original motivation to study the magneto-optical response from VP states.

In this section, I present first the calculated optical conductivity for the 2D toy model (4.10) in the presence and absence of a magnetic field. Only the real part of the diagonal terms in the optical conductivity tensor is given. While the calculation of the optical conductivity of edge states in the 2D model may be of limited experimental interest, it allows us to illustrate the basic effects. Then, the same calculations are also done for the more realistic, yet more involved 3DTI model (4.11). The use of the linearized models is justified since only optical transition between the surface states are considered and the bulk system is gapped. As I will strengthen the argument by calculations in the following, the transition between surface and bulk states will not wash out the key signature of the transition between surface states. Finally, I will briefly discuss the effect of an electric field perpendicular to the surface. The temperature is set to be zero ($T = 0$). For simplicity, I also suppose the chemical potential to coincide with the charge neutral point ($\mu = 0$).

5.1.1 TWO-DIMENSIONAL TOY MODEL

Consider a very smooth surface $\ell \gg \xi$ for the topological heterojunction modeled by the linearized 2D toy model (4.10) whose form after transformation I recall below:

$$H_T = THT^\dagger = \hbar v \begin{bmatrix} k_y & k_x + i\frac{x}{\ell\xi} \\ k_x - i\frac{x}{\ell\xi} & -k_y \end{bmatrix} \quad (5.1)$$

where the same notation as in Chapter 4 is adopted and k_y is a good quantum number. In the following calculations, I fix the characteristic length of the interface smoothness to be $\ell = 5\xi$ for illustrations.

The optical conductivity in the clean limit for this Hamiltonian is thus

$$\sigma_{ij}(\omega) = i\hbar e^2 \sum_{\substack{m,n \in \mathbb{N} \\ \lambda, \lambda'}} \int \frac{dk_y}{2\pi} \frac{f_D(E_n^\lambda) - f_D(E_m^{\lambda'})}{E_m^{\lambda'} - E_n^\lambda - \hbar\omega + i0^+} \frac{\langle \psi_m^{\lambda'} | \hat{v}_i | \psi_n^\lambda \rangle \langle \psi_m^{\lambda'} | \hat{v}_j | \psi_n^\lambda \rangle^*}{E_m^{\lambda'} - E_n^\lambda} \quad (5.2)$$

where $\lambda = \pm$ indicates if a band belongs to valence or conduction bands;³ the index $i, j = x, y$ represents the linear polarization of the photon;⁴ the two positive integers m, n are the band index and $|\psi_n^\lambda\rangle$ is the corresponding Bloch wavefunction;. Taking the real part of the optical conductivity, the diagonal term reads

$$\begin{aligned} \Re[\sigma_{ii}(\omega \neq 0)] &= \frac{\pi e^2}{\omega} \sum_{\substack{m,n \in \mathbb{N} \\ \lambda, \lambda'}} \int \frac{dk_y}{2\pi} [f_D(E_n^\lambda) - f_D(E_m^{\lambda'})] |\langle \psi_m^{\lambda'} | \hat{v}_i | \psi_n^\lambda \rangle|^2 \\ &\times \delta[\hbar\omega - (E_m^{\lambda'} - E_n^\lambda)] \end{aligned} \quad (5.3)$$

where δ is the Dirac distribution. As explained in Chapter 3, the matrix elements encode the selection rules and $\sum \delta[\hbar\omega - (E_m^{\lambda'} - E_n^\lambda)]$ is the joint density of states (JDOS), which determines the shape of the optical conductivity σ by the thumb rule

$$\sigma \sim \frac{\text{JDOS}}{\omega}. \quad (5.4)$$

Here, the Hamiltonian H_T (5.1) is in practice derived by $\mathbf{k} \cdot \mathbf{p}$ perturbation theory [26]. One should replace the ket $|\psi_n^\lambda\rangle$ by its cell-periodic part $|u_n^\lambda\rangle$. In the basis of $|u_n^\lambda\rangle$ and the velocity operator (see Chapter 3) thus reads

$$\hat{v}_{\mathbf{k}} = \frac{1}{\hbar} \nabla_{\mathbf{k}} H_{\mathbf{k}} \quad (5.5)$$

³One should not confound it with the chirality λ in Chapter 4.

⁴One should not confound it with the complex i at the beginning of the formula.

5.1 Optical conductivity: smoking gun for the existence of Volkov-Pankratov states

where $H_{\mathbf{k}}$ is the Bloch $\mathbf{k} \cdot \mathbf{p}$ Hamiltonian in the basis $|u_n^\lambda\rangle$. The analytical expressions of the optical conductivity are given in App. E.

In the following plots, I suppose a very smooth interface $\ell = 5\xi$ and I set the magnetic field (if present) to be $\ell_B = 1.5\ell_S$ which corresponds to $B = 20.8$ T if $2\Delta_0 = 0.3$ eV and $v = 2.5$ eV \cdot \AA . The parameters are of typical magnitude for Bi_2Se_3 [135, 136]. I choose a rather strong magnetic field for illustration, to render the shift of the peaks visible in the plots.

IN THE ABSENCE OF A MAGNETIC FIELD

When the magnetic field is absent, the spectrum of (5.1) reads

$$\begin{aligned} E_n^\lambda &= \lambda\hbar v \sqrt{k_y^2 + \frac{2n}{\ell_S^2}} && \text{if } n \geq 1 \\ E_0 &= \hbar v k_y && \text{if } n = 0, \end{aligned} \quad (5.6)$$

and the velocity operators are

$$\hat{v}_x = v\sigma_x \quad \text{and} \quad \hat{v}_y = v\sigma_z. \quad (5.7)$$

Since σ_x is off-diagonal and σ_z diagonal, the selection rules are different for the two polarizations:

$$\begin{aligned} \text{Polarization along } x: & && n \rightarrow n \pm 1 \\ \text{Polarization along } y: & && n \rightarrow n, \end{aligned}$$

so that the absorption spectra depend on the polarization of the incident photon. The off-diagonal elements of the conductivity must vanish, $\sigma_{xy} = \sigma_{yx} = 0$, for the selection rules are incompatible for the two polarizations. Being a 2D Hamiltonian in the 3D space, photons that can interact with the system propagate in the out-of-plane direction to probe the surface states. The above selection rules match with those in the Voigt geometry (see in Chapter 3) in the presence of a magnetic field in the y -direction, justifying the analogy of smoothness with magnetic field.

As shown in Fig. 5.2 by the blue lines, the real part of optical conductivity consists of a series of peaks with decaying tail to higher frequency. The decreasing rate is proportional to $\omega^{-\frac{3}{2}}$ as expected for the optical conductivity of a 1D massive Dirac band (see in Chapter 3) since the DOS of a 1D parabolic band scales as $\omega^{-\frac{1}{2}}$ and the definition of optical conductivity contributes the other ω^{-1} . The onsets of the peaks indicates the optical gap of different transitions. For $\Re[\sigma_{xx}]$ [see blue lines in Fig. 5.2(a)], except the first step-like peak, all the peaks represent singularities in the clean limit because

5 Spectroscopic properties of Volkov-Pankratov states

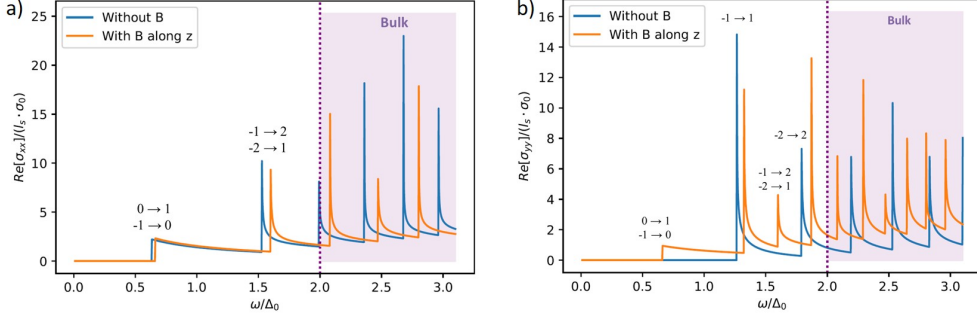


Figure 5.2: (a) $\Re[\sigma_{xx}]$ and (b) $\Re[\sigma_{yy}]$ for the 2D model, in the absence (blue) and presence (orange) of a magnetic field, measured in units of $\sigma_0 = e^2/h$, while the excitation energy is represented in units of Δ_0 . The sharp peaks are singularities and their corresponding optical transitions are labeled above. The dashed perpendicular line denotes the onset of absorption by bulk states, for $\omega \geq 2\Delta_0$. The peaks in the purple shaded area are immersed in the bulk spectrum and thus cannot be seen experimentally.

the interband transition between VP states at $k_y = 0$ has a diverging JDOS. They have different heights because of finite mesh points in the plot. The first regular peak originates from the transition between the massless $n = 0$ topological state and the $n = 1$ VP state whose JDOS is not diverging thanks to the chiral linear dispersion of the topological state. This is also the reason why its decay rate of the tail is slower. Similar to $\Re[\sigma_{xx}]$, $\Re[\sigma_{yy}]$ [see blue lines in Fig. 5.2(b)] has the same shape of peaks placed at different frequencies because of the different selection rules. Since optical transitions involving the massless state are forbidden by the selection rule $n \rightarrow n$, all the peaks are singular for the 1D diverging JDOS of the VP bands.

While the diverging peaks at high frequency are immersed in the bulk continuum represented by the purple shaded area, the peaks in the gap are supposed to be observable. Especially, thanks to the polarization-dependent selection rules, one can continuously measure the optical conductivity, for example from $\Re[\sigma_{xx}]$ to $\Re[\sigma_{yy}]$, by rotating the linear polarization of photon. The selection rules are a manifestation of the pseudo-magnetic field interpretation of the origin of VP states, unlike any other defect-induced trivial in-gap surface states. Therefore, this can serve as a smoking gun for the unequivocal identification of VP states.

IN THE PRESENCE OF A MAGNETIC FIELD PARALLEL TO THE INTERFACE

The application of a real magnetic field offers richer features of VP states helping to understand further the similarities and differences between smoothness and magnetic field. Since the Hamiltonian (5.1) describes a 2D system, only an out-of-plane magnetic field is relevant. By the Peierls substitution, one chooses the Landau gauge $\mathbf{A} = (0, Bx, 0)$ with ($B > 0$) to preserve the translational invariance along the y -axis. After replacing k_y by $k_y + x/\ell_B^2$, where $\ell_B = \sqrt{\hbar/eB}$ is the magnetic length, one

5.1 Optical conductivity: smoking gun for the existence of Volkov-Pankratov states

clearly notices here the similarity between the smoothness via the linear variation of the gap and the magnetic field: both couple linearly to the space coordinate of the x -direction, but through different Pauli matrices. The Hamiltonian (5.1) then becomes

$$H = \hbar v \frac{x}{\ell_T^2} (\sin \theta \sigma_z - \cos \theta \sigma_y) + \hbar v (k_x \sigma_x + k_y \sigma_z) \quad (5.8)$$

where a characteristic length ℓ_T and an angle θ are defined by

$$\frac{1}{\ell_T^4} = \frac{1}{\ell_S^4} + \frac{1}{\ell_B^4} \quad \Longleftrightarrow \quad B_{\text{tot}}^2 = B_{\text{pseudo}}^2 + B_{\text{real}}^2 \quad (5.9a)$$

$$\cos \theta = \frac{\ell_T^2}{\ell_S^2} \quad (5.9b)$$

$$\sin \theta = \frac{\ell_T^2}{\ell_B^2}. \quad (5.9c)$$

With this form, the recipe given in Chapter 2 shows that the unitary transformation $T = \exp(i\theta\sigma_x/2)$ simplifies further the Hamiltonian to:

$$H_T = \hbar v \begin{bmatrix} k_y \cos \theta & k_x + i \left(\frac{x}{\ell_T^2} + k_y \sin \theta \right) \\ k_x - i \left(\frac{x}{\ell_T^2} + k_y \sin \theta \right) & -k_y \cos \theta \end{bmatrix}. \quad (5.10)$$

such that one can diagonalize the Hamiltonian again with the help of a pair of ladder operators,

$$\hat{a}^\dagger = \frac{\ell_T}{\sqrt{2}} \left[k_x + i \left(\frac{x}{\ell_T^2} + k_y \sin \theta \right) \right] \quad (5.11a)$$

$$\hat{a} = \frac{\ell_T}{\sqrt{2}} \left[k_x - i \left(\frac{x}{\ell_T^2} + k_y \sin \theta \right) \right] \quad (5.11b)$$

that satisfy $[\hat{a}, \hat{a}^\dagger] = 1$. The spectrum of this Hamiltonian thus reads

$$\begin{aligned} E_n^\lambda &= \lambda \hbar v \sqrt{k_y^2 \cos^2 \theta + \frac{2n}{\ell_T^2}} & \text{if } n \geq 1 \\ E_0 &= \hbar v k_y \cos \theta & \text{if } n = 0 \end{aligned} \quad (5.12)$$

where $\lambda = \pm$. Comparing this result to that in the absence of a magnetic field (5.6), the velocity of the massless $n = 0$ state is contracted by a factor of $\cos \theta$ and the spacing between the bands is amplified because the characteristic length ℓ_T , which assembles the influence from smoothness and magnetic

field, is strictly smaller than ℓ_S . The definition of an angle θ suggests that the smoothness and the magnetic field are two perpendicular components of a total magnetic field in the direction defined by θ with respect to the plane. This is compatible with what is suggested before. The total magnetic field is geometrically composed of a pseudo-magnetic field in the y -direction and a real magnetic field in the z -direction.

However, the statement is not true in all the aspects because the selection rules

$$\begin{aligned} \text{Polarization along } x: & & n \rightarrow n \pm 1 \\ \text{Polarization along } y: & & n \rightarrow n \quad \text{and} \quad n \rightarrow n \pm 1 \end{aligned}$$

disprove it. A magnetic field along the direction neither parallel nor perpendicular to the polarization of photon should not only allow the transition $n \rightarrow n \pm 1$. The result can be understood in the following manner. The velocity operators associated with the Hamiltonian (5.10) are,

$$\hat{v}_x = v\sigma_x \quad \text{and} \quad \hat{v}_y = v \cos \theta \sigma_z - v \sin \theta \sigma_y, \quad (5.13)$$

and the unitary transformation T thus mixes the σ_y - and σ_z -components of the Hamiltonian so that \hat{v}_y acquires an off-diagonal part while \hat{v}_x is untouched. The selection rules for the polarization in the x -direction are therefore unaffected by the magnetic field while those in the y -direction acquires an additional dipolar component $n \rightarrow n \pm 1$. For the same reason, the conductivity tensor is *a priori* not diagonal.

The real part of the optical conductivity in the presence of a magnetic field is represented by orange lines in Fig. 5.2. Comparing with those in the absence of a magnetic field, the peaks in the presence of a magnetic field have the same shape but the spacing between the two nearest peaks is larger. This reflects the enhanced spacing at $k_y = 0$ of the surface bands [see Eq. (5.12)]. Furthermore, one notices that the optical conductivity is larger when the magnetic field is switched on. This is due to the band dispersion that is contracted by $\cos \theta$, in other words, the JDOS is enhanced by the same amount. As a consequence of the supplementary $n \rightarrow n \pm 1$ selection rules due to the unitary transformation, additional peaks appear in $\Re[\sigma_{yy}]$ at the same energies of the peaks in $\Re[\sigma_{xx}]$. These peaks are all the more intense for a stronger magnetic field. Indeed, one can retrieve the selection rules $n \rightarrow n \pm 1$ for both polarization, x and y , matched with those in the Faraday geometry by taking $B \rightarrow \infty$ for which the quantization by smoothness is totally washed out.

In spite of the simplicity of the 2D toy model, it is already informative about the key signatures of the optical responses from VP states, i.e., the specific selection rules similar to those for Landau levels in a real magnetic field. Applying a real magnetic field does not change radically the shape of

5.1 Optical conductivity: smoking gun for the existence of Volkov-Pankratov states

the signals but mixes the selection rules and shifts the peaks. This is due to the alliance between the smoothness and the magnetic field, which is encoded in ℓ_T . Therefore, the intricate interplay between interface smoothness and magnetic field allows in principle for a detailed experimental identification and investigation of VP states. As shown later, the results of the 2D model can be easily extended to the realistic 3DTI model.

5.1.2 THREE-DIMENSIONAL TOPOLOGICAL INSULATOR

Proceeding exactly the same way as for 2D toy model, the matrix form of the Hamiltonian (4.11) after a unitary transformation $T = \exp(i\pi\tau_y/4)$ reads

$$H = \hbar v \begin{bmatrix} 0 & k_y + ik_x & \frac{\sqrt{2}}{\ell_S} \hat{a} & 0 \\ k_y - ik_x & 0 & 0 & \frac{\sqrt{2}}{\ell_S} \hat{a} \\ \frac{\sqrt{2}}{\ell_S} \hat{a}^\dagger & 0 & 0 & -k_y - ik_x \\ 0 & \frac{\sqrt{2}}{\ell_S} \hat{a}^\dagger & -k_y + ik_x & 0 \end{bmatrix} \quad (5.14)$$

where the wavevector components $k_{x,y}$ remain good quantum numbers and the ladder operators \hat{a} and \hat{a}^\dagger are defined as

$$\hat{a}^\dagger = -\frac{\ell_S}{\sqrt{2}} \left(\frac{z}{\ell_S^2} - ik_z \right) \quad (5.15a)$$

$$\hat{a} = -\frac{\ell_S}{\sqrt{2}} \left(\frac{z}{\ell_S^2} + ik_z \right) \quad (5.15b)$$

with $[\hat{a}, \hat{a}^\dagger] = 1$.

The optical conductivity in the clean limit for this Hamiltonian is

$$\sigma_{ij}(\omega) = i\hbar e^2 \sum_{\substack{m,n \in \mathbb{N} \\ \lambda, \lambda'}} \iint \frac{dk_x dk_y}{4\pi^2} \frac{f_D(E_n^\lambda) - f_D(E_m^{\lambda'})}{E_m^{\lambda'} - E_n^\lambda - \hbar\omega + i0^+} \frac{\langle \psi_m^{\lambda'} | \hat{v}_i | \psi_n^\lambda \rangle \langle \psi_m^{\lambda'} | \hat{v}_j | \psi_n^\lambda \rangle^*}{E_m^{\lambda'} - E_n^\lambda} \quad (5.16)$$

where the index for the polarization of photon now runs over the three components $i, j = x, y, z$, and the other notations have the same meaning as for the 2D toy model. Taking the real part of the diagonal term of the conductivity tensor, one has

$$\begin{aligned} \Re[\sigma_{ii}(\omega \neq 0)] &= \frac{\pi e^2}{\omega} \sum_{\substack{m,n \in \mathbb{N} \\ \lambda, \lambda'}} \int \frac{dk_x dk_y}{4\pi^2} [f_D(E_n^\lambda) - f_D(E_m^{\lambda'})] |\langle \psi_m^{\lambda'} | \hat{v}_i | \psi_n^\lambda \rangle|^2 \\ &\quad \times \delta[\hbar\omega - (E_m^{\lambda'} - E_n^\lambda)]. \end{aligned} \quad (5.17)$$

5 Spectroscopic properties of Volkov-Pankratov states

For the reasons explained previously for 2D toy model, one should replace the ket $|\psi_n^\lambda\rangle$ by its periodic part $|u_n^\lambda\rangle$ and the velocity operators are just \mathbf{k} -derivatives of the Bloch Hamiltonian. The analytic results of the optical conductivity are given in the supplementary material of our work [159].

As for the 2D toy model, the following figures are plotted with a very smooth interface $\ell = 5\xi$.

IN THE ABSENCE OF A MAGNETIC FIELD

The spectrum of (5.1) is obtained by diagonalizing it in the harmonic oscillator wavefunctions:

$$\begin{aligned} E_n^\lambda &= \lambda\hbar v \sqrt{k_x^2 + k_y^2 + \frac{2n}{\ell_S^2}} & \text{if } n \geq 1 \\ E_0^\lambda &= \lambda\hbar v \sqrt{k_x^2 + k_y^2} & \text{if } n = 0 \end{aligned} \quad (5.18)$$

where the $n = 0$ state represents precisely the famed single Dirac cone on the surface of a 3DTI and the $n \geq 1$ states are the massive VP states which are twice spin-degenerate. The velocity operators are

$$\hat{v}_z = v\tau_y, \quad \hat{v}_x = -v\tau_z\sigma_y \quad \text{and} \quad \hat{v}_y = v\tau_z\sigma_x. \quad (5.19)$$

Since τ_y is off-diagonal and τ_z diagonal, the selection rules for the polarization in the z -direction are different from those for the polarization in the x, y -directions as shown below

$$\begin{aligned} \text{Polarization along } z: & & n \rightarrow n \pm 1 \\ \text{Polarization along } x, y: & & n \rightarrow n. \end{aligned}$$

The selection rules in the absence of a magnetic field in the 3DTI model are similar to the 2D model where $n \rightarrow n \pm 1$ for the polarization perpendicular to the interface and $n \rightarrow n$ for that parallel to the interface. The selection rules for the polarization in the x - and y -directions must be identical due to the rotational symmetry of the Hamiltonian around the z -axis. Unlike the 2D toy model, the polarization-dependent selection rules cannot fit in any configuration of a real magnetic field, neither Faraday nor Voigt, since the two polarizations have the $n \rightarrow n$ rule. It again shows the intrinsic difference between smoothness and magnetic field.

Fig. 5.3 shows the optical conductivity in the absence of a magnetic field for different polarizations. The singularities in the 2D toy model become finite step-like peaks in the 3DTI model. This is due to the change in the dimensionality of the surface bands. Their 2D character now yields an essentially flat JDOS and thus steps in the conductivity that decays as ω^{-1} . In $\Re[\sigma_{zz}]$ [see Fig. 5.3(c)], the response from the $0 \rightarrow 1$ and $-1 \rightarrow 0$ transition has different forms from others due to the DOS of the

5.1 Optical conductivity: smoking gun for the existence of Volkov-Pankratov states

$n = 0$ band scaling as ω . The behavior of the $n = 0$ DOS has an even more spectacular manifestation in $\Re[\sigma_{xx,yy}]$ where the $0 \rightarrow 0$ transition is allowed [see Fig. 5.3(a,b)]. The additional ω^{-1} factor in the Kubo formula thus yields a constant optical conductivity, as it is known for graphene, where the frequency-independent absorption is given in terms of the fine-structure constant $\alpha \simeq 1/137$ of quantum electrodynamics [111, 160]. In fact, this is the signature of the optical transition in the 2D Dirac cone. This constant optical conductivity can be expressed only by the intrinsic physical constant:

$$\sigma_c = \frac{\pi}{8} \sigma_0 \quad (5.20)$$

for a single cone, with $\sigma_0 = e^2/h$.

IN THE PRESENCE OF A MAGNETIC FIELD PARALLEL TO THE INTERFACE

Suppose now that a magnetic field is applied parallel to the interface, for example, in the x -direction. For illustration purposes, I have chosen a field strength so that $\ell_B = 1.5\ell_S$. Choosing the gauge $\mathbf{A} = (0, -Bz, 0)$, the Hamiltonian (5.14) after the Peierls substitution becomes:

$$H = -\hbar v \left(\frac{z}{\ell_S^2} \tau_x + \frac{z}{\ell_B^2} \tau_z \sigma_x \right) + \hbar v k_z \tau_y + \hbar v \tau_z (k_y \sigma_x - k_x \sigma_y). \quad (5.21)$$

After a unitary transformation $T = \exp(-i\theta\tau_y\sigma_x/2)$ found by the recipe given in Chapter 2, the Hamiltonian reads:

$$H_{B_x} = \hbar v \begin{bmatrix} 0 & k_y \cos \theta + ik_x & \frac{\sqrt{2}}{\ell_T} \hat{a} & 0 \\ k_y \cos \theta - ik_x & 0 & 0 & \frac{\sqrt{2}}{\ell_T} \hat{a} \\ \frac{\sqrt{2}}{\ell_T} \hat{a}^\dagger & 0 & 0 & -k_y \cos \theta - ik_x \\ 0 & \frac{\sqrt{2}}{\ell_T} \hat{a}^\dagger & -k_y \cos \theta + ik_x & 0 \end{bmatrix} \quad (5.22)$$

where the angle θ is the same as the one introduced in Eq. (5.9) and the ladder operators are defined as

$$\hat{a}^\dagger = \frac{\ell_T}{\sqrt{2}} \left(k_y \sin \theta - \frac{z}{\ell_T^2} + ik_z \right) \quad (5.23a)$$

$$\hat{a} = \frac{\ell_T}{\sqrt{2}} \left(k_y \sin \theta - \frac{z}{\ell_T^2} - ik_z \right) \quad (5.23b)$$

5 Spectroscopic properties of Volkov-Pankratov states

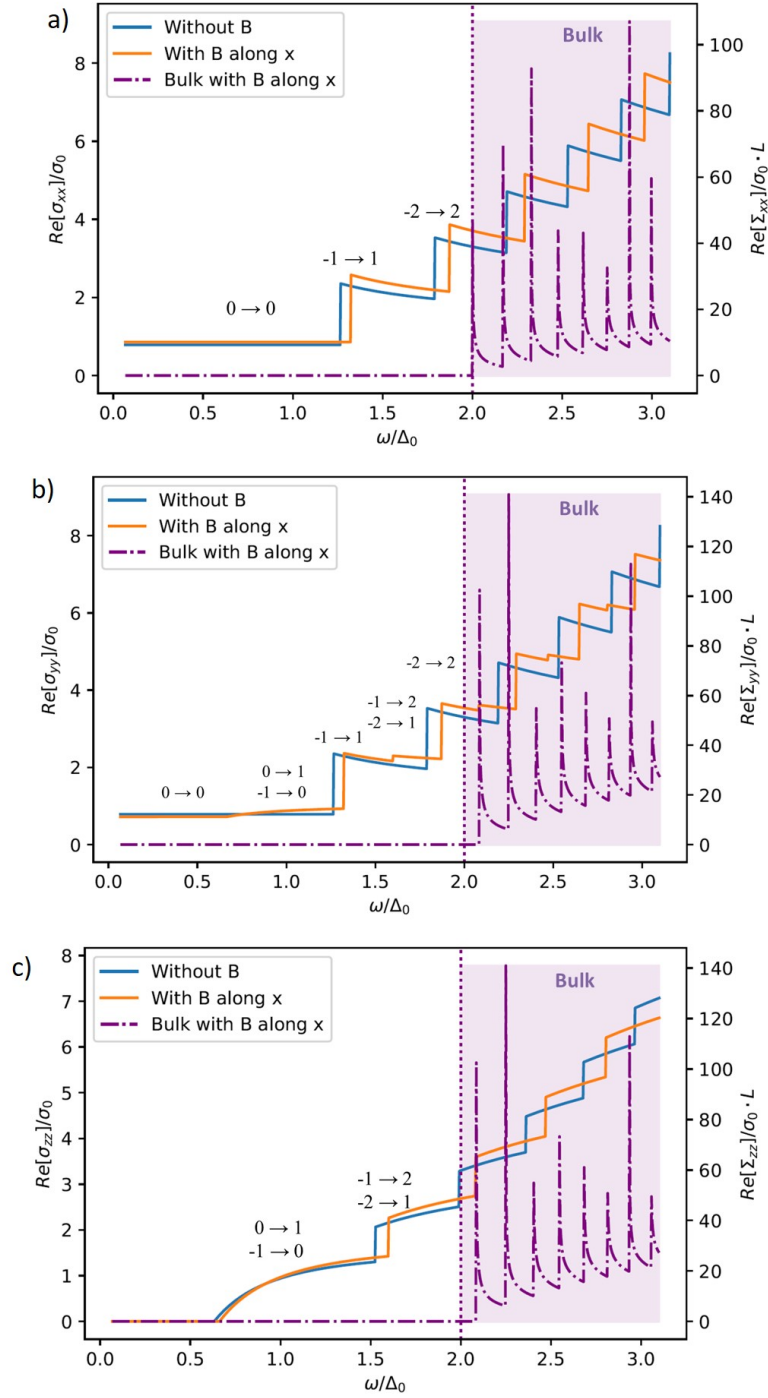


Figure 5.3: (a) $\Re[\sigma_{xx}]$, (b) $\Re[\sigma_{yy}]$ and (c) $\Re[\sigma_{zz}]$ for the 3DTI model, in the absence (blue) and presence (orange) of a parallel magnetic field given $\ell_B = 1.5\ell_S$, measured by unity of $\sigma_0 = e^2/h$ and excitation energy by the half bulk gap. The corresponding optical transitions of each peak are labeled above. The blue and orange peaks in the light-purple shaded area, where the bulk responses are plotted as purple dot-dashed line, are immersed in the bulk responses and thus cannot be seen experimentally.

5.1 Optical conductivity: smoking gun for the existence of Volkov-Pankratov states

which satisfy $[\hat{a}, \hat{a}^\dagger] = 1$. The spectrum of this Hamiltonian is

$$\begin{aligned} E_n^\lambda &= \lambda \hbar v \sqrt{k_x^2 + k_y^2 \cos^2 \theta + \frac{2n}{\ell_T^2}} & \text{if } n \geq 1 \\ E_0^\lambda &= \lambda \hbar v \sqrt{k_x^2 + k_y^2 \cos^2 \theta} & \text{if } n = 0 \end{aligned} \quad (5.24)$$

where $\lambda = \pm$. The impact of a parallel magnetic field in the 3D model is similar to that in the 2D model. The velocity of the massless topological state is contracted by a factor of $\cos \theta$ along k_y while the dispersion in the k_x -direction (that is the direction of the magnetic field) is unaffected. The equi-energy profile of the Dirac cones becomes oval and the spacing between the Landau bands increases since the characteristic length ℓ_T is shorter than ℓ_S as discussed in the 2D toy model.

The effect of a parallel magnetic field in the 3D model on the selection rules is also similar to the 2D model as shown below:

$$\begin{aligned} \text{Polarization along } z: & & n \rightarrow n \pm 1 \\ \text{Polarization along } x: & & n \rightarrow n \\ \text{Polarization along } y: & & n \rightarrow n \quad \text{and} \quad n \rightarrow n \pm 1. \end{aligned}$$

It mixes the rules $n \rightarrow n \pm 1$ and $n \rightarrow n$ for the photon polarized along the y -axis, while those in the x, z -directions remain the same as in the absence of a magnetic field. This also can be understood in terms of the unitary transformation $T = \exp(-i\theta\tau_y\sigma_x/2)$ that adds a new Pauli matrix in \hat{v}_y . Indeed, the velocity operators now read

$$\hat{v}_z = v\tau_y, \quad \hat{v}_x = -v\tau_z\sigma_y \quad \text{and} \quad \hat{v}_y = v \cos \theta \tau_z \sigma_x + v \sin \theta \tau_x. \quad (5.25)$$

As shown in Fig. 5.3 by orange lines, the enhanced level spacing yields a shift of the the optical conductivity to higher energy. The plateau in $\Re[\sigma_{xx}]$ [see Fig. 5.3(a)] before the first peak is also enhanced in a magnetic field with

$$\sigma_{cB} = \frac{\sigma_c}{\cos \theta} = \frac{\ell_S^2}{\ell_T^2} \sigma_c. \quad (5.26)$$

Furthermore, $\Re[\sigma_{yy}]$ acquires additional peaks as a consequence of the unitary transformation that admixes a σ_{zz} component to $\Re[\sigma_{yy}]$ [see Fig. 5.3(b)]. As in the 2D toy model, a parallel magnetic field does not change radically the shape of the optical conductivity but mixes the selection rules and shifts the peaks.

IN THE PRESENCE OF A MAGNETIC FIELD PERPENDICULAR TO THE INTERFACE

Since the system is 3D, it is physically relevant to apply a magnetic field perpendicular to the interface, i.e., in the z -direction. For example, I set here $\ell_B = 2.15\ell_S$.⁵ The situation changes drastically. Taking a gauge $\mathbf{A} = (0, Bx, 0)$ to apply a magnetic field $\mathbf{B} = B\mathbf{e}_z$ ($B > 0$), the Hamiltonian (5.14) becomes

$$H_{B_z} = \sqrt{2}\hbar v \begin{bmatrix} 0 & \frac{\hat{b}}{\ell_B} & \frac{\hat{a}}{\ell_S} & 0 \\ \frac{\hat{b}^\dagger}{\ell_B} & 0 & 0 & \frac{\hat{a}}{\ell_S} \\ \frac{\hat{a}^\dagger}{\ell_S} & 0 & 0 & -\frac{\hat{b}}{\ell_B} \\ 0 & \frac{\hat{a}^\dagger}{\ell_S} & -\frac{\hat{b}^\dagger}{\ell_B} & 0 \end{bmatrix} \quad (5.27)$$

where \hat{a} and \hat{a}^\dagger are defined in (5.14) and the applied magnetic field yields now a second pair of ladder operators:

$$\hat{b}^\dagger = \frac{\ell_B}{\sqrt{2}} \left(k_y - ik_x + \frac{x}{\ell_B^2} \right) \quad (5.28a)$$

$$\hat{b} = \frac{\ell_B}{\sqrt{2}} \left(k_y + ik_x + \frac{x}{\ell_B^2} \right), \quad (5.28b)$$

which satisfy $[\hat{b}, \hat{b}^\dagger] = 1$. Note that the operators \hat{a} and \hat{b} act on the two orthogonal directions so they commute with each other. In other words, they yield two independent quantum numbers n and m . The velocity operators are still given by Eq. (5.19), and the spectrum of this Hamiltonian reads

$$E_{n,m}^\lambda = \lambda\hbar v_F \sqrt{\frac{2n}{\ell_S^2} + \frac{2m}{\ell_B^2}} \quad (5.29)$$

where $\lambda = \pm$ and $n, m \in \mathbb{N}$. One notices that the spectrum is now completely quantized by the two effects, smoothness and perpendicular magnetic field, and labeled by the two decoupled quantum numbers, n and m , respectively. As explained in Chapter 4, smoothness as a quantum confinement effect quantizes the motion only in the z -direction while magnetic field quantizes the motion in the x, y -directions. Comparing (5.29) with (5.24), one can already anticipate that the optical conductivity for a dispersionless energy spectrum consists of a series of Dirac peaks with no tail. To calculate the optical conductivity, one should replace the integral of $k_{x,y}$ in Eq. (5.17) by the density of magnetic flux quanta $n_B = eB/h$.

⁵This choice for the magnitude of the magnetic field allows the readers to clearly associate the optical response with their corresponding interband transition.

5.1 Optical conductivity: smoking gun for the existence of Volkov-Pankratov states

It is instructive to juxtapose the selection rules for the two quantum numbers n and m according to the polarization of photon as shown below:

$$\begin{array}{lll} \text{Polarization along } z: & m \rightarrow m, & n \rightarrow n \pm 1 \\ \text{Polarization along } x, y: & n \rightarrow n, & m \rightarrow m \pm 1. \end{array}$$

One finds the usual selection rules for transitions between the Landau levels under magnetic field for the quantum number m , while the quantum number n describing the smoothness as a pseudo-magnetic field respects a different but complementary set of selection rules. This underlines that smoothness and magnetic field are two distinct quantization fields. Since the selection rules are incompatible for the two sets of polarization, the tensor σ_{ij} is diagonal.

The results of our analytical calculations are shown in Fig. 5.4. One does not have to depict $\Re[\sigma_{yy}]$, which is identical to $\Re[\sigma_{xx}]$ because the perpendicular magnetic field does not break the isotropy in the $x - y$ plane. Since the spectrum (5.29) is now composed of discrete energy levels, the optical conductivity consists of a set of Dirac peaks that are represented by Lorentzian functions of finite width for visibility. The width of the Lorentzian function encodes phenomenologically the peak broadening by disorders. For a magnetic field such that $\ell_B \gg \ell_S$, one should identify different groups among all the Dirac peaks. To illustrate this phenomenon, I plot separately different groups of peaks in different colors so that the whole optical conductivity should be the sum of all peaks. For $\Re[\sigma_{zz}]$ [see Fig. 5.4(b)], the blue peaks correspond to the transition between the $n = 0$ and $n = 1$ levels and the orange peaks to the transition between $n = 1$ and $n = 2$. Each of these transitions which are associated with smoothness is now split into additional $m \rightarrow m$ transitions that are separated by a characteristic energy of $\hbar v / \ell_B$ due to Landau level quantization by the physical magnetic field. The two groups of peaks are interleaved with each other like two hair combs. Likewise, for $\Re[\sigma_{zz}]$ [see Fig. 5.4(a)], the blue peaks correspond to the transition between the $n = 0$ levels, the orange peaks to the transition between the $n = 1$ levels and the green ones to the transition between the $n = 2$ levels. More and more peaks will overlap if n is increased.

In this part, I have discussed the effect of a parallel and perpendicular magnetic field to the interface. If magnetic field is along an arbitrary direction, it can always be decomposed to a component perpendicular to the interface and the other component parallel to the interface. Suppose that the magnetic field forms an angle ϕ with respect to the interface plane. By using the gauge $\mathbf{A} = (0, Bx \sin \phi - Bz \cos \phi, 0)$, the problem is divided into the two problems whose solution I have already provided.

Besides the in-gap features shared also by the 2D toy model, the optical conductivity in the 3DTI model depend crucially on the orientation of the magnetic field. A magnetic field parallel to the inter-

5 Spectroscopic properties of Volkov-Pankratov states

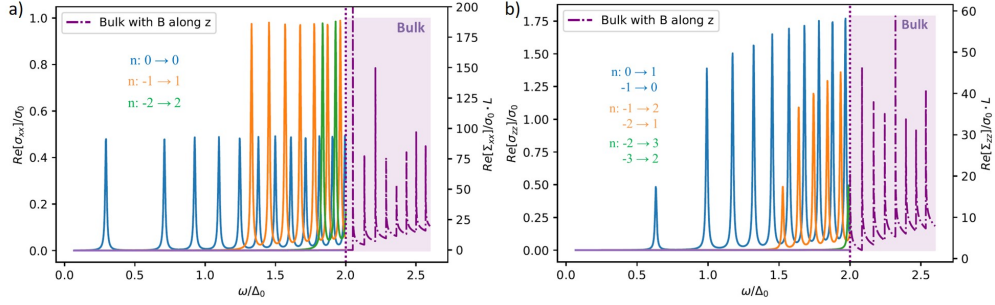


Figure 5.4: Different groups of signal of (a) $\Re[\sigma_{xx}]$ and (b) $\Re[\sigma_{zz}]$ for 3D model in the presence of a perpendicular magnetic field given $\ell_B = 2.15\ell_S$, measured by unity of $\sigma_0 = \frac{e^2}{h}$ and excitation energy by half of the bulk gap Δ_0 . I make Dirac distributions visible by replacing them by Lorentzian functions with width 0.001 which can be seen as broadening effects by finite temperature or disorders. Different groups of peaks are colored and their corresponding optical transitions are labeled. The bulk signals are plotted as purple dot-dashed line. The surface signal which are immersed in the bulk spectrum cannot be seen experimentally.

face simply changes the position of the peaks and slightly modifies the optical selection rules, whereas a magnetic field perpendicular to the interface fully quantizes the surface bands and thus yields prominent peaks. The orientation of magnetic field is therefore an excellent probe of both massless and massive surface states. Therefore, the other perspicuous way to reveal the VP states by magneto-optical spectroscopy is to monitor the spectra of absorption while rotating the magnetic field from parallel to perpendicular direction. The shape of the optical conductivity will evolve continuously from a step-like function of photon energy into a series of Lorentzian peaks during this rotation. This transformation of the shape of the optical conductivity by rotating the magnetic field is a smoking gun to distinguish the VP states from other in-gap surface states.

5.1.3 BULK-SURFACE TRANSITIONS

The surface-to-surface transitions are not the only contribution to the optical response below the gap. Optical transitions are also possible between delocalized bulk states and localized surface states. These transitions also yield the sub-gap signal in the optical conductivity. Thus, it is necessary to consider the relative magnitude of the bulk-surface transitions compared to the surface-surface transitions and their modification to the shape of the optical conductivity. Here, I numerically calculate the optical conductivity of the bulk-surface transitions for a topological heterojunction modeled by (5.14) in the absence of a magnetic field. The conclusions are general for other systems hosting VP states.

To treat this problem, I model the bulk states as plane waves [161] considering an interface in the z -direction at $z = 0$ between two very large systems of size $L \gg \ell$ so that one can still model it by a single topological heterojunction. Although the bulk spectrum of these two systems is exactly the same, their

5.1 Optical conductivity: smoking gun for the existence of Volkov-Pankratov states

eigenstates which encode their topological properties are certainly different. So, one has to separate the space into two parts, $z > 0$ and $z < 0$ to calculate the overlap between the wave-functions. The Kubo formula reads:

$$\sigma_{ij}(\omega) = i\hbar e^2 L \sum_{\substack{n \in \mathbb{N} \\ (n, \lambda, \lambda')}} \iiint \frac{dk_x dk_y dk_z}{8\pi^3} \frac{f_D(E_n^\lambda) - f_D(E^{B, \lambda'})}{E^{B, \lambda'} - E_n^\lambda - \hbar\omega + i0^+} \frac{\langle \psi_B^{\lambda'} | \hat{v}_i | \psi_n^\lambda \rangle \langle \psi_B^{\lambda'} | \hat{v}_j | \psi_n^\lambda \rangle^*}{E^{B, \lambda'} - E_n^\lambda} \quad (5.30)$$

where the superscript B for energy means the energy of the bulk. Note that the optical conductivity is still for two dimensions even though one considers here a 3D system. Since the bulk states are inherently 3D and the surface states are essentially 2D, one should limit the definition of the optical conductivity in 2D in order to have compatibility in the thermodynamic limit. Therefore, L in the prefactor is crucial because the matrix elements have another factor of $1/L$ from the normalization of the bulk states. As a result, the final expression of the optical conductivity for the bulk-surface transitions is in the unit of e^2/h and independent of the size of the bulk. This also allows one to compare its magnitude with the magnitude of the surface-surface transitions.

Suppose as before that the chemical potential is at the charge neutral point, the temperature is zero and $\ell = 5\xi$. As shown in Fig. 5.5, the contribution from bulk-surface transitions starts to be visible at the half band gap ($\omega \approx \Delta_0$) and it is a continuous function of photon energy with three kink spots. Each of the kink spots is the onset of one kind of transitions. For example, the first one is due to the transition between the bulk states and the chiral states and the second one stems from the transition between the bulk states and the $n = 1$ massive VP states. Only three kinks exist because only one massless state and two massive VP states are present in the band gap. Fortunately, even though the magnitude of the bulk-surface transition is not negligible as compared to that of the surface-surface transition especially for energy near the gap, the total optical conductivity still has step-like feature thanks to the continuity of the bulk-surface contribution as a function of photon energy.

In the optical conductivity from the transition between two states with dispersion of different dimensions, the singularities from lower-dimensional states are integrated out due to higher dimensional state. This is due to the fact that the JDOS, which determines the functional shape of the optical conductivity, has a higher-dimensional behavior. For example, when one considers a transition from a 2D surface state to a 3D bulk one, the JDOS is $\sum \delta[\hbar\omega - E_{3D}(\mathbf{k}_{3D}) + E_{2D}(\mathbf{k}_{2D})]$ so that the JDOS is essentially 3D. Comparing the contribution of bulk-surface transitions and that of surface-surface ones in Fig. 5.5, the step-like feature from 2D surface states are smeared out by integrating k_z , a parameter for 3D bulk states [see Eq. (5.30)]. Thus, the bulk-surface contribution is a continued function of energy but with kinks with no jumps (see orange lines in Fig. 5.5).

5 Spectroscopic properties of Volkov-Pankratov states

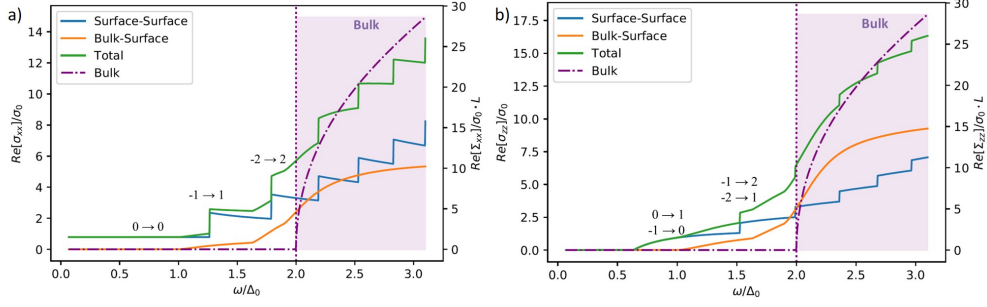


Figure 5.5: Different contributions in (a) $\Re[\sigma_{xx}]$ and (b) $\Re[\sigma_{zz}]$ for 3D model for $\ell = 5\xi$: surface-surface (blue), bulk-surface (orange) and total contribution (green), measured by unity of $\sigma_0 = \frac{e^2}{h}$ and excitation energy by the half bulk gap. The bulk signals are plotted as purple dot-dashed line. The signal which are immersed in the bulk spectrum cannot be seen experimentally.

Similar arguments should also apply to the case in the presence of a perpendicular magnetic field where the surface states are 0D, i.e., dispersionless, and the bulk states are 1D. The total optical conductivity should have additional one-dimensional band contributions with onsets at energies corresponding to the bulk-surface transitions. However, the hair-comb-like shape should still be visible and thus remains a valid signature for the identification of VP states. More interestingly, in the presence of a parallel magnetic field, the surface states are 2D whereas the bulks states are 1D. As a result, the contribution from the bulk-surface transition is a series of steps. Therefore, additional steps will appear in the total conductivity. This is indeed another spectroscopic signature of the VP states.

To conclude, the features of the VP states in magneto-optical spectroscopy due to the surface-surface transition are still palpable even the bulk-surface transitions are considered.

5.1.4 ELECTRIC FIELD PERPENDICULAR TO THE INTERFACE: RELATIVISTIC RENORMALIZATION

I briefly discuss in this part the case of an electric field perpendicular to the interface. In a topological heterojunction modeled by 3DTI, the Hamiltonian including an electric field \mathcal{E} in the z -direction reads

$$H = e\mathcal{E}z\mathbb{I} + \hbar vk_z\tau_y + \hbar v\tau_z(k_y\sigma_x - k_x\sigma_y) - \Delta_0\frac{z}{\ell}\tau_x \quad (5.31)$$

where \mathbb{I} is the identity matrix. Here, I define not only $\ell_S = \sqrt{\ell\xi}$ characterizing the smoothness but also a length characterizing the electric field $\ell_{\mathcal{E}} = \sqrt{\hbar v/e\mathcal{E}}$. The Hamiltonian can be rewritten as

$$H = -\hbar v\left(\frac{z}{\ell_S^2}\tau_x - \frac{z}{\ell_{\mathcal{E}}^2}\mathbb{I}\right) + \hbar vk_z\tau_y + \hbar v\tau_z(k_y\sigma_x - k_x\sigma_y). \quad (5.32)$$

This is the form suitable for a hyperbolic transformation which can merge \mathbb{I} into τ_x if the electric field is weak (see Chapter 2). The critical electric field is defined by $\ell_S = \ell_E$. One finds again the electric and magnetic regimes as for NbAs₂ in Chapter 3 and as for graphene in a crossed electric and magnetic fields in Chapter 2. If the electric field is too strong, the VP states no longer exist and the spectrum becomes a continuum due to the electric breakdown. For a subcritical electric field, the mismatch of the centers around which the wavefunctions are localized yields the proliferation of peaks exactly as for NbAs₂ in Chapter 3. The presence of a magnetic field perpendicular to the interface will not change the argument since the corresponding ladder operators commute with all the z -dependent terms. If the applied magnetic field is parallel to the interface, one just needs to use the same argument after replacing ℓ_S by ℓ_T , the length scale encoding both smoothness and magnetic field.

Before going to the next part, I want to mention that the study of the optical conductivity has also been done for WSMs [151]. As a metal, the chemical potential turns out to be another tunable parameter that gives even richer feature to characterize the VP states in WSMs. The effect of an electric field is also discussed for WSMs in [128].

5.2 FARADAY AND KERR ROTATION

In this section, I briefly discuss other magneto-optical effects, namely Faraday and Kerr rotations, due to the presence of VP states. Using the results already known in the literature on 3DTI [162, 163, 164, 165], I would like to simply point out another possible way to identify VP states in magneto-optical spectroscopy.

When time-reversal symmetry is broken by an out-of-plane magnetic field, a conventional 2D electron gas yields quantized magnetic Faraday and Kerr effects due to the Landau quantization [166]. 3DTI films have also been shown to exhibit interesting magneto-optical Faraday and Kerr effect [162, 163]. Thanks to surface Hall conductivity arising from surface Dirac cone, the magnetic Faraday rotation angle is quantized as multiples of the fine-structure constant $\alpha = 1/137$ and the magnetic Kerr rotation angle is surprisingly large and close to $\pi/2$ for normal incidence. These effects are observable in experiments if:

- The thickness of 3DTI film is smaller than the wavelength so that the electric components in an electromagnetic wave are nearly constant through the whole sample;
- The system is in the quantum Hall regime and thus the longitudinal conductivity is vanishing if the chemical potential is in the gap;
- The frequency of incident wave is smaller than any gap including Zeeman gap and the cyclotron gap $\hbar\omega_c$ so that no interband transitions are allowed.

Alternatively, the wavelength of the incident wave is the largest one of all the length scales of the system. It turns out that the wavelength is in the far infrared regime for typical parameters in practice [162]. Here, it is also important to neglect any residual bulk conductivity and the coupling between two surfaces. In other words, the 3DTI film is just a stacking of two surface Dirac cones quantized by an out-of-plane magnetic field.

When the above conditions are fulfilled, the Faraday and Kerr angles read

$$\theta_F = \tan^{-1}[(\nu_T + \nu_B)\alpha] \approx (\nu_T + \nu_B)\alpha \quad (5.33)$$

$$\theta_K = -\tan^{-1}\left[\frac{1}{(\nu_T + \nu_B)\alpha}\right] \approx -\frac{\pi}{2} \quad (5.34)$$

where $\nu_{T,B}$ are the filling factor of the top and bottom surface and $\alpha = 1/137$ is the fine structure constant. The details of the derivation can be found in [164]. Note that $\nu_{T,B}$ can be different if two surfaces differently doped or gated. Recent experiments have demonstrated the possibility of controlling separately the chemical potential of two surfaces of 3DTIs [167].

One can perfectly extend the arguments above to 3DTI thin films with smooth surfaces ($\ell > \xi$) when VP states are present in the bulk gap. The smoothness ℓ should be much smaller than the thickness of the sample so that the coupling between the two surfaces of the film can be neglected.

As shown by Eq. (5.29), Landau levels are indexed by two quantum numbers n and m associated with the smoothness and the magnetic field, respectively. So, the filling factor ν counts at the same time n and m . An interesting situation arises when $\ell_B \ll \ell_S$. Tuning continuously the chemical potential from the charge neutral point to positive values, one would find increments of the Faraday angle θ_F given only by n when the chemical potential is still smaller than $\hbar v/\ell_B$. This is yet another possible way to corroborate the existence of VP states.

Note that time-reversal symmetry can be also broken by an exchange field, i.e., a Zeeman gap. The single Dirac cone would open a gap and the spin degeneracy of VP states is lifted. Since all the states are now non-degenerate 2D massive Dirac fermions which are known to have 1/2 Chern number [67], Faraday and Kerr rotations should yield interesting behavior varying the surface chemical potential [162, 168]. From this perspective, the topological properties of VP states are encoded in the spinor structure of wavefunctions as for 2D massive Dirac fermion.

Although an elaborate discussion on the Faraday and Kerr rotations of topological heterojunction is out of the scope of this part, I just want to point out that this could be a promising direction for future research.

5.3 SURFACE PLASMONS OF WEYL SEMIMETALS

Until now, I have only discussed the single-particle physics of VP states. In this section, I will discuss how electron-electron interactions enrich the spectroscopic properties of VP states, one of which is the surface plasmon. Two reasons have encouraged me to study plasmon physics. On the one hand, a plasmon is measurable by EELS and it could be useful for future plasmonic applications. On the other hand, the calculations of the dielectric function by which plasmon is theoretically predicted is in principle analytically tractable using the RPA.

It has been well-known in the community that the FA states can induce a chiral linear FA surface plasmon with total non-reciprocity [169, 170, 171, 172, 173, 174, 175], i.e., it propagates only in one direction determined by the chirality of the FA dispersion. Linear dispersion and total non-reciprocity are highly desirable for further plasmonic applications. This is why WSMs are chosen to be the system to study surface plasmons arising from surface states. The study of surface plasmons in WSMs in the presence of VP states are thus valuable both from a fundamental and from an applied point of view.

In this part, I will first show how to solve the Hamiltonian of a topological heterojunction modeled by WSM. The analogy of smoothness with magnetic field is more plausible in WSMs than TIs. Then, I will apply the RPA to the Hamiltonian of interest. In particular, I will prove that in the long wavelength limit the RPA leads to a scalar dielectric function while considering only the FA state and the first VP states. Finally, I will bestow the physical meaning upon the numerical results on plasmon modes using the analytical expressions.

5.3.1 HAMILTONIAN, SPECTRUM AND WAVEFUNCTIONS

Consider a single boundary problem, i.e., a smooth interface in the x -direction between a time-reversal breaking two-node WSM and a trivial insulator modeled by the Hamiltonian (4.12) in Chapter 4, which I recall here

$$H = \hbar v(k_x \sigma_x + k_y \sigma_y) + \left(\frac{k_z^2}{2m} - \Delta_0 + 2\Delta_0 \frac{x}{\ell} \right) \sigma_z \quad (5.35)$$

where the inverted gap of WSM is closed at $x = \ell$. The Hamiltonian (4.12) after a unitary transformation $T = \exp(i\pi\sigma_x/4)$ reads:

$$H_T = \hbar v \begin{bmatrix} -k_y & \frac{\sqrt{2}}{\ell_S} \hat{a} \\ \frac{\sqrt{2}}{\ell_S} \hat{a}^\dagger & k_y \end{bmatrix} \quad (5.36)$$

5 Spectroscopic properties of Volkov-Pankratov states

where the characteristic length $\ell_S = \sqrt{\ell\hbar v/2\Delta_0}$. The creation and annihilation operators, a^\dagger and a , are constructed from linear combinations of the k_x - and the x -dependent terms and read

$$\hat{a}^\dagger = \frac{\ell_S}{\sqrt{2}} \left(k_x + i \frac{x - \langle x \rangle}{\ell_S^2} \right), \quad (5.37a)$$

$$\hat{a} = \frac{\ell_S}{\sqrt{2}} \left(k_x - i \frac{x - \langle x \rangle}{\ell_S^2} \right), \quad (5.37b)$$

with

$$\langle x \rangle = \ell \frac{\Delta - k_z^2/2m}{2\Delta} \quad (5.37c)$$

where $\langle x \rangle$ determines the average position of the surface state. Compared to the ladder operators defined for TIs, for example, Eq. (4.14), the ladder operators defined here depend on the surface momentum k_z through $\langle x \rangle$. Therefore, the analogy of smoothness with magnetic field is more appropriate in WSMs. From Eq. (5.36), one can already anticipate that the spectrum is only dispersive in k_y . The 3D dispersive energy spectrum of WSMs is quantized to be 1D, exactly like what a true magnetic field would do. One can identify here a Weyl cone chirality-resolved pseudo-magnetic field in the y -direction with $\mathbf{B}_p = \pm 2\Delta/ev\ell\mathbf{e}_y$ [128]. This is further confirmed by analyzing the selection rules [151]. The selection rules for light polarized along the y -axis are $n \rightarrow n$ (Voigt geometry) while those for light polarized along the x, z -axes are $n \rightarrow n \pm 1$ (Faraday geometry).

The eigenstates are thus of the form as

$$\begin{aligned} |\psi_n^\lambda\rangle &= \frac{1}{\sqrt{2}} \begin{pmatrix} u_{n,\lambda}(k_y)|n-1, k_z\rangle \\ \lambda v_{n,\lambda}(k_y)|n, k_z\rangle \end{pmatrix} & \text{if } n \geq 1 \\ |\psi_0\rangle &= \begin{pmatrix} 0 \\ |0, k_z\rangle \end{pmatrix} & \text{if } n = 0 \end{aligned} \quad (5.38)$$

where λ indicating valence ($\lambda = -$) or conduction ($\lambda = +$) band; $u_{n,\lambda}(k_y)$ and $v_{n,\lambda}(k_y)$ are two k_y -dependent spinor coefficients; $|n, k_z\rangle$ are the eigenstates of quantum harmonic oscillator defined by $\hat{a}^\dagger(k_z)$ and $\hat{a}(k_z)$. I explicitly mark k_z in the notations to emphasize the dependence on k_z in the ladder operators and the spinor components $|n, k_z\rangle$. The $n = 0$ state is precisely the famed FA state, which is chiral also in the sense that one of the spinor components is zero. The $n \geq 1$ states are the VP states emerging on the smooth surface of WSMs.

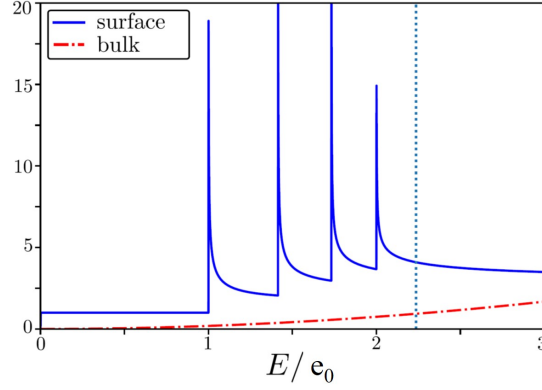


Figure 5.6: Comparison of density of states of the VP states with that of the bulk. The dotted vertical line denotes the onset of the bulk continuum. Figure adapted from [151].

The energy spectrum is thus

$$\begin{aligned}
 E_n^\lambda &= \lambda \sqrt{(\hbar v k_y)^2 + n e_0^2} && \text{if } n \geq 1 \\
 E_0 &= \hbar v k_y && \text{if } n = 0
 \end{aligned} \tag{5.39}$$

where the VP band gap $e_0 = \sqrt{2}\hbar v/\ell_S$, which is the separation between the $n = 0$ and $n = 1$ bands at $\mathbf{k} = 0$, sets the characteristic energy scale of this surface model. On the one hand, the FA state ($n = 0$) has linear dispersion in k_y breaking the parity symmetry $k_y \rightarrow -k_y$, while its counterpart with opposite sign of the dispersion is localized at the other surface of the WSM that I do not consider here. The VP states has parity symmetry. On the other hand, the FA state is independent of the surface details such as its smoothness, i.e., the band dispersion does not depend on ℓ , indicating its topological nature. In contrast, the $n \geq 1$ VP bands depend strongly on the surface modeling. In the sharp-surface limit ($\ell \rightarrow 0$), the VP bands rise up in energy and eventually merge with the bulk states when $e_0 \sim \Delta_0$, while the FA state survives. These two facts reflect the non-topological nature of VP states.

Compared to the spectrum of a topological heterojunction modeled by 3DTI [see Eq. (5.18)], although the eigenstates live on a two-dimensional manifold (k_y, k_z) , their energies disperse only in the k_y -direction, i.e., the direction perpendicular to the interface and the line connecting the two Weyl nodes at $k_z = \pm\sqrt{2m\Delta_0}$ in the reciprocal space. The bands are thus quasi-1D and the DOS of the VP states diverges at the band extremum (see Fig. 5.6). The dependence on k_z is only encoded in the wavefunctions, more precisely the cyclotron center of $|n, k_z\rangle$. Indeed, this strong anisotropy in the energy dispersion induces the peculiar properties of plasmon due to the edge states as shown immediately.

5.3.2 NON-INTERACTING DYNAMICAL POLARIZATION AND QUASI-TWO-DIMENSIONAL RANDOM PHASE APPROXIMATION

The details of full derivation of the RPA is given in the supplementary material of [176]. Here, I briefly summarize the results. As shown in Chapter 3, the non-interacting dynamical polarization, i.e., non-interacting charge susceptibility is the building block for the RPA. For a multi-band system, the non-interacting dynamical polarization denoted by $\chi_{i,j}^{(0)}$ is [177, 178]

$$\chi_{i,j}^{(0)}(\mathbf{q}, \omega) = \frac{1}{V} \sum_{\mathbf{k}} \frac{f_D(E_i(\mathbf{k})) - f_D(E_j(\mathbf{k} + \mathbf{q}))}{\omega + E_i(\mathbf{k}) - E_j(\mathbf{k} + \mathbf{q}) + i0^+} |F_{i,j}(\mathbf{k}, \mathbf{k} + \mathbf{q})|^2, \quad (5.40)$$

where the i, j indices are shorthand notations for both band labels n and λ . In general, the overlap matrix $F_{i,j}$ is not diagonal because of the aforementioned k_z -dependence of the eigenstates so that $\chi_{i,j}^{(0)}$ is generally a tensor (see in the supplementary material of [176]). However, for $q_z = 0$, the particle-hole excitations are also 1D and $F_{i,j}$ becomes diagonal meaning that only excitations from n to n are possible. $\chi_{i,j}^{(0)}$ can be thus treated as a scalar. Although the contribution from the bulk states is not explicitly taken into account, the VP states interpreted as leakage of bulk states include implicitly this contribution.

For the same reason, if $q_z = 0$, the Coulomb interacting matrix becomes a scalar. The RPA dielectric function then retrieves its usual form

$$\epsilon^{\text{RPA}}(q_y, \omega) = 1 - V_{2\text{D}}(q_y) \chi^{(0)}(q_y, \omega), \quad (5.41)$$

where a 2D Coulomb interaction $V_{2\text{D}}(q_y) = e^2/2\epsilon_0\epsilon_r|q_y|$ is used with vacuum permittivity ϵ_0 , and the static screening is encoded in the environmental dielectric constant ϵ_r . The reader may be curious why the application of the RPA to a 3D system uses a 2D Coulomb interaction. This is because I discuss here surface states that are localized at the interface. Their spatial extension is cut off by ℓ_S . For smooth interfaces with $\ell \gg \ell_S$, the dominant contribution to the Coulomb matrix comes from the region where $q(\langle x \rangle - \langle x' \rangle) \ll 1$. The Coulomb potential is effectively 2D in the long wavelength limit, i.e., $q\ell_S \ll 1$. This is the reason why I qualify the RPA used in the section *quasi-two-dimensional*.

When $q_z \neq 0$, the overlap matrix element $F_{i,j}(\mathbf{k}, \mathbf{k} + \mathbf{q})$ is mathematically more involved. However, in the long-wavelength limit, the off-diagonal term $F_{i,j}$ is proportional to $q_z^{|n_i - n_j|}$ so that the $n \rightarrow n$ excitations still remain the leading contributions to the charge susceptibility. Nevertheless, due to the complicated form of the off-diagonal terms, the Coulomb interaction is no longer a scalar even in the long-wavelength limit when several VP bands are present. However, if one considers only

the chiral FA and the two $n = 1$ VP bands (*three-band model*), the RPA dielectric function for $q_z \neq 0$ is simplified to

$$\epsilon^{\text{RPA}}(\mathbf{q}, \omega) = 1 - V_{2\text{D}}(\mathbf{q})\chi^{(0)}(\mathbf{q}, \omega), \quad (5.42)$$

which is again a scalar equation.

5.3.3 PLASMON IN THE THREE-BAND MODEL

Now I investigate in detail the simplified three-band model where I consider the two $n = 1$ VP bands in addition to the chiral state ($n = 0$). The zero of the real part of ϵ^{RPA} in the (\mathbf{q}, ω) phase space determines the dispersion relation of the plasmon. All the analytical results for the three-band model are reported in the supplementary material of our work [176] in which we show that the analytical calculations result in a complicated transcendental equation even in the long wavelength limit. The main difficulty comes from the system being multi-band, leading to some features that one cannot account for by considering separately the FA and VP states. So, I numerically do the calculations to find the plasmon dispersion and analyze the results to interpret them with the help of analytical expression. Because of the log-divergence at the plasma edge in the dynamical polarization, the numerical evaluation of the analytical expression requires a fine mesh in the vicinity of the position of divergence, which requires long execution time and large amount of memory. The trick is to do a linear interpolation in the integral that keeps the fingerprint of the log-divergence and largely accelerates the calculations [179]. The details on analytical calculations are shown in the supplementary material of our work [176].

EXCITATION WITH $q_z = 0$

Setting $q_z = 0$, the profile of $-\text{Im}(\chi^{(0)})$ in the $(q_y > 0, \omega > 0)$ -plane, for different values of the chemical potential $\mu > 0$ and a given disorder amplitude by replacing 0^+ with 0.001 in Eq. (5.40), is shown in Fig. 5.7. The imaginary part of $\chi^{(0)}$ bears important information about possible electronic excitations and therefore Landau damping region for the plasmon modes. The dispersion of plasmon is indicated by the red dashed lines (zeros of the real part of ϵ^{RPA}). The plasmon modes are only long-lived and undamped in the black regions where $\text{Im}(\chi^{(0)}) = 0$. Within the three-band model, one obtains three particle-hole continua, with $-\text{Im}(\chi^{(0)}) \neq 0$, shown in Fig. 5.7.

When the chemical potential is below the band edge of the first VP band, two domains of particle-hole continua exist. One of them extends linearly in the $(q_y > 0, \omega > 0)$ -plane, i.e., the signature of FA particle-hole continuum. Due to the linear dispersion of the FA state, its particle-hole continuum is independent of μ . The second particle-hole spectrum is delimited from below by $\omega > \sqrt{4e_0^2 + \hbar^2 v^2 q_y^2}$ due to interband excitations involving the two $n = 1$ VP conduction and valence

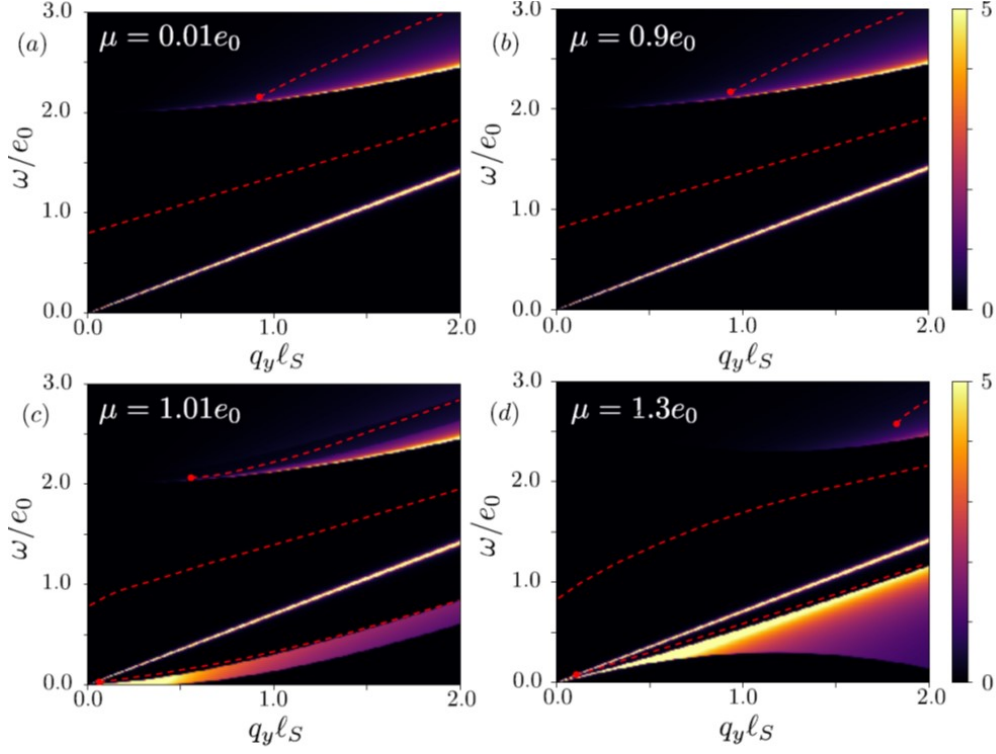


Figure 5.7: Profile of the imaginary part of the non-interacting dynamical polarization $-\text{Im}(\chi^{(0)})$ in the (q_y, ω) phase space at $\mu = 0.01e_0, 0.90e_0, 1.01e_0$ and $1.30e_0$ for $q_z = 0$. The zeros of the real part of ϵ^{RPA} (red dashed lines) indicate the plasmon modes. The fixed parameters are chosen to be $v = 1 \text{ eV} \cdot \text{\AA}$, $\ell = 10 \text{ \AA}$, $\Delta = 1 \text{ eV}$ and $k_0 = 10 \text{ \AA}^{-1}$.

bands. However, it vanishes at small momenta because the eigenstates associated with the VP conduction and valence bands are orthogonal at $\mathbf{q} = 0$. Since only the interband excitations are involved, the particle-hole continuum for VP states is also invariant of μ as long as the chemical potential is in the VP band gap.

As one increases μ above the VP conduction band, the particle-hole continuum of FA excitations remains unchanged due to the linearity of the FA dispersion whereas that of VP states gets heavily modified due to Pauli blocking at the conduction band minima. The particle-hole continuum shifts to higher frequency and larger momentum. Most saliently, the intraband excitations of the VP conduction band induce a third particle-hole continuum at low frequencies. With $\mu > e_0$ just above the conduction band minimum, the VP band is approximately parabolic, and its quasi-1D character is apparent in the form of the particle-hole intraband spectrum with its typical exclusion dome for $q\ell_S < 2k_F$ with k_F defined as $\mu = \sqrt{\hbar^2 v^2 k_F^2 + e_0^2}$.

In the $q_z = 0$ limit, two plasmon modes are present for $\mu < e_0$ as shown by red dashed lines in Fig. 5.7. The first one is the linearly dispersing FA plasmon with a gap at $q_y = 0$, in agreement

with theoretical approaches using classical electrodynamics [169], hydrodynamic description [174], or quantum-mechanical calculations [170, 172, 173, 175]. From the zeros of the real part of the equation $\epsilon^{\text{RPA}}(q_y, \omega) = 0$, the FA-plasmon dispersion reads

$$\hbar\omega \approx \text{sgn}(q_y) \frac{k_0 e^2}{4\pi^2 \epsilon_0 \epsilon_r} + \left(1 + \frac{2k_F}{\sqrt{k_F^2 + \frac{2}{\ell_S^2}}} \delta_{n_F,1} \right) \hbar v q_y \quad (5.43)$$

where $2k_0 = 2\sqrt{2m\Delta_0}$ is the separation between two Weyl nodes in the bulk, $\delta_{i,j}$ is the Kronecker δ -function and n_F is the integer part of the ratio between μ and e_0 . If $n_F = 0$ ($\mu < e_0$), for positive ω , the FA plasmon is allowed to propagate only in the direction of positive q_y , due to the FA being chiral. For the usual 2D electron gas or graphene, recall that their plasmon dispersion is square-root due to the Coulomb potential being 2D [180, 181, 182]. In spite of the the quasi-1D nature of the FA, the Coulomb potential remains 2D here, and one might naively expect a square-root plasmon dispersion. Surprisingly, this is not the case, and one finds a *linear gapped* plasmon mode thanks to its chiral nature. As simple as it is, Eq. (5.43) accurately describes the mode found numerically in Fig. 5.7. The result is the same if considering the FA states alone because the influence from the interband transition between VP states is prohibited for small q_y . I emphasize that the experimentally measurable FA plasmon gap,

$$\gamma_{\text{FA}} = \frac{k_0 e^2}{4\pi^2 \epsilon_0 \epsilon_r}, \quad (5.44)$$

yields direct information about the separation $2k_0$ between the bulk Weyl nodes knowing the dielectric constant of the substrate ϵ_r .

VP intraband excitations significantly modify the dispersion of the FA plasmon when $n_F = 1$ ($\mu > e_0$). The plasmon gap sticks to the same value γ_{FA} . The dispersion of FA plasmon at large q_y remains almost linear with the same velocity v .⁶ At small q_y , the FA plasmon acquires an enhanced velocity that can be further boosted by increasing the chemical potential [see Eq. (5.43)]. However, the change of velocity for finite q_y , as seen in Fig. 5.7, is not captured by Eq. (5.43) since the long wavelength limit is approaching its limit.

The second plasmon mode in Fig. 5.7, is the VP interband plasmon, which stems mostly from the VP interband excitations. It is also gapped and starts at a finite momentum for the same reason that the spectral weight of the particle-hole continuum is vanishingly small at $q_y \sim 0$, which makes sustained plasmonic oscillations impossible. The interband VP plasmon mode lies in the VP interband particle-hole region and is thus Landau-damped. However, since the amplitude of $-\text{Im}(\chi^{(0)})$ drops at high energy, this plasmon may be visible as an additional bump in EELS as shown later.

⁶Here, what I mean large is to approach $q_y \ell_S \sim 1$ while assuming that the long wavelength limit is still valid.

The third plasmon mode emerges when $\mu > e_0$. This mode exists in a region delimited by the particle-hole continua of the FA and the VP conduction bands. It starts at small but finite momentum and its energy disperses along with the upper boundary of the intraband continuum and eventually gets merged in it at larger momentum. One may naively think that this VP intraband plasmon originates only from intraband excitations and has a square-root dispersion at small momenta (see yellow dashed lines in Fig. 5.9). However, the numerical calculations invalidate this picture. This is because one needs to take into account the other particle-hole continua, namely the linear one associated with the FA, which prohibits such a square-root dependence of an undamped plasmon (see in the supplementary material of our work [176]). Moreover, when the chemical potential crosses a VP conduction band, remote VP interband excitations cannot simply be accounted in ϵ_r because of the diverging density of states. This significantly modifies the dynamical screening. Thus, the VP intraband plasmon acquires positive energy only at non-zero finite momentum and disperses linearly with a velocity smaller than v . The terminating point of the plasmon dispersion is indicated by red dots in Fig. 5.7. Increasing μ from 1.01 to $1.3e_0$, the exclusion dome at low frequencies becomes wider. The available phase space for the VP intraband plasmon between the FA and the VP intraband continua is reduced even further making this plasmon less visible at larger values of μ .

EXCITATION WITH $q_z \neq 0$

Since the bands are effectively 1D, the particle-hole continua are independent of q_z if the coupling between FA and VP bands is omitted. It is indeed legitimate to neglect this coupling in the long-wavelength limit where it scales as $\sim (q_z \ell_S)^2$. As shown in Fig. 5.8, most of the conclusions for the case $q_z = 0$ are applicable for $q_z \neq 0$ except that the dispersion of FA plasmon gets strongly modified for $q_y < q_z$ due to the q_z -dependence of the Coulomb interaction.

Neglecting a small hybridization between the VP bands and the FA state, the FA-plasmon gap at small momenta becomes

$$\gamma'_{\text{FA}} = \gamma_{\text{FA}} \frac{q_y}{\sqrt{q_y^2 + q_z^2}}. \quad (5.45)$$

When $q_z = 0$, Eqs. (5.45) and (5.44) coincide, and the FA plasmon is gapped as shown earlier. However, when $q_z \neq 0$, the gap vanishes at $q_y = 0$ as a consequence of the strong anisotropy of the FA state, which is only quasi-1D but embedded in a 2D manifold. When $q_y \gg q_z$, the FA plasmon disperses again linearly with slope v . This is then validated by the numerical calculations shown in Fig. 5.8. The FA plasmon gap vanishes when $\mathbf{q} = q_z \mathbf{e}_z$. This singular behavior of the gap at $\mathbf{q} = 0$ is also reported in the literature [169, 170, 172, 173, 174, 175]. Therefore, one would always measure a gapless plasmon

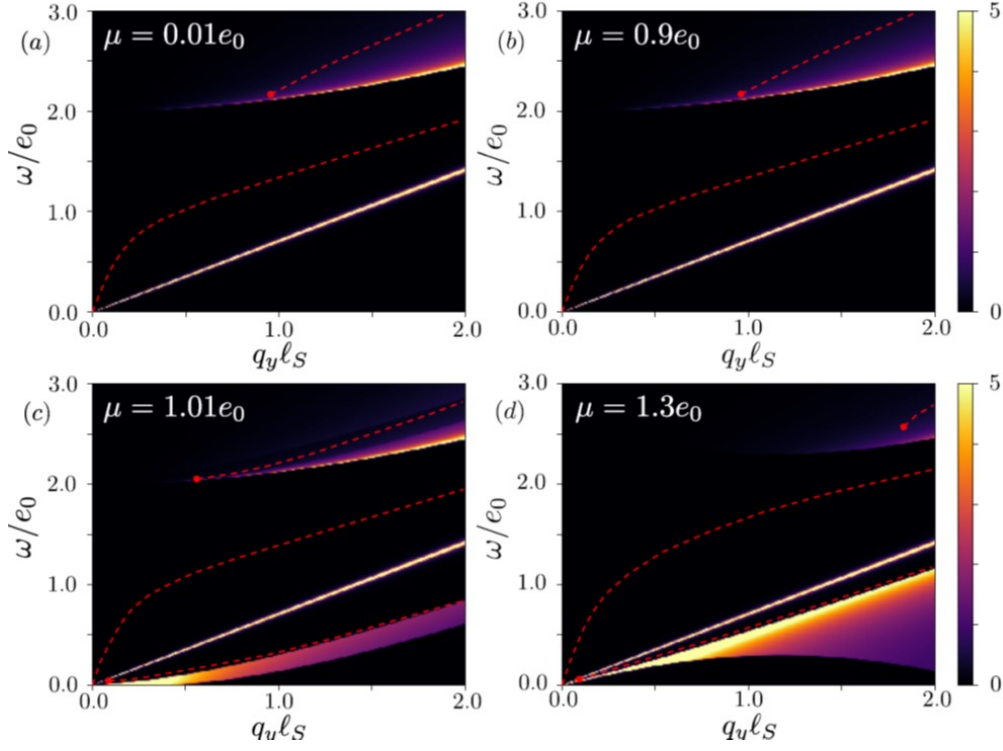


Figure 5.8: Profile of the imaginary part of the non-interacting dynamical polarization $-\text{Im}(\chi^{(0)})$ in the (q_y, ω) phase space. The parameters are kept to be the same as Fig. 5.7 except for $q_z \ell_S = 0.2$. The zeros of the real part of ϵ^{RPA} (red dashed lines) indicate the plasmon modes.

mode stemming from the FA plasmon in experiments since it is difficult to limit $q_z = 0$. Notwithstanding, the FA-plasmon gap can be retrieved by extrapolating the linear dispersion with slope v at $q_y \ell_S \sim 1$ to $q_y = 0$ so that the intercept gives the value of γ_{FA} .

NON-RECIPROCITY OF PLASMON

To show what one can see in experiments, the electron loss function $-\Im[1/\epsilon^{\text{RPA}}]$, directly measurable by EELS, is plotted in Fig. 5.9 in the $(q_y, \omega > 0)$ -plane with intensity indicated by colorbar. One of the intriguing properties of FA is the non-reciprocity of the FA plasmon, reflecting the chiral nature of the FA state. Therefore, one should also study $-\Im[1/\epsilon^{\text{RPA}}]$ for $(q_y < 0, \omega > 0)$. The result for $\omega < 0$ can be easily retrieved by reversing simultaneously the sign of ω and \mathbf{q} in known results. As shown in Fig where $\mu = 1.01 e_0$, the FA plasmon is completely absent when $q_y < 0$ as well as the corresponding particle-hole continuum. Being non-reciprocal, the FA plasmon only propagates in one direction with fixed velocity, highly desirable for applications. Strikingly, the VP intraband plasmon is

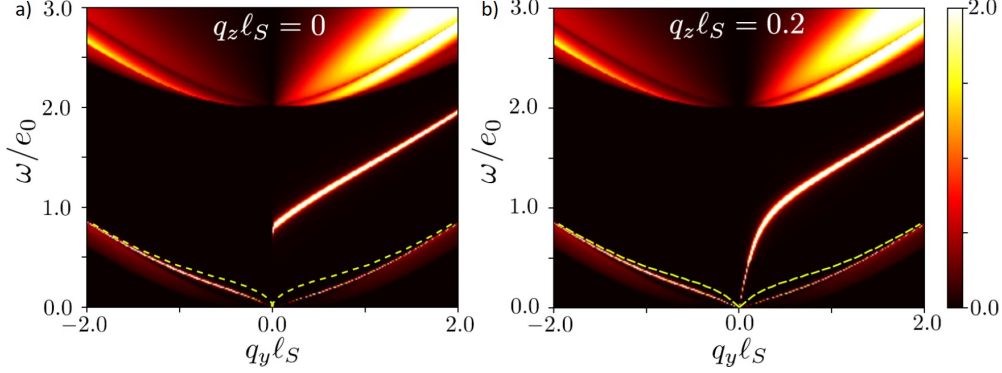


Figure 5.9: Electron loss function at $\mu = 1.01e_0$ for $q_y \ell_S \in [-2.0, 2.0]$: (a) for $q_z = 0$ and (b) for $q_z \ell_S = 0.2$. Yellow dashed lines show the symmetric VP intraband plasmon in the absence of the FA state. Three plasmon modes are all non-reciprocal and visible.

also non-reciprocal even if it involves the $k_y \leftrightarrow -k_y$ symmetry of the VP bands [see Eq. (5.39)]: it has a different dispersion for $q_y < 0$, which can be calculated analytically

$$\omega \approx \text{sgn}(-q_y)v \left(|q_y| + \frac{2k_F}{\sqrt{k_F^2 + \frac{2n}{\ell_S^2}}} \sqrt{q_y^2 + q_z^2} \right). \quad (5.46)$$

Contrary to $q_y > 0$, it starts from the origin of (q_y, ω) and disperses with a velocity larger than v which can be enhanced further by increasing μ . This non-reciprocity is a consequence of the hybridization with the FA mode and particle-hole continuum, which is in close vicinity of the intraband VP plasmon for $q_y > 0$ but further well separated in energy for $q_y < 0$ (see in the supplementary material of our work [176]). The chirality of the FA modes thus induces non-reciprocity in other excitations due to their mutual coupling. This can also be seen in the VP interband plasmon, where the starting point moves to higher frequency and larger momentum. As anticipated above, the VP interband plasmon is submerged amid the particle-hole continuum but nevertheless visible on EELS.

In this section, the effect of surface smoothness on the charge oscillation spectrum of a WSM surface has been investigated. Within quasi-2D RPA, I have shown the emergence of two collective modes stabilized by the inter- and intra-VP band excitations, in addition to the FA plasmon. The plasmons exhibit anisotropy and non-reciprocity inherited from the underlying surface model. The findings could be verified experimentally in EELS, which could probe the chirality of the FA and offer an alternative way to prove the presence of the VP states. Furthermore, the FA-plasmon gap gives us a direct experimental measure of the separation between the Weyl nodes.

5.4 SUMMARY

In this chapter, I have shown all the theoretical results on the spectroscopic properties of VP states that I have obtained during my PhD.

First, I have calculated the optical conductivity of VP states. Playing with the polarization of incident photon and the orientation of magnetic field, the optical response from VP states has rich features. First, additional absorption peaks appear below the gap aside from those due to topological states. Furthermore, the shape of peaks, which is intimately determined by the dimensionality-sensitive DOS, are tunable by the orientation of the magnetic field which modifies the dimensionality of VP bands. In particular, the in-plane magnetic field and the smoothness quantization conspire to form a composed magnetic field which keeps the shape of peaks but yields new peaks for photons of certain polarization. Therefore, these specific features from VP states in the optical conductivity are a smoking gun to identify the existence of VP states in TIs. These results have been published in *Europhysics Letters* [159]. I have also suggested that interesting phenomena in Faraday and Kerr rotations could occur in the presence of VP states. Finally, I have given a first taste of how Coulomb interactions could enrich the physics of VP states by showing multiple plasmon modes in WSMs. This work has been recently published in *Physical Review B* [176]. All these spectroscopic properties of VP states would inspire both fundamental and applied research on VP states in the future.

6 CONCLUSIONS AND PERSPECTIVES

The important thing is to never stop questioning [or learning].

Albert Einstein

The Dirac equation, originally derived for particle physics, has been the guideline of this thesis whose topic belongs to condensed matter theory. The benefit of the application of the Dirac equation in condensed matter is mutual. Thanks to the interplay between lattice potential and electrons, the Dirac equation, even the ultra-relativistic one, emerges unexpectedly in the low-energy description of Dirac materials. Many theoretically predicted high-energy phenomena, which cannot be tested in particle physics experiments due to inaccessible experimental conditions and astronomical costs, are conceivable in materials with convenient tunability and affordable costs. Even those which have not yet been discovered in high-energy physics, such as supersymmetry [75], find their representation in condensed matter physics. Most saliently, the low-energy Hamiltonian of Dirac materials is not restricted by the Lorentz symmetry in contrast to elementary particles. The imagination of theorists is thus further freed. One can legitimately consider the variations of the original Dirac equation with no associated elementary particles that exist in nature. However, they may exist in condensed matter physics.

Reciprocally, the condensed matter community benefits the formalism that are well established in the context of particle physics. It offers a rejuvenating and complementary understanding for the electronic properties of materials. Various unusual observations in Dirac materials, which cannot be explained by the Schrödinger equation, are elegantly explained by the Dirac equation and its inherent symmetries. The application of the formalism further boosts the discovery of various Dirac materials. Most saliently, it is one of the momenta to give birth to topological band theory, a ground-breaking progress in solid-state physics. Many surprising properties of matter such as the bulk-edge correspondence in topological materials are also captured by the Dirac equation.

Therefore, my thesis has been also unfolded in these two aspects. In the first part, I have shown how Einstein's theory of special relativity applies on the electrodynamics in Dirac materials. In Chapter 2, I have reviewed previous works on the magnetic-field-induced relativistic renormalization in graphene subject to crossed electric field and magnetic field. Based on this simple example, I have introduced the

6 Conclusions and perspectives

unitary and hyperbolic transformations which can be further extended to other Dirac materials such as Weyl semimetals, tilted gapped graphene and gapped nodal line semimetals. While previous works have been concerned with the gapless system, my contribution is to reveal the gap renormalization in the gapped system. Furthermore, I also provide an interpretation of the relativistic renormalization by the language of condensed matter physics, which completes the understanding of the phenomena of interest.

In Chapter 3 where I have included a short introduction to theoretical approaches to spectroscopy, I have elaborated the theoretical study on the magneto-optics a gapped nodal line semimetal, NbAs_2 . This is a project in collaboration with my colleagues of the LNCMI in Grenoble who have made industrious efforts and conducted wonderful magneto-optical measurements on NbAs_2 . The most exciting moment of this project has come recently when the gap renormalization in NbAs_2 was clearly observed by our collaborators and the results fit extremely well with our theory.

In the second part, I have shown that the Dirac equation is a unifying theoretical framework to study the surface states of topological materials. Especially, additional massive Volkov-Pankratov states emerge in smooth topological heterojunctions. In Chapter 4, I have offered different perspectives to understand the origin of Volkov-Pankratov states. I have started by showing a point of view given by previous work by Sergueï Tchoumakov, who initiated the work on surface states in our group during his thesis, that the smoothness plays the role of pseudo-magnetic field quantifying surface bands to Landau bands. Then, I have challenged this perspective by the dimensionality reduction, which has inspired me to interpret the origin of Volkov-Pankratov states in terms of quantum well physics denoted as Dirac quantum well. One of the advantages of this complementary perspective is to permit me to discuss the tunneling between Volkov-Pankratov states of two sides of topological materials in an intuitive way. Especially, the topological protection of topological states is interpreted as the absence of resonant tunneling. To be complete, I have also shared the point of view of mathematician-physicist who may treat the problem by identifying a differential equation in supersymmetry. Finally, a tight-binding approach has been given to further confirm the presence of Volkov-Pankratov states.

In Chapter 5, I have discussed the spectroscopy properties of Volkov-Pankratov states using the techniques presented in Chapter 3. The key signature in (magneto-)optical conductivity revealing the presence of Volkov-Pankratov states has been shown to be a smoking gun to distinguish them from trivial surface states. I have also studied plasmonics on the surface of Weyl semimetal. In addition to the well-know Fermi-arc plasmon, Volkov-Pankratov states yield inter- and intra-band plasmons. Unexpectedly, the hybridization between the Fermi-arc and Volkov-Pankratov plasmons attributes the non-reciprocity to Volkov-Pankratov plasmons, which are supposed to be reciprocal.

There are many other research topics that I have conceived for future. One possible branch is to pursue the idea of “doing high-energy physics in low-energy systems”. An interesting branch is to ap-

ply not only special relativity but also general relativity to materials. There are already some pioneering works on Weyl semimetal going in this direction. Another possible branch is to further investigate the possibilities given by Volkov-Pankratov states. For example, the flat bands in twisted bilayer graphene can be interpreted as pseudo-Landau levels [183, 184]. In the continuum model for twisted bilayer graphene [185], the emergence of the flat bands is the consequence of the twisted boundary condition, which inherently constitutes a smooth boundary between different domains in real space. It seems thus plausible to re-interpret the flat bands in terms of Volkov-Pankratov states, which are generalizable to other twisted systems. Here, I have discussed only the spectroscopic properties. The transport properties of Volkov-Pankratov states are worth to be further investigated. Finally, I have given first hints on the promising physics induced by electron-electron interactions by looking at the physics of plasmon. Nevertheless, the interaction effects in the presence of Volkov-Pankratov states remain also unclear and wait for future investigations.

A SHORT REVIEW ON SPECIAL RELATIVITY

In 1905, Einstein postulated in his seminal work on the theory of special relativity that the speed of light is the same to all observers at rest in inertial frames of references and the laws of nature are identical in all inertial frames of reference. An important consequence of his statement is that the spatial and temporal dimensions must be interwoven. This four dimensional space where time is merely another dimension just like space is called space-time. A complete introduction on special relativity could be found in [80, 186].

A.1 LORENTZ BOOST AND FOUR-VECTORS

I first show a direct consequence of the two assumptions above. Say a flash of light is emitted at $t = 0$ from the spatial origin in the point-of-view of the frame \mathcal{R} . The trajectory of the light signal propagating spherically at the speed of light (first axiom) should verify

$$c^2t^2 - x^2 - y^2 - z^2 = 0 \quad (\text{A.1})$$

where (t, x, y, z) is the space-time coordinate of the front of the light wave in \mathcal{R} . Therefore, the trajectory of the light in another inertial frame \mathcal{R}' is characterized by the same equation (second axiom)

$$c^2t'^2 - x'^2 - y'^2 - z'^2 = 0. \quad (\text{A.2})$$

By the fact that the space is homogeneous and isotropic, one can prove that the transformation law between the space-time coordinates of different inertial frames of reference is linear known as the Lorentz boost or transformation. For example, if the frame \mathcal{R}' moves at the speed $v < c$ in the x -direction relative to \mathcal{R} , the coordinate (t', x', y', z') is written as the linear combination of (t, x, y, z) as

$$\begin{pmatrix} ct' \\ x' \\ y' \\ z' \end{pmatrix} = \begin{pmatrix} \gamma & -\gamma\beta & 0 & 0 \\ -\gamma\beta & \gamma & 0 & 0 \\ 0 & 0 & 1 & 0 \\ 0 & 0 & 0 & 1 \end{pmatrix} \begin{pmatrix} ct \\ x \\ y \\ z \end{pmatrix} \quad (\text{A.3})$$

A Short review on special relativity

where β and γ called Lorentz factor are defined

$$\beta = \frac{v}{c}, \quad \gamma = \frac{1}{\sqrt{1 - \beta^2}}. \quad (\text{A.4})$$

Generally, one can write

$$x'^{\mu} = \Lambda^{\mu}_{\nu} x^{\nu} \quad (\text{A.5})$$

where the Λ matrix represents the Lorentz transformation in the four-dimensional vector space.

The four-dimensional vector space is a pseudo-Euclidean space called the Minkowski space-time because the Minkowski inner product is not positive-definite. The Minkowski inner product is defined as

$$\underline{u} \cdot \underline{v} = \eta_{\mu\nu} u^{\mu} v^{\nu} = u^T \eta v \quad (\text{A.6})$$

where u, v are two four-vectors and $\eta = \text{Diag}(1, -1, -1, -1)$.¹ As the rotations are isometries of three-dimensional Euclidean space that preserve the Euclidean scalar product, the Lorentz transformations are isometries of the Minkowski four-dimensional space-time that preserve the Minkowski inner product. Note that rotations acting on the three spatial dimensions of four-vector are also isometries of the Minkowski space-time. The isometries preserving the Minkowski inner product form a group called the Lorentz group. The elements of the Lorentz group are Lorentz transformation containing both rotations and Lorentz boosts. If translations are included, the larger group is called the Poincaré group.

Practically, all the quantities that can be written as a total contraction of upper and low indices such as $u^{\alpha\beta\gamma} v_{\alpha\beta\gamma}$ are invariant under the Lorentz transformations. Such quantities are called Lorentz invariant. For example, $c^2 t^2 - \mathbf{r}^2$ for a given event of coordinate (ct, \mathbf{r}) in the frame \mathcal{R} is independent of the choice of frames. Depending its sign, the event is time-like if positive, space-like if negative and light-like if zero.

Pursuing the logic in this four-dimensional vector space, other physical quantities can also be arranged in four-vector form. The physical quantities that can be expressed in four-vector, say in group theory, furnish a four-vector representation of the Lorentz group and transforms by Lorentz transformations when changing the frame of reference. Remarkably, these physical quantities follows the Lorentz transformation while changing the frame of reference: coordinates of different frame are re-

¹ $\eta_{\mu\nu} = \eta^{\mu\nu} = \text{Diag}(1, -1, -1, -1)$

lated to each other by a linear transformation Λ . I list a set of physical quantities, that will be useful in the following, in the contravariant form:

$$r^\mu = (ct, \mathbf{r}) \quad \text{four-position} \quad (\text{A.7})$$

$$\partial^\mu = \left(\frac{1}{c} \frac{\partial}{\partial t}, -\nabla \right) \quad \text{four-gradient} \quad (\text{A.8})$$

$$p^\mu = \left(\frac{E}{c}, \mathbf{p} \right) \quad \text{four-momentum} \quad (\text{A.9})$$

$$k^\mu = \left(\frac{\omega}{c}, \mathbf{k} \right) \quad \text{four-wavevector} \quad (\text{A.10})$$

$$J^\mu = (\rho c, \mathbf{J}) \quad \text{four-current} \quad (\text{A.11})$$

$$A^\mu = \left(\frac{\phi}{c}, \mathbf{A} \right) \quad \text{four-potential} \quad (\text{A.12})$$

where $\mu = \{0, 1, 2, 3\}$ in which index 0 corresponds to the temporal dimension and indices 1, 2, 3 are the spatial ones.

A.2 MAXWELL'S EQUATIONS ARE LORENTZ INVARIANT

One can write Maxwell's equations in a form of four-vector (or more precisely, four-tensor). In terms of electric and magnetic field (\mathcal{E} , \mathbf{B}), Maxwell's equations are written as

$$\nabla \cdot \mathcal{E} = \frac{\rho}{\epsilon_0} \quad (\text{A.13})$$

$$\nabla \cdot \mathbf{B} = 0 \quad (\text{A.14})$$

$$\nabla \times \mathcal{E} = -\frac{\partial}{\partial t} \mathbf{B} \quad (\text{A.15})$$

$$\nabla \times \mathbf{B} = \mu_0 \mathbf{J} + \mu_0 \epsilon_0 \frac{\partial}{\partial t} \mathcal{E} \quad (\text{A.16})$$

and the electric and magnetic field is gradient of potential:

$$\mathcal{E} = -\frac{\partial}{\partial t} \mathbf{A} - \nabla \phi \quad (\text{A.17})$$

$$\mathbf{B} = \nabla \times \mathbf{A}. \quad (\text{A.18})$$

A Short review on special relativity

It turns out that both fields can be gathered in an anti-symmetric four-tensor called the electromagnetic field tensor:

$$F^{\mu\nu} = \partial^\mu A^\nu - \partial^\nu A^\mu = \begin{bmatrix} 0 & -\frac{\mathcal{E}_x}{c} & -\frac{\mathcal{E}_y}{c} & -\frac{\mathcal{E}_z}{c} \\ \frac{\mathcal{E}_x}{c} & 0 & -B_z & B_y \\ \frac{\mathcal{E}_y}{c} & B_z & 0 & -B_x \\ \frac{\mathcal{E}_z}{c} & -B_y & B_x & 0 \end{bmatrix}. \quad (\text{A.19})$$

With the help of the electromagnetic field tensor and other four-vectors given previously, Maxwell's equations are written in a Lorentz covariant form

$$\partial_\mu F^{\mu\nu} = \mu_0 J^\nu \quad (\text{A.20})$$

$$\partial_\mu \epsilon^{\mu\nu\rho\sigma} F_{\rho\sigma} = 0 \quad (\text{A.21})$$

where $\epsilon^{\mu\nu\alpha\beta}$ is the Levi-Civita anti-symmetric tensor. Using this Lorentz covariant form, one can derive how electric and magnetic field transforms under the Lorentz transformations. For example, a frame \mathcal{R}' moves relative to the lab frame \mathcal{R} at velocity \mathbf{v} , then

$$\mathcal{E}'_{\parallel} = \mathcal{E}_{\parallel}, \quad \mathcal{E}'_{\perp} = \gamma(\mathcal{E}_{\perp} + \mathbf{v} \times \mathbf{B}) \quad (\text{A.22})$$

$$\mathbf{B}'_{\parallel} = \mathbf{B}_{\parallel}, \quad \mathbf{B}'_{\perp} = \gamma\left(\mathbf{B}_{\perp} - \frac{1}{c^2} \mathbf{v} \times \mathcal{E}\right). \quad (\text{A.23})$$

The signification of this Lorentz covariant form is that Maxwell's equations are exactly the same for every inertial frame of reference using the four-vectors attached to itself. In other words, Maxwell's equations are Lorentz invariant.

B SIMPLIFICATION OF THE GENERIC MODEL

The goal of the present appendix is to simplify the generic model (2.69), which I recall below

$$H(\mathbf{q}) = \mathbf{w} \cdot \mathbf{q} + \sum_{i,j=1}^3 v_{ij} q_i q_j + \Delta \sigma_3. \quad (\text{B.1})$$

As shown below, one can legitimately use on an isotropic model to discuss the Landau quantization of the generic Hamiltonian (2.69). The anisotropy of velocity is erased by rescaling the wavevectors and the magnetic field.

B.1 DIAGONALIZATION OF THE SYMMETRIC VELOCITY TENSOR

The first step is to find the principle axes defined by the eigenvectors of the real symmetric tensor v_{ij} , which can be diagonalized as a matrix

$$v = R v^* R^T \quad (\text{B.2})$$

where $R \in SO(3)$ is an orthogonal rotation matrix and the diagonal matrix v^* contains the three eigenvalues v_i^* . Therefore, in the new basis of space defined by R , the velocity tensor v_{ij} is diagonal with the coefficients v_i^* and the wavevector \mathbf{q} is written as

$$\mathbf{q}^* = R^T \mathbf{q} \quad (\text{B.3})$$

so that

$$\sum_{i=1}^3 v_{ij} q_i = v_j^* q_j^*. \quad (\text{B.4})$$

B Simplification of the generic model

The Hamiltonian becomes

$$H(\mathbf{q}^*) = \mathbf{w}^* \cdot \mathbf{q}^* + \sum_{i=1}^3 v_i^* q_i^* \sigma_i + \Delta \sigma_3 \quad (\text{B.5})$$

where

$$\mathbf{w}^* = R^T \mathbf{w}. \quad (\text{B.6})$$

In the following, I will use the basis R as the starting Cartesian coordinate system.

B.2 RESCALING OF THE WAVEVECTORS AND THE MAGNETIC FIELD

Now getting rid of the star * for simplicity and replacing $i = 1, 2, 3$ by $i = x, y, z$, the Hamiltonian to be rescaled becomes

$$H(\mathbf{q}) = \mathbf{w} \cdot \mathbf{q} + \sum_{i=x,y,z}^3 v_i q_i \sigma_i + \Delta \sigma_z. \quad (\text{B.7})$$

After the rescaling

$$v q'_i = v_i q_i, \quad w'_i q'_i = w_i q_i \quad \text{and thus} \quad w'_i = w_i \frac{v}{v_i}, \quad (\text{B.8})$$

the Hamiltonian becomes

$$H(\mathbf{q}') = \mathbf{w}' \cdot \mathbf{q}' + v \mathbf{q}' \cdot \boldsymbol{\sigma} + \Delta \sigma_z. \quad (\text{B.9})$$

Note that one is free to choose the value of v which would not alter the spectrum of the Hamiltonian.

When a magnetic field is applied to the system, the Peierls substitution with the

$$q_i \rightarrow q_i + e A_i \quad (\text{B.10})$$

becomes

$$q'_i \rightarrow q'_i + e A'_i \quad \text{with} \quad A'_i = A_i \frac{v_i}{v} \quad (\text{B.11})$$

where the vector potential \mathbf{A} is also rescaled by the rescaling of the wavevectors. The magnetic field \mathbf{B} is rescaled by

$$B_k = \epsilon_{ijk} \partial_i A_j \quad \rightarrow \quad B'_k = \epsilon_{ijk} \partial'_i A'_j \quad (\text{B.12})$$

where

$$\partial'_i = \frac{v_i}{v} \partial_i. \quad (\text{B.13})$$

In this way, I transform an anisotropic model in the presence of a magnetic field \mathbf{B} to an isotropic model in the presence of a rescaled magnetic field \mathbf{B}' . The relation between \mathbf{B} and \mathbf{B}' is

$$B'_k = \frac{v_i v_j}{v^2} \epsilon_{ijk} \partial_i A_j = \frac{v_i v_j}{v^2} B_k \quad (\text{B.14})$$

where i, j are two other indices than k and $i \neq j$. Note that this derivation is gauge-independent.

B.3 DIRECTION OF THE TILTING TERM

One can simplify further the Hamiltonian (B.9) by writing

$$w \cdot \mathbf{q} = w \tilde{q}_z \quad (\text{B.15})$$

where the prime ' is omitted and w is the modulus of \mathbf{w} . This defines a new basis in which \mathbf{q} is written as $\tilde{\mathbf{q}}$ and they are related by $\tilde{\mathbf{q}} = T \mathbf{q}$ with $T \in SO(3)$. After a unitary transformation defined by T , the Hamiltonian (B.9) becomes

$$H(\tilde{\mathbf{q}}) = w \tilde{q}_z + v \tilde{\mathbf{q}} \cdot \boldsymbol{\sigma} + \Delta(\cos \theta \sigma_z + \sin \theta \sigma_x) \quad (\text{B.16})$$

where the angle θ is also given by T .

Finally, removing the tilde, the simplified Hamiltonian reads

$$H(\mathbf{q}) = w q_z + v \mathbf{q} \cdot \boldsymbol{\sigma} + \Delta(\cos \theta \sigma_z + \sin \theta \sigma_x) \quad (\text{B.17})$$

or sometimes another form is also useful in practice [see (2.74) where $w_x = 0$]

$$H(\mathbf{q}) = w_x q_x + w_z q_z + v \mathbf{q} \cdot \boldsymbol{\sigma} + \Delta \sigma_z. \quad (\text{B.18})$$

C GAPPED NODAL LINE SEMIMETAL NIOBIUM DI-ARSENIDE

This appendix provides supplementary information on the crystal structure of the gapped nodal line semimetal NbAs₂ discussed in Chapter 2 and 3. The details on the theoretical modeling and the derivation of velocity operators are also given in the present appendix. To simplify the notation, I use $\hbar = 1$.

C.1 CRYSTAL STRUCTURE

The nodal-line semi-metal NbAs₂ belongs to the transition metal di-pnictides family whose atoms are arranged in a monoclinic unit-cell classified in the centrosymmetric space group $C_{12/m1}$. As shown in Fig. C.1, the unit-cell has four copies of NbAs₂. By convention in crystallography, the b -axis is defined as the axis that is perpendicular to the two other axis, a and c , between which the angle β is 119.42° [187]. This is also the convention used in [118]. The lattice parameters are [187]:

a	9.368(2)Å
b	3.396(1)Å
c	7.799(3)Å

Table C.1: Lattice parameter for NbAs₂ unit-cell.

By the previous convention in real space, the three k -vectors in the reciprocal space are defined with respect to the a -, b - and c -axis as k_a , k_b and k_c . k_b is perpendicular to k_a and k_c and the angle formed between k_a and k_c equals to β (or equivalently $\pi - \beta$). The Brillouin zone of NbAs₂ marked by high symmetry point is shown in Fig. C.2(a) where the two yellow lines are tracking the position of the two nodal lines of NbAs₂ in k -space. Along the nodal lines, $Z - I_1$ is the dispersive part and $Y - X_1$ is the flat part. Here, $Z - I_1$ and $Y - X_1$ are segments in k -space perpendicular to the nodal line.

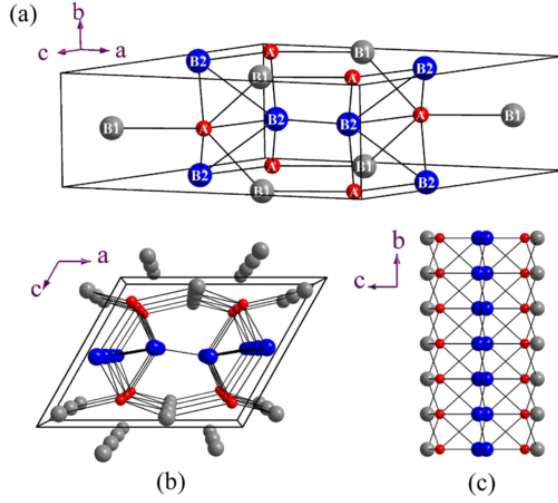


Figure C.1: Crystal structure of NbAs₂: B1 and B2 represent As atoms and A is Nb atom. Picture reprinted from [188].

C.2 LOW ENERGY MODEL FOR TWO NODAL LINES

In this section, I will show how to build a low-energy model for two nodal lines in NbAs₂. First, I restrict the analysis to an energy domain within 0.3 eV where the two nodal lines are the only relevant parts of the band structure for optical measurements in optical measurements [see Fig. C.2(b)].

C.2.1 POSITION OF THE NODAL LINES

The two nodal lines are symmetric with respect to the mirror plane $\Gamma - Z - Y$. They are well-separated in k -space so that one can treat these two lines separately by assigning a valley index to them. The position of the two nodal lines in reciprocal space is shown in Fig. C.3. The two lines are weakly wiggling along the direction $F_1 - Z$ near the plane $F_1 - Z - I_1$. The wiggling amplitude is 0.1 \AA^{-1} which is much smaller than the length of the lines ($\sim 1 \text{ \AA}^{-1}$) [118]. In the first approximation, the nodal lines can be thought to be parallel to the direction $F_1 - Z$ on the the plane $F_1 - Z - I_1$ (or equivalently the a, c -plane) (see Fig. C.3). More accurately, one has to use the natural coordinate system along the line and consider our approximation as a projection on the direction $F_1 - Z$ as shown by the purple triad in the lower panel of Fig. C.3.

C.2.2 LOW-ENERGY HAMILTONIAN

As shown in Shao *et al.*'s work [118], the nodal lines have a flat part and a linearly dispersive part which yield different contributions in the (magneto-)optical responses. In Fig. C.4, the energy profile along one of the two nodal lines is plotted where only half of the full line is shown. The other half can be

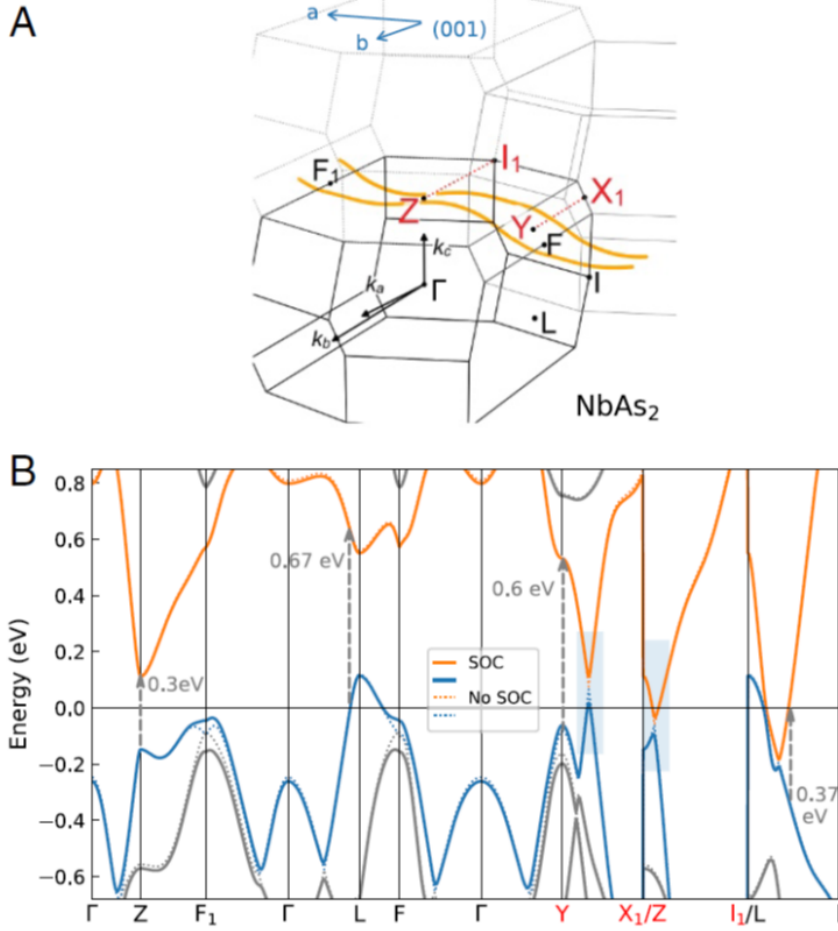


Figure C.2: (A) Brillouin zone of NbAs₂ expanded by k_a , k_b and k_c vectors; (B) Band structure of NbAs₂ calculated by density functional theory (DFT) with and without spin-orbit coupling (SOC). Figures reprinted from [118].

found by mirror and inversion symmetry of the crystal. In our modeling, each nodal line is divided into four parts: ZA , AB , BC and CY segments. Among the four segments, ZA and CY are flat while AB and BC are dispersive.

Nevertheless, the energy profile of all the four segments can be described by the Hamiltonian below ($\hbar = 1$)

$$H(\mathbf{k}) = \epsilon(k_\alpha)\mathbb{I}_2 + \Delta(k_\alpha)\sigma_z + v(\xi k_\beta\sigma_x + k_\gamma\sigma_y) \quad (\text{C.1})$$

where $\sigma_{x,y,z}$ are Pauli matrices, $\xi = \pm 1$ is the valley index and $\epsilon(k_\alpha)$ is defined with respect to the chemical potential. In the following, I consider only one line $\xi = +1$ and the result for the line $\xi = -1$

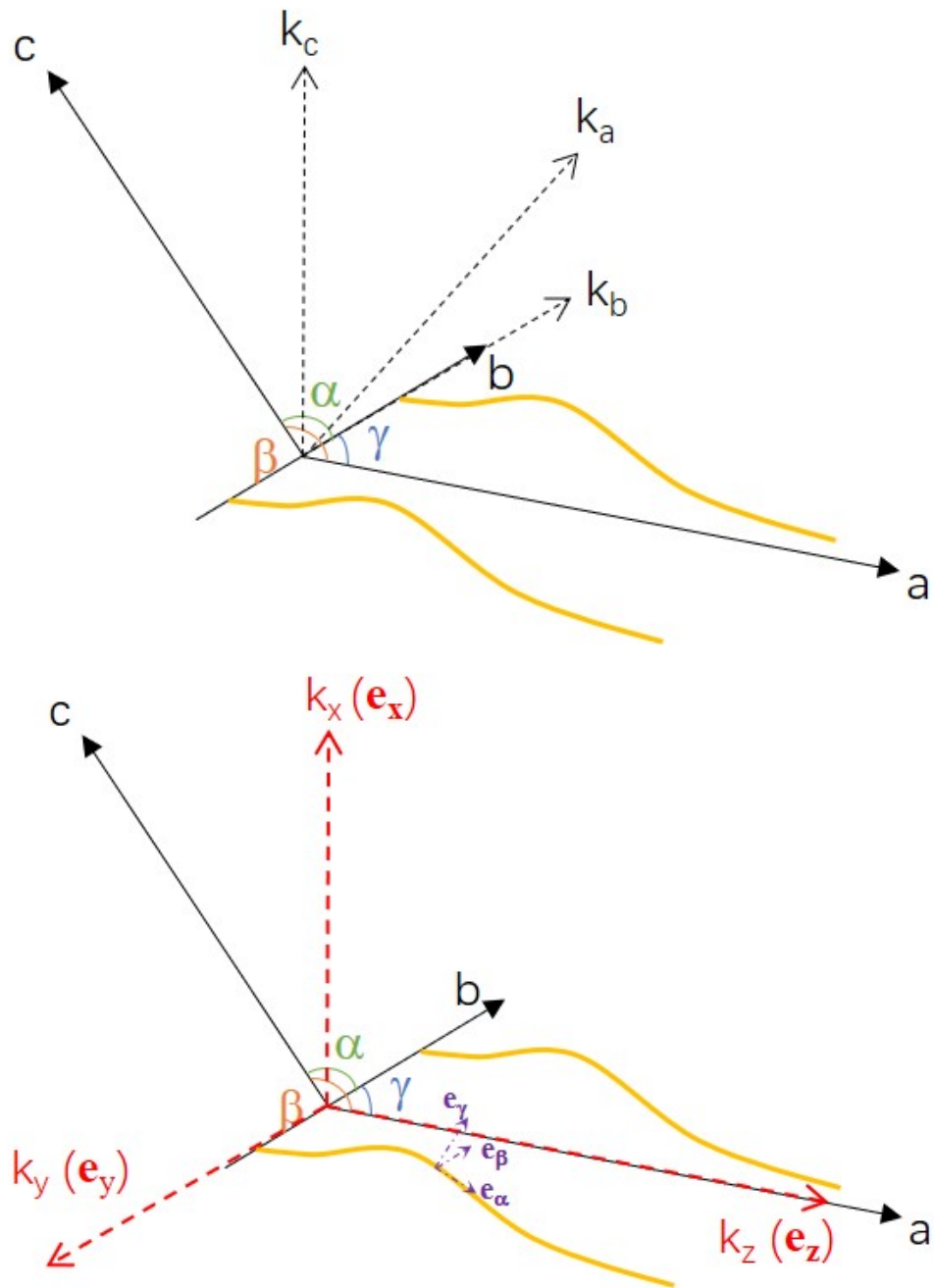


Figure C.3: Schematic illustration of the position of the nodal lines in k -space. The upper panel shows the position of the nodal lines with respect to the real space crystal axes a , b , c and their corresponding reciprocal space axes k_a , k_b , k_c . The lower panel shows the local axes along the nodal line: e_α is parallel to the line and $e_{\beta,\gamma}$ is orthogonal to the line. In the first approximation, e_β is parallel to the b -axis and $e_{\alpha,\gamma}$ is orthogonal to the b -axis.

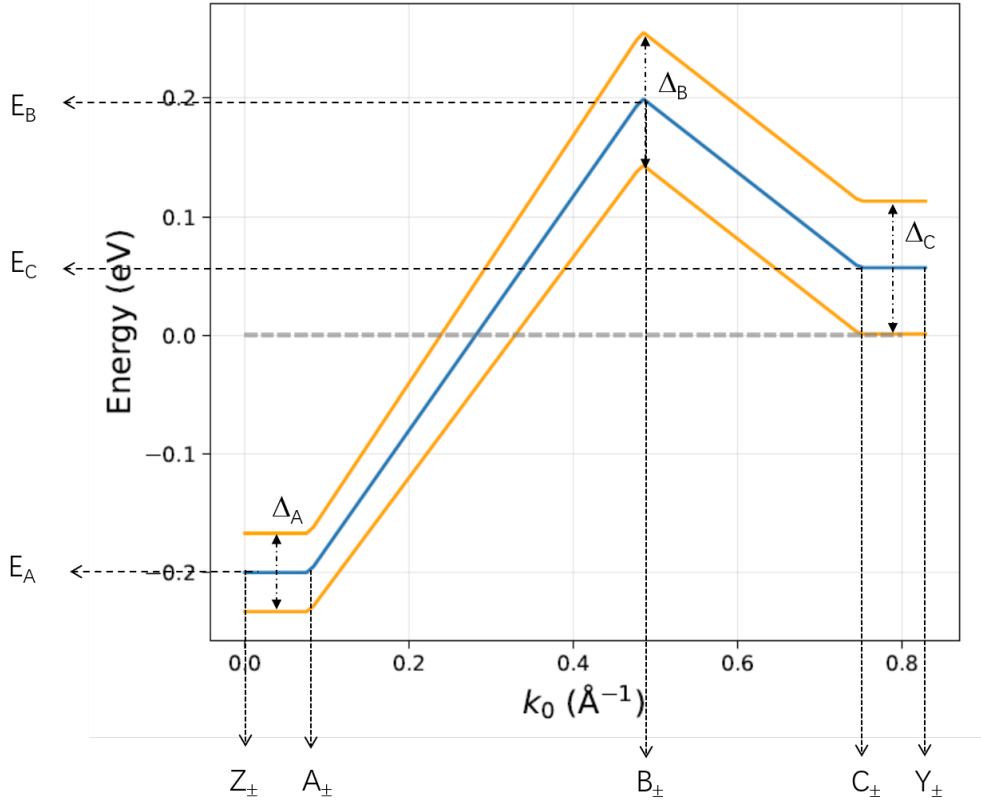


Figure C.4: Energy profile along the nodal line after fitting. k_0 indicates the increment following the nodal line in \mathbf{k} -space. The subscript \pm indicates the two nodal lines according to their position in the coordinate system (k_x, k_y, k_z) . The positions of Z_{\pm} and Y_{\pm} are given by [118].

can be easily deduced for that of $\xi = +1$. Given the parameters $\Delta_{A,B,C}$ and $E_{A,B,C}$ as indicated in Fig. C.4, one can thus determine the exact form of $\Delta(k_{\alpha})$ and $\epsilon(k_{\alpha})$ by doing a linear interpolation between the points Z, A, B, C, Y . $\epsilon(k_{\alpha})$ is constant for the flat parts and linearly dispersive for the dispersive parts. $\Delta(k_{\alpha})$ is defined in the same way as $\epsilon(k_{\alpha})$. For example, the Hamiltonian for the segment AB is

$$H(\mathbf{k}) = E_A + \frac{E_B - E_A}{k_B - k_A}(k_{\alpha} - k_A)\mathbb{I}_2 + \left[\Delta_A + \frac{\Delta_B - \Delta_A}{k_B - k_A}(k_{\alpha} - k_A) \right] \sigma_z + v(\xi k_{\beta} \sigma_x + k_{\gamma} \sigma_y)$$

where $k_{A/B}$ are the coordinates of the points A/B along the nodal line, respectively. Here, I consider an isotropic model where $v_{\beta} = v_{\gamma} = v$. The anisotropy of the Fermi velocity can be added *a posteriori* as a tuning parameter in the fit of the optical conductivity.

C.3 OPTICAL CONDUCTIVITY IN THE ABSENCE OF A MAGNETIC FIELD

In this section, I will give the analytical expression of the optical conductivity in the absence of a magnetic field. Since the nodal lines consist of the four segments in our model, one can separately and analytically calculate the optical conductivity for each segment and sum them all to get the final total optical conductivity.

One only needs to calculate $\Re[\sigma_{\beta\beta}(\omega)]$ and $\Re[\sigma_{\alpha\alpha}(\omega)]$ and $\Re[\sigma_{\beta\beta}(\omega)] = \Re[\sigma_{\gamma\gamma}(\omega)]$ by isotropy. In the absence of a magnetic field,

$$\begin{aligned} \Re[\sigma_{\beta\beta}(\omega)] &= \frac{e^2}{4\pi} \int dk_\alpha \frac{4\Delta^2 + \omega^2}{8\omega^2} [f(\epsilon(k_\alpha) - \omega/2) - f(\epsilon(k_\alpha) + \omega/2)] \\ &\quad \times \Theta(\omega - 2\Delta) \end{aligned} \quad (\text{C.2})$$

$$\begin{aligned} \Re[\sigma_{\alpha\alpha}(\omega)] &= \frac{e^2}{4\pi v^2} \int dk_\alpha \left(\frac{\partial \Delta}{\partial k_\alpha} \right)^2 \frac{\omega^2 - \Delta^2}{4\omega^2} [f(\epsilon(k_\alpha) - \omega/2) - f(\epsilon(k_\alpha) + \omega/2)] \\ &\quad \times \Theta(\omega - 2\Delta) \end{aligned} \quad (\text{C.3})$$

where f is the Fermi-Dirac distribution and Θ is the Heaviside function. Since the dispersion in $\Delta(k_\alpha)$ is small, the contribution from $\sigma_{\alpha\alpha}$ is negligible in practice. To retrieve the optical conductivity in the SI units, one only has to multiply \hbar^{-1} . In practice, one calculates the optical conductivity only for the half of one of the two nodal lines as shown in Fig. C.4 and then multiply by a factor of 4 as the consequence of the mirror and inversion symmetries.

In the reflectivity measurements, incident photons are linearly polarized to the a - and b -axis so that

$$\sigma_{aa} = \cos^2 \theta_a \sigma_{\alpha\alpha} + \sin^2 \theta_a \sigma_{\gamma\gamma} \quad (\text{C.4})$$

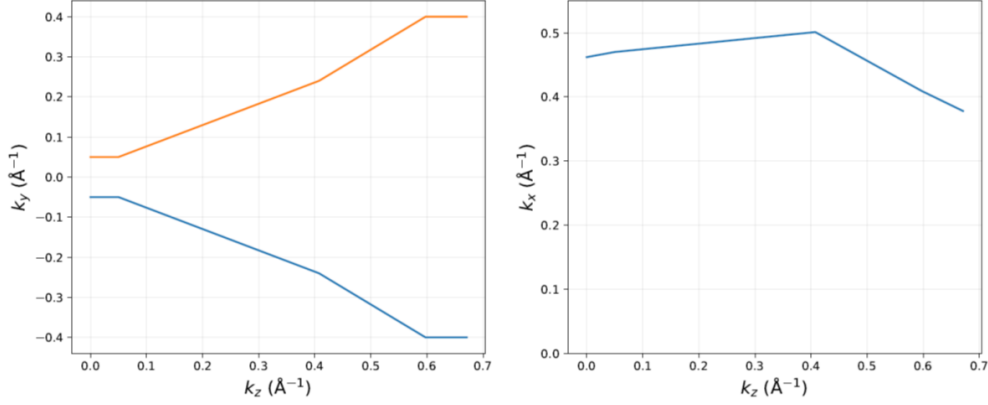
$$\sigma_{bb} = \cos^2 \theta_b \sigma_{\alpha\alpha} + \sin^2 \theta_b \sigma_{\beta\beta} \quad (\text{C.5})$$

where $\theta_{a,b}$ is the angle between e_α and the a, b -axes, respectively. The angles $\theta_{a,b}$ are determined by the position of A, B, C in reciprocal space (see Fig. C.5).

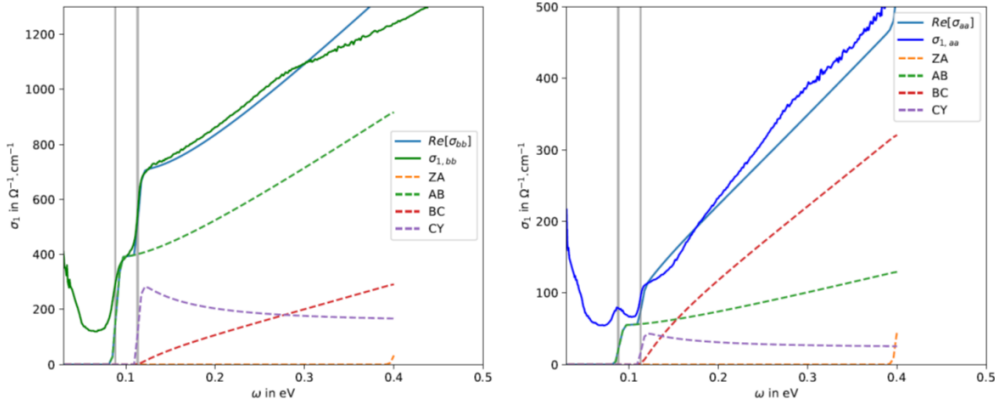
To take into account the anisotropy of the Fermi velocity, one can add a multiplicative constant r such that $\sigma_{\beta\beta} = r\sigma_{\gamma\gamma}$. The ration r depends on the segments of the nodal line. For example, $r_{AB} \neq r_{BC}$.

C.4 FITTING

After fitting, the position of the nodal line in reciprocal space is shown below.


 Figure C.5: Position of the nodal line in k -space after fitting. $k_{x,y,z}$ are given in Fig. C.3

The optical conductivities measured by experiments and those by analytical calculations are shown below. In addition, the contributions from different segments of the nodal line are separately plotted.


 Figure C.6: Optical conductivities measured by experiments $\sigma_{1,aa/bb}$ and those by analytical calculations $\Re[\sigma_{aa/bb}]$.

C.5 SELECTION RULES IN THE PRESENCE OF A MAGNETIC FIELD

Suppose that the gapped nodal line is modeled by the following isotropic Hamiltonian

$$H(\mathbf{k}) = wk_\alpha \mathbb{I}_2 + \Delta\sigma_z + v(k_\beta\sigma_x + k_\gamma\sigma_y) \quad (\text{C.6})$$

where $w < v$ and the subscripts α, β, γ indicate the local triad shown in Fig. C.3.

C.5.1 LANDAU LEVELS

Since Eq. (C.6) is isotropic in the β, γ -plane, one sets with no loss of generality that $\mathbf{B} = B(\cos \theta \mathbf{e}_\alpha + \sin \theta \mathbf{e}_\gamma) = B \mathbf{e}_z$ for $0 < \theta < \pi/2$. Here, a new basis is defined (see the lower panel of Fig. C.3)

$$\{\mathbf{e}_x, \mathbf{e}_y, \mathbf{e}_z\} = \{\cos \theta \mathbf{e}_\gamma - \sin \theta \mathbf{e}_\alpha, -\mathbf{e}_\beta, \cos \theta \mathbf{e}_\alpha + \sin \theta \mathbf{e}_\gamma\}. \quad (\text{C.7})$$

Writing the Hamiltonian in this new basis and choosing the Landau gauge $\mathbf{A} = -By \mathbf{e}_x$, the Hamiltonian becomes¹

$$H = w[\cos \theta k_z - \sin \theta (k_x - eBy)] + v[\cos \theta (k_x - eBy) + \sin \theta k_z] \sigma_x - vk_y \sigma_y + \Delta \sigma_z. \quad (\text{C.8})$$

The Hamiltonian H can be solved using the hyperbolic transformation $M = \exp(\phi \sigma_x / 2)$ with the rapidity $\beta = \tanh \phi = w \tan \theta / v$. The transformed Hamiltonian reads

$$H_T = M H M \\ = \frac{wv}{v^*} k_z + \frac{w^2 + v^2}{v^*} k_z \sin \theta \cos \theta \sigma_x + v^* (k_x - eBy) \sigma_x - vk_y \sigma_y + \Delta \sigma_z \quad (\text{C.9})$$

where a new velocity v^* is defined as

$$v^{*2} = v^2 \cos^2 \theta - w^2 \sin^2 \theta \quad \text{with} \quad \gamma = \frac{1}{\sqrt{1 - \beta^2}} = \cosh \phi = \frac{v \cos \theta}{v^*} \quad (\text{C.10})$$

where $\gamma > 1$ is the relativistic Lorentz factor. Note that H_T does not have the same spectrum as H . In the basis of $|\psi_T\rangle = \gamma^{-1/2} M^{-1} |\psi\rangle$ given the eigenstate $|\psi\rangle$ of H , one can construct from H_T another Hamiltonian $H_E = (H_T - E \sinh \phi \sigma_x) / \cosh \phi$ with the same spectrum as H

$$H_E = \frac{wk_z}{\cos \theta} + \frac{1}{\gamma} \begin{bmatrix} \Delta & \frac{\sqrt{2vv^*}}{\ell_B} a_E^\dagger \\ \frac{\sqrt{2vv^*}}{\ell_B} a_E & -\Delta \end{bmatrix} \quad (\text{C.11})$$

¹Compared to the Hamiltonian in the main text, the additional negative sign in front of the k_y term is to keep the triad x, y, z to be a right-hand system. There is no influence for the final conclusions if the two mirror-symmetric lines are simultaneously considered.

where a pair of energy-dependent ladder operators is defined

$$\begin{aligned}
 a_E &= -\frac{\ell_B}{\sqrt{2vv^*}} \left(\frac{v^*}{\ell_B} (y - \langle y \rangle_E) + ivk_y \right) \\
 a_E^\dagger &= -\frac{\ell_B}{\sqrt{2vv^*}} \left(\frac{v^*}{\ell_B} (y - \langle y \rangle_E) - ivk_y \right) \\
 \langle y \rangle_E &= \frac{\ell_B^2}{v^*} \left(v^* k_x + k_z (w^2 + v^2) \sin \theta \cos \theta - E \frac{w \sin \theta}{v^*} \right)
 \end{aligned} \tag{C.12}$$

with $[a_E, a_E^\dagger] = 1$. The subscript E indicates the dependence on energy E . In particular, the center of cyclotron $\langle y \rangle_E$ shifts with energy.

Since the energy-dependent term in H_E is absorbed in the definition of the ladder operators, the energy spectrum is self-consistently found in the eigenstates of energy E_n^λ in the form

$$|\psi_{T,n,\lambda}\rangle = \begin{pmatrix} \cos \alpha_{n,\lambda} |n, E_n^\lambda\rangle \\ \sin \alpha_{n,\lambda} |n-1, E_n^\lambda\rangle \end{pmatrix} \tag{C.13}$$

where $\alpha_{n,\lambda}$ is an angle depending on n and the sign of energy $\lambda = \pm$; $|n', E_n^\lambda\rangle$ is the wavefunction of the one-dimensional quantum harmonic oscillator defined by the previous ladder operators. Given the Landau level index n , $n' = n$ or $n-1$. The energy spectrum is thus

$$\begin{aligned}
 E_n^\pm &= \frac{wk_z}{\cos \theta} \pm \frac{1}{\gamma} \sqrt{\Delta^2 + \frac{2nv^2 \cos \theta}{\gamma \ell_B^2}} && \text{for } n > 0 \\
 E_0 &= \frac{wk_z}{\cos \theta} + \frac{\Delta}{\gamma} && \text{for } n = 0
 \end{aligned} \tag{C.14}$$

C.5.2 VELOCITY OPERATORS

To study the magneto-optical properties of NbAs₂, one evaluates the matrix element $\langle \psi_n | \hat{v}_{\mathbf{k}} | \psi_m \rangle$. Indeed, it is more practical with the basis $|\psi_{T,n}\rangle$ already in hands by remarking that

$$\langle \psi_n | \nabla_{\mathbf{k}} H | \psi_{n'} \rangle = \gamma \langle \psi_{T,n} | \nabla_{\mathbf{k}} H_T | \psi_{T,n'} \rangle \tag{C.15}$$

thanks to the fact that M is k -independent. So, in the basis $|\psi_T\rangle$, the velocity operators for H_T are

$$\hat{v}_{T,x} = v^* \sigma_x \tag{C.16}$$

$$\hat{v}_{T,y} = -v \sigma_y \tag{C.17}$$

$$\hat{v}_{T,z} = \frac{wv}{v^*} + \frac{w^2 + v^2}{v^*} \sin \theta \cos \theta \tag{C.18}$$

C Gapped nodal line semimetal niobium di-arsenide

where one notices an emergent anisotropy of Fermi velocity induced by the magnetic field.

D CALCULATIONS FOR DOUBLE DIRAC QUANTUM WELL

This appendix shows the details of calculations of how to derive the spectrum of the double Dirac quantum well (QW) modeled in Chapter 4. In particular, I derive the energy splitting for the topological $n = 0$ states for sharp and smooth surfaces.

D.1 DERIVE AND SOLVE THE SECULAR EQUATION FOR DOUBLE DIRAC QUANTUM WELL

In this section, I solve Eq. (4.20) for $\Delta(z)$ described by Eq. (4.28). In all the following discussions, the subscript L and R mean the left and right Dirac QW. One should not confound L in the subscript with the separation between two adjacent Dirac QWs L .

If $z < -L/2 - \ell$ or $z > L/2 + \ell$ or $z \in [-\frac{L}{2} + \ell, \frac{L}{2} - \ell]$, the equation reads

$$\partial_z^2 \chi_\lambda - K^2 \chi_\lambda = 0 \quad (\text{D.1})$$

where $K^2 = (1 - \omega_r^2)/\xi^2$. Recall that $\xi = \hbar v/\Delta_0$. The solutions are a linear combination of $\exp(Kz)$ and $\exp(-Kz)$. If $z \in [-\frac{L}{2} - \ell, -\frac{L}{2} + \ell]$, one can carry out a change of variable $z + L/2 = \alpha t_L$ and $\alpha^2 = \ell\xi/2$. The equation then reads

$$\partial_{t_L}^2 \chi_\lambda - \left(\frac{1}{4} t_L^2 + a_{L,\lambda} \right) \chi_\lambda = 0 \quad (\text{D.2})$$

where

$$a_{L,\lambda} = -\frac{\lambda}{2} - \frac{\ell}{2\xi} \omega_r^2. \quad (\text{D.3})$$

D Calculations for double Dirac quantum well

Eq. (D.2) is the standard form of the Weber differential equation whose solution is parabolic cylinder function [189, 190]. By concern for symmetry of the wavefunction, I represent the solution in terms of confluent hypergeometric function $M(a; b; z)$ [189, 190]. The even and odd solutions read

$$\begin{aligned} u_S(a_{L,\lambda}; t_L) &= e^{-\frac{t_L^2}{4}} M\left(\frac{1}{2}a_{L,\lambda} + \frac{1}{4}; \frac{1}{2}; \frac{t_L^2}{2}\right) \\ u_A(a_{L,\lambda}; t_L) &= t_L e^{-\frac{t_L^2}{4}} M\left(\frac{1}{2}a_{L,\lambda} + \frac{3}{4}; \frac{3}{2}; \frac{t_L^2}{2}\right) \end{aligned} \quad (\text{D.4})$$

where S and A mean symmetric and anti-symmetric, respectively.

If $z \in [\frac{L}{2} - \ell, \frac{L}{2} + \ell]$, one can solve the differential equation and represent the solutions in the similar way. After a change of variable $z - L/2 = \alpha t_R$,

$$\partial_{t_R}^2 \chi_\lambda - \left(\frac{1}{4}t_R^2 + a_{R,\lambda}\right) \chi_\lambda = 0 \quad (\text{D.5})$$

where

$$a_{R,\lambda} = \frac{\lambda}{2} - \frac{\ell}{2\xi} \omega_1^2. \quad (\text{D.6})$$

Similarly, the solutions for Eq. (D.5) are

$$\begin{aligned} u_S(a_{R,\lambda}; t_R) &= e^{-\frac{t_R^2}{4}} M\left(\frac{1}{2}a_{R,\lambda} + \frac{1}{4}; \frac{1}{2}; \frac{t_R^2}{2}\right) \\ u_A(a_{R,\lambda}; t_R) &= t_R e^{-\frac{t_R^2}{4}} M\left(\frac{1}{2}a_{R,\lambda} + \frac{3}{4}; \frac{3}{2}; \frac{t_R^2}{2}\right) \end{aligned} \quad (\text{D.7})$$

Using the fact that the wavefunction is vanishing at infinity and it is continuous as well as its derivative, one can match the solution in different regions at their common point along the z -direction. For simplicity, I note

$$\begin{aligned} u_{S/A,L/R,\lambda} &= u_{S/A}\left(a_{L/R,\lambda}; \sqrt{\frac{2\ell}{\xi}}\right) \\ v_{S/A,L/R,\lambda} &= \frac{\partial}{\partial t_{L/R}} u_{S/A}(a_{L/R,\lambda}; t_{L/R}) \Big|_{t_{L/R}=\sqrt{\frac{2\ell}{\xi}}}. \end{aligned} \quad (\text{D.8})$$

Since $\lambda = \pm$ are equivalent when one considers double Dirac QW, I will omit λ in the following discussion. The final secular equation reads

$$\begin{aligned}
 & \left(\sqrt{\frac{\ell(1-\omega_r^2)}{\xi}} u_{S,L} + v_{S,L} \right) \times \left(\sqrt{\frac{\ell(1-\omega_r^2)}{\xi}} u_{A,L} + v_{A,L} \right) \\
 & \times \left(\sqrt{\frac{\ell(1-\omega_r^2)}{\xi}} u_{S,R} + v_{S,R} \right) \times \left(\sqrt{\frac{\ell(1-\omega_r^2)}{\xi}} u_{A,R} + v_{A,R} \right) \\
 & = e^{-2\frac{\sqrt{1-\omega_r^2}}{\xi}(L-2\ell)} \left(\frac{\ell(1-\omega_r^2)}{\xi} u_{S,R} u_{A,R} - v_{S,R} v_{A,R} \right) \left(\frac{\ell(1-\omega_r^2)}{\xi} u_{S,L} u_{A,L} - v_{S,L} v_{A,L} \right)
 \end{aligned} \tag{D.9}$$

One can try several particular solution to check the validity of the model. Suppose now $\omega_r = 0$ which it is in principle impossible to be a solution for finite L and non-zero ℓ . Eq. (D.9) would become

$$\frac{\ell}{2\xi} e^{-\frac{2(L-2\ell)}{\xi}} (\dots)(\dots) = 0 \tag{D.10}$$

which cannot be true except when the surface is sharp ($\ell \ll \xi$) and the distance between two QWs is large ($L \gg \ell, \xi$). In fact, when $\ell \rightarrow 0$, there are only three domains along the z -direction: $z < -L/2$, $z \in]-L/2, L/2[$ and $z > L/2$. So, there are only two continuity relations for four coefficients, which means two degenerate solutions for $\omega_r = 0$. Another interesting value for ω_r is $\omega_r = 1$. One can check that $\omega_r = 1$ is always a solution of Eq. (D.9) for any parameters. So, one also retrieves automatically the bulk spectrum, $E = \pm \sqrt{\hbar^2 v^2 k_{\parallel}^2 + \Delta_0^2}$, within the model.

D.2 ENERGY SPLITTING FOR THE TOPOLOGICAL STATE

I consider first a sharp surface when $\ell \ll \xi$ and derive a formula to evaluate the mass gap of the chiral mode. To do so, one can develop Eq. (D.9) in terms ℓ/ξ and suppose in the first approximation that ω_r is at most of same order of $\sqrt{\ell/\xi}$. After some algebra, one has

$$2\Delta E = 2\Delta_0 e^{-\frac{L}{\xi}} \sqrt{1 + \frac{4\ell^2}{3\xi^2}}. \tag{D.11}$$

Next, I calculate the energy splitting for the $n = 0$ state for a smooth surface ($\ell > \xi$) to the first-order in perturbation theory. As explained in the main text, the leading order of perturbation to open a gap is given by the process that the chiral state is weakly affected by the deviation of the potential $U_{\lambda}(z)$ from Δ_0^2 in the exponential tail.

D Calculations for double Dirac quantum well

Consider, for example, the chirality $\lambda = +$, in which the $n = 0$ state is located in the left QW. The wavefunction is centered at $z = -L/2$ of form

$$\chi_+^0 \sim \begin{cases} e^{-(z+L/2)^2/2\xi\ell} & \text{for } |z + L/2| < \ell \\ e^{-|z+L/2|/\xi} & \text{for } |z + L/2| > \ell, \end{cases} \quad (\text{D.12})$$

This wavefunction represents the exact zero-energy state when the QW potential is constant when $z > -L/2 + \ell$ so that $U_+(z > -L/2 + \ell) = \Delta_0^2$, i.e., when there is no second QW. The other QW at $z = L/2$ therefore gives rise to a deviation

$$\Delta U_+(z) = \Delta_0^2 \left[\left(\frac{\xi}{\ell} - 1 \right) + \left(\frac{2z - L}{2\ell} \right)^2 \right], \quad (\text{D.13})$$

and the deviation in energy of the zero mode can be calculated as

$$\Delta E_0^2 = \int_{-\infty}^{\infty} dz \chi_+^{0*}(z) \Delta U_+(z) \chi_+^0(z). \quad (\text{D.14})$$

In terms of $\Delta\omega_r^2$, the formula reads

$$\Delta\omega_r^2 = A^2 \frac{\xi^3}{2\ell^2} e^{-\frac{2L-\ell}{\xi}} \left[\sinh\left(\frac{2\ell}{\xi}\right) - \frac{2\ell}{\xi} e^{-\frac{2\ell}{\xi}} \right] \quad (\text{D.15})$$

where A is the normalization factor of the wavefunction χ_+^0 :

$$A^{-2} = \sqrt{\pi\ell\xi} \operatorname{erf}\left(\sqrt{\frac{\ell}{\xi}}\right) + \xi e^{-\frac{\ell}{\xi}} \quad (\text{D.16})$$

where $\operatorname{erf}(x)$ is the error function. When $\ell/\xi \gg 1$, we have

$$\Delta E_0 = \frac{\Delta_0}{2\pi^{1/4}} \left(\frac{\xi}{\ell} \right)^{5/4} e^{-\frac{L_{\text{eff}}}{\xi}} \quad (\text{D.17})$$

where L_{eff} is now $L - 1.5\ell$. One can easily remark that this formula captures the exponential decay of E_0 as a function of L/ξ . In the other hand, the formula (D.17), though limited at the first order of perturbation, gives a rather good approximation to the result by the secular equation Eq. (D.9) especially when ℓ/ξ is not too large [green line in Fig. 4.8(b)]. The reason for the discrepancy is that higher order contributions in perturbation theory are non-negligible when L_{eff} becomes smaller. In a

D.2 Energy splitting for the topological state

tunneling point of view, since the energy spacing between the $n = 1$ VP states and the chiral state is a decreasing function of ℓ/ξ , the hybridization between them is thus stronger with increasing ℓ/ξ .

E MAGNETO-OPTICAL CONDUCTIVITY OF 2D TOPOLOGICAL HETEROJUNCTION

In this appendix, I show the details of calculations of the optical conductivity of the 2D toy model given in Chapter 4 in the absence and the presence of a magnetic field. The idea is to show how the machinery of the Kubo formula (3.12) works in a concrete example. The calculations for 3D heterojunctions have been exactly performed in the same way as shown in detail in the supplementary material of [159].

For notational simplicity, $\hbar = 1$. The temperature is set to be zero and the chemical potential is at the charge neutrality point.

E.1 WAVEFUNCTIONS OF THE 2D TOY MODEL

E.1.1 IN THE ABSENCE OF A MAGNETIC FIELD

The Hamiltonian to study is

$$H_T = v \begin{bmatrix} k_y & \frac{\sqrt{2}}{\ell_S} \hat{a}^\dagger \\ \frac{\sqrt{2}}{\ell_S} \hat{a} & -k_y \end{bmatrix} \quad (\text{E.1})$$

The eigenstates have the shape of

$$\begin{aligned} |\psi_n^\lambda\rangle &= \begin{pmatrix} a_{1,n}^\lambda |n\rangle \\ a_{2,n}^\lambda |n-1\rangle \end{pmatrix} && \text{if } n \geq 1 \\ |\psi_0\rangle &= \begin{pmatrix} a_{1,0} |0\rangle \\ 0 \end{pmatrix} && \text{if } n = 0 \end{aligned} \quad (\text{E.2})$$

with $\lambda = \pm$. In this basis, the Hamiltonian becomes

$$H_{T,n} = v \begin{bmatrix} k_y & \frac{\sqrt{2n}}{\ell_S} \\ \frac{\sqrt{2n}}{\ell_S} & -k_y \end{bmatrix} = v \sqrt{k_y^2 + \frac{2n}{\ell_S^2}} \begin{bmatrix} \cos \alpha_n & \sin \alpha_n \\ \sin \alpha_n & -\cos \alpha_n \end{bmatrix} \quad (\text{E.3})$$

where

$$\begin{aligned} \text{if } n \geq 1 \quad \cos \alpha_n &= \frac{k_y}{\sqrt{k_y^2 + \frac{2n}{\ell_S^2}}} \\ \sin \alpha_n &= \frac{\frac{\sqrt{2n}}{\ell_S}}{\sqrt{k_y^2 + \frac{2n}{\ell_S^2}}}, \\ \text{if } n = 0 \quad \cos \alpha_0 &= 1 \\ \sin \alpha_0 &= 0 \end{aligned}$$

so that $\alpha_n \in [0, \pi]$. The corresponding eigenvectors are

$$\psi_n^+ = \begin{pmatrix} \cos \frac{\alpha_n}{2} \\ \sin \frac{\alpha_n}{2} \end{pmatrix} \quad \text{if } n \geq 1 \quad (\text{E.4})$$

$$\psi_n^- = \begin{pmatrix} -\sin \frac{\alpha_n}{2} \\ \cos \frac{\alpha_n}{2} \end{pmatrix} \quad (\text{E.5})$$

$$\psi_0 = \begin{pmatrix} 1 \\ 0 \end{pmatrix} \quad \text{if } n = 0 \quad (\text{E.6})$$

E.1.2 IN THE PRESENCE OF A MAGNETIC FIELD

The Hamiltonian is

$$H_T = v \begin{bmatrix} k_y \cos \theta & \frac{\sqrt{2}}{\ell_T} \hat{a}^\dagger \\ \frac{\sqrt{2}}{\ell_T} \hat{a} & -k_y \cos \theta \end{bmatrix} \quad (\text{E.7})$$

where the definition of ℓ_T is given by (5.9). The eigenstates have the form of

$$\begin{aligned} |\psi_n^\lambda\rangle &= \begin{pmatrix} a_{1,n}^\lambda |n-1\rangle \\ a_{2,n}^\lambda |n\rangle \end{pmatrix} \quad \text{if } n \geq 1 \\ |\psi_0\rangle &= \begin{pmatrix} 0 \\ a_{2,0} |0\rangle \end{pmatrix} \quad \text{if } n = 0 \end{aligned} \quad (\text{E.8})$$

The Hamiltonian in this basis reads

$$H_{T,n} = v \begin{bmatrix} k_y \cos \theta & \frac{\sqrt{2n}}{\ell_T} \\ \frac{\sqrt{2n}}{\ell_T} & -k_y \cos \theta \end{bmatrix} = v \sqrt{k_y^2 \cos^2 \theta + \frac{2n}{\ell_T^2}} \begin{bmatrix} \cos \beta_n & \sin \beta_n \\ \sin \beta_n & -\cos \beta_n \end{bmatrix} \quad (\text{E.9})$$

where

$$\begin{aligned} \text{if } n \geq 1 \quad \cos \beta_n &= \frac{k_y \cos \theta}{\sqrt{k_y^2 \cos^2 \theta + \frac{2n}{\ell_T^2}}} \\ \sin \beta_n &= \frac{\frac{\sqrt{2n}}{\ell_T}}{\sqrt{k_y^2 \cos^2 \theta + \frac{2n}{\ell_T^2}}}, \\ \text{if } n = 0 \quad \cos \beta_0 &= 1 \\ \sin \beta_0 &= 0 \end{aligned}$$

so that $\beta_n \in [0, \pi]$. The corresponding eigenvectors are

$$\psi_n^+ = \begin{pmatrix} \cos \frac{\beta_n}{2} \\ \sin \frac{\beta_n}{2} \end{pmatrix} \quad \text{if } n \geq 1 \quad (\text{E.10})$$

$$\psi_n^- = \begin{pmatrix} -\sin \frac{\beta_n}{2} \\ \cos \frac{\beta_n}{2} \end{pmatrix} \quad (\text{E.11})$$

$$\psi_0 = \begin{pmatrix} 1 \\ 0 \end{pmatrix} \quad \text{if } n = 0 \quad (\text{E.12})$$

E.2 DERIVATION OF THE SELECTION RULES

E.2.1 IN THE ABSENCE OF A MAGNETIC FIELD

The velocity operators are

$$\hat{v}_x = \nabla_{k_x} H_T = v \sigma_x \quad (\text{E.13})$$

$$\hat{v}_y = \nabla_{k_y} H_T = v \sigma_z \quad (\text{E.14})$$

The matrix elements are evaluated below

$$\langle \psi_m^{\lambda'} | \hat{v}_x | \psi_n^\lambda \rangle = v (a_{1,m}^{\lambda'} a_{2,n}^\lambda \delta_{m,n-1} + a_{2,m}^{\lambda'} a_{1,n}^\lambda \delta_{m-1,n}) \quad (\text{E.15})$$

$$\langle \psi_m^{\lambda'} | \hat{v}_y | \psi_n^\lambda \rangle = v (a_{1,m}^{\lambda'} a_{1,n}^\lambda \delta_{m,n} - a_{2,m}^{\lambda'} a_{2,n}^\lambda \delta_{m-1,n-1}). \quad (\text{E.16})$$

E Magneto-optical conductivity of 2D topological heterojunction

The selection rules are thus

$$\text{Polarization along the } x\text{-axis:} \quad n \rightarrow n \pm 1 \quad (\text{E.17})$$

$$\text{Polarization along the } y\text{-axis:} \quad n^\lambda \rightarrow n^{-\lambda} \quad (\text{E.18})$$

E.2.2 IN THE PRESENCE OF A MAGNETIC FIELD

The velocity operators read

$$\hat{v}_x = \nabla_{k_x} H_T = v \sigma_x \quad (\text{E.19})$$

$$\hat{v}_y = \nabla_{k_y} H_T = v \cos \theta \sigma_z - v \sin \theta \sigma_y \quad (\text{E.20})$$

The matrix elements then have the form of

$$\langle \psi_m^{\lambda'} | \hat{v}_x | \psi_n^\lambda \rangle = v (a_{1,m}^{\lambda'} a_{2,n}^\lambda \delta_{m-1,n} + a_{2,m}^{\lambda'} a_{1,n}^\lambda \delta_{m,n-1}) \quad (\text{E.21})$$

$$\begin{aligned} \langle \psi_m^{\lambda'} | \hat{v}_y | \psi_n^\lambda \rangle = & v [\cos \theta (a_{1,m}^{\lambda'} a_{1,n}^\lambda - a_{2,m}^{\lambda'} a_{2,n}^\lambda) \delta_{m,n} \\ & + i \sin \theta (a_{1,m}^{\lambda'} a_{2,n}^\lambda \delta_{m-1,n} + a_{2,m}^{\lambda'} a_{1,n}^\lambda \delta_{m,n-1})] \end{aligned} \quad (\text{E.22})$$

The selection rules are

$$\text{Polarization along the } x\text{-axis:} \quad n \rightarrow n \pm 1$$

$$\text{Polarization along the } y\text{-axis:} \quad n^\lambda \rightarrow n^{-\lambda}$$

$$n \rightarrow n \pm 1$$

E.3 OPTICAL CONDUCTIVITY IN THE ABSENCE OF A MAGNETIC FIELD

E.3.1 POLARIZATION ALONG THE x -AXIS

The Kubo formula is

$$\begin{aligned} \Re[\sigma_{xx}(\omega \neq 0)] = & \frac{\pi e^2}{\omega} \sum_{\substack{m,n \in \mathbb{N} \\ (n,\lambda), (m,\lambda')}} \int_{-\infty}^{+\infty} \frac{dk_y}{2\pi} (f_D(E_n^\lambda) - f_D(E_m^{\lambda'})) |\langle \psi_m^{\lambda'} | \hat{v}_x | \psi_n^\lambda \rangle|^2 \\ & \times \delta[\omega - (E_m^{\lambda'} - E_n^\lambda)]. \end{aligned} \quad (\text{E.23})$$

This expression is an even function of ω , one can thus suppose $\omega > 0$ and focus on the absorption ($E_m^\lambda > E_n^\lambda$). Since the temperature $T = 0$, the Fermi-Dirac distribution f_D is the Heaviside function. The sum can be divided into three parts:

$$\begin{aligned} \sum_{\substack{m,n \in \mathbb{N} \\ (n,\lambda),(m,\lambda')}} \int_{-\infty}^{+\infty} \frac{dk_y}{2\pi} \dots &= \sum_{\substack{m,n \geq 1 \\ (n,-),(m,+)}} \int_{-\infty}^{+\infty} \frac{dk_y}{2\pi} \dots + \sum_{(0,0),(m,+)} \int_{-\infty}^0 \frac{dk_y}{2\pi} \dots \\ &+ \sum_{(n,-),(0,0)} \int_0^{+\infty} \frac{dk_y}{2\pi} \dots \end{aligned}$$

Therefore, one can evaluate them separately.

The first contribution is

$$\begin{aligned} \sum_{\substack{m,n \geq 1 \\ (n,-),(m,+)}} \dots &= \sum_{\substack{m,n \geq 1 \\ (n,-),(m,+)}} v^2 (a_{1,m}^+ a_{2,n}^- \delta_{m,n-1} + a_{2,m}^+ a_{1,n}^- \delta_{m-1,n})^2 \delta[\omega - (E_m^+ - E_n^-)] \\ &= \sum_{\substack{m,n \geq 1 \\ (n,-),(m,+)}} v^2 \left(\cos \frac{\alpha_m}{2} \cos \frac{\alpha_n}{2} \delta_{m,n-1} - \sin \frac{\alpha_m}{2} \sin \frac{\alpha_n}{2} \delta_{m-1,n} \right)^2 \delta[\omega - (E_m^+ - E_n^-)] \\ &= \sum_{m \geq 1} v^2 \cos^2 \frac{\alpha_m}{2} \cos^2 \frac{\alpha_{m+1}}{2} \delta[\omega - (E_m^+ + E_{m+1}^+)] \\ &+ \sum_{n \geq 1} v^2 \sin^2 \frac{\alpha_n}{2} \sin^2 \frac{\alpha_{n+1}}{2} \delta[\omega - (E_n^+ + E_{n+1}^+)] \\ &= \sum_{n \geq 1} \frac{v^2}{2} (\cos \alpha_n \cos \alpha_{n+1} + 1) \delta \left[\omega - v \sqrt{k_y^2 + \frac{2n}{\ell_S^2}} - v \sqrt{k_y^2 + \frac{2(n+1)}{\ell_S^2}} \right] \end{aligned}$$

Using the identity $\delta(f(x)) = \sum_i \frac{\delta(x-x_i)}{|f'(x_i)|}$ where the x_i are the simple roots of the function $f(x)$, one can do the integrals. I note here

$$f_n(r) = \omega - v \left(\sqrt{r^2 + \frac{2n}{\ell_S^2}} + \sqrt{r^2 + \frac{2(n+1)}{\ell_S^2}} \right) \quad (\text{E.24})$$

with the roots

$$r_{n,\pm} = \pm \frac{1}{2\ell_S^2 \omega v} \sqrt{\ell_S^4 \omega^4 - 4(2n+1)\ell_S^2 \omega^2 v^2 + 4v^4} \quad (\text{E.25})$$

and

$$|f'_n(r_{n,+})| = |f'_n(r_{n,-})| = v r_{n,+} \left(\frac{1}{\sqrt{r_{n,+}^2 + \frac{2n}{\ell_S^2}}} + \frac{1}{\sqrt{r_{n,+}^2 + \frac{2(n+1)}{\ell_S^2}}} \right) \quad (\text{E.26})$$

These roots exist if and only if the photon energy can overcome the gap. Finally, one has

$$\begin{aligned}
 \sum_{\substack{m,n \geq 1 \\ (n,-),(m,+)}} \int_{-\infty}^{+\infty} \frac{dk_y}{2\pi} \dots &= \sum_{n \geq 1} \int_{-\infty}^{+\infty} \frac{dk_y}{2\pi} \frac{v^2}{2} (\cos \alpha_n \cos \alpha_{n+1} + 1) \\
 &\times \delta \left[\omega - v \left(\sqrt{k_y^2 + \frac{2n}{\ell_S^2}} + \sqrt{k_y^2 + \frac{2(n+1)}{\ell_S^2}} \right) \right] \\
 &= \sum_{n \geq 1} \int_{-\infty}^{+\infty} \frac{dk_y}{2\pi} \frac{v^2}{2} (\cos \alpha_n \cos \alpha_{n+1} + 1) \frac{\delta(k_y - r_{n,+}) + \delta(k_y - r_{n,-})}{|f'_n(r_{n,+})|} \\
 &\times \Theta \left(\omega - \frac{\sqrt{2}v}{\ell_S} (\sqrt{n} + \sqrt{n+1}) \right) \\
 &= \sum_{n \geq 1} \frac{v^2}{4\pi |f'_n(r_{n,+})|} [(\cos \alpha_n(r_{n,+}) \cos \alpha_{n+1}(r_{n,+}) + 1) \\
 &+ (\cos \alpha_n(r_{n,-}) \cos \alpha_{n+1}(r_{n,-}) + 1)] \times \Theta \left(\omega - \frac{\sqrt{2}v}{\ell_S} (\sqrt{n} + \sqrt{n+1}) \right) \\
 &= \sum_{n \geq 1} \frac{v^2}{2\pi |f'_n(r_{n,+})|} (\cos \alpha_n(r_{n,+}) \cos \alpha_{n+1}(r_{n,+}) + 1) \\
 &\times \Theta \left(\omega - \frac{\sqrt{2}v}{\ell_S} (\sqrt{n} + \sqrt{n+1}) \right)
 \end{aligned}$$

Similar calculations lead to the two other contributions to the total optical conductivity. The second contribution is

$$\begin{aligned}
 \sum_{(0,0),(m,+)} \int_{-\infty}^0 \frac{dk_y}{2\pi} \dots &= \sum_{(0,0),(m,+)} \int_{-\infty}^0 \frac{dk_y}{2\pi} v^2 (a_{1,m}^+ a_{2,0} \delta_{m,-1} + a_{2,m}^+ a_{1,0} \delta_{m-1,0})^2 \\
 &\times \delta[\omega - (E_m^+ - E_0)] \\
 &= \int_{-\infty}^0 \frac{dk_y}{2\pi} v^2 \sin^2 \frac{\alpha_1}{2} \delta \left[\omega - v \sqrt{k_y^2 + \frac{2}{\ell_S^2}} - v|k_y| \right] \\
 &= \int_{-\infty}^0 \frac{dk_y}{2\pi} v^2 \sin^2 \frac{\alpha_1}{2} \times \frac{\delta(k_y - r_{0,+}) + \delta(k_y - r_{0,-})}{|f'_0(r_{0,+})|} \times \Theta \left(\omega - \frac{\sqrt{2}v}{\ell_S} \right) \\
 &= \frac{v^2}{2\pi |f'_0(r_{0,+})|} \sin^2 \frac{\alpha_1(r_{0,-})}{2} \times \Theta \left(\omega - \frac{\sqrt{2}v}{\ell_S} \right)
 \end{aligned}$$

The third contribution is

$$\begin{aligned}
 \sum_{(n,-),(0,0)} \int_0^{+\infty} \frac{dk_y}{2\pi} \dots &= \sum_{(n,-),(0,0)} \int_0^{+\infty} \frac{dk_y}{2\pi} v^2 (a_{1,0} a_{2,n}^- \delta_{0,n-1} + a_{2,0} a_{1,n}^- \delta_{-1,n})^2 \\
 &\times \delta[\omega - (E_0 - E_n^-)] \\
 &= \int_0^{+\infty} \frac{dk_y}{2\pi} v^2 \cos^2 \frac{\alpha_1}{2} \delta \left[\omega - v \sqrt{k_y^2 + \frac{2}{\ell_S^2}} - v |k_y| \right] \\
 &= \int_0^{+\infty} \frac{dk_y}{2\pi} v^2 \cos^2 \frac{\alpha_1}{2} \times \frac{\delta(k_y - r_{0,+}) + \delta(k_y - r_{0,-})}{|f'_0(r_{0,+})|} \times \Theta \left(\omega - \frac{\sqrt{2}v}{\ell_S} \right) \\
 &= \frac{v^2}{2\pi |f'_0(r_{0,+})|} \cos^2 \frac{\alpha_1(r_{0,+})}{2} \times \Theta \left(\omega - \frac{\sqrt{2}v}{\ell_S} \right)
 \end{aligned}$$

The final expression for $\Re[\sigma_{xx}]$ becomes

$$\begin{aligned}
 \Re[\sigma_{xx}(\omega > 0)] &= \frac{e^2 v^2}{2\omega} \sum_{n \in \mathbb{N}} (\cos \alpha_n(r_{n,+}) \cos \alpha_{n+1}(r_{n,+}) + 1) \\
 &\times \frac{\Theta \left(\omega - \frac{\sqrt{2}v}{\ell_S} (\sqrt{n} + \sqrt{n+1}) \right)}{|f'_n(r_{n,+})|}
 \end{aligned} \tag{E.27}$$

E.3.2 POLARIZATION ALONG THE y -AXIS

The Kubo formula for $\Re[\sigma_{yy}]$ reads

$$\begin{aligned}
 \Re[\sigma_{yy}(\omega \neq 0)] &= \frac{\pi e^2}{\omega} \sum_{\substack{m,n \in \mathbb{N} \\ (n,\lambda),(m,\lambda')}} \int_{-\infty}^{+\infty} \frac{dk_y}{2\pi} (f_D(E_n^\lambda) - f_D(E_m^{\lambda'})) |\langle \psi_m^{\lambda'} | \hat{v}_y | \psi_n^\lambda \rangle|^2 \\
 &\times \delta[\omega - (E_m^{\lambda'} - E_n^\lambda)] \\
 &= \frac{\pi e^2}{\omega} \sum_{n \in \mathbb{N}^*} \int_{-\infty}^{+\infty} \frac{dk_y}{2\pi} |\langle \psi_n^+ | \hat{v}_y | \psi_n^- \rangle|^2 \delta(\omega - 2E_n^+)
 \end{aligned} \tag{E.28}$$

The matrix element reads

$$\begin{aligned}
 |\langle \psi_n^+ | \hat{v}_y | \psi_n^- \rangle|^2 &= v^2 \left(2 \cos \frac{\alpha_n}{2} \sin \frac{\alpha_n}{2} \right)^2 \\
 &= v^2 \sin^2 \alpha_n
 \end{aligned} \tag{E.29}$$

E Magneto-optical conductivity of 2D topological heterojunction

Denote

$$g_n(r) = \omega - 2E_n^+ = \omega - 2v\sqrt{r^2 + \frac{2n}{\ell_S^2}}. \quad (\text{E.30})$$

The corresponding roots are

$$r_{n,\pm} = \pm \frac{\sqrt{\ell_S^2 \omega^2 - 8nv^2}}{2\ell_S v} \quad (\text{E.31})$$

and

$$|g'_n(r_{n,+})| = |g'_n(r_{n,-})| = 2v\sqrt{1 - \frac{8nv^2}{\ell_S^2 \omega^2}} \quad (\text{E.32})$$

The integral to do becomes

$$\begin{aligned} \int_{-\infty}^{+\infty} \frac{dk_y}{2\pi} |\langle \psi_n^+ | \hat{v}_y | \psi_n^- \rangle|^2 \delta(\omega - 2E_n^+) &= \int_{-\infty}^{+\infty} \frac{dk_y}{2\pi} v^2 \sin^2 \alpha_n \frac{\delta(k_y - r_{n,+}) + \delta(k_y - r_{n,-})}{|g'_n(r_{n,+})|} \\ &\times \Theta\left(\omega - \frac{2\sqrt{2nv}}{\ell_S}\right) \\ &= \frac{v^2}{\pi |g'_n(r_{n,+})|} \sin^2 \alpha_n \times \Theta\left(\omega - \frac{2\sqrt{2nv}}{\ell_S}\right) \end{aligned}$$

Finally, the real part of σ_{yy} is

$$\boxed{\Re[\sigma_{yy}(\omega > 0)] = \frac{e^2 v^2}{\omega} \sum_{n \in \mathbb{N}^*} \sin^2 \alpha_n \times \frac{\Theta\left(\omega - \frac{2\sqrt{2nv}}{\ell_S}\right)}{|g'_n(r_{n,+})|}} \quad (\text{E.33})$$

E.4 OPTICAL CONDUCTIVITY IN THE PRESENCE OF A MAGNETIC FIELD

E.4.1 POLARIZATION ALONG THE x -AXIS

The Kubo formula has exactly the same form as (E.23). Similarly, one can divide the sum into three parts:

$$\sum_{\substack{m, n \in \mathbb{N} \\ (n, \lambda), (m, \lambda')}} \int_{-\infty}^{+\infty} \frac{dk_y}{2\pi} \dots = \sum_{\substack{m, n \geq 1 \\ (n, -), (m, +)}} \int_{-\infty}^{+\infty} \frac{dk_y}{2\pi} \dots + \sum_{(0,0), (m,+)} \int_{-\infty}^0 \frac{dk_y}{2\pi} \dots + \sum_{(n,-), (0,0)} \int_0^{+\infty} \frac{dk_y}{2\pi} \dots$$

The first part is

$$\begin{aligned}
 \sum_{\substack{m,n \geq 1 \\ (n,-),(m,+)}} \dots &= \sum_{\substack{m,n \geq 1 \\ (n,-),(m,+)}} v^2 (a_{1,m}^+ a_{2,n}^- \delta_{m-1,n} + a_{2,m}^+ a_{1,n}^- \delta_{m,n-1})^2 \delta(\omega - (E_m^+ - E_n^-)) \\
 &= \sum_{n \geq 1} \frac{v^2}{2} (\cos \beta_n \cos \beta_{n+1} + 1) \\
 &\quad \times \delta \left(\omega - v \sqrt{k_y^2 \cos^2 \theta + \frac{2n}{\ell_T^2}} - v \sqrt{k_y^2 \cos^2 \theta + \frac{2(n+1)}{\ell_T^2}} \right)
 \end{aligned}$$

Denote

$$p_n(r) = \omega - v \sqrt{r^2 + \frac{2n}{\ell_T^2}} - v \sqrt{r^2 + \frac{2(n+1)}{\ell_T^2}} \quad (\text{E.34})$$

The corresponding roots are

$$r_{n,\pm} = \pm \frac{1}{2\ell_T^2 \omega v} \sqrt{\ell_T^4 \omega^4 - 4(2n+1)\ell_T^2 \omega^2 v^2 + 4v^4} \quad (\text{E.35})$$

and

$$|p'_n(r_{n,+})| = |p'_n(r_{n,-})| = v r_{n,+} \left(\frac{1}{\sqrt{r_{n,+}^2 + \frac{2n}{\ell_T^2}}} + \frac{1}{\sqrt{r_{n,+}^2 + \frac{2(n+1)}{\ell_T^2}}} \right) \quad (\text{E.36})$$

When one do a change of variable $k_y \cos \theta \rightarrow k_y$ in the integral, the integral has exactly the same form by a multiplicative factor as that without a magnetic field (E.23). However, one has to use a new definition:

$$\cos \alpha_n = \frac{k_y}{\sqrt{k_y^2 + \frac{2n}{\ell_T^2}}}.$$

The final result reads

$$\begin{aligned}
 \Re[\sigma_{xx}(\omega > 0)] &= \frac{e^2 v^2}{2\omega \cos \theta} \sum_{n \in \mathbb{N}} (\cos \alpha_n(r_{n,+}) \cos \alpha_{n+1}(r_{n,+}) + 1) \\
 &\quad \times \frac{\Theta \left(\omega - \frac{\sqrt{2}v}{\ell_T} (\sqrt{n} + \sqrt{n+1}) \right)}{|p'_n(r_{n,+})|}
 \end{aligned} \quad (\text{E.37})$$

where the factor $1/\cos \theta$ is the consequence of the change of variable $k_y \cos \theta \rightarrow k_y$ in the integral.

E.4.2 POLARIZATION ALONG THE y -AXIS

The matrix element reads

$$|\langle \psi_m^{\lambda'} | \hat{v}_y | \psi_n^\lambda \rangle|^2 = v^2 [\cos^2 \theta (a_{1,m}^{\lambda'} a_{1,n}^\lambda - a_{2,m}^{\lambda'} a_{2,n}^\lambda)^2 \delta_{m,n} + \sin^2 \theta (a_{1,m}^{\lambda'} a_{2,n}^\lambda \delta_{m-1,n} + a_{2,m}^{\lambda'} a_{1,n}^\lambda \delta_{m,n-1})^2]. \quad (\text{E.38})$$

The second term in the matrix element yields σ_{xx} with a prefactor $\sin^2 \theta$ in σ_{yy} . Thus, one only needs to focus on the first term in the matrix element which gives rise to a contribution in the optical conductivity

$$\frac{\pi e^2}{\omega} \sum_{n \in \mathbb{N}^*} \int_{-\infty}^{+\infty} \frac{dk_y}{2\pi} v^2 \cos^2 \theta \sin^2 \beta_n \delta(\omega - 2E_n^+)$$

Denote

$$q_n(r) = \omega - 2E_n^+ = \omega - 2v \sqrt{r^2 + \frac{2n}{\ell_T^2}}. \quad (\text{E.39})$$

The corresponding roots are

$$r_{n,\pm} = \pm \frac{\sqrt{\ell_T^2 \omega^2 - 8nv^2}}{2\ell_T v} \quad (\text{E.40})$$

and

$$|q'_n(r_{n,+})| = |q'_n(r_{n,-})| = 2v \sqrt{1 - \frac{8nv^2}{\ell_T^2 \omega^2}} \quad (\text{E.41})$$

Proceed in exactly the same way as before. One can easily retrieve $\Re[\sigma_{yy}]$ in the presence of a magnetic field using the expression in the absence of a magnetic field after the change of variable $k_y \cos \theta \rightarrow k_y$. Compared to (E.28), the contribution of the first term is

$$\begin{aligned} \frac{\pi e^2}{\omega} \sum_{n \in \mathbb{N}^*} \int_{-\infty}^{+\infty} \frac{dk_y}{2\pi} v^2 \cos^2 \theta \sin^2 \beta_n \delta(\omega - 2E_n^+) &= \cos^2 \theta \times \frac{e^2 v^2}{\omega \cos \theta} \sum_{n \in \mathbb{N}^*} \sin^2 \alpha_n(r_{n,+}) \\ &\times \frac{\Theta\left(\omega - \frac{2\sqrt{2nv}}{\ell_T}\right)}{|q'_n(r_{n,+})|} \end{aligned} \quad (\text{E.42})$$

with

$$\sin \alpha_n = \frac{\sqrt{\frac{2n}{\ell_T^2}}}{\sqrt{k_y^2 + \frac{2n}{\ell_T^2}}}.$$

Finally, the real part of σ_{yy} reads

$$\begin{aligned}
 \Re[\sigma_{yy}(\omega > 0)] &= \frac{e^2 v^2 \sin^2 \theta}{2\omega \cos \theta} \sum_{n \in \mathbb{N}} (\cos \alpha_n(r_{n,+}) \cos \alpha_{n+1}(r_{n,+}) + 1) \\
 &\quad \times \frac{\Theta\left(\omega - \frac{\sqrt{2}v}{\ell_T}(\sqrt{n} + \sqrt{n+1})\right)}{|p'_n(r_{n,+})|} \\
 &\quad + \frac{e^2 v^2 \cos \theta}{\omega} \sum_{n \in \mathbb{N}^*} \sin^2 \alpha_n(r_{n,+}) \\
 &\quad \times \frac{\Theta\left(\omega - \frac{2\sqrt{2}nv}{\ell_T}\right)}{|q'_n(r_{n,+})|}
 \end{aligned} \tag{E.43}$$

or alternatively,

$$\begin{aligned}
 \Re[\sigma_{yy}(\omega > 0)] &= \sin^2 \theta \times \Re[\sigma_{xx}(\omega > 0)] \\
 &\quad + \frac{e^2 v^2 \cos \theta}{\omega} \sum_{n \in \mathbb{N}^*} \sin^2 \alpha_n(r_{n,+}) \times \frac{\Theta\left(\omega - \frac{2\sqrt{2}nv}{\ell_T}\right)}{|q'_n(r_{n,+})|}
 \end{aligned} \tag{E.44}$$

SYNTHÈSE EN FRANÇAIS

La pensée n'est qu'un éclair au milieu d'une longue nuit, mais c'est cet éclair qui est tout.

Henri Poincaré

C'est l'une des découvertes récentes les plus spectaculaires dans le domaine de la physique de la matière condensée : l'équation de Dirac relativiste pour des particules sans masse ou ses variantes peuvent décrire la physique autour du niveau de Fermi de matériaux réels tels que le graphène, les semi-métaux de Dirac/Weyl, les semi-métaux de lignes nodales, etc. Ces matériaux sont appelés matériaux de Dirac dans lesquels le traitement mathématique des électrons est parfaitement identique à celui des particules élémentaires relativistes de la physique des hautes énergies.

L'application de l'équation de Dirac aux matériaux n'est pas seulement bénéfique pour la physique de la matière condensée, mais féconde aussi la physique des hautes énergies. Grâce à l'interaction entre les électrons et leur réseau cristallin sous-jacent, l'équation de Dirac, même ultrarelativiste, émerge de manière inattendue dans la description à basse énergie des matériaux de Dirac. Des expériences fondamentales de la physique des particules, qui ne peuvent pas être réalisées en raison des conditions expérimentales inaccessibles ou des coûts astronomiques, deviennent alors concevables dans des matériaux dans des conditions plus pratiques et économiques. Ainsi des phénomènes qui n'ont pas encore été découverts en physique des hautes énergies, comme la supersymétrie, peuvent être réalisés en physique de la matière condensée. En outre, l'hamiltonien de basse énergie des matériaux de Dirac n'est pas limité par la symétrie de Lorentz contrairement aux particules élémentaires. L'imagination des théoriciens est ainsi davantage libérée. On peut légitimement considérer des variantes de l'équation originale de Dirac sans que celles-ci correspondent à des particules élémentaires existantes. Cependant, rien n'empêche leur apparition en physique de la matière condensée.

Réciproquement, la communauté de la physique de la matière condensée profite du formalisme mathématique déjà établi en physique des particules. Il offre une compréhension rajeunissante et complémentaire des propriétés électroniques des matériaux. Diverses observations inhabituelles dans les matériaux de Dirac, qui ne peuvent pas être expliquées dans le cadre de l'équation de Schrödinger, trou-

vent une explication naturelle et concise par l'équation de Dirac et ses symétries inhérentes. L'application du formalisme stimule davantage la découverte de divers matériaux de Dirac. En particulier, c'est l'une des forces motrices pour donner naissance à la théorie des bandes topologiques, un progrès révolutionnaire en physique du solide. De nombreuses propriétés surprenantes, par exemple la correspondance volume-bord dans les matériaux topologiques, sont également capturées par l'équation de Dirac.

Ces deux aspects de l'équation de Dirac – l'apparition de nouvelles particules et la correspondance volume-bord dans des matériaux topologiques – constituent l'objet de cette thèse dont l'équation de Dirac est donc le fil rouge. Dans la première partie, je montre comment la théorie de la relativité restreinte s'applique à l'électrodynamique dans les matériaux de Dirac. Dans le chapitre 2 après une introduction à l'aspect historique de l'équation de Dirac, je passe en revue les travaux antérieurs sur la renormalisation relativiste dans le graphène soumis à un champ électrique et un champ magnétique croisés [53]. Sur la base de cet exemple simple, j'introduis les transformations unitaires et hyperboliques qui se généralisent à d'autres matériaux de Dirac tels que les semi-métaux de Weyl, le graphène avec gap et inclinaison et les semi-métaux de lignes nodales dispersives avec gap. Alors que des travaux antérieurs se sont intéressés au système sans gap, cette thèse se concentre sur la renormalisation des énergies dans le système avec gap. On trouve en utilisant correctement le formalisme mathématique que le gap du système semble renormalisé en présence d'un champ magnétique par le facteur de Lorentz, γ , qui est déterminé par l'inclinaison dans le hamiltonien. Paradoxalement, le gap est une des propriétés intrinsèques du matériau qui ne devrait pas être modifiée par une perturbation extérieure faible. Surtout, dans certains semi-métaux de lignes nodales dispersives avec gap, la renormalisation du gap dépend de l'orientation du champ magnétique par rapport aux lignes nodales. Autrement dit, le gap du système est contrôlable par le champ magnétique. Pour comprendre ce paradoxe, j'explique la renormalisation relativiste dans le langage de la physique de la matière condensée, ce qui complète la compréhension des phénomènes d'intérêt. D'une part, quand on applique un champ magnétique, le spectre du système est quantifié sous la forme des niveaux de Landau. Ces derniers peuvent être retrouvés semi-classiquement en utilisant la relation d'Onsager qui relie la quantification en orbites des cyclotrons à la surface de Fermi. La renormalisation des énergies est donc interprétée comme la retouche de la forme de la surface de Fermi par le terme de l'inclinaison dans le hamiltonien des matériaux de Dirac. D'autre part, la renormalisation du gap est en effet le résultat de l'existence des deux types de gap, direct et indirect, induite par l'inclinaison. Par exemple, pour un cône de Dirac 2D gappé et incliné [voir Fig. 1(a)], le gap direct est 2Δ mais la séparation minimale entre les bandes de valence et de conduction est $2\Delta/\gamma$, i.e., le gap indirect. Quand le champ magnétique est présent, les bandes deviennent les niveaux de Landau. Après avoir extrapolé le champ magnétique à zéro, le gap extrait est donc le gap indirect, d'où la renormalisation du gap [voir Fig. 1(b)]. Expérimentalement, le gap direct est sondé par la spec-

troscopie infra-rouge sans champ magnétique. En revanche, le gap indirect n'est que mesurable par la spectroscopie magnéto-optique, d'où la motivation de l'étude des propriétés spectroscopiques.

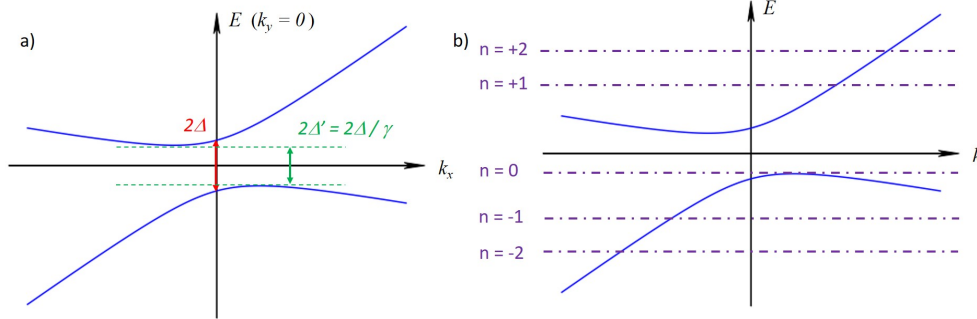


Figure 1: (a) Spectre du graphène gappé et incliné pour $k_y = 0$ sans champ magnétique. Le gap direct marqué en rouge est 2Δ et le gap indirect en vert est $2\Delta' = 2\Delta/\gamma$. (b) Niveaux de Landau du graphène gappé et incliné.

Dans le chapitre 3, j'inclus de façon succincte une introduction aux approches théoriques de la spectroscopie. En particulier, j'y élabore l'étude théorique de la spectroscopie magnéto-optique d'un semi-métal de lignes nodales avec gap, NbAs_2 . Il s'agit d'un projet en collaboration avec mes collègues du LNCMI de Grenoble qui ont réalisé des mesures magnéto-optiques fascinantes de NbAs_2 . Dans ce cadre, la renormalisation des gaps dans ce matériau a été clairement observée (voir Fig. 2), en accord quantitatif avec nos résultats théoriques

$$\Delta_{\text{mesuré}} = \frac{\Delta_{\text{direct}}}{\gamma(\theta)}$$

où γ dépend de l'orientation du champ magnétique appliqué définie par l'angle θ . Dans le même chapitre, je présente aussi la physique du plasmon et l'approche théorique pour l'étudier, i.e., approximation des phases aléatoires. Cette méthode est utile pour discuter le plasmon de surface sur la surface des semi-métaux de Weyl dans le dernier chapitre.

Dans la deuxième partie, je montre que l'équation de Dirac est un cadre théorique unificateur pour étudier les états de surface des matériaux topologiques surtout des états de Volkov-Pankratov. Ces derniers sont des états de surface massifs qui émergent à des surfaces douces des matériaux topologiques en plus des états de surface topologiques. Leur présence est en principe universelle dans toutes les hétérojonctions topologiques, i.e. dans des interfaces douces entre une phase topologique et une phase topologiquement triviale. Dans le chapitre 4, je propose des perspectives particulières pour comprendre l'origine des états de Volkov-Pankratov. Je commence par montrer un point de vue donné par les travaux antérieurs de Sergueï Tchoumakov [132], qui a initié les travaux sur ces états massifs dans notre groupe au cours de sa thèse : la douceur de la surface joue le rôle d'un pseudo-champ magnétique quan-

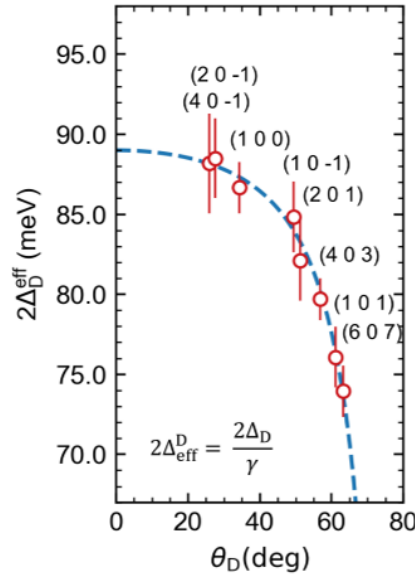


Figure 2: Comparaison entre le gap mesuré par nos collaborateurs du LNCMI à Grenoble (points avec barre d'erreur) et celui prédit par les calculs théoriques. Figure dû à Jan Wyzula du LNCMI.

tifiant les bandes de surface en bandes de Landau. Ensuite, j'élaboré cette perspective en regardant la réduction de la dimensionnalité, ce qui m'a inspiré à interpréter l'origine des états de Volkov-Pankratov en termes de puits quantiques appelés *puits quantiques de Dirac* [137]. Cette dernière perspective, complémentaire du concept *hétérojonctions topologiques* [72], a l'avantage de permettre de discuter de manière intuitive l'effet tunnel entre les états de Volkov-Pankratov situés aux deux côtés d'une tranche d'un matériau topologique. En particulier, la protection topologique des états topologiques est interprétée comme l'absence d'effet tunnel résonant (voir Fig. 3). En outre, je développe aussi le point de vue d'un mathématicien-physicien qui pourrait traiter ce problème en étudiant une équation différentielle dans le cadre de la supersymétrie. Enfin, une approche de liaisons fortes est présentée pour mettre en évidence davantage la présence des états de Volkov-Pankratov et l'hybridation entre les états de Volkov-Pankratov localisés sur les deux surfaces d'un isolant topologique 3D d'épaisseur finie.

Dans le chapitre 5, je discute les propriétés spectroscopiques des états de Volkov-Pankratov en utilisant les techniques présentées au chapitre 3. La signature dans la conductivité (magnéto-)optique révélant la présence d'états de Volkov-Pankratov s'avère être une preuve irréfutable pour les distinguer des états de surface triviaux [159]. En particulier, quand un champ magnétique s'oriente à la direction perpendiculaire à la surface, la conductivité optique se transforme des signaux réguliers en une série des pics divergents (voir Fig. 4). Finalement, j'étudie la plasmonique à la surface du semi-métal de Weyl [176]. En plus du plasmon d'arc de Fermi bien connu, les états de Volkov-Pankratov produisent des

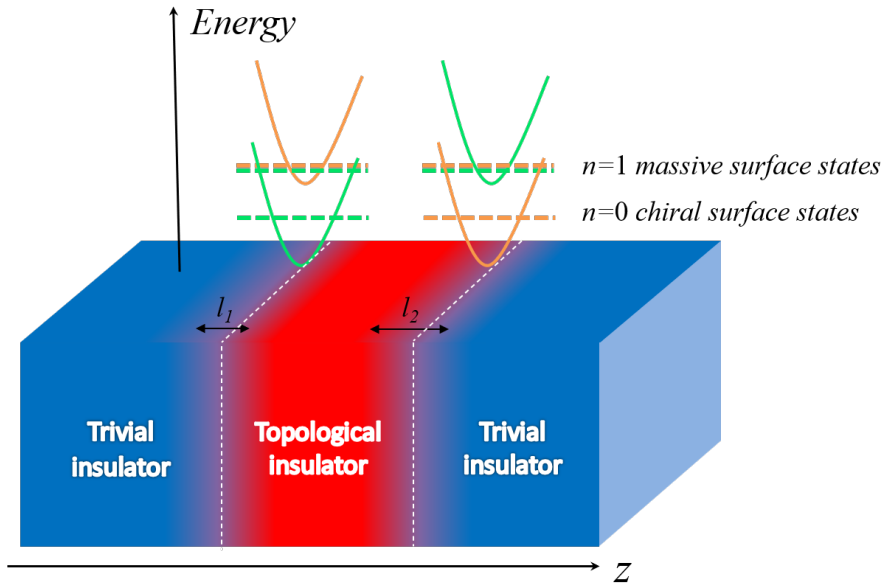


Figure 3: Illustration du double puits de Dirac. Les états chiraux topologiques ont une chiralité définitive, représentée par deux couleurs différentes. Par contre, les états de Volkov-Pankratov ont à la fois deux chiralités opposées. Pour une chiralité donnée, l'effet tunnel est donc résonant entre les états de Volkov-Pankratov, ce qui n'est pas le cas des états chiraux.

plasmons inter- et intra-bandes. De façon inattendue, l'hybridation entre l'arc de Fermi et les plasmons de Volkov-Pankratov transfère la non-réciprocité de l'arc de Fermi aux plasmons de Volkov-Pankratov, qui devraient être réciproques sans cette hybridation. Concrètement, le plasmon se propage avec une vitesse différente dans les directions opposées.

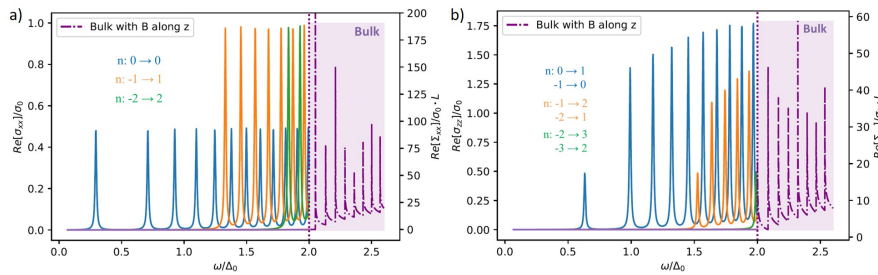


Figure 4: Conductivité optique de la surface douce d'un isolant topologique 3D en présence d'un champ magnétique perpendiculaire à la surface.

Il y a plusieurs ramifications possibles de ma recherche effectuée dans le cadre de cette thèse. Une branche possible consiste à poursuivre l'idée de « faire de la physique des hautes énergies dans des systèmes à basse énergie ». Une branche intéressante consiste à appliquer non seulement la relativité

Synthèse en français

restreinte mais aussi la relativité générale aux matériaux. Une autre branche possible consiste à approfondir les possibilités offertes par les états de Volkov-Pankratov. Dans cette thèse, je n'ai discuté que leurs propriétés spectroscopiques. Les propriétés de transport des états de Volkov-Pankratov méritent d'être étudiées en détail dans un futur proche. Finalement, les effets d'interaction en présence d'états de Volkov-Pankratov pourraient être l'objet de futures études.

ACRONYMS

0,1,2,3D	0,1,2,3 dimensions
ARPES	angle-resolved photoemission spectroscopy
DFT	density functional theory
DOS	density of states
EELS	electron energy loss spectroscopy
FA	Fermi arc
hBN	hexagonal boron nitride
JDOS	joint density of states
NI	topologically trivial normal insulator
QW	quantum well
RPA	random phase approximation
SOC	spin-orbit coupling
STM	scanning tunneling microscope
TI	topological insulator
TRS	time-reversal symmetry
VP	Volkov-Pankratov
WSM	Weyl semimetal

LIST OF SYMBOLS

θ, ϕ	Angles
$\{A, B\}$	Anti-commutator $\{A, B\} = AB + BA$
\mathcal{A}	Berry connection
\mathcal{B}	Berry curvature
$\langle \psi , \psi \rangle$	Bra and ket of the eigenstate ψ
$[A, B]$	Commutator $[A, B] = AB - BA$
σ_{ij}	Conductivity tensor
ω_c	Cyclotron frequency
ϵ	Dielectric function
v_D	Drift velocity
\mathcal{E}	Electric field
e	Elementary charge
E	Energy
v, v_F	Fermi velocity
f_D	Fermi-Dirac distribution function
c^\dagger, c	Fermionic creation and annihilation operators
γ^μ	Gamma matrices in the Dirac equation
\hat{H}, H	Hamiltonian operator, matrix
\hbar	Reduced Planck constant
H.c.	Hermitian conjugate
i	Complex number with $i^2 = -1$
I_2, I_4	Two-by-two, four-by-four identity matrix
$a^\dagger, a, b^\dagger, b$	Bosonic creation and annihilation operators
γ	Lorentz factor
\mathbf{B}	Magnetic field
ℓ_B	Magnetic length
$\eta^{\mu\nu}$	Minkowski metric
\mathbf{p}	Momentum

List of Symbols

∇	Nabla operator
$ n\rangle$	Number state defined by the corresponding ladder operators
σ_i, τ_j	Pauli matrices with $i, j = 1, 2, 3$ or x, y, z
\perp, \parallel	Perpendicular and parallel
π	3.141592657...
\mathbf{r}	Position
$V(\mathbf{r}, t)$	Electric potential at position \mathbf{r} and time t
\mathbf{A}	Potential vector
ω	Angular frequency
β	Rapidity
\Re, \Im	Real and imaginary part
Δ	Dirac mass and/or half of the band gap
ω_r	Reduced energy
ℓ	Characteristic length scale of smoothness
c	Speed of light
χ_{ij}	Charge susceptibility tensor
\mathbf{w}	Tilting speed
$\hat{\mathbf{n}}$	Unit vector
$\psi(\mathbf{r}, t)$	Wavefunction at position \mathbf{r} and time t
\mathbf{q}, \mathbf{k}	Wavevectors

BIBLIOGRAPHY

1. P. A. M. Dirac and R. H. Fowler. “The quantum theory of the electron”. *Proceedings of the Royal Society of London. Series A, Containing Papers of a Mathematical and Physical Character* 117:778, 1928, pp. 610–624. DOI: [10.1098/rspa.1928.0023](https://doi.org/10.1098/rspa.1928.0023). eprint: <https://royalsocietypublishing.org/doi/pdf/10.1098/rspa.1928.0023>. URL: <https://royalsocietypublishing.org/doi/abs/10.1098/rspa.1928.0023>.
2. P. A. M. Dirac. *The principles of quantum mechanics*. 27. Oxford university press, 1981.
3. R. Winkler, S. Papadakis, E. De Poortere, and M. Shayegan. *Spin-Orbit Coupling in Two-Dimensional Electron and Hole Systems*. Vol. 41. Springer, 2003.
4. H. Weyl. “Gravitation and the electron”. *Proceedings of the National Academy of Sciences of the United States of America* 15:4, 1929, p. 323.
5. P. W. Anderson. “More Is Different”. *Science* 177:4047, 1972, pp. 393–396. ISSN: 0036-8075. DOI: [10.1126/science.177.4047.393](https://doi.org/10.1126/science.177.4047.393). eprint: <https://science.sciencemag.org/content/177/4047/393.full.pdf>. URL: <https://science.sciencemag.org/content/177/4047/393>.
6. K. S. Novoselov, A. K. Geim, S. V. Morozov, D. Jiang, Y. Zhang, S. V. Dubonos, I. V. Grigorieva, and A. A. Firsov. “Electric Field Effect in Atomically Thin Carbon Films”. *Science* 306:5696, 2004, pp. 666–669. ISSN: 0036-8075. DOI: [10.1126/science.1102896](https://doi.org/10.1126/science.1102896). eprint: <https://science.sciencemag.org/content/306/5696/666.full.pdf>. URL: <https://science.sciencemag.org/content/306/5696/666>.
7. A. H. Castro Neto, F. Guinea, N. M. R. Peres, K. S. Novoselov, and A. K. Geim. “The electronic properties of graphene”. *Rev. Mod. Phys.* 81, 1 2009, pp. 109–162. DOI: [10.1103/RevModPhys.81.109](https://doi.org/10.1103/RevModPhys.81.109). URL: <https://link.aps.org/doi/10.1103/RevModPhys.81.109>.
8. N. P. Armitage, E. J. Mele, and A. Vishwanath. “Weyl and Dirac semimetals in three-dimensional solids”. *Rev. Mod. Phys.* 90, 1 2018, p. 015001. DOI: [10.1103/RevModPhys.90.015001](https://doi.org/10.1103/RevModPhys.90.015001). URL: <https://link.aps.org/doi/10.1103/RevModPhys.90.015001>.

Bibliography

9. B. Yan and C. Felser. “Topological Materials: Weyl Semimetals”. *Annual Review of Condensed Matter Physics* 8:1, 2017, pp. 337–354. DOI: [10.1146/annurev-conmatphys-031016-025458](https://doi.org/10.1146/annurev-conmatphys-031016-025458). eprint: <https://doi.org/10.1146/annurev-conmatphys-031016-025458>. URL: <https://doi.org/10.1146/annurev-conmatphys-031016-025458>.
10. M. Z. Hasan, S.-Y. Xu, I. Belopolski, and S.-M. Huang. “Discovery of Weyl Fermion Semimetals and Topological Fermi Arc States”. *Annual Review of Condensed Matter Physics* 8:1, 2017, pp. 289–309. DOI: [10.1146/annurev-conmatphys-031016-025225](https://doi.org/10.1146/annurev-conmatphys-031016-025225). eprint: <https://doi.org/10.1146/annurev-conmatphys-031016-025225>. URL: <https://doi.org/10.1146/annurev-conmatphys-031016-025225>.
11. C. Fang, H. Weng, X. Dai, and Z. Fang. “Topological nodal line semimetals”. *Chinese Physics B* 25:11, 2016, p. 117106. DOI: [10.1088/1674-1056/25/11/117106](https://doi.org/10.1088/1674-1056/25/11/117106). URL: <https://doi.org/10.1088/1674-1056/25/11/117106>.
12. F. Bloch. “Über die quantenmechanik der elektronen in kristallgittern”. *Zeitschrift für physik* 52:7, 1929, pp. 555–600.
13. F. D. M. Haldane. “Model for a quantum Hall effect without Landau levels: Condensed-matter realization of the “parity anomaly””. *Physical Review Letters* 61:18, 1988, p. 2015.
14. D. J. Thouless, M. Kohmoto, M. P. Nightingale, and M. den Nijs. “Quantized Hall Conductance in a Two-Dimensional Periodic Potential”. *Phys. Rev. Lett.* 49, 6 1982, pp. 405–408. DOI: [10.1103/PhysRevLett.49.405](https://link.aps.org/doi/10.1103/PhysRevLett.49.405). URL: <https://link.aps.org/doi/10.1103/PhysRevLett.49.405>.
15. N. W. Ashcroft, N. D. Mermin, et al. *Solid state physics*. 1976.
16. N. Savage. “Topological materials move from the world of theoretical physics to experimental chemistry”. *The Guardian*. URL: <https://cen.acs.org/materials/electronic-materials/Topological-materials-move-world-theoretical/96/i26>.
17. R. Jackiw and C. Rebbi. “Solitons with fermion number $\frac{1}{2}$ ”. *Phys. Rev. D* 13, 12 1976, pp. 3398–3409. DOI: [10.1103/PhysRevD.13.3398](https://link.aps.org/doi/10.1103/PhysRevD.13.3398). URL: <https://link.aps.org/doi/10.1103/PhysRevD.13.3398>.
18. Y. Aharonov and A. Casher. “Ground state of a spin-1/2 charged particle in a two-dimensional magnetic field”. *Phys. Rev. A* 19, 6 1979, pp. 2461–2462. DOI: [10.1103/PhysRevA.19.2461](https://link.aps.org/doi/10.1103/PhysRevA.19.2461). URL: <https://link.aps.org/doi/10.1103/PhysRevA.19.2461>.
19. A. K. Cheng. “Electric Transport in Hybrid Carbon Nanotube-Graphene Devices”. PhD thesis. 2019. URL: <https://dash.harvard.edu/handle/1/42029669>.

20. E. Schrödinger. “An Undulatory Theory of the Mechanics of Atoms and Molecules”. *Phys. Rev.* 28, 6 1926, pp. 1049–1070. DOI: [10.1103/PhysRev.28.1049](https://doi.org/10.1103/PhysRev.28.1049). URL: <https://link.aps.org/doi/10.1103/PhysRev.28.1049>.
21. A. Einstein. “Zur elektrodynamik bewegter körper”. *Annalen der physik* 4, 1905.
22. O. Klein. “Quantentheorie und fünfdimensionale Relativitätstheorie”. *Zeitschrift für Physik* 37:12, 1926, pp. 895–906.
23. W. Gordon. “Der comptoneffekt nach der schrödingerschen theorie”. *Zeitschrift für Physik* 40:1-2, 1926, pp. 117–133.
24. A. Zee. *Quantum field theory in a nutshell*. Vol. 7. Princeton university press, 2010.
25. P. A. M. Dirac and R. H. Fowler. “A theory of electrons and protons”. *Proceedings of the Royal Society of London. Series A, Containing Papers of a Mathematical and Physical Character* 126:801, 1930, pp. 360–365. DOI: [10.1098/rspa.1930.0013](https://doi.org/10.1098/rspa.1930.0013). eprint: <https://royalsocietypublishing.org/doi/pdf/10.1098/rspa.1930.0013>. URL: <https://royalsocietypublishing.org/doi/abs/10.1098/rspa.1930.0013>.
26. Y. Peter and M. Cardona. *Fundamentals of semiconductors: physics and materials properties*. Springer Science & Business Media, 2010.
27. G. W. Semenoff. “Condensed-Matter Simulation of a Three-Dimensional Anomaly”. *Phys. Rev. Lett.* 53, 26 1984, pp. 2449–2452. DOI: [10.1103/PhysRevLett.53.2449](https://doi.org/10.1103/PhysRevLett.53.2449). URL: <https://link.aps.org/doi/10.1103/PhysRevLett.53.2449>.
28. D. P. DiVincenzo and E. J. Mele. “Self-consistent effective-mass theory for intralayer screening in graphite intercalation compounds”. *Phys. Rev. B* 29, 4 1984, pp. 1685–1694. DOI: [10.1103/PhysRevB.29.1685](https://doi.org/10.1103/PhysRevB.29.1685). URL: <https://link.aps.org/doi/10.1103/PhysRevB.29.1685>.
29. H. Nielsen and M. Ninomiya. “The Adler-Bell-Jackiw anomaly and Weyl fermions in a crystal”. *Physics Letters B* 130:6, 1983, pp. 389–396. ISSN: 0370-2693. DOI: [https://doi.org/10.1016/0370-2693\(83\)91529-0](https://doi.org/10.1016/0370-2693(83)91529-0). URL: <http://www.sciencedirect.com/science/article/pii/0370269383915290>.
30. X.-F. Zhou, X. Dong, A. R. Oganov, Q. Zhu, Y. Tian, and H.-T. Wang. “Semimetallic Two-Dimensional Boron Allotrope with Massless Dirac Fermions”. *Phys. Rev. Lett.* 112, 8 2014, p. 085502. DOI: [10.1103/PhysRevLett.112.085502](https://doi.org/10.1103/PhysRevLett.112.085502). URL: <https://link.aps.org/doi/10.1103/PhysRevLett.112.085502>.

Bibliography

31. M. O. Goerbig, J.-N. Fuchs, G. Montambaux, and F. Piéchon. “Tilted anisotropic Dirac cones in quinoid-type graphene and α -(BEDT-TTF)₂I₃”. *Phys. Rev. B* 78, 4 2008, p. 045415. DOI: [10.1103/PhysRevB.78.045415](https://doi.org/10.1103/PhysRevB.78.045415). URL: <https://link.aps.org/doi/10.1103/PhysRevB.78.045415>.
32. L. Pauling. “THE STRUCTURE AND PROPERTIES OF GRAPHITE AND BORON NITRIDE”. *Proceedings of the National Academy of Sciences* 56:6, 1966, pp. 1646–1652. ISSN: 0027-8424. DOI: [10.1073/pnas.56.6.1646](https://doi.org/10.1073/pnas.56.6.1646). eprint: <https://www.pnas.org/content/56/6/1646.full.pdf>. URL: <https://www.pnas.org/content/56/6/1646>.
33. A. Kobayashi, S. Katayama, Y. Suzumura, and H. Fukuyama. “Massless Fermions in Organic Conductor”. *Journal of the Physical Society of Japan* 76:3, 2007, p. 034711. DOI: [10.1143/JPSJ.76.034711](https://doi.org/10.1143/JPSJ.76.034711). eprint: <https://doi.org/10.1143/JPSJ.76.034711>. URL: <https://doi.org/10.1143/JPSJ.76.034711>.
34. H. Nielsen and M. Ninomiya. “A no-go theorem for regularizing chiral fermions”. *Physics Letters B* 105:2, 1981, pp. 219–223. ISSN: 0370-2693. DOI: [https://doi.org/10.1016/0370-2693\(81\)91026-1](https://doi.org/10.1016/0370-2693(81)91026-1). URL: <https://www.sciencedirect.com/science/article/pii/0370269381910261>.
35. E. Witten. “Three lectures on topological phases of matter”. *arXiv preprint arXiv:1510.07698*, 2015.
36. C. Herring. “Accidental Degeneracy in the Energy Bands of Crystals”. *Phys. Rev.* 52, 4 1937, pp. 365–373. DOI: [10.1103/PhysRev.52.365](https://doi.org/10.1103/PhysRev.52.365). URL: <https://link.aps.org/doi/10.1103/PhysRev.52.365>.
37. G. E. Volovik. *The universe in a helium droplet*. Vol. 117. Oxford University Press on Demand, 2003.
38. A. A. Soluyanov, D. Gresch, Z. Wang, Q. Wu, M. Troyer, X. Dai, and B. A. Bernevig. “Type-ii weyl semimetals”. *Nature* 527:7579, 2015, pp. 495–498.
39. S.-M. Huang, S.-Y. Xu, I. Belopolski, C.-C. Lee, G. Chang, B. Wang, N. Alidoust, G. Bian, M. Neupane, C. Zhang, et al. “A Weyl Fermion semimetal with surface Fermi arcs in the transition metal monpnictide TaAs class”. *Nature communications* 6:1, 2015, pp. 1–6.
40. Z. Wang, H. Weng, Q. Wu, X. Dai, and Z. Fang. “Three-dimensional Dirac semimetal and quantum transport in Cd₃As₂”. *Phys. Rev. B* 88, 12 2013, p. 125427. DOI: [10.1103/PhysRevB.88.125427](https://doi.org/10.1103/PhysRevB.88.125427). URL: <https://link.aps.org/doi/10.1103/PhysRevB.88.125427>.

41. Z. K. Liu, B. Zhou, Y. Zhang, Z. J. Wang, H. M. Weng, D. Prabhakaran, S.-K. Mo, Z. X. Shen, Z. Fang, X. Dai, Z. Hussain, and Y. L. Chen. “Discovery of a Three-Dimensional Topological Dirac Semimetal, Na_3Bi ”. *Science* 343:6173, 2014, pp. 864–867. ISSN: 0036-8075. DOI: [10.1126/science.1245085](https://doi.org/10.1126/science.1245085). eprint: <https://science.sciencemag.org/content/343/6173/864.full.pdf>. URL: <https://science.sciencemag.org/content/343/6173/864>.
42. R. Okugawa and S. Murakami. “Dispersion of Fermi arcs in Weyl semimetals and their evolutions to Dirac cones”. *Phys. Rev. B* 89, 23 2014, p. 235315. DOI: [10.1103/PhysRevB.89.235315](https://doi.org/10.1103/PhysRevB.89.235315). URL: <https://link.aps.org/doi/10.1103/PhysRevB.89.235315>.
43. X. Wan, A. M. Turner, A. Vishwanath, and S. Y. Savrasov. “Topological semimetal and Fermi-arc surface states in the electronic structure of pyrochlore iridates”. *Phys. Rev. B* 83, 20 2011, p. 205101. DOI: [10.1103/PhysRevB.83.205101](https://doi.org/10.1103/PhysRevB.83.205101). URL: <https://link.aps.org/doi/10.1103/PhysRevB.83.205101>.
44. A. A. Burkov, M. D. Hook, and L. Balents. “Topological nodal semimetals”. *Phys. Rev. B* 84, 23 2011, p. 235126. DOI: [10.1103/PhysRevB.84.235126](https://doi.org/10.1103/PhysRevB.84.235126). URL: <https://link.aps.org/doi/10.1103/PhysRevB.84.235126>.
45. L. M. Schoop, M. N. Ali, C. Straßer, A. Topp, A. Varykhalov, D. Marchenko, V. Duppel, S. S. Parkin, B. V. Lotsch, and C. R. Ast. “Dirac cone protected by non-symmorphic symmetry and three-dimensional Dirac line node in ZrSiS ”. *Nature communications* 7:1, 2016, pp. 1–7.
46. M. Neupane, I. Belopolski, M. M. Hosen, D. S. Sanchez, R. Sankar, M. Szlowska, S.-Y. Xu, K. Dimitri, N. Dhakal, P. Maldonado, P. M. Oppeneer, D. Kaczorowski, F. Chou, M. Z. Hasan, and T. Durakiewicz. “Observation of topological nodal fermion semimetal phase in ZrSiS ”. *Phys. Rev. B* 93, 20 2016, p. 201104. DOI: [10.1103/PhysRevB.93.201104](https://doi.org/10.1103/PhysRevB.93.201104). URL: <https://link.aps.org/doi/10.1103/PhysRevB.93.201104>.
47. A. F. Young and P. Kim. “Quantum interference and Klein tunnelling in graphene heterojunctions”. *Nature Physics* 5:3, 2009, pp. 222–226.
48. E. B. Sonin. “Effect of Klein tunneling on conductance and shot noise in ballistic graphene”. *Phys. Rev. B* 79, 19 2009, p. 195438. DOI: [10.1103/PhysRevB.79.195438](https://doi.org/10.1103/PhysRevB.79.195438). URL: <https://link.aps.org/doi/10.1103/PhysRevB.79.195438>.
49. P. E. Allain and J.-N. Fuchs. “Klein tunneling in graphene: optics with massless electrons”. *The European Physical Journal B* 83:3, 2011, pp. 301–317.
50. I. Pomeranchuk and Y. Smorodinsky. “On the energy levels of systems with $Z > 137$ ”. *J. Phys. Ussr* 9:2, 1945, pp. 97–100.

Bibliography

51. Y. B. Zeldovich and V. S. Popov. “ELECTRONIC STRUCTURE OF SUPERHEAVY ATOMS”. *Soviet Physics Uspekhi* 14:6, 1972, pp. 673–694. DOI: [10.1070/pu1972v014n06abeh004735](https://doi.org/10.1070/pu1972v014n06abeh004735). URL: <https://doi.org/10.1070/pu1972v014n06abeh004735>.
52. Y. Wang, D. Wong, A. V. Shytov, V. W. Brar, S. Choi, Q. Wu, H.-Z. Tsai, W. Regan, A. Zettl, R. K. Kawakami, S. G. Louie, L. S. Levitov, and M. F. Crommie. “Observing Atomic Collapse Resonances in Artificial Nuclei on Graphene”. *Science* 340:6133, 2013, pp. 734–737. ISSN: 0036-8075. DOI: [10.1126/science.1234320](https://doi.org/10.1126/science.1234320). eprint: <https://science.sciencemag.org/content/340/6133/734.full.pdf>. URL: <https://science.sciencemag.org/content/340/6133/734>.
53. V. Lukose, R. Shankar, and G. Baskaran. “Novel Electric Field Effects on Landau Levels in Graphene”. *Phys. Rev. Lett.* 98, 11 2007, p. 116802. DOI: [10.1103/PhysRevLett.98.116802](https://doi.org/10.1103/PhysRevLett.98.116802). URL: <https://link.aps.org/doi/10.1103/PhysRevLett.98.116802>.
54. N. Gu, M. Rudner, A. Young, P. Kim, and L. Levitov. “Collapse of Landau Levels in Gated Graphene Structures”. *Phys. Rev. Lett.* 106, 6 2011, p. 066601. DOI: [10.1103/PhysRevLett.106.066601](https://doi.org/10.1103/PhysRevLett.106.066601). URL: <https://link.aps.org/doi/10.1103/PhysRevLett.106.066601>.
55. M. V. Berry. “Quantal phase factors accompanying adiabatic changes”. *Proceedings of the Royal Society of London. A. Mathematical and Physical Sciences* 392:1802, 1984, pp. 45–57. DOI: [10.1098/rspa.1984.0023](https://doi.org/10.1098/rspa.1984.0023). eprint: <https://royalsocietypublishing.org/doi/pdf/10.1098/rspa.1984.0023>. URL: <https://royalsocietypublishing.org/doi/abs/10.1098/rspa.1984.0023>.
56. Y. Aharonov and D. Bohm. “Significance of Electromagnetic Potentials in the Quantum Theory”. *Phys. Rev.* 115, 3 1959, pp. 485–491. DOI: [10.1103/PhysRev.115.485](https://doi.org/10.1103/PhysRev.115.485). URL: <https://link.aps.org/doi/10.1103/PhysRev.115.485>.
57. R. G. Chambers. “Shift of an Electron Interference Pattern by Enclosed Magnetic Flux”. *Phys. Rev. Lett.* 5, 1 1960, pp. 3–5. DOI: [10.1103/PhysRevLett.5.3](https://doi.org/10.1103/PhysRevLett.5.3). URL: <https://link.aps.org/doi/10.1103/PhysRevLett.5.3>.
58. P. Bocchieri and A. Loinger. “Nonexistence of the Aharonov-Bohm effect”. *Il Nuovo Cimento A (1965-1970)* 47:4, 1978, pp. 475–482.
59. C. Kittel, P. McEuen, and P. McEuen. *Introduction to solid state physics*. Vol. 8. Wiley New York, 1996.
60. M. F. Atiyah and I. M. Singer. “The index of elliptic operators on compact manifolds”. *Bulletin of the American Mathematical Society* 69:3, 1963, pp. 422–433.
61. M. Nakahara. *Geometry, Topology and Physics*. CRC Press, 2018. ISBN: 9781420056945. URL: <https://books.google.fr/books?id=p2C1DwAAQBAJ>.

62. T. Neupert and F. Schindler. “Topological crystalline insulators”. In: *Topological Matter*. Springer, 2018, pp. 31–61.
63. S. Ryu, A. P. Schnyder, A. Furusaki, and A. W. W. Ludwig. “Topological insulators and superconductors: tenfold way and dimensional hierarchy”. *New Journal of Physics* 12:6, 2010, p. 065010. DOI: [10.1088/1367-2630/12/6/065010](https://doi.org/10.1088/1367-2630/12/6/065010). URL: <https://doi.org/10.1088/1367-2630/12/6/065010>.
64. M. Z. Hasan and C. L. Kane. “Colloquium: Topological insulators”. *Rev. Mod. Phys.* 82, 4 2010, pp. 3045–3067. DOI: [10.1103/RevModPhys.82.3045](https://doi.org/10.1103/RevModPhys.82.3045). URL: <https://link.aps.org/doi/10.1103/RevModPhys.82.3045>.
65. R. Karplus and J. M. Luttinger. “Hall Effect in Ferromagnetics”. *Phys. Rev.* 95, 5 1954, pp. 1154–1160. DOI: [10.1103/PhysRev.95.1154](https://doi.org/10.1103/PhysRev.95.1154). URL: <https://link.aps.org/doi/10.1103/PhysRev.95.1154>.
66. E. Blount. “Formalisms of Band Theory”. In: ed. by F. Seitz and D. Turnbull. Vol. 13. Solid State Physics. Academic Press, 1962, pp. 305–373. DOI: [https://doi.org/10.1016/S0081-1947\(08\)60459-2](https://doi.org/10.1016/S0081-1947(08)60459-2). URL: <https://www.sciencedirect.com/science/article/pii/S0081194708604592>.
67. D. Xiao, M.-C. Chang, and Q. Niu. “Berry phase effects on electronic properties”. *Rev. Mod. Phys.* 82, 3 2010, pp. 1959–2007. DOI: [10.1103/RevModPhys.82.1959](https://doi.org/10.1103/RevModPhys.82.1959). URL: <https://link.aps.org/doi/10.1103/RevModPhys.82.1959>.
68. K. v. Klitzing, G. Dorda, and M. Pepper. “New Method for High-Accuracy Determination of the Fine-Structure Constant Based on Quantized Hall Resistance”. *Phys. Rev. Lett.* 45, 6 1980, pp. 494–497. DOI: [10.1103/PhysRevLett.45.494](https://doi.org/10.1103/PhysRevLett.45.494). URL: <https://link.aps.org/doi/10.1103/PhysRevLett.45.494>.
69. J. Cayssol. “Introduction to Dirac materials and topological insulators”. *Comptes Rendus Physique* 14:9-10, 2013, pp. 760–778.
70. B. A. Bernevig, T. L. Hughes, and S.-C. Zhang. “Quantum Spin Hall Effect and Topological Phase Transition in HgTe Quantum Wells”. *Science* 314:5806, 2006, pp. 1757–1761. ISSN: 0036-8075. DOI: [10.1126/science.1133734](https://doi.org/10.1126/science.1133734). URL: <https://science.sciencemag.org/content/314/5806/1757>.
71. W. P. Su, J. R. Schrieffer, and A. J. Heeger. “Solitons in Polyacetylene”. *Phys. Rev. Lett.* 42, 25 1979, pp. 1698–1701. DOI: [10.1103/PhysRevLett.42.1698](https://doi.org/10.1103/PhysRevLett.42.1698). URL: <https://link.aps.org/doi/10.1103/PhysRevLett.42.1698>.

Bibliography

72. S. Tchoumakov, V. Jouffrey, A. Inhofer, E. Bocquillon, B. Plaçais, D. Carpentier, and M. O. Goerbig. “Volkov-Pankratov states in topological heterojunctions”. *Phys. Rev. B* 96, 20 2017, 201302(R). DOI: [10.1103/PhysRevB.96.201302](https://doi.org/10.1103/PhysRevB.96.201302). URL: <https://link.aps.org/doi/10.1103/PhysRevB.96.201302>.
73. J. Cayssol and J. N. Fuchs. “Topological and geometrical aspects of band theory”. *Journal of Physics: Materials* 4:3, 2021, p. 034007. DOI: [10.1088/2515-7639/abf0b5](https://doi.org/10.1088/2515-7639/abf0b5). URL: <https://doi.org/10.1088/2515-7639/abf0b5>.
74. B. Volkov and O. Pankratov. “Two-dimensional massless electrons in an inverted contact”. *JETP Lett.* 42:49, 1985, p. 178. URL: http://www.jetpletters.ac.ru/ps/1420/article_21570.shtml.
75. O. Pankratov, S. Pakhomov, and B. Volkov. “Supersymmetry in heterojunctions: Band-inverting contact on the basis of $\text{Pb}_{1-x}\text{Sn}_x\text{Te}$ and $\text{Hg}_{1-x}\text{Cd}_x\text{Te}$ ”. *Solid state communications* 61:2, 1987, pp. 93–96.
76. D. Vanderbilt. *Berry Phases in Electronic Structure Theory: Electric Polarization, Orbital Magnetization and Topological Insulators*. Cambridge University Press, 2018. DOI: [10.1017/9781316662205](https://doi.org/10.1017/9781316662205).
77. A. Altland and B. D. Simons. *Condensed Matter Field Theory*. 2nd ed. Cambridge University Press, 2010. DOI: [10.1017/CBO9780511789984](https://doi.org/10.1017/CBO9780511789984).
78. M. O. Goerbig. “Electronic properties of graphene in a strong magnetic field”. *Rev. Mod. Phys.* 83, 4 2011, pp. 1193–1243. DOI: [10.1103/RevModPhys.83.1193](https://doi.org/10.1103/RevModPhys.83.1193). URL: <https://link.aps.org/doi/10.1103/RevModPhys.83.1193>.
79. M. O. Goerbig. *Quantum Hall Effects*. 2009. arXiv: [0909.1998](https://arxiv.org/abs/0909.1998) [cond-mat.mes-hall].
80. J. D. Jackson. *Classical electrodynamics*. 1999.
81. X.-L. Qi and S.-C. Zhang. “Topological insulators and superconductors”. *Rev. Mod. Phys.* 83, 4 2011, pp. 1057–1110. DOI: [10.1103/RevModPhys.83.1057](https://doi.org/10.1103/RevModPhys.83.1057). URL: <https://link.aps.org/doi/10.1103/RevModPhys.83.1057>.
82. J. Sári, M. O. Goerbig, and C. Tóke. “Magneto-optics of quasirelativistic electrons in graphene with an inplane electric field and in tilted Dirac cones in $\alpha - (\text{BEDT TTF})_2\text{I}_3$ ”. *Phys. Rev. B* 92, 3 2015, p. 035306. DOI: [10.1103/PhysRevB.92.035306](https://doi.org/10.1103/PhysRevB.92.035306). URL: <https://link.aps.org/doi/10.1103/PhysRevB.92.035306>.
83. S. Tchoumakov, M. Civelli, and M. O. Goerbig. “Magnetic-Field-Induced Relativistic Properties in Type-I and Type-II Weyl Semimetals”. *Phys. Rev. Lett.* 117, 8 2016, p. 086402. DOI: [10.1103/PhysRevLett.117.086402](https://doi.org/10.1103/PhysRevLett.117.086402). URL: <https://link.aps.org/doi/10.1103/PhysRevLett.117.086402>.

84. P. West. “Supergravity, brane dynamics and string duality”. *arXiv preprint hep-th/9811101*, 1998.
85. M. O. Goerbig. “The quantum Hall effect in graphene – a theoretical perspective”. *Comptes Rendus Physique* 12:4, 2011. Quantum Hall Effect and Metrology, pp. 369–378. ISSN: 1631-0705. DOI: <https://doi.org/10.1016/j.crhy.2011.04.012>. URL: <https://www.sciencedirect.com/science/article/pii/S1631070511000958>.
86. P. R. Wallace. “The Band Theory of Graphite”. *Phys. Rev.* 71, 9 1947, pp. 622–634. DOI: [10.1103/PhysRev.71.622](https://doi.org/10.1103/PhysRev.71.622). URL: <https://link.aps.org/doi/10.1103/PhysRev.71.622>.
87. R. Peierls. “Zur theorie des diamagnetismus von leitungselektronen”. *Zeitschrift für Physik* 80:11-12, 1933, pp. 763–791.
88. X.-L. Qi, T. L. Hughes, and S.-C. Zhang. “Topological field theory of time-reversal invariant insulators”. *Phys. Rev. B* 78, 19 2008, p. 195424. DOI: [10.1103/PhysRevB.78.195424](https://doi.org/10.1103/PhysRevB.78.195424). URL: <https://link.aps.org/doi/10.1103/PhysRevB.78.195424>.
89. Y. Chen, S. Wu, and A. A. Burkov. “Axion response in Weyl semimetals”. *Phys. Rev. B* 88, 12 2013, p. 125105. DOI: [10.1103/PhysRevB.88.125105](https://doi.org/10.1103/PhysRevB.88.125105). URL: <https://link.aps.org/doi/10.1103/PhysRevB.88.125105>.
90. A. V. Shytov, N. Gu, and L. S. Levitov. *Transport in Graphene p-n Junctions in Magnetic Field*. 2007. arXiv: [0708.3081](https://arxiv.org/abs/0708.3081) [cond-mat.mes-hall].
91. B. Delamotte. “Un soupçon de théorie des groupes: groupe des rotations et groupe de Poincaré”. DEA. Lecture. 2006. URL: <https://cel.archives-ouvertes.fr/cel-00092924>.
92. A. Zee. *Group theory in a nutshell for physicists*. Vol. 17. Princeton University Press, 2016.
93. H. K. Pal, F. Piéchon, J.-N. Fuchs, M. Goerbig, and G. Montambaux. “Chemical potential asymmetry and quantum oscillations in insulators”. *Phys. Rev. B* 94, 12 2016, p. 125140. DOI: [10.1103/PhysRevB.94.125140](https://doi.org/10.1103/PhysRevB.94.125140). URL: <https://link.aps.org/doi/10.1103/PhysRevB.94.125140>.
94. L. Onsager. “Interpretation of the de Haas-van Alphen effect”. *The London, Edinburgh, and Dublin Philosophical Magazine and Journal of Science* 43:344, 1952, pp. 1006–1008. DOI: [10.1080/14786440908521019](https://doi.org/10.1080/14786440908521019). eprint: <https://doi.org/10.1080/14786440908521019>. URL: <https://doi.org/10.1080/14786440908521019>.
95. L. M. Roth. “Semiclassical Theory of Magnetic Energy Levels and Magnetic Susceptibility of Bloch Electrons”. *Phys. Rev.* 145, 2 1966, pp. 434–448. DOI: [10.1103/PhysRev.145.434](https://doi.org/10.1103/PhysRev.145.434). URL: <https://link.aps.org/doi/10.1103/PhysRev.145.434>.

Bibliography

96. Y. Gao and Q. Niu. “Zero-field magnetic response functions in Landau levels”. *Proceedings of the National Academy of Sciences* 114:28, 2017, pp. 7295–7300. ISSN: 0027-8424. DOI: [10.1073/pnas.1702595114](https://doi.org/10.1073/pnas.1702595114). eprint: <https://www.pnas.org/content/114/28/7295.full.pdf>. URL: <https://www.pnas.org/content/114/28/7295>.
97. J. N. Fuchs, F. Piéchon, and G. Montambaux. “Landau levels, response functions and magnetic oscillations from a generalized Onsager relation”. *SciPost Phys.* 4, 5 2018, p. 24. DOI: [10.21468/SciPostPhys.4.5.024](https://doi.org/10.21468/SciPostPhys.4.5.024). URL: <https://scipost.org/10.21468/SciPostPhys.4.5.024>.
98. G. P. Mikitik and Y. V. Sharlai. “Analysis of Dirac and Weyl points in topological semimetals via oscillation effects”. *Low Temperature Physics* 47:4, 2021, pp. 312–317. DOI: [10.1063/10.0003743](https://doi.org/10.1063/10.0003743). eprint: <https://doi.org/10.1063/10.0003743>. URL: <https://doi.org/10.1063/10.0003743>.
99. M. A. Mojarro, R. Carrillo-Bastos, and J. A. Maytorena. “Optical properties of massive anisotropic tilted Dirac systems”. *Phys. Rev. B* 103, 16 2021, p. 165415. DOI: [10.1103/PhysRevB.103.165415](https://doi.org/10.1103/PhysRevB.103.165415). URL: <https://link.aps.org/doi/10.1103/PhysRevB.103.165415>.
100. F. Wooten. *Optical properties of solids*. Academic press, 2013.
101. M. Fox. *Optical properties of solids*. American Association of Physics Teachers, 2002.
102. M. Dresselhaus, G. Dresselhaus, S. B. Cronin, and A. G. Souza Filho. *Solid State Properties*. Springer, 2018.
103. M. O. Scully and M. S. Zubairy. *Quantum optics*. 1999.
104. C. Kurtsiefer, S. Mayer, P. Zarda, and H. Weinfurter. “Stable Solid-State Source of Single Photons”. *Phys. Rev. Lett.* 85, 2 2000, pp. 290–293. DOI: [10.1103/PhysRevLett.85.290](https://doi.org/10.1103/PhysRevLett.85.290). URL: <https://link.aps.org/doi/10.1103/PhysRevLett.85.290>.
105. A. Aspect, P. Grangier, and G. Grynberg. *Optique quantique 2: photons*. École polytechnique, Département de physique, 2004.
106. D. P. Craig and T. Thirunamachandran. *Molecular quantum electrodynamics: an introduction to radiation-molecule interactions*. Courier Corporation, 1998.
107. H. Eyring, J. Walter, and G. E. Kimball. *Quantum chemistry*. Wiley, 1944.
108. H. Bruus and K. Flensberg. *Many-body quantum theory in condensed matter physics: an introduction*. Oxford university press, 2004.
109. M. Hakl. “Infrared magneto-spectroscopy of relativistic-like electrons in three-dimensional solids”. 2017GREAY085. PhD thesis. 2017. URL: <http://www.theses.fr/2017GREAY085/document>.

110. A. B. Kuzmenko, E. van Heumen, F. Carbone, and D. van der Marel. “Universal Optical Conductance of Graphite”. *Phys. Rev. Lett.* 100, 11 2008, p. 117401. DOI: [10.1103/PhysRevLett.100.117401](https://doi.org/10.1103/PhysRevLett.100.117401). URL: <https://link.aps.org/doi/10.1103/PhysRevLett.100.117401>.
111. R. R. Nair, P. Blake, A. N. Grigorenko, K. S. Novoselov, T. J. Booth, T. Stauber, N. M. Peres, and A. K. Geim. “Fine structure constant defines visual transparency of graphene”. *Science* 320:5881, 2008, pp. 1308–1308.
112. J. Holovsky and C. Ballif. “Thin-film limit formalism applied to surface defect absorption”. *Opt. Express* 22:25, 2014, pp. 31466–31472. DOI: [10.1364/OE.22.031466](https://doi.org/10.1364/OE.22.031466). URL: <http://www.opticsexpress.org/abstract.cfm?URI=oe-22-25-31466>.
113. R. Atkinson and P. H. Lissberger. “Sign conventions in magneto-optical calculations and measurements”. *Appl. Opt.* 31:28, 1992, pp. 6076–6081. DOI: [10.1364/AO.31.006076](https://doi.org/10.1364/AO.31.006076). URL: <http://ao.osa.org/abstract.cfm?URI=ao-31-28-6076>.
114. L. Onsager. “Reciprocal Relations in Irreversible Processes. I.” *Phys. Rev.* 37, 4 1931, pp. 405–426. DOI: [10.1103/PhysRev.37.405](https://doi.org/10.1103/PhysRev.37.405). URL: <https://link.aps.org/doi/10.1103/PhysRev.37.405>.
115. M. L. Sadowski, G. Martinez, M. Potemski, C. Berger, and W. A. de Heer. “Landau Level Spectroscopy of Ultrathin Graphite Layers”. *Phys. Rev. Lett.* 97, 26 2006, p. 266405. DOI: [10.1103/PhysRevLett.97.266405](https://doi.org/10.1103/PhysRevLett.97.266405). URL: <https://link.aps.org/doi/10.1103/PhysRevLett.97.266405>.
116. G. Giuliani and G. Vignale. *Quantum Theory of the Electron Liquid*. Cambridge University Press, 2005. DOI: [10.1017/CB09780511619915](https://doi.org/10.1017/CB09780511619915).
117. G. Landwehr and E. Rashba. *Landau Level Spectroscopy*. ISSN. Elsevier Science, 2012. ISBN: 9780444600431. URL: <https://books.google.fr/books?id=yas7AAAAQBAJ>.
118. Y. Shao, Z. Sun, Y. Wang, C. Xu, R. Sankar, A. J. Breindel, C. Cao, M. M. Fogler, A. J. Millis, F. Chou, Z. Li, T. Timusk, M. B. Maple, and D. N. Basov. “Optical signatures of Dirac nodal lines in NbAs₂”. *Proceedings of the National Academy of Sciences* 116:4, 2019, pp. 1168–1173. ISSN: 0027-8424. DOI: [10.1073/pnas.1809631115](https://doi.org/10.1073/pnas.1809631115). eprint: <https://www.pnas.org/content/116/4/1168.full.pdf>. URL: <https://www.pnas.org/content/116/4/1168>.
119. R. Brydson. *Electron energy loss spectroscopy*. Garland Science, 2020.
120. R. F. Egerton. *Electron energy-loss spectroscopy in the electron microscope*. Springer Science & Business Media, 2011.

Bibliography

121. P. Shekhar, M. Malac, V. Gaiнд, N. Dalili, A. Meldrum, and Z. Jacob. “Momentum-Resolved Electron Energy Loss Spectroscopy for Mapping the Photonic Density of States”. *ACS Photonics* 4:4, 2017, pp. 1009–1014. DOI: [10.1021/acsp Photonics.7b00103](https://doi.org/10.1021/acsp Photonics.7b00103). eprint: <https://doi.org/10.1021/acsp Photonics.7b00103>. URL: <https://doi.org/10.1021/acsp Photonics.7b00103>.
122. G. D. Mahan. *Many-particle physics*. Springer Science & Business Media, 2013.
123. M. König, S. Wiedmann, C. Brüne, A. Roth, H. Buhmann, L. W. Molenkamp, X.-L. Qi, and S.-C. Zhang. “Quantum Spin Hall Insulator State in HgTe Quantum Wells”. *Science* 318:5851, 2007, pp. 766–770. ISSN: 0036-8075. DOI: [10.1126/science.1148047](https://doi.org/10.1126/science.1148047). URL: <http://science.sciencemag.org/content/318/5851/766>.
124. A. Inhofer, S. Tchoumakov, B. A. Assaf, G. Fève, J. M. Berroir, V. Jouffrey, D. Carpentier, M. O. Goerbig, B. Pla çais, K. Bendias, D. M. Mahler, E. Bocquillon, R. Schlereth, C. Brüne, H. Buhmann, and L. W. Molenkamp. “Observation of Volkov-Pankratov states in topological HgTe heterojunctions using high-frequency compressibility”. *Phys. Rev. B* 96, 19 2017, p. 195104. DOI: [10.1103/PhysRevB.96.195104](https://doi.org/10.1103/PhysRevB.96.195104). URL: <https://link.aps.org/doi/10.1103/PhysRevB.96.195104>.
125. D. M. Mahler, J.-B. Mayer, P. Leubner, L. Lunczer, D. Di Sante, G. Sangiovanni, R. Thomale, E. M. Hankiewicz, H. Buhmann, C. Gould, and L. W. Molenkamp. “Interplay of Dirac Nodes and Volkov-Pankratov Surface States in Compressively Strained HgTe”. *Phys. Rev. X* 9, 3 2019, p. 031034. DOI: [10.1103/PhysRevX.9.031034](https://doi.org/10.1103/PhysRevX.9.031034). URL: <https://link.aps.org/doi/10.1103/PhysRevX.9.031034>.
126. T. L. van den Berg, M. R. Calvo, and D. Bercioux. “Living on the edge: Topology, electrostatics, and disorder”. *Phys. Rev. Research* 2, 1 2020, p. 013171. DOI: [10.1103/PhysRevResearch.2.013171](https://doi.org/10.1103/PhysRevResearch.2.013171). URL: <https://link.aps.org/doi/10.1103/PhysRevResearch.2.013171>.
127. A. G. Grushin, J. W. F. Venderbos, A. Vishwanath, and R. Ilan. “Inhomogeneous Weyl and Dirac Semimetals: Transport in Axial Magnetic Fields and Fermi Arc Surface States from Pseudo-Landau Levels”. *Phys. Rev. X* 6, 4 2016, p. 041046. DOI: [10.1103/PhysRevX.6.041046](https://doi.org/10.1103/PhysRevX.6.041046). URL: <https://link.aps.org/doi/10.1103/PhysRevX.6.041046>.
128. S. Tchoumakov, M. Civelli, and M. O. Goerbig. “Magnetic description of the Fermi arc in type-I and type-II Weyl semimetals”. *Phys. Rev. B* 95, 12 2017, p. 125306. DOI: [10.1103/PhysRevB.95.125306](https://doi.org/10.1103/PhysRevB.95.125306). URL: <https://link.aps.org/doi/10.1103/PhysRevB.95.125306>.
129. T. L. van den Berg, A. De Martino, M. R. Calvo, and D. Bercioux. “Volkov-Pankratov states in topological graphene nanoribbons”. *Phys. Rev. Research* 2, 2 2020, p. 023373. DOI: [10.1103/PhysRevResearch.2.023373](https://doi.org/10.1103/PhysRevResearch.2.023373).

- PhysRevResearch.2.023373. URL: <https://link.aps.org/doi/10.1103/PhysRevResearch.2.023373>.
130. D. J. Alspaugh, D. E. Sheehy, M. O. Goerbig, and P. Simon. “Volkov-Pankratov states in topological superconductors”. *Phys. Rev. Research* 2, 2 2020, p. 023146. DOI: [10.1103/PhysRevResearch.2.023146](https://doi.org/10.1103/PhysRevResearch.2.023146). URL: <https://link.aps.org/doi/10.1103/PhysRevResearch.2.023146>.
 131. S.-Y. Xu, Y. Xia, L. A. Wray, S. Jia, F. Meier, J. H. Dil, J. Osterwalder, B. Slomski, A. Bansil, H. Lin, R. J. Cava, and M. Z. Hasan. “Topological Phase Transition and Texture Inversion in a Tunable Topological Insulator”. *Science* 332:6029, 2011, pp. 560–564. ISSN: 0036-8075. DOI: [10.1126/science.1201607](https://doi.org/10.1126/science.1201607). eprint: <https://science.sciencemag.org/content/332/6029/560.full.pdf>. URL: <https://science.sciencemag.org/content/332/6029/560>.
 132. S. Tchoumakov. “Signatures relativistes en spectroscopie de matériaux topologiques : en volume et en surface”. 2017SACLS258. PhD thesis. 2017. URL: <http://www.theses.fr/2017SACLS258/document>.
 133. H. Zhang, C.-X. Liu, X.-L. Qi, X. Dai, Z. Fang, and S.-C. Zhang. “Topological insulators in Bi_2Se_3 , Bi_2Te_3 and Sb_2Te_3 with a single Dirac cone on the surface”. *Nature physics* 5:6, 2009, pp. 438–442.
 134. F. Zhang, C. L. Kane, and E. J. Mele. “Surface states of topological insulators”. *Phys. Rev. B* 86, 8 2012, p. 081303. DOI: [10.1103/PhysRevB.86.081303](https://doi.org/10.1103/PhysRevB.86.081303). URL: <https://link.aps.org/doi/10.1103/PhysRevB.86.081303>.
 135. Y. Xia, D. Qian, D. Hsieh, L. Wray, A. Pal, H. Lin, A. Bansil, D. Grauer, Y. S. Hor, R. J. Cava, et al. “Observation of a large-gap topological-insulator class with a single Dirac cone on the surface”. *Nature physics* 5:6, 2009, p. 398.
 136. M. Bianchi, D. Guan, S. Bao, J. Mi, B. B. Iversen, P. D. King, and P. Hofmann. “Coexistence of the topological state and a two-dimensional electron gas on the surface of Bi_2Se_3 ”. *Nature communications* 1, 2010, p. 128. DOI: [10.1038/ncomms1131](https://doi.org/10.1038/ncomms1131).
 137. X. Lu and M. O. Goerbig. “Dirac quantum well engineering on the surface of a topological insulator”. *Phys. Rev. B* 102, 15 2020, p. 155311. DOI: [10.1103/PhysRevB.102.155311](https://doi.org/10.1103/PhysRevB.102.155311). URL: <https://link.aps.org/doi/10.1103/PhysRevB.102.155311>.
 138. J.-L. Basdevant and J. Dalibard. *Quantum Mechanics*. Springer Verlag (Berlin, Heidelberg), 2002. ISBN: 978-3-540-27706-4. DOI: [10.1007/3-540-28805-8](https://doi.org/10.1007/3-540-28805-8). URL: <https://www.springer.com/gp/book/9783540277064>.

Bibliography

139. M. Neupane, A. Richardella, J. Sánchez-Barriga, S. Xu, N. Alidoust, I. Belopolski, C. Liu, G. Bian, D. Zhang, D. Marchenko, et al. “Observation of quantum-tunnelling-modulated spin texture in ultrathin topological insulator Bi_2Se_3 films”. *Nature communications* 5, 2014, p. 3841.
140. J. Linder, T. Yokoyama, and A. Sudbø. “Anomalous finite size effects on surface states in the topological insulator Bi_2Se_3 ”. *Phys. Rev. B* 80, 20 2009, p. 205401. DOI: [10.1103/PhysRevB.80.205401](https://doi.org/10.1103/PhysRevB.80.205401). URL: <https://link.aps.org/doi/10.1103/PhysRevB.80.205401>.
141. H.-Z. Lu, W.-Y. Shan, W. Yao, Q. Niu, and S.-Q. Shen. “Massive Dirac fermions and spin physics in an ultrathin film of topological insulator”. *Phys. Rev. B* 81, 11 2010, p. 115407. DOI: [10.1103/PhysRevB.81.115407](https://doi.org/10.1103/PhysRevB.81.115407). URL: <https://link.aps.org/doi/10.1103/PhysRevB.81.115407>.
142. C.-X. Liu, H. Zhang, B. Yan, X.-L. Qi, T. Frauenheim, X. Dai, Z. Fang, and S.-C. Zhang. “Oscillatory crossover from two-dimensional to three-dimensional topological insulators”. *Phys. Rev. B* 81, 4 2010, p. 041307. DOI: [10.1103/PhysRevB.81.041307](https://doi.org/10.1103/PhysRevB.81.041307). URL: <https://link.aps.org/doi/10.1103/PhysRevB.81.041307>.
143. W.-Y. Shan, H.-Z. Lu, and S.-Q. Shen. “Effective continuous model for surface states and thin films of three-dimensional topological insulators”. *New Journal of Physics* 12:4, 2010, p. 043048. DOI: [10.1088/1367-2630/12/4/043048](https://doi.org/10.1088/1367-2630/12/4/043048). URL: <https://doi.org/10.1088/1367-2630/12/4/043048>.
144. I. Belopolski, S.-Y. Xu, N. Koirala, C. Liu, G. Bian, V. N. Strocov, G. Chang, M. Neupane, N. Alidoust, D. Sanchez, H. Zheng, M. Brahlek, V. Rogalev, T. Kim, N. C. Plumb, C. Chen, F. Bertran, P. Le Fèvre, A. Taleb-Ibrahimi, M.-C. Asensio, M. Shi, H. Lin, M. Hoesch, S. Oh, and M. Z. Hasan. “A novel artificial condensed matter lattice and a new platform for one-dimensional topological phases”. *Science Advances* 3:3, 2017. DOI: [10.1126/sciadv.1501692](https://doi.org/10.1126/sciadv.1501692). eprint: <https://advances.sciencemag.org/content/3/3/e1501692.full.pdf>. URL: <https://advances.sciencemag.org/content/3/3/e1501692>.
145. P. P. Shibayev, E. J. König, M. Salehi, J. Moon, M.-G. Han, and S. Oh. “Engineering Topological Superlattices and Phase Diagrams”. *Nano Letters* 19:2, 2019. PMID: 30663307, pp. 716–721. DOI: [10.1021/acs.nanolett.8b03751](https://doi.org/10.1021/acs.nanolett.8b03751). eprint: <https://doi.org/10.1021/acs.nanolett.8b03751>. URL: <https://doi.org/10.1021/acs.nanolett.8b03751>.
146. G. Krizman, B. A. Assaf, T. Phuphachong, G. Bauer, G. Springholz, G. Bastard, R. Ferreira, L. A. de Vaultier, and Y. Guldner. “Tunable Dirac interface states in topological superlattices”. *Phys. Rev. B* 98, 7 2018, p. 075303. DOI: [10.1103/PhysRevB.98.075303](https://doi.org/10.1103/PhysRevB.98.075303). URL: <https://link.aps.org/doi/10.1103/PhysRevB.98.075303>.

147. G. Krizman, B. A. Assaf, G. Bauer, G. Springholz, L. A. de Vaulchier, and Y. Guldner. “Mini-band engineering and topological phase transitions in topological-insulator–normal-insulator superlattices”. *Phys. Rev. B* 103, 23 2021, p. 235302. DOI: [10.1103/PhysRevB.103.235302](https://doi.org/10.1103/PhysRevB.103.235302). URL: <https://link.aps.org/doi/10.1103/PhysRevB.103.235302>.
148. M. Costa, A. T. Costa, W. A. Freitas, T. M. Schmidt, M. Buongiorno Nardelli, and A. Fazzio. “Controlling Topological States in Topological/Normal Insulator Heterostructures”. *ACS Omega* 3:11, 2018, pp. 15900–15906. DOI: [10.1021/acsomega.8b01836](https://doi.org/10.1021/acsomega.8b01836). eprint: <https://doi.org/10.1021/acsomega.8b01836>. URL: <https://doi.org/10.1021/acsomega.8b01836>.
149. E. Witten. “Dynamical breaking of supersymmetry”. *Nuclear Physics B* 188:3, 1981, pp. 513–554. ISSN: 0550-3213. DOI: [https://doi.org/10.1016/0550-3213\(81\)90006-7](https://doi.org/10.1016/0550-3213(81)90006-7). URL: <http://www.sciencedirect.com/science/article/pii/0550321381900067>.
150. R. Roy. “Integer Quantum Hall Effect on a Square Lattice with Zero Net Magnetic Field”. *arXiv preprint cond-mat/0603271*, 2006.
151. D. K. Mukherjee, D. Carpentier, and M. O. Goerbig. “Dynamical conductivity of the Fermi arc and the Volkov-Pankratov states on the surface of Weyl semimetals”. *Physical Review B* 100:19, 2019, p. 195412.
152. W. Mönch. “Electronic Properties of Semiconductor Interfaces”. In: *Springer Handbook of Electronic and Photonic Materials*. Ed. by S. Kasap and P. Capper. Springer International Publishing, Cham, 2017, pp. 1–1. ISBN: 978-3-319-48933-9. DOI: [10.1007/978-3-319-48933-9_8](https://doi.org/10.1007/978-3-319-48933-9_8). URL: https://doi.org/10.1007/978-3-319-48933-9_8.
153. H. Lüth. *Surfaces and interfaces of solid materials*. Springer Science & Business Media, 2013.
154. P. D. C. King, T. D. Veal, and C. F. McConville. “Nonparabolic coupled Poisson-Schrödinger solutions for quantized electron accumulation layers: Band bending, charge profile, and subbands at InN surfaces”. *Phys. Rev. B* 77, 12 2008, p. 125305. DOI: [10.1103/PhysRevB.77.125305](https://doi.org/10.1103/PhysRevB.77.125305). URL: <https://link.aps.org/doi/10.1103/PhysRevB.77.125305>.
155. A. Kamgar, P. Kneschaurek, G. Dorda, and J. F. Koch. “Resonance Spectroscopy of Electronic Levels in a Surface Accumulation Layer”. *Phys. Rev. Lett.* 32, 22 1974, pp. 1251–1254. DOI: [10.1103/PhysRevLett.32.1251](https://doi.org/10.1103/PhysRevLett.32.1251). URL: <https://link.aps.org/doi/10.1103/PhysRevLett.32.1251>.
156. M. Bahramy, P. King, A. De La Torre, J. Chang, M. Shi, L. Patthey, G. Balakrishnan, P. Hofmann, R. Arita, N. Nagaosa, et al. “Emergent quantum confinement at topological insulator surfaces”. *Nature communications* 3:1, 2012, pp. 1–7.

Bibliography

157. C. Chen, S. He, H. Weng, W. Zhang, L. Zhao, H. Liu, X. Jia, D. Mou, S. Liu, J. He, Y. Peng, Y. Feng, Z. Xie, G. Liu, X. Dong, J. Zhang, X. Wang, Q. Peng, Z. Wang, S. Zhang, F. Yang, C. Chen, Z. Xu, X. Dai, Z. Fang, and X. J. Zhou. “Robustness of topological order and formation of quantum well states in topological insulators exposed to ambient environment”. *Proceedings of the National Academy of Sciences* 109:10, 2012, pp. 3694–3698. ISSN: 0027-8424. DOI: [10.1073/pnas.1115555109](https://doi.org/10.1073/pnas.1115555109). URL: <https://www.pnas.org/content/109/10/3694>.
158. M. Bianchi, R. C. Hatch, J. Mi, B. B. Iversen, and P. Hofmann. “Simultaneous Quantization of Bulk Conduction and Valence States through Adsorption of Nonmagnetic Impurities on Bi_2Se_3 ”. *Phys. Rev. Lett.* 107, 8 2011, p. 086802. DOI: [10.1103/PhysRevLett.107.086802](https://doi.org/10.1103/PhysRevLett.107.086802). URL: <https://link.aps.org/doi/10.1103/PhysRevLett.107.086802>.
159. X. Lu and M. O. Goerbig. “Magneto-optical signatures of Volkov-Pankratov states in topological insulators”. *EPL (Europhysics Letters)* 126:6, 2019, p. 67004. DOI: [10.1209/0295-5075/126/67004](https://doi.org/10.1209/0295-5075/126/67004). URL: <https://doi.org/10.1209/0295-5075/126/67004>.
160. A. W. Ludwig, M. P. Fisher, R. Shankar, and G. Grinstein. “Integer quantum Hall transition: An alternative approach and exact results”. *Physical Review B* 50:11, 1994, p. 7526.
161. M. Trushin, E. J. R. Kelleher, and T. Hasan. “Theory of edge-state optical absorption in two-dimensional transition metal dichalcogenide flakes”. *Phys. Rev. B* 94, 15 2016, p. 155301. DOI: [10.1103/PhysRevB.94.155301](https://doi.org/10.1103/PhysRevB.94.155301). URL: <https://link.aps.org/doi/10.1103/PhysRevB.94.155301>.
162. W.-K. Tse and A. H. MacDonald. “Giant Magneto-Optical Kerr Effect and Universal Faraday Effect in Thin-Film Topological Insulators”. *Phys. Rev. Lett.* 105, 5 2010, p. 057401. DOI: [10.1103/PhysRevLett.105.057401](https://doi.org/10.1103/PhysRevLett.105.057401). URL: <https://link.aps.org/doi/10.1103/PhysRevLett.105.057401>.
163. W.-K. Tse and A. H. MacDonald. “Magneto-optical and magnetoelectric effects of topological insulators in quantizing magnetic fields”. *Phys. Rev. B* 82, 16 2010, p. 161104. DOI: [10.1103/PhysRevB.82.161104](https://doi.org/10.1103/PhysRevB.82.161104). URL: <https://link.aps.org/doi/10.1103/PhysRevB.82.161104>.
164. W.-K. Tse and A. H. MacDonald. “Magneto-optical Faraday and Kerr effects in topological insulator films and in other layered quantized Hall systems”. *Phys. Rev. B* 84, 20 2011, p. 205327. DOI: [10.1103/PhysRevB.84.205327](https://doi.org/10.1103/PhysRevB.84.205327). URL: <https://link.aps.org/doi/10.1103/PhysRevB.84.205327>.
165. L. Wu, M. Salehi, N. Koirala, J. Moon, S. Oh, and N. P. Armitage. “Quantized Faraday and Kerr rotation and axion electrodynamics of a 3D topological insulator”. *Science* 354:6316, 2016, pp. 1124–1127. ISSN: 0036-8075. DOI: [10.1126/science.aaf5541](https://doi.org/10.1126/science.aaf5541). eprint: <https://science>.

- [sciencemag.org/content/354/6316/1124.full.pdf](https://science.sciencemag.org/content/354/6316/1124.full.pdf). URL: <https://science.sciencemag.org/content/354/6316/1124>.
166. V. Suresh, E. Pinsolle, C. Lupien, T. J. Martz-Oberlander, M. P. Lilly, J. L. Reno, G. Gervais, T. Szkopek, and B. Reulet. “Quantitative measurement of giant and quantized microwave Faraday rotation”. *Phys. Rev. B* 102, 8 2020, p. 085302. DOI: [10.1103/PhysRevB.102.085302](https://doi.org/10.1103/PhysRevB.102.085302). URL: <https://link.aps.org/doi/10.1103/PhysRevB.102.085302>.
 167. Y. Xia, D. Qian, D. Hsieh, R. Shankar, H. Lin, A. Bansil, A. V. Fedorov, D. Grauer, Y. S. Hor, R. J. Cava, and M. Z. Hasan. *Topological Control: Systematic control of topological insulator Dirac fermion density on the surface of Bi₂Te₃*. 2009. arXiv: [0907.3089](https://arxiv.org/abs/0907.3089) [cond-mat.mes-hall].
 168. G. Catarina, N. M. R. Peres, and J. Fernández-Rossier. “Magneto-optical Kerr effect in spin split two-dimensional massive Dirac materials”. *2D Materials* 7:2, 2020, p. 025011. DOI: [10.1088/2053-1583/ab6781](https://doi.org/10.1088/2053-1583/ab6781). URL: <https://doi.org/10.1088/2053-1583/ab6781>.
 169. J. C. W. Song and M. S. Rudner. “Fermi arc plasmons in Weyl semimetals”. *Phys. Rev. B* 96, 20 2017, p. 205443. DOI: [10.1103/PhysRevB.96.205443](https://doi.org/10.1103/PhysRevB.96.205443). URL: <https://link.aps.org/doi/10.1103/PhysRevB.96.205443>.
 170. G. M. Andolina, F. M. D. Pellegrino, F. H. L. Koppens, and M. Polini. “Quantum nonlocal theory of topological Fermi arc plasmons in Weyl semimetals”. *Phys. Rev. B* 97, 12 2018, p. 125431. DOI: [10.1103/PhysRevB.97.125431](https://doi.org/10.1103/PhysRevB.97.125431). URL: <https://link.aps.org/doi/10.1103/PhysRevB.97.125431>.
 171. Ž. B. Lošić. “Surface plasmons in Weyl semimetals”. *Journal of Physics: Condensed Matter* 30:36, 2018, p. 365003. DOI: [10.1088/1361-648x/aad6f5](https://doi.org/10.1088/1361-648x/aad6f5). URL: <https://doi.org/10.1088/1361-648x/aad6f5>.
 172. F. Adinehvand, Z. Faraei, T. Farajollahpour, and S. A. Jafari. “Sound of Fermi arcs: a linearly dispersing gapless surface plasmon mode in undoped Weyl semimetals”. *Phys. Rev. B* 100, 19 2019, p. 195408. DOI: [10.1103/PhysRevB.100.195408](https://doi.org/10.1103/PhysRevB.100.195408). URL: <https://link.aps.org/doi/10.1103/PhysRevB.100.195408>.
 173. Q. Chen, A. R. Kutayiah, I. Oladyshkin, M. Tokman, and A. Belyanin. “Optical properties and electromagnetic modes of Weyl semimetals”. *Phys. Rev. B* 99, 7 2019, p. 075137. DOI: [10.1103/PhysRevB.99.075137](https://doi.org/10.1103/PhysRevB.99.075137). URL: <https://link.aps.org/doi/10.1103/PhysRevB.99.075137>.
 174. E. V. Gorbar, V. A. Miransky, I. A. Shovkovy, and P. O. Sukhachov. “Hydrodynamics of Fermi arcs: Bulk flow and surface collective modes”. *Phys. Rev. B* 99, 15 2019, p. 155120. DOI: [10.1103/PhysRevB.99.155120](https://doi.org/10.1103/PhysRevB.99.155120). URL: <https://link.aps.org/doi/10.1103/PhysRevB.99.155120>.

Bibliography

175. S. Ghosh and C. Timm. “Dynamical density and spin response of Fermi arcs and their consequences for Weyl semimetals”. *Phys. Rev. B* 101, 16 2020, p. 165402. DOI: [10.1103/PhysRevB.101.165402](https://doi.org/10.1103/PhysRevB.101.165402). URL: <https://link.aps.org/doi/10.1103/PhysRevB.101.165402>.
176. X. Lu, D. K. Mukherjee, and M. O. Goerbig. “Surface plasmonics of Weyl semimetals”. *Phys. Rev. B* 104, 15 2021, p. 155103. DOI: [10.1103/PhysRevB.104.155103](https://doi.org/10.1103/PhysRevB.104.155103). URL: <https://link.aps.org/doi/10.1103/PhysRevB.104.155103>.
177. S. Das Sarma and A. Madhukar. “Collective modes of spatially separated, two-component, two-dimensional plasma in solids”. *Phys. Rev. B* 23, 2 1981, pp. 805–815. DOI: [10.1103/PhysRevB.23.805](https://doi.org/10.1103/PhysRevB.23.805). URL: <https://link.aps.org/doi/10.1103/PhysRevB.23.805>.
178. S. Das Sarma. “Quantum size effects on the plasma dispersion in quasi-two-dimensional electron systems”. *Phys. Rev. B* 29, 4 1984, pp. 2334–2336. DOI: [10.1103/PhysRevB.29.2334](https://doi.org/10.1103/PhysRevB.29.2334). URL: <https://link.aps.org/doi/10.1103/PhysRevB.29.2334>.
179. J. Rath and A. J. Freeman. “Generalized magnetic susceptibilities in metals: Application of the analytic tetrahedron linear energy method to Sc”. *Phys. Rev. B* 11, 6 1975, pp. 2109–2117. DOI: [10.1103/PhysRevB.11.2109](https://doi.org/10.1103/PhysRevB.11.2109). URL: <https://link.aps.org/doi/10.1103/PhysRevB.11.2109>.
180. B. Wunsch, T. Stauber, F. Sols, and F. Guinea. “Dynamical polarization of graphene at finite doping”. *New Journal of Physics* 8:12, 2006, pp. 318–318. DOI: [10.1088/1367-2630/8/12/318](https://doi.org/10.1088/1367-2630/8/12/318). URL: <https://doi.org/10.1088/1367-2630/8/12/318>.
181. E. H. Hwang and S. Das Sarma. “Dielectric function, screening, and plasmons in two-dimensional graphene”. *Phys. Rev. B* 75, 20 2007, p. 205418. DOI: [10.1103/PhysRevB.75.205418](https://doi.org/10.1103/PhysRevB.75.205418). URL: <https://link.aps.org/doi/10.1103/PhysRevB.75.205418>.
182. S. Das Sarma and E. H. Hwang. “Collective Modes of the Massless Dirac Plasma”. *Phys. Rev. Lett.* 102, 20 2009, p. 206412. DOI: [10.1103/PhysRevLett.102.206412](https://doi.org/10.1103/PhysRevLett.102.206412). URL: <https://link.aps.org/doi/10.1103/PhysRevLett.102.206412>.
183. J. Liu, J. Liu, and X. Dai. “Pseudo Landau level representation of twisted bilayer graphene: Band topology and implications on the correlated insulating phase”. *Phys. Rev. B* 99, 15 2019, p. 155415. DOI: [10.1103/PhysRevB.99.155415](https://doi.org/10.1103/PhysRevB.99.155415). URL: <https://link.aps.org/doi/10.1103/PhysRevB.99.155415>.
184. G. Tarnopolsky, A. J. Kruchkov, and A. Vishwanath. “Origin of Magic Angles in Twisted Bilayer Graphene”. *Phys. Rev. Lett.* 122, 10 2019, p. 106405. DOI: [10.1103/PhysRevLett.122.106405](https://doi.org/10.1103/PhysRevLett.122.106405). URL: <https://link.aps.org/doi/10.1103/PhysRevLett.122.106405>.

185. R. Bistritzer and A. H. MacDonald. “Moiré bands in twisted double-layer graphene”. *Proceedings of the National Academy of Sciences* 108:30, 2011, pp. 12233–12237. ISSN: 0027-8424. DOI: [10.1073/pnas.1108174108](https://doi.org/10.1073/pnas.1108174108). eprint: <https://www.pnas.org/content/108/30/12233.full.pdf>. URL: <https://www.pnas.org/content/108/30/12233>.
186. A. Rougé. *Introduction à la relativité*. Editions Ecole Polytechnique, 2002.
187. W. Bensch and W. Heid. “NbAs₂”. *Acta Crystallographica Section C* 51:11, 1995, pp. 2205–2207. DOI: [10.1107/S0108270195007062](https://doi.org/10.1107/S0108270195007062). URL: <https://doi.org/10.1107/S0108270195007062>.
188. Y.-Y. Wang, Q.-H. Yu, P.-J. Guo, K. Liu, and T.-L. Xia. “Resistivity plateau and extremely large magnetoresistance in NbAs₂ and TaAs₂”. *Physical Review B* 94:4, 2016, p. 041103.
189. F. W. Olver, D. W. Lozier, R. F. Boisvert, and C. W. Clark. *NIST handbook of mathematical functions hardback and CD-ROM*. Cambridge university press, 2010.
190. M. Abramowitz and I. A. Stegun. *Handbook of mathematical functions with formulas, graphs, and mathematical tables*. Vol. 55. US Government printing office, 1964.

CURRICULUM VITAE

Xin Lu

PhD in Physics

xin.lu@universite-paris-saclay.fr

Laboratoire de Physique des Solides

(+33) 0637237899

University Paris-Saclay

(+86) 13971001499

Orsay, France

EDUCATION

University Paris-Saclay, Orsay, France

Ph.D. Student in Physics, 2018-2021

École Normale Supérieure Paris, Paris, France

Master 2 (eq. M.Sc.) in Condensed Matter Physics of ICFP Program, 2017-2018

École Polytechnique, Palaiseau, France

Titre d'Ingénieur diplômé de l'École Polytechnique (Graduate Engineer), 2014-2017

Master 1 (eq. first year of M.Sc.) in Physics, 2016-2017

Licence 3 (eq. B.S.) in Physics, 2014-2016

Lycée Louis Le Grand, Paris, France

Classes Préparatoires aux Grandes Ecoles in Physics-Chemistry, 2012-2014

- Two-year training for the competitive examinations to French engineer school,

- eq. first two years of undergraduate study

AWARDS & SCHOLARSHIPS

Allocations Doctorales AMX, French Ministry of Higher Education and Research, 2018-2021

Bourse de la Fondation de l'X, Fondation de l'X, 2014-2018

PUBLICATIONS

1. [X. Lu](#) and M. O. Goerbig, “Magneto-optical signatures of Volkov-Pankratov states in topological insulators”, 2019 *EPL*, **126** 67004.
2. [X. Lu](#) and M. O. Goerbig, “Dirac quantum well engineering on the surface of topological insulator”, 2020 *Physical Review B*, **102**(15), 155311. (*Editors' Suggestion*)
3. [X. Lu](#) D. K. Mukherjee and M. O. Goerbig, “Surface plasmonics of Weyl semimetals”, 2021 *Physical Review B*, **104**(14), 155103.
4. S. Zhang, [X. Lu](#) and J. Liu, “Correlated insulators, density wave states, and their nonlinear optical response in magic-angle twisted bilayer graphene”, arXiv:2109.11441
5. J. Wyzula, [X. Lu](#), D. Santos-Cottin, D. K. Mukherjee, I. Mohelsky, F. Le Mardele, J. Novak, M. Novak, R. Sankar, Y. Krupko, B. A. Piot, W.-L. Lee, A. Akrap, M. Potemski, M. O. Goerbig and M. Orlita, “Lorentz-boost-driven magneto-optics in a Dirac nodal-line semimetal”, arXiv:2110.07266

SCHOOLS & CONFERENCES

731. WE-Heraeus-Seminar, on line, Germany, Oct. 2020

Topic: Dynamics of emerging quasiparticles in topological Dirac materials

Ecole de Physique des Houches - Summer School, on line, France, Jul. 2020

Topic: Emergent electronic states confined at interfaces

GDR 2426 Physique Quantique Mésooscopique, Aussois, France, Dec. 2019

Poster: Magneto-optical signatures of gapped nodal lines in NbAs₂ and the hyperbolic transformation

Emergent Phenomena in Correlated Quantum Matter - Summer School, Cargèse, France, Aug. 2019

GDR 2426 Physique Quantique Mésooscopique, Aussois, France, Dec. 2018

Poster: Magneto-optical Signatures of Volkov-Pankratov States in Topological Insulators

LANGUAGE

Chinese: native

English: fluent and professional

French: fluent and professional

REFERENCE

Dr. Mark-Oliver Goerbig

Directeur de recherche

Laboratoire de Physique des Solides, CNRS, Université Paris-Saclay

Bureau S112-1er-Sud - Bâtiment 510, 91405 Orsay cedex

mark-oliver.goerbig@universite-paris-saclay.fr

+33.1.69.15.76.65

TITRE: Propriétés spectroscopiques des matériaux topologiques étudiées à l'aide de l'équation de Dirac

MOTS CLÉS: Matériaux topologiques, Équation de Dirac, Spectroscopie magnéto-optique, États de surface

RÉSUMÉ: L'équation de Dirac et ses variantes sont omniprésentes dans la description à basse énergie des matériaux topologiques incluant les isolants topologiques et les semi-métaux topologiques mais aussi leurs états de surface protégés. Leurs propriétés spectroscopiques pourraient être étudiées théoriquement en se basant sur le Hamiltonien de Dirac correspondant. D'une part, grâce à la symétrie de Lorentz sous-jacente des Hamiltoniens de Dirac, la renormalisation relativiste se manifeste sous la forme de la renormalisation de gap qui offre une signature expérimentale claire et directe dans la spectroscopie magnéto-optique.

D'autre part, la théorie de la réponse linéaire appliquée au Hamiltonien de Dirac correspondant prédit une signature magnéto-optique des états de surface massifs au-delà des états de surface chiraux et topologiquement protégés. Ces états de surface massifs, qui sont aussi appelés états de Volkov-Pankratov, émergent génériquement aux surfaces douces des matériaux topologiques. L'origine de leur apparition peut être considérée de façon équivalente comme une conséquence soit d'un pseudo-champs magnétique soit d'un effet du confinement quantique.

TITLE: Dirac equation approach to the spectroscopic properties of topological materials

KEYWORDS: Topological materials, Dirac equation, Magneto-optics, Surface states

ABSTRACT: The Dirac equation and its variants are ubiquitous in the low-energy description of topological materials ranging from topological insulators to semimetals as well as their topologically protected surface states. Their spectroscopic properties can be studied theoretically with the help of the corresponding Dirac Hamiltonian. On the one hand, thanks to the underlying Lorentz symmetry of the Dirac Hamiltonians, the relativistic renormalization manifests itself as the renormalization of the band gap resulting in a

clear-cut experimental signature in magneto-optics. On the other hand, the magneto-optical signature of additional massive surface states of topological materials are also predicted using linear response theory and the corresponding Dirac Hamiltonians. These massive states called Volkov-Pankratov states arise generically on a smooth surface of topological materials. Their emergence can be equivalently seen as a consequence of a pseudo-magnetic field and/or of a quantum confinement effect.